

ADVANCES IN GRAVITY BASED HEIGHT SYSTEMS

ROBERT KINGDON

January 2012



TECHNICAL REPORT
NO. 292

ADVANCES IN GRAVITY BASED HEIGHT SYSTEMS

Robert Kingdon

Department of Geodesy and Geomatics Engineering
University of New Brunswick
P.O. Box 4400
Fredericton, N.B.
Canada
E3B 5A3

January 2012

© Robert Kingdon, 2012

PREFACE

This technical report is a reproduction of a dissertation submitted in partial fulfillment of the requirements for the degree of Doctor of Philosophy in the Department of Geodesy and Geomatics Engineering, January 2012. The research was supervised by Dr. Marcelo Santos and Dr. Petr Vaníček, and funding was provided by Natural Sciences and Engineering Research Council of Canada (NSERC), Taiwan's National Science Council (NSC), Geomatics for Informed Decisions (GEOIDE) Network of Centres of Excellence, and Trainor Surveys. Delayed publication of this technical report was due to an oversight.

As with any copyrighted material, permission to reprint or quote extensively from this report must be received from the author. The citation to this work should appear as follows:

Kingdon, Robert (2012). *Advances in Gravity Based Height Systems*. Ph.D. dissertation, Department of Geodesy and Geomatics Engineering, Technical Report No. 292, University of New Brunswick, Fredericton, New Brunswick, Canada, 275 pp.

Dedication

To my wife, family, and friends, who have supported and sustained me during my research and writing. Also, to the scientists who have come before me, upon whose shoulders I stand.

Abstract

In order to have physical meaning, a height system must have some relation to the Earth's gravity field. Of the height systems that do, orthometric heights match best with our intuitive understanding of height. The orthometric height of a point is the distance travelled along a plumbline from that point to the geoid, and can be arrived at either directly from leveling and gravity observations or indirectly by converting geodetic heights to orthometric heights using a geoid model. This dissertation investigates recent advances in orthometric height determination, to find out whether orthometric height determinations can meet modern centimetre-level accuracy requirements. Persistent barriers to improving orthometric height accuracy have been the impossibility of fully modeling topographical density effects, the lack of suitable numerical methods, and the lack of sufficient data.

The problem is addressed in six articles. The first two deal with direct calculation of orthometric heights, providing a practical implementation of a rigorous theory of orthometric heights able to deliver sub-centimetre accuracy in most cases, and showing that numerical errors in this process can be kept below the one centimetre level. The next two articles address the problem of the unknown density distribution in geoid determination, describing a framework for including the full three-dimensional effect of topographical density, and demonstrating that existing laterally-varying density models can provide sub-centimetre results in most areas. Vertical density variations neglected in such models are only expected to reduce accuracy to a few centimetres in mountainous areas. The fifth article demonstrates a new method for downward continuation of gravity

anomalies, one of the largest numerical barriers to accurate geoid determination. The final article evaluates satellite altimetry as a source of gravity data over lakes, finding it promising but in need of further refinement.

The ultimate conclusion is that the physically meaningful system of orthometric heights can be now realized to about a centimetre in most areas, given suitable data, although in some especially challenging areas (e.g. mountain ranges) errors of several centimetres must be accepted.

Acknowledgements

Thanks especially to Profs. Petr Vaníček and Marcelo Santos. Since my undergraduate days, Prof. Vaníček has fed me a perfect mix of critique and affirmation, spurring my intellectual growth. His uncompromising pursuit of truth in scientific research has been a welcome counter to the ever-present temptation to resign myself to an incomplete understanding. Dr. Santos has repeatedly shown me the value of my work when I have not seen it, and has taught me to share it with others. I would not have progressed so far, nor had such a rich variety of experiences, without him. I am grateful also to Dr. Karl Butler for his careful readings of my drafts and thoughtful suggestions as a member of my supervisory committee and of my examining board, and to my external reviewer, Dr. Spiros Pagiatakis, who did a thorough and very helpful reading of my dissertation even over the Christmas holidays. Thanks also to the remainder of my examining board, Dr. Peter Dare and Dr. Sanjeev Seahra, whose reviews and questions made my dissertation accessible to readers beyond my own discipline.

I am grateful for the advice and encouragement of Drs. Robert Tenzer and Artu Ellmann in the first few years of my studies, and to Dr. Chienway Huang, Dr. Mavuto Tembo, and Mr. Lucky Kabanga, all of whom I have been privileged to work with and learn from with at various times. I am also grateful to Prof. James Secord who, in all of our academic interactions, has shown me the value of honesty and of careful, diligent work.

I acknowledge the various organizations that have funded my research over the years, especially the National Sciences and Engineering Research Council of Canada

(NSERC), but also the National Science Council (NSC) of Taiwan, the Geomatics for Informed Decisions (GEOIDE) network, and Trainor Surveys. I am grateful also for the various scientific organizations that have facilitated my interactions with other researchers; especially the Canadian Geophysical Union (CGU), but also the American Geophysical Union (AGU) and the International Association of Geodesy (IAG). Furthermore, I acknowledge the International Baccalaureate (IB) program, which laid in my mind a strong foundation in physics, mathematics, logic and language, but more importantly which maintained my interest in learning in a public school system that had otherwise ceased to challenge me. Without the IB program, I would never have progressed so far in the academic world.

I am grateful for the friendship and helpfulness of my fellow graduate students at the university. This applies to all of the students with whom I have interacted, but most especially to David Avalos, Liliana Sukeova, Maciej Bazanowski, Felipe Nievinski, James Mtamakaya, and Azadeh Koohzare. Their companionship has eased my passage through graduate school. I have also appreciated the advice of Professor Arthur James of the Classics department, who over years has given the best and most serendipitous advice on my academic career.

Finally, and most importantly, I thank my wife, Susan Kingdon; my parents, David and Anita; my siblings, Laura and Andrew; and my friends, especially Garth Christie and David Brodie. These people were breadcrumbs in my maze of geodetic thoughts, reminding me that there are important things in the world apart from geodesy. They have helped me to develop the character and wisdom necessary to pursue my studies with diligence, honesty, and prudence.

Table of Contents

Dedication	ii
Abstract	iii
Acknowledgements	v
Table of Contents	vii
List of Figures	xi
List of Tables.....	xiv
List of Symbols	xv
Chapter 1: Introduction	1
1.1 Definition of objectives	1
1.2 Background to orthometric height determination.....	4
1.2.1 Determination of orthometric heights from leveling and gravity observations	4
1.2.2 Effects on gravity of the topographical masses.....	7
1.2.3 Effects on gravity of the non-topographical masses	10
1.2.4 Helmert mean gravity and its improvements	11
1.3 Background to geoid calculations.....	14
1.3.1 Calculation of orthometric heights from geodetic height observations	14
1.3.2 Methods of geoid determination	16
1.3.3 Gravity anomalies in the Stokes-Helmert method	17
1.3.4 Transformation to and from the Helmert space	19
1.3.5 Downward continuation of gravity anomalies	24
1.3.6 Determination of cogeoidal heights by Stokes’s integration	26
1.4 Review of developments in orthometric height and Stokes–Helmert geoid determination.....	29
1.4.1 Developments in determining orthometric heights from leveling	29
1.4.2 Developments in the Stokes-Helmert method of geoid modeling	33
1.4.3 Data sources for determination of orthometric heights and the geoid.....	37
1.5 Significance of included articles.....	40
1.5.1 General comments on included articles	40
1.5.2 Articles dealing with corrections to Helmert orthometric heights	41
1.5.3 Articles on errors in laterally-varying density models for geoid determination	44
1.5.4 Articles dealing with numerical and data issues	46
Chapter 1 References.....	48
Chapter 2: Toward an improved orthometric height system for Canada	62
Chapter 2 Abstract	63
2.1 Introduction.....	64
2.2 Corrections to Helmert orthometric heights	66

2.3 The test area.....	70
2.4 The effect of terrain roughness.....	73
2.5 The effect of laterally-varying anomalous density.....	76
2.6 The geoid-generated gravity disturbance.....	80
2.7 Total corrections to Helmert orthometric height.....	83
2.8 Summary and conclusions.....	86
Chapter 2 Acknowledgements.....	86
Chapter 2 References.....	88
Chapter 3: Computationally efficient corrections to Helmert orthometric heights for terrain and density effects.....	90
Chapter 3 Abstract.....	90
3.1 Introduction.....	91
3.2 Framework for calculating topographical corrections.....	96
3.2.1 General form of second order corrections to mean gravity.....	96
3.2.2 Evaluation of terrain and topographical density corrections using Newton integrals.....	98
3.2.3 Application for terrain and density effects.....	101
3.3 Approach to numerical integration.....	106
3.3.1 Reduction of integral dimensionality.....	106
3.3.2 Approach to numerical integration.....	109
3.3.3 Computation overview.....	114
3.4 Results.....	116
3.4.1 Testing integration zone parameters using a “tower” scenario.....	116
3.4.2 Canadian test area.....	118
3.4.3 Magnitude of the corrective terms.....	123
3.4.4 Improvements in computation time.....	125
3.5 Conclusions.....	127
Chapter 3 References.....	130
Chapter 3 Appendix I: Simplified integration kernels.....	134
Chapter 3 Appendix II: Removal of Newton kernel singularities.....	136
Chapter 4: Modeling topographical density for geoid determination.....	140
Chapter 4 Abstract.....	141
4.1 Introduction.....	142
4.2 Methodology.....	147
4.2.1 Modeling of topographical density.....	147
4.2.2 The Newton kernel and its radial derivative for calculation of effects on gravity and gravity potential.....	148
4.2.3 Mathematical representation of 3-D density and condensed density models.....	151
4.2.4 Calculations of 3-D anomalous density effects on geoid and gravity.....	154
4.2.5 Numerical evaluation of the DTE, PITE, and SITE.....	157
4.2.6 Criteria for verification of results.....	163

4.3 Results and discussion	167
4.3.1 Results demonstrating the capability of simulation software.....	167
4.3.2 Verification of results.....	175
4.4 Conclusions.....	181
Chapter 4 Acknowledgements.....	183
Chapter 4 References.....	184
Chapter 5: Effects of hypothetical complex mass-density distributions	
on geoidal height.....	188
Chapter 5 Abstract.....	188
5.1 Introduction.....	189
5.2 Methodology.....	192
5.2.1 3D density modeling in the Stokes-Helmert context	192
5.2.2 Numerical considerations.....	196
5.2.3 Proposed tests.....	198
5.3 Results.....	202
5.3.1 Case A	202
5.3.2 Case B	204
5.4 Conclusions.....	205
Chapter 5 References.....	206
Chapter 6: Poisson downward continuation solution by the Jacobi method.....	208
Chapter 6 Abstract.....	208
6.1 Introduction.....	209
6.2 The theory.....	214
6.3 Results and discussion.....	219
6.3.1 Test area and data sets.....	219
6.3.2 Comparison of three methods for solving the downward continuation.....	222
6.3.3 Comparison of Jacobi results using varying tolerances	225
6.3.4 Testing the choice of tolerance based on the condition number	228
6.4 Conclusions.....	230
Chapter 6 References.....	232
Chapter 7: Gravity anomalies from retracked ERS and Geosat altimetry	
over the Great Lakes: accuracy assessment and problems	234
Chapter 7 Abstract.....	235
7.1 Introduction.....	236
7.2 Methodology.....	238
7.2.1 Preparation of terrestrial gravity data.....	238
7.2.2 Preparation of ERS-1/GM and Geosat/GM data.....	241
7.2.3 Calculation of gravity anomalies from terrestrial and satellite altimetry data.....	245
7.2.4 Assessment of results	247
7.3 Results.....	248

7.3.1 Comparison of area results	248
7.3.2 Comparisons along test profiles	251
7.3.3 Statistical examination of results	260
7.4 Conclusion	262
Chapter 7 References	264
Chapter 8: Conclusion	266
8.1 Summary of findings from the 6 articles	266
8.1.1 Articles dealing with corrections to Helmert orthometric heights	266
8.1.2 Articles on errors in laterally-varying density models for geoid determination	267
8.1.3 Articles dealing with numerical and data issues	270
8.1.4 Summary of Contributions	271
8.2 Recommendations for further study	272
Chapter 8 References	275

Vita

Publications

Conference Papers

List of Figures

1.1	The plumbline and the geoid.	2
1.2	Bouguer shell representation of topography.	8
1.3	Masses inducing the terrain effect.	9
1.4	Masses inducing the anomalous density effect.	10
1.5	Relationship between geodetic and orthometric heights (after Heiskanen and Moritz [1967, Figure 4-7]).	15
1.6	Base map of the test area for Chapters 2 and 3, with 1 km contours.	42
2.1	Components of rigorous gravity related to topography.	67
2.2	Orthometric heights within the test area, 500 m contours.	71
2.3	Laterally-varying anomalous densities within the test area, anomalous density indicated by tone. Data from the Geological Survey of Canada.	72
2.4	NT Geoid-generated gravity disturbances within the test area, 50 mGal contours.	72
2.5	Correction to Helmert mean gravity for terrain roughness within the test area, 40 mGal contours.	75
2.6	Correction to Helmert orthometric heights for terrain roughness within the test area, 10 cm contours.	75
2.7	Correction to Helmert mean gravity for laterally-varying anomalous density within the test area, 10 mGal contours.	78
2.8	Correction to Helmert orthometric heights for laterally-varying anomalous density within the test area, 2 cm contours.	79
2.9	Correction to Helmert mean gravity for the geoid-generated gravity disturbance within the test area, 10 mGal contours.	82
2.10	Correction to Helmert orthometric heights for the geoid- generated gravity disturbance within the test area, 5 cm contours.	82
2.11	Total corrections to Helmert mean gravity for the spherical terrain effect, the effect of laterally-varying anomalous density, and the geoid-generated gravity disturbance, within the test area. 30 mGal contours.	84
2.12	Total corrections to Helmert orthometric height for the spherical terrain effect, the effect of laterally-varying anomalous density, and the geoid-generated gravity disturbance within the test area. 5 cm contours.	85
3.1	Masses causing the terrain effect on gravity.	103
3.2	Masses inducing the density effect on gravity modeled as horizontally varying only.	105

3.3	Arrangement of integration zones about a computation point.....	112
3.4	Flow chart of computation.....	115
3.5	Heights (a) and rock densities (b) in the test area.....	119
3.6	Density correction for values of outer zone radius incremented by 1°.....	121
3.7	Terrain (a) and density (b) corrections to orthometric height.....	124
3.A1	Radially integrated integration kernel with respect to distance from the computation point, for $r = R + H_{max}$, $r_a = R$ and $r_b = r$, and $H_{max} = 8,800$ m.....	136
4.1	Spherical coordinate system for evaluation of Newton integrals. See text for definition of parameters.....	148
4.2	DTE on gravity and PITE on gravity potential, resulting from a disc 500 m thick, 40 km in diameter, with anomalous density of 660 kg/m ³ , with center 500 m deep, and embedded in 2000 m thick topography.....	168
4.3	DTE, PITE, and the total effect of anomalous density on geoidal height for discs 500 m thick, 40 km in diameter, with anomalous density of 660 kg/m ³ , with centers 1000 m deep, embedded in 2000 m thick topography, and rotated to 0.5°, 1°, and 5° from horizontal.....	171
4.4	Effects of 3-D anomalous density of Lake Superior on geoidal height.....	174
4.5	DTE and PITE against height to disc center for discs 200 m thick, 40 km in diameter, with anomalous density of 660 kg/m ³ , embedded in 2000 m thick topography, with varying heights to disc center, and with varying horizontal integration intervals.....	176
4.6	DTE and PITE against height to disc center for discs 200 m thick, 40 km in diameter, with anomalous density of 660 kg/m ³ , embedded in 2000 m thick topography, and with varying heights to disc center, from both analytical and numerical integration with 1 arcsecond step.....	178
5.1	Topographical density distribution used for testing. $w = 3300$ m for DTE tests, and $w = 110\,000$ m for PITE tests.....	201
5.2	DTE on gravity for case A.....	202
5.3	DTE on geoidal height for case A.....	203
5.4	PITE on geoidal height for case B.....	204
6.1	Helmert gravity anomalies over the study area.....	221
6.2	Heights of topography over the study area.....	222
6.3	Result for Δg from Jacobi iterative approach based on norm of the δt vector.....	224
6.4	Downward continuation effect from the Jacobi iterative method with testing of the δt vector with (a) 0.05 mGal, (b) 0.5 mGal, (c) 5 mGal and (d) 50 mGal tolerances.....	226
6.5	Number of iterations of the Jacobi method vs. tolerance chosen for convergence testing.....	228

6.6	Downward continuation effect of Jacobi method using a tolerance of 6.7 mGal.	229
7.1	Terrestrial (a) and shipborne/airborne (b) gravity coverage around the Great Lakes.	240
7.2	ERS-1/GM (a) and Geosat/GM (b) data coverage for the Great Lakes.	242
7.3	ERS-1/GM (a) and Geosat/GM (b) outliers for the Great Lakes.	243
7.4	Results of free-air anomaly calculation for the Great Lakes.	248
7.5	Bathymetry of the Great Lakes.	249
7.6	EIGEN-GL04C free-air anomalies over the Great Lakes.	250
7.7	Results of comparisons with terrestrial gravity results.	252
7.8	Profiles showing gravity for P1 (a) and P4 (b) from EIGEN-GL04C, shipborne, and satellite altimetry results.	254
7.9	Profiles showing gravity for P9 (a) and P10 (b) from EIGEN-GL04C, airborne, and satellite altimetry results.	256
7.10	Profiles showing gravity for P6 (a) and P13 (b) from EIGEN-GL04C, shipborne, and satellite altimetry results.	258

List of Tables

2.1	Corrections to Helmert orthometric height for the spherical terrain effect, the effect of laterally-varying anomalous density, and the geoid-generated gravity disturbance within the test area.....	86
3.1	Integration parameters before refinement.....	117
3.2	Integration parameters sufficient to accurately sample the integration kernel for the terrain effect.....	118
3.3	Zonal contributions to the terrain and density effects.	122
3.4	Statistics of the terrain and density corrections to orthometric height.	125
3.5	Computation time with and without various modifications.	126
4.1	Integration zone sizes and resolutions.	158
4.2	Worst case errors to date for DTE and PITE, determined by comparison with an analytical result for a disc having density contrast of 660 kg/m ³ in 2000 m thick topography.....	181
6.1	Statistics of results from three computation methods.....	224
6.2	Statistics of the downward continuation effect for the Jacobi iterative method with testing of the δt vector using various tolerances.	227
7.1	Statistics of differences in free-air anomalies between altimetry, EIGEN-GL04C and shipborne/airborne results (all values in mGal).....	260

List of Symbols

Symbol	Meaning	Chapters
$(p_1)_a^r$	value calculated in simplified kernel evaluation	3
$(p_2)_b^r$	value calculated in simplified kernel evaluation	3
$(p_3)_a^r$	value calculated in simplified kernel evaluation	3
$(p_4)_b^r$	value calculated in simplified kernel evaluation	3
(p_5)	value calculated in simplified kernel evaluation	3
(p_6)	value calculated in simplified kernel evaluation	3
(p_7)	value calculated in simplified kernel evaluation	3
$(p_8)_{a,b}^r$	value calculated in simplified kernel evaluation	3
A	gravity from a mass distribution.....	4
A^a	effect of real atmospheric masses on gravity	1
A_c^a	effect of condensed atmospheric masses on gravity	1
$A_{\delta p}^c$	effect of condensed 3D anomalous masses on gravity.....	4
A^t	effect of real topographical masses on gravity	1
A_c^t	effect of condensed topographical masses on gravity	1
$A_{\delta p}^t$	effect of real 3D anomalous masses on gravity.....	4
b_{ij}	i -th and j -th element of the \mathbf{B} matrix	6
\mathbf{B}	matrix representing the discrete Poisson upward continuation.....	1,6
c_g	correction to mean gravity.....	1
$c_{\bar{g}}^H$	correction to Helmert mean gravity	1
c_H^D	density correction to Helmert height.....	3
$c_{\bar{g}}^E$	correction to mean gravity for effect E	3
$c_{H^H}^E$	correction to Helmert orthometric height for effect E	3
c_H^T	terrain correction to Helmert height	3
C	geopotential number	1,3
C_{ee}	geoid gradient- geoid gradient covariance matrix.....	7
C_{eg}	geoid gradient-gravity anomaly covariance matrix.....	7
C_{ge}	gravity anomaly-geoid gradient covariance matrix.....	7
C_{gg}	gravity anomaly- gravity anomaly covariance matrix.....	7
C_H^D	central cell contribution to density correction to height.....	3
D_e	matrix representing noise in the geoid gradient data.....	7
D_g	matrix representing noise in the gravity anomaly data	7
e	geoid gradient.....	7

e_{ref}	reference geoid gradient	7
e_{res}	residual geoid gradient	7
f	function being integrated.....	3
f_{ij}	value of function f at Ω_{ij}	3
g	gravity at an integration point	1,3
g^E	contribution of effect E to point gravity.....	3
g_B^T	Bouguer shell effect on gravity	2
g_R^T	terrain roughness effect on gravity.....	2
$g^{\delta\rho}$	anomalous density effect on gravity.....	2
\bar{g}	mean gravity along a plumbline	1–3
\bar{g}^E	contribution of effect E to mean gravity along the plumbline	3
\bar{g}^H	Helmert mean gravity	1–3
\bar{g}_B^T	Bouguer shell effect on gravity	2
\bar{g}_R^T	terrain roughness effect on gravity.....	2
$\bar{g}^{\delta\rho}$	anomalous density effect on gravity.....	2
G	Newton’s gravitational constant.....	3,4
h	geodetic height	1,3
H	height along the plumbline of an integration point	1
	orthometric height of a point.....	2,3
H_{max}	maximum height in computation area.....	6
H_t	height of a point on the topographical surface	4
H^H	Helmert orthometric height	1,3
H^{max}	maximum height on Earth	3
H^O	orthometric height	1–3
i	counter in a summation	1,3,4
	computation point number	6
I	identity matrix	6
j	counter in a summation	3
	integration point number	6
K	height effect integration kernel in spherical coordinates	3
	Newton kernel	5
K^P	height effect kernel in planar coordinates	3
\tilde{K}	radially integrated height effect kernel.....	3
L	Euclidean distance between two points.....	3,4
$L_{p,q}$	Euclidean distance between points p and q	4
L^P	Euclidean distance between two points, calculated in planar coordinates	3
\widetilde{L}^{-1}	Radial integral of inverse Euclidean distance between two points	4
M	number of integration points	6

n	height along the normal to the ellipsoidal surface.....	1
	number of data points in numerical integration	3
	number of density layers in a 3D topographical density distribution	4
	number of sub-cells used for calculating averaged Poisson kernel.....	6
N	geoid-ellipsoid separation	1
	Newton kernel	2,3
	number of computation points.....	6
N^H	cogeoid-ellipsoid separation.....	1
\tilde{N}	radially integrated Newton kernel	3
O	order of error in numerical integration.....	3
p	precision of the input gravity anomalies	6
r	geocentric radius of a computation point	1–6
r'	geocentric radius of an integration point.....	1–6
r_a	lower boundary of radial integration.....	3
r_b	upper boundary of radial integration.....	3
	geocentric radius of lake bed.....	4
r_g	geocentric radius of a point on the geoid	1,4,5
r_i	geocentric radius to the bottom of the i -th density layer.....	4
	geocentric radius of the i -th computation point	6
r_l	geocentric radius to the bottom of a disc.....	4
r_{max}	maximum geocentric radius in a test area	6
r_t	geocentric radius of a point on the Earth's surface	4,5
r_u	geocentric radius to the top of a disc.....	4
R	mean radius of the reference ellipsoid.....	1,3–6
S	Stokes's kernel	1,4,5
T	tolerance for convergence of Jacobi iterations.....	6
T^H	disturbing potential in the Helmert space.....	1
U	normal potential.....	1
v	integration volume element.....	3
V	gravitational potential from a density distribution	4
V^a	effect of real atmospheric masses on gravity potential	1
V_c^a	effect of condensed atmospheric masses on gravity potential	1
$V_{\delta p}^c$	effect of condensed 3D anomalous masses on gravity potential.....	4
V^t	effect of real topographical masses on gravity potential.....	1
V_c^t	effect of condensed topographical masses on gravity potential.....	1
$V_{\delta p}^t$	effect of real 3D anomalous masses on gravity potential.....	4
V^E	contribution of effect E to gravity potential	3
W	gravity potential.....	1
W^H	gravity potential in the Helmert space.....	1
W_0	gravity potential at the geoid.....	1

x	planar coordinate of computation point	3
\mathbf{x}_P	coordinate triplet for point P	3
x'	planar coordinate of integration point	3
y	planar coordinate of computation point	3
y'	planar coordinate of integration point	3
z	distance along the plumbline / planar coordinate of computation point.....	3
z'	planar coordinate of integration point	3
γ	normal gravity	1–3
	normal gravity on the reference ellipsoid.....	4,5
γ_0	normal gravity on the reference ellipsoid.....	1
$\bar{\gamma}$	mean normal gravity along the plumbline.....	2
$\delta^{g(k)}$	difference between the k -th and $(k-1)$ -st estimate of gravity anomalies on the geoid.....	6
$\delta^{t(k)}$	difference between the k -th estimate of gravity anomalies on the surface and the known anomalies on the surface	6
δA^a	direct atmospheric effect (DAE)	1
δA^t	direct topographical effect on gravity (DTE).....	1
$\delta A_{PITE, \delta\rho}$	PITE on gravity from 3D anomalous density.....	4
$\delta A_{\delta\rho}$	DTE on gravity from 3D anomalous density	4
δg	gravity disturbance	1
δg_i	gravity difference along the i -th segment of a leveling line.....	1
δg^{NT}	no-topography gravity disturbance.....	2
$\overline{\delta g}^{NT}$	mean no-topography gravity disturbance along the plumbline	2
δL_i	height difference along the i -th segment of a leveling line	1
$\delta N_{DTE, \delta\rho}$	DTE on the geoid from 3D anomalous density.....	4
$\delta N_{PITE, \delta\rho}$	PITE on the geoid from 3D anomalous density	4
$\delta N_{SITE, \delta\rho}$	SITE on the geoid from 3D anomalous density	4
δN^a	primary indirect atmospheric effect (PIAE).....	1
δN^t	primary indirect topographical effect (PITE).....	1
$\delta N_{DTE}^{\delta\rho}$	DTE on geoid from 3D anomalous density.....	5
$\delta N_{PITE}^{\delta\rho}$	PITE on geoid from 3D anomalous density	5
$\delta V_{\delta\rho}$	PITE on gravity from 3D anomalous density.....	4
$\delta\gamma^t$	secondary indirect topographical effect (SITE)	1
$\delta\gamma^a$	secondary indirect atmospheric effect (SIAE)	1
$\delta\rho$	laterally-varying anomalous topographical density	3
	3D or laterally-varying anomalous topographical density	4
	3D anomalous topographical density	5
$\overline{\delta\rho}$	laterally-varying anomalous topographical density	5
$\delta\rho_i$	topographical density of mass i	1
$\delta\rho_D$	topographical density of a disc.....	4

$\delta\rho_{i,i+1}$	topographical density of mass between interfaces i and $i+1$	4
$\delta\sigma$	condensed anomalous density	4,5
$\delta\sigma_D$	condensed anomalous density of a disc.....	4
Δd	horizontal distance between along-track points from altimetry	7
Δg	gravity anomaly	1,7
$\Delta \mathbf{g}_g$	vector of gravity anomalies on the geoid	1
Δg_{ref}	reference gravity anomaly	7
Δg_{res}	residual gravity anomaly over lakes.....	7
$\Delta \mathbf{g}_s$	vector of gravity anomalies on the topographical surface.....	1
$\Delta \mathbf{g}^g$	vector of gravity anomalies on the geoid	6
$\Delta \mathbf{g}^{g(k)}$	k-th estimate of vector of gravity anomalies on the geoid	6
Δg^h	Helmert gravity anomaly.....	6
$\Delta \mathbf{g}^s$	vector of gravity anomalies on the topographical surface.....	6
$\Delta \mathbf{g}^{s(k)}$	k-th estimate of vector of gravity anomalies on the topographical surface	6
Δg^H	Helmert gravity anomaly.....	1
Δg_i^h	Helmert gravity anomaly at the i -th computation point	6
Δg_j^h	Helmert gravity anomaly at the j -th integration point.....	6
Δg_{res}^{land}	residual gravity anomaly over land	7
Δh	height difference between along-track points from altimetry	7
$\Delta \varphi$	size of cell in latitude direction	3,6
$\Delta \lambda$	size of cell in longitude direction	3,6
$\Delta \Omega$	cell size in radians squared.....	6
$\Delta \Omega_{ij}$	area of cell surrounding Ω_{ij}	3
ε_{g-qg}	geoid-quasigeoid correction	1
$\varepsilon_{\bar{g}}$	correction to Helmert's mean gravity.....	2
ε_{H^o}	correction to Helmert's orthometric height.....	2
$\varepsilon_{\bar{g}g}$	ellipsoidal correction	1
$\varepsilon^{(k)}$	downward continuation effect.....	6
$\varepsilon_{DTE}^{\delta\rho}$	effect on the DTE on gravity of 3D anomalous density.....	5
$\varepsilon_{PITE}^{\delta\rho}$	effect on the PITE on gravity potential of 3D anomalous density	5
κ_{max}	maximum condition number of the \mathbf{B} matrix	6
κ	condition number of the \mathbf{B} matrix	6
λ	computation point longitude.....	1,3,4,6
λ_i	longitude of computation point i	6
λ_j	longitude of integration point j	6
$\lambda_{j,k}$	latitude of interpolation point k within integration cell j	6
λ'	integration point longitude	3,4,6
ρ	topographical density	1, 3–5

ρ_0	mean topographical density.....	1, 3–5
ρ_1	topographical density other than ρ_0	4
$\bar{\rho}$	mean topographical density, averaged vertically or throughout crust	4
φ	computation point latitude.....	1,3,4,6
φ'	integration point latitude	3,4,6
φ_i	i -th latitude coordinate in a numerical integration region	3
	latitude of computation point i	6
φ_j	latitude of integration point j	6
$\varphi_{j,k}$	latitude of interpolation point k within integration cell j	6
ψ	spherical angular distance between two points	1–4
ψ_D	spherical angular distance between the centre and edge of a disc	4
Ω	solid angle denoting the latitude and longitude of a computation point.....	1–5
Ω'	solid angle denoting the latitude and longitude of an integration point	1–5
Ω_0	radius of a spherical cap	3–5
Ω_c	spherical coordinates of the axis of symmetry of a disc	4
Ω_{ij}	value of Ω for the i -th latitude and j -th longitude in a numerical integration region	3
ℓ	Euclidean distance between two points.....	1,2,6
$\ \cdot\ _{L1}$	L_1 norm.....	6

Chapter 1: Introduction

1.1 Definition of objectives

This dissertation seeks to answer the question: can a physically meaningful height system be precisely realized? A physically meaningful height system must be related to the Earth's gravity field. The most intuitive such system is orthometric heights, which takes the geoid as its datum, and defines the height of a point as the length of the plumbline extending from that point to the geoid (e.g., Heiskanen and Moritz [1967, chapter 4]). The goal for precise heights for the past 20 years has been an accuracy of 1 cm or better (e.g., Vaníček and Martinec [1994]; Sansò and Rummel [1997]; Roman and Smith [2002]; Ellmann and Vaníček [2007]).

A plumbline is a line always tangent to the direction of Earth's gravity, or in other words, always perpendicular to the equipotential surfaces of Earth's gravity field [Heiskanen and Mortiz, 1967], as shown in Figure 1.1.

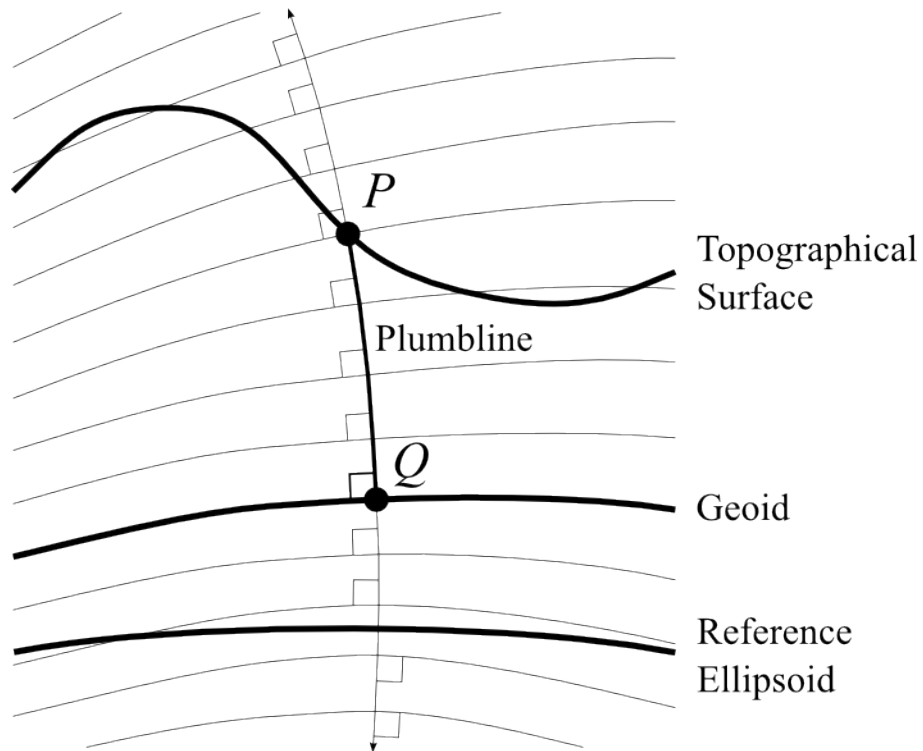


Figure 1.1: The plumblines and the geoid.

For any point in space, only one plumblines exists. The orthometric height of the point is the distance along the plumblines from the point to the geoid, as indicated by the bold line between P and Q in Figure 1.1. While systems other than orthometric heights may be useful for specific computational purposes, as is the case with geodetic or dynamic heights (e.g., Heiskanen and Moritz [1967, chapter 4]), only orthometric heights are defined in this intuitive manner.

The term “geoid” was introduced by Listing [1873] to refer to the “mathematical figure of the Earth” first described by Gauss in [1828]. It is defined as the equipotential surface of the Earth’s gravity field that fits best to the global mean sea level (e.g., Heiskanen and Moritz [1967, chapter 2-2]; Vaníček and Krakiwsky [1986, chapter 6.4]).

The geoid is physically meaningful because it is tied to the Earth's gravity field, like the plumbline, but also because it represents the level at which seawaters would stabilize if they were at rest. The real sea surface deviates from the geoid by up to 1.5 m [Knudsen et al., 2011], because of ocean currents and atmospheric effects [Wunsch, 1993].

Although heights in the similarly popular normal height system (e.g., Heiskanen and Moritz [1967, chapter 4-6]) evaluated at the geoid will all equal zero, they are otherwise not distances from a point to the geoid, and the geoid serves as a datum only for orthometric heights, dynamic heights, and geopotential numbers (e.g., Vaniček and Krakiwsky [1986, section 16.4]). Normal heights [Molodensky, 1945] measured at the topographical surface give distance from the point of interest to the quasigeoid [Molodensky et al., 1962], a surface similar to the geoid and having a geometrical meaning, but not an equipotential surface of the Earth's real gravity field, and without any physical meaning [Heiskanen and Moritz, 1967, section 8-3]. Normal heights may differ from orthometric heights by up to several decimetres for very mountainous areas (e.g., Sjöberg [1995]; Flury [2009]). Dynamic heights, first proposed by Helmert [1884], have no geometrical meaning [Heiskanen and Moritz, 1967, section 4-6], and are only used in specific applications dealing with water flow [Vaniček and Krakiwsky, 1986, section 16.4]. Geopotential numbers, while arguably more physically meaningful than orthometric heights, are not given as linear distances [Vaniček and Krakiwsky, 1986, section 16.4] and so are not heights as we normally conceive them. Of all the height systems orthometric heights describe heights as they are usually conceived and used, i.e. above the geoid and in standard linear units. Thus, they are the heights most useful in engineering practice (e.g., Vaniček and Krakiwsky [1986, section 16.4]; Featherstone et

al. [1998]). By contrast, for normal heights of points not on the topographical surface, and dynamic heights, the linear units used to state the height of such points will vary in length depending on the point's height.

1.2 Background to orthometric height determination

1.2.1 Determination of orthometric heights from leveling and gravity observations

Orthometric heights are determined from: (1) geodetic leveling and gravity observations (e.g., Heiskanen and Moritz [1967, Chapter 4]), or (2) geodetic heights above a reference ellipsoid. In the latter case, geodetic heights are converted to orthometric heights using a model of the geoid-ellipsoid separation, a.k.a. the geoidal height [Featherstone et al., 1998]. In the former case, geopotential numbers of points of interest are calculated using observations of gravity and height differences, and these are converted into orthometric heights.

For a point P at geodetic latitude, φ_P , and longitude, λ_P (indicated by the dummy variable Ω_P) and geocentric radius r_P , the geopotential number, $C(\Omega_P, r_P)$, is defined as the difference between the gravity potential, W_0 , at the geoid, and the gravity potential, $W(\Omega_P, r_P)$, at P (Heiskanen and Moritz [1967, eq. 4-8]):

$$C(\Omega_P, r_P) = W_0 - W(\Omega_P, r_P). \quad (1.1)$$

The geopotential number at any point on the geoid, therefore, is zero. The geopotential number of a point of interest is determined relative to the geopotential number at another

nearby point, P_0 , by summing up the products of leveled height differences, δL_i , and observed gravity differences, δg_i , along the i segments of a leveling line running from P_0 to P (cf., Vaniček and Krakiwsky [1986, eq. 16.88]):

$$C(\Omega_P, r_P) \approx C(\Omega_{P_0}, r_{P_0}) + \sum_i \delta L_i \delta g_i . \quad (1.2)$$

Once the geopotential number is obtained, the orthometric height, $H^O(\Omega_P, r_P)$, is found by dividing by the integral mean value of gravity along the plumbline [Heiskanen and Moritz, 1967, eq. 4-21]:

$$H^O(\Omega_P, r_P) = \frac{C(\Omega_P, r_P)}{\bar{g}(\Omega_P, r_P)} , \quad (1.3)$$

where [Heiskanen and Moritz, 1967, eq. 4-20]:

$$\bar{g}(\Omega_P, r_P) = \frac{1}{H^O(\Omega_P, r_P)} \int_{H=0}^{H_P^O} g(\Omega, H) dH , \quad (1.4)$$

where H is an integration variable representing height along the plumbline, and Ω represents the geodetic coordinates of the point along the plumbline at height H , so that eq. (1.4) is the line integral of gravity along the plumbline. In practice, the integral mean value of gravity is not directly observed. Its observation may be possible using borehole

gravimetry (e.g., Strange [1982]), but it would not be cost effective to apply this method for every benchmark in a leveling network. Instead, the integral mean is calculated using a model of Earth's gravity field and topographical masses (e.g., Tenzer et al. [2005]).

As an alternative to using eqs. (1.2) through (1.4), individual leveled height differences can be converted to orthometric height differences, by applying an *orthometric correction*. This approach is discussed in a variety of publications (e.g., Heiskanen and Mortiz [1967, section 4-4]; Strang van Hees [1992]; Hwang and Hsiao [2003]). While not pursued within this dissertation, the orthometric correction approach also relies on mean gravity along the plumbline, and so the present document has bearing on it.

For the purpose of evaluating mean gravity along the plumbline, the Earth's gravity field is divided into topographical and non-topographical effects [Santos et al., 2006]. The topographical effects are induced by masses between the geoid and the surface of the Earth (i.e. the topography), and include the Bouguer shell effect, the terrain effect, and the anomalous density effect. The non-topographical effects include the normal gravity, the geoid-generated gravity disturbance, and the atmospheric effects. Orthometric heights incorporating all of these gravitational effects in their calculation are called *rigorous orthometric heights* [Tenzer et al., 2005]. When we discuss these effects on gravity, we mean their contribution to gravity at a computation point, and not the horizontal components of their gravitational effect.

1.2.2 Effects on gravity of the topographical masses

The Bouguer shell effect is an approximation of the whole topographical effect. It is the effect on gravity of a spherical shell, with thickness equal to the topographical height at the point of interest, which we designate P , and homogeneous density normally equal to the average topographical density of 2670 kg/m^3 (e.g., Takin and Talwani [1966]; Karl [1971]; Vaniček et al. [2001]). The shell approximates topography exactly at P , and well in the immediate neighbourhood of P , especially for smooth topography. It is a bad approximation far from P , but the resulting inaccuracy in the topographical effect on gravity at P is relatively small, because distant masses have far less influence on the gravitational effect at P than nearby ones. As a result, the Bouguer shell is a good approximation for estimating the topographical effects on gravity. Since its second order and higher effects are relatively small (e.g., Takin and Talwani [1966]), the gravitational effect of the Bouguer shell is reasonably well approximated by using only first order (linear) terms to calculate its effect. The Bouguer shell representation of topography is shown in Figure 1.2, where the shaded area indicates the masses inducing the gravitational effect. The density of the masses, ρ , is considered equal to the average topographical density ρ_0 , and is usually assigned the value 2670 kg/m^3 .

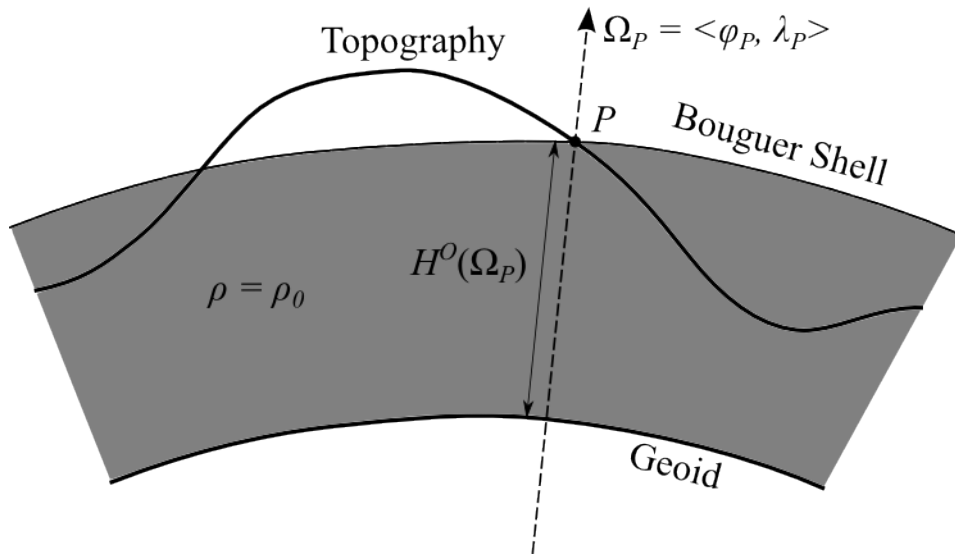


Figure 1.2: Bouguer shell representation of topography.

Most of the error in the Bouguer shell representation of topography can be corrected by adding the effects of the variations of the actual topographical surface relative to the upper surface of the spherical shell. These variations are called *terrain*, and their effects are calculated using a model of the actual topographical surface, nowadays taken from a digital elevation model, or DEM (e.g., Bott [1959]; Sünkel [1986]; Tenzer [2005]). Gravitational effects of the topography above the shell, which were omitted from the Bouguer shell approximation, are added when applying the terrain effect on gravity. Effects of the topography erroneously included within the Bouguer shell are removed. Since both of these operations decrease gravity at P , except for effects of topography above the shell but below the horizon, the terrain effect on gravity at P is expected to be mostly negative. The masses generating the terrain effect are shown in Figure 1.3.

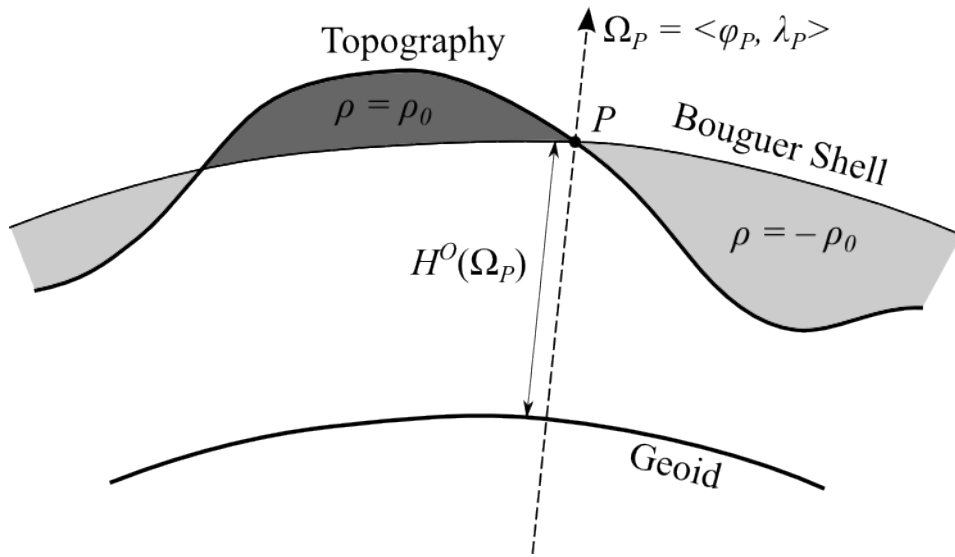


Figure 1.3: Masses inducing the terrain effect.

The sum of the terrain and Bouguer shell effects completely models topography of constant density. However, in reality the density of topography varies three-dimensionally above and below the assumed constant value. The gravitational effect induced by these positive and negative density anomalies is called the anomalous density effect [Tenzer et al., 2005], and can be calculated by integration over density variations given by a digital density model, or DDM (Sünkel [1986]; Tenzer et al. [2005]). Masses generating the anomalous density effect are shown in Figure 1.4, where $\delta\rho_i$ indicates the anomalous density of mass i , calculated using $\delta\rho_i = \rho_i - \rho_0$, and ρ_i is the actual density of mass i .

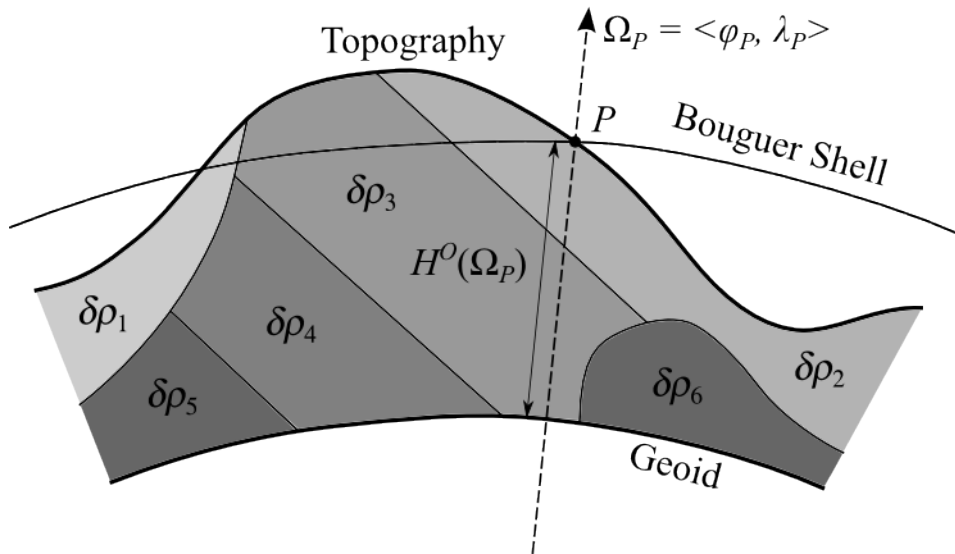


Figure 1.4: Masses inducing the anomalous density effect.

In practice, the full three-dimensional distribution of topographical density is unknown, and so assumptions must be made in creating DDMs from existing data (e.g., Sünkel [1986]; Chiou [1997]; Fraser et al. [1998]; Allister and Featherstone [2001]).

1.2.3 Effects on gravity of the non-topographical masses

The normal gravity is the gravity generated by a biaxial reference ellipsoid; that is, an ellipsoid that best approximates the geoid, as described by Pizzetti [1894] and Somigliana [1930]. Normal gravity comprises over 99.9% of the Earth's gravity, and for this reason normal heights, which are calculated based only on the normal gravity component of mean gravity, approximate orthometric heights relatively well [Flury, 2009]. The normal gravity can be calculated exactly using a simple formula for any set of ellipsoidal parameters (e.g., Moritz [2000]). Also, the gradient of normal gravity along the normal to the ellipsoid is known exactly, and the first vertical derivative

provides an accurate first order estimate of differences in normal gravity with respect to height [Heiskanen and Moritz, 1967]. If a better estimate is required, the second and higher order vertical derivatives of the normal gravity may be used as well [Tenzer et al., 2005].

The no-topography (NT) geoid-generated gravity disturbance [Vaniček et al., 2004] is the effect on gravity of the masses not modeled by the other effects. This includes the effect of masses contained between the geoid and the surface of the reference ellipsoid, and variations of mass density within the reference ellipsoid that are not symmetric about its primary axis (and thus not included in normal gravity formulas). The NT gravity disturbance is determined by subtracting the other gravitational effects from observed gravity at the topographical surface [Vaniček et al., 2004], and then continuing the result downward as required. By calculating the average value of the disturbance along the plumbline, its contribution to mean gravity may be determined [Tenzer et al., 2005]. The downward continuation is an inverse operation, and requires that the NT gravity disturbance be known over an area surrounding the point of interest (cf., Martinec [1996]). If the NT gravity disturbance is already known on the geoid as the byproduct of geoid determination efforts, it may be upward continued to the desired level [Santos et al., 2006].

1.2.4 Helmert mean gravity and its improvements

An alternative to evaluating mean gravity directly as the sum of the above effects, is to consider gravity observed on the topographical surface at a particular computation point

as a first estimate of the mean value of gravity, and to refine this estimate by adding corrective terms. The mean gravity computed according to this approach is given by:

$$\bar{g}(\Omega_P, r_P) = g(\Omega_P, r_P) + c_g(\Omega_P, r_P), \quad (1.5)$$

where g_P is the gravity at point P , and the correction, c_g , is calculated using a trivial rearrangement of eq. (1.5) (cf., the correction to Helmert gravity in Santos et al. [2006, eq. (14)]):

$$c_g(\Omega_P, r_P) = \bar{g}(\Omega_P, r_P) - g(\Omega_P, r_P). \quad (1.6)$$

The original Helmert prescription for mean gravity [Helmert, 1890] follows the formulation in eq. (1.6). The corrective term is always very small, since the gravitational effects of most masses on mean and on surface gravity are similar.

The corrective term in eq. (1.5) can be separated into the contributions of several gravitational effects, just as with the effects on mean gravity in sections 1.2.2 and 1.2.3 [Santos et al., 2006]. Originally, it was evaluated using only the first order components of the normal gravity effect and the Bouguer shell effect (e.g., Helmert [1890]; Heiskanen and Moritz [1967]). Evaluated in this way, eq. (1.6) becomes a linear function of computation point height, and eq. (1.5) becomes the well-known formula for Helmert mean gravity (Heiskanen and Moritz [1967, eq. 4-24]):

$$\bar{g}^H(\Omega_p, r_p) = g(\Omega_p, r_p) + 0.0424 \text{ mgal/m} \times H^O(\Omega_p, r_p). \quad (1.7)$$

Heights determined using the mean gravity from eq. (1.7), called Helmert heights or Helmert orthometric heights (e.g., Heiskanen and Moritz [1967, section 4-4]), may be further refined by adding some or all of the remaining corrective terms [Santos et al., 2006]. A correction, $c_{\bar{g}^H}(\Omega_p, r_p)$, can be applied to Helmert mean gravity (cf., Santos et al. [2006, eq. (14)]):

$$\bar{g}(\Omega_p, r_p) = \bar{g}^H(\Omega_p, r_p) + c_{\bar{g}^H}(\Omega_p, r_p), \quad (1.8)$$

or, the correction can be applied to already calculated Helmert heights, $H^H(\Omega_p, r_p)$, using [Santos et al., 2006, eq. (15)]:

$$H^O(\Omega_p, r_p) = H^H(\Omega_p, r_p) - \frac{H^H(\Omega_p, r_p)}{\bar{g}^H(\Omega_p, r_p)} c_{\bar{g}^H}(\Omega_p, r_p), \quad (1.9)$$

based on the first two terms of the Taylor series:

$$\begin{aligned} H^O(\Omega_p, r_p) &= H^H(\Omega_p, r_p) - \frac{H^H(\Omega_p, r_p)}{\bar{g}^H(\Omega_p, r_p)} c_{\bar{g}^H}(\Omega_p, r_p) + \frac{H^H(\Omega_p, r_p)}{[\bar{g}^H(\Omega_p, r_p)]^2} [c_{\bar{g}^H}(\Omega_p, r_p)]^2 - \dots \\ &= H^H(\Omega_p, r_p) \sum_{i=0}^{\infty} \left(\frac{-c_{\bar{g}^H}(\Omega_p, r_p)}{\bar{g}^H(\Omega_p, r_p)} \right)^i. \end{aligned} \quad (1.10)$$

The truncation after the first order term is sufficient because the magnitude of the effects neglected in the Helmert approach are less than 0.05% of Helmert's mean gravity in magnitude [Santos et al., 2006].

1.3 Background to geoid calculations

1.3.1 Calculation of orthometric heights from geodetic height observations

Three-dimensional terrestrial or satellite positioning provide heights of a point P above a specified ellipsoid (e.g., Vaníček and Krakiwsky [1986, part IV]). In modern applications, this is always a reference ellipsoid, such as the GRS80 [Moritz, 2000] or the almost identical WGS-84 ellipsoid [National Imaging and Mapping Agency, 2000]. The resulting geodetic heights, h_P , are different from the heights previously discussed because they are geometric quantities [Vaníček and Krakiwsky, 1986, section 16.4]. If the geoidal height corresponding to point P , $N(\Omega_P)$, is known, the orthometric height can be calculated from the geodetic height using the formula (e.g., Featherstone et al. [1998, eq. (1)]):

$$H(\Omega_P, r_P) \approx h(\Omega_P, r_P) - N(\Omega_P), \quad (1.11)$$

based on the approximate geometrical relationship shown in Figure 1.5.

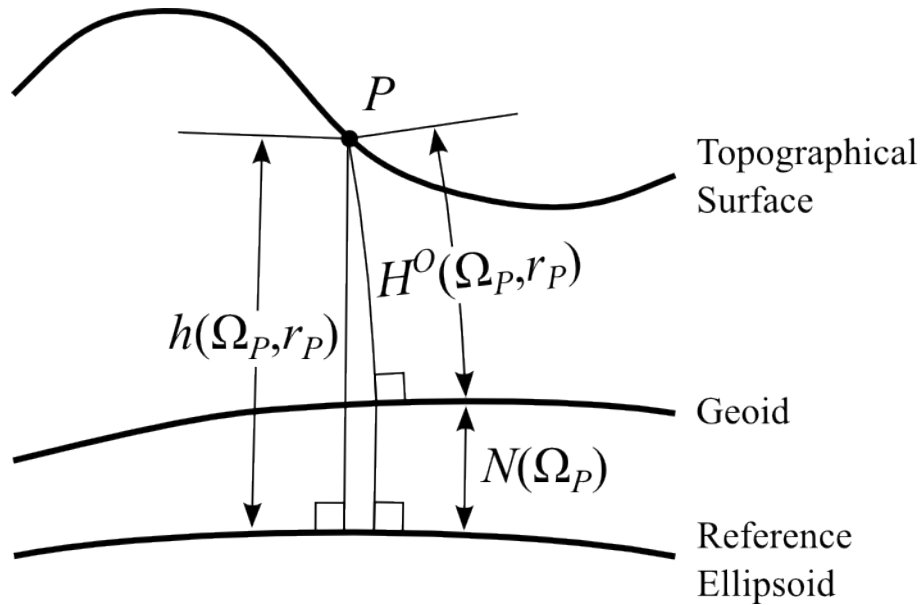


Figure 1.5: Relationship between geodetic and orthometric heights (after Heiskanen and Moritz [1967, Figure 4-7]).

Eq. (1.11) is approximate because the orthometric height, geoidal height and geodetic height are all measured along different paths; however, the approximation is good to better than 1 mm anywhere on Earth, and is considered negligible in practice (e.g., Zilkoski and Hothem [1989]; Henning et al. [1998]; Meyer et al. [2006]). Eq. (1.11) is valuable because it allows heights to be determined using global navigation satellite systems (GNSS), which can now produce height observations far more quickly than traditional leveling methods, and with similar accuracies so long as an accurate geoid model is used [Featherstone, 2008]. In practice GNSS is especially accurate when determining geodetic height differences along a baseline. The geodetic height difference between two points, P and Q may be converted into an orthometric height difference according to (e.g., Engelis et al. [1984, eq. (2)]):

$$[H(\Omega_P, r_P) - H(\Omega_Q, r_Q)] \approx [h(\Omega_P, r_P) - h(\Omega_Q, r_Q)] - [N(\Omega_P) - N(\Omega_Q)]. \quad (1.12)$$

1.3.2 Methods of geoid determination

The above method of determining orthometric heights relies heavily on accurate geoid determination. Methods of determining the geoid use gravimetric or geometric data sets, or a mixture of both. Common gravimetric data include measurements of Earth's gravity or spherical harmonic representations of the Earth's gravity potential (e.g., Sjöberg [2003]; Véronneau et al. [2006]; Ellmann and Vaníček [2007]). Geometric data includes measures of the geometry of Earth's gravity field, such as sea surface heights or gradients, or geoidal heights from GPS observations at orthometric height benchmarks (e.g. Völgyesi [2005]). Deflections of the vertical (e.g. Vaníček and Merry [1973]) may be seen as either gravimetric or geometric data sets. These data sources may be combined through statistical methods such as least squares collocation (e.g., Roman et al. [2004]; Featherstone and Sproule [2006]), though this is a complex and sometimes unreliable procedure. While recent statistical approaches show promise (e.g., Featherstone and Sproule [2006]), gravimetric methods, and especially the Stokes-Helmert method (e.g., Vaníček and Krakiwsky [1987]; Vaníček and Martinec [1994]), promise centimetre-level accuracy, if adequate data are available [Ellmann and Vaníček, 2007]. This accuracy is expected to improve as new gravity data become available. Promising new missions such as the European Space Agency's Gravity Field and Steady-state Ocean Circulation Explorer (GOCE) [Rummel et al., 2009], the Jason-2 Ocean Surface Topography Mission (OSTM) [Lambin et al., 2010], and new airborne

gravity campaigns, such as the National Geodetic Survey's GRAV-D project [NOAA/NGS, 2007], provide gravity anomalies of progressively higher accuracy and resolution.

There are several common approaches to calculating gravimetric geoids, all of which address the problem by the same four general steps, which are (cf., Martinec et al. [1993]; Huang et al. [2001]):

1. transforming gravity data into a suitable computation space (e.g., the Helmert space),
2. reducing transformed anomalies to the cogeoid level,
3. converting the anomalies on the cogeoid into cogeoidal heights, and
4. transforming the cogeoidal heights into geoidal heights.

The *cogeoid* is the equipotential surface in the computation space corresponding to the geoid in the real space. The following discussion will describe how these steps are performed in the *Stokes-Helmert method* (e.g., Vaníček and Martinec [1994]; Vaníček et al. [1999]), a common and accurate implementation, in which the computation space is called the *Helmert space*.

1.3.3 Gravity anomalies in the Stokes-Helmert method

The Stokes-Helmert method takes gravity anomalies, $\Delta g(\Omega_P, r_P)$, as its input. The gravity anomaly is calculated from observed gravity according to (e.g., Vaníček et al. [2004, eq. (8)]):

$$\Delta g(\Omega_P, r_P) = g(\Omega_P, r_P) - \gamma(\Omega_P, r_T), \quad (1.13)$$

where $g(\Omega_P, r_P)$ is the observed gravity at point P , and $\gamma(\Omega_P, r_T)$ is the normal gravity evaluated at the point on the telluroid corresponding to P . The *telluroid* is the surface whose normal height above the reference ellipsoid is equal to the orthometric height of topography above the geoid [e.g. Vaníček and Krakiwsky, 1986, section 7.4]. Since eq. (1.13) uses evaluations of gravity at particular surfaces, and is blind to its three-dimensional variation, it is called the *surface gravity* anomaly [Vaníček et al., 2004]. Historically, eq. (1.13) has sometimes been evaluated using normal gravity on the ellipsoid rather than on the telluroid; however such a formulation is only valid when the computation point is on the geoid.

The similar Hotine method of geoid computation [Hotine, 1969], instead of the gravity anomaly, uses the gravity disturbance, $\delta g(\Omega_P, r_P)$ (e.g., Heiskanen and Moritz [1967, eq. 2-141]), which is the difference between the observed and normal gravity at P . The values of the gravity disturbance are becoming more readily available with the widespread use of satellite positioning systems (e.g., Hackney and Featherstone [2003]). However, since most gravity data are associated with orthometric heights, the gravity anomaly is still especially useful [Vaníček et al., 2004].

Gravity anomalies are transformed into a computation space so the usual methods of solving boundary-value problems (e.g., Kellogg [1929]) for potential fields can be applied (e.g., Vaníček and Martinec [1994]). These methods require the gravity potential to be harmonic outside of the boundary, which in our application will be the geoid.

Thus, the computation must be performed in a space where all masses above the geoid have been displaced on or below it, and several such spaces have been proposed (e.g., Helmert [1884]; Bjerhammer [1964]; Heck [2003]). Computing the transformation of gravity anomalies to such a space is strictly impossible, because the distribution of rock-densities within the topography is not known and their effects cannot be exactly modeled [Vaníček and Martinec, 1994]. However, approximate modeling of these effects is feasible (e.g., Huang et al. [2001]; Kuhn [2003]), and choosing a computation space that displaces the masses as little as possible minimizes the approximation errors. Such a space is the Helmert space, formed according to Helmert's second condensation method, in which all topographical masses are compressed in an infinitesimally thin layer on the geoid called the *condensation layer* [Helmert, 1884]. The gravity anomalies once converted to the Helmert space are called Helmert anomalies.

1.3.4 Transformation to and from the Helmert space

The most significant component of the transformation into the Helmert space is the *direct topographical effect* (DTE), $\delta A^t(\Omega_p, r_p)$, and is given by [Martinec, 1993, eq. (4.12)]:

$$\delta A^t(\Omega_p, r_p) = A_c^t(\Omega_p, r_p) - A^t(\Omega_p, r_p), \quad (1.14)$$

where $A_c^t(\Omega_p, r_p)$ is the gravitational attraction of the condensed topography, and $A^t(\Omega_p, r_p)$ is the gravitational attraction of the real topography. The second term on the right

hand side of eq. (1.14) is evaluated by Newton integration over the volume of topography, exactly as with the gravimetric effects in orthometric height determination. The first term is evaluated by integration over the two-dimensional condensed topographical masses [Vaniček and Martinec, 1994b]. As with all of the topographical and atmospheric terms in the transformation, the effect of the real masses is removed, and replaced with the effect of the condensed masses.

For computational purposes, topographical effects in the transformations to and from Helmert space are often decomposed in the same way as the effect on the mean gravity in section 1.2, into a Bouguer shell effect, a terrain effect, and an anomalous density effect (e.g., Martinec [1993]). While calculating the Bouguer shell effect requires only that the height of computation point P be known, calculating the terrain effect additionally requires topographical heights from a DEM (e.g., Martinec et al. [1996]), and the anomalous density effect requires a DDM [Huang et al., 2001].

Since all mass exterior to the geoid must be condensed onto its surface, a *direct atmospheric effect* (DAE), $\delta A^a(\Omega_P, r_P)$, must also be applied. This is done analogously to the DTE (e.g., Novák [2000, eq. (4.120)]):

$$\delta A^a(\Omega_P, r_P) = A_c^a(\Omega_P, r_P) - A^a(\Omega_P, r_P), \quad (1.15)$$

where $A_c^a(\Omega_P, r_P)$ is the gravitational attraction of the condensed atmospheric masses and $A^a(\Omega_P, r_P)$ is the gravitational attraction of the real atmospheric masses. For calculating the atmospheric effect, a DEM provides topographical heights while an

atmospheric density model (e.g., ISO [1972]; Picone et al. [2002]) gives the atmospheric density variation.

When the topographical and atmospheric masses are displaced, the Earth's gravity potential field changes, affecting the shape and location of both the geoid and the telluroid, as well as the normal gravity evaluated on the telluroid [Vaníček et al., 1999]. The difference in geoidal height between the Helmert and real spaces arising from the difference in the topographical gravity potential is called the *primary indirect topographical effect* (PITE), $\delta N^t(\Omega_P)$. The PITE on geoidal height is given by (cf., Martinec [1993, eqs. (1.5) and (1.16)]):

$$\delta N^t(\Omega_P) = \frac{V'_c(\Omega_P, r_g[\Omega_P]) - V'(\Omega_P, r_g[\Omega_P])}{\gamma_0(\Omega_P)}, \quad (1.16)$$

where $V'_c(\Omega_P, r_g[\Omega_P])$ is the gravitational potential induced by the condensed topographical masses at the point on the geoid with horizontal coordinates Ω_P , which are the same horizontal coordinates as P , and radial coordinate $r_g[\Omega_P]$, and $V'(\Omega_P, r_g[\Omega_P])$ is the gravitational potential induced by the real topographic masses at that point. Since the PITE on geoidal height reflects a transformation of potential from the real to the Helmert space, it can be subtracted from cogeoidal heights to convert them back to geoidal heights in the real space [Martinec and Vaníček, 1994a]. It is thus the main component of the transformation of the cogeoid into the geoid. As with the DTE, the PITE requires

a DEM to evaluate the terrain component, and a DDM to calculate the anomalous density component.

The atmospheric effect corresponding to the PITE is the *primary indirect atmospheric effect* (PIAE), $\delta N^a(\Omega_P)$. It is calculated according to (cf., Novák [2000, eq. (4.110)]):

$$\delta N^a(\Omega_P) = \frac{V_c^a(\Omega_P, r_g[\Omega_P]) - V^a(\Omega_P, r_g[\Omega_P])}{\gamma_0(\Omega_P)}, \quad (1.17)$$

where $V_c^a(\Omega_P, r_g[\Omega_P])$ is the gravitational potential induced by the condensed atmospheric masses at the geoid, and $V^a(\Omega_P, r_g[\Omega_P])$ is the gravitational potential induced by the real atmospheric masses at the geoid. Like the PITE, this must be subtracted to convert the calculated cogeoid back to the geoid in the real space (e.g., Ellmann and Vaníček [2007]).

The effect of condensation on normal gravity at the telluroid is very small, and the resulting effect on the geoid is on the order of a few millimetres [Vaníček et al., 1999]. This topographical effect on the normal gravity is called the *secondary indirect topographical effect* (SITE), $\delta\gamma^t(\Omega_P, r_P)$, and the atmospheric effect is called the *secondary indirect atmospheric effect* (SIAE), $\delta\gamma^a(\Omega_P, r_P)$. The latter is so small that it is rarely calculated, while the first is calculated by (cf., Vaníček et al. [1999, eq. (36)]):

$$\delta\gamma^t(\Omega_P, r_P) = \frac{2}{r_g(\Omega_P)} [V_c^t(\Omega_P, r_P) - V^t(\Omega_P, r_P)]. \quad (1.18)$$

Some additional terms are required for accurate transformation to the Helmert space, to account for errors introduced by the formulation of the problem in spherical coordinates ($\varepsilon_{\delta g}$) and for the use of orthometric rather than normal heights in calculating the normal gravity at the telluroid (ε_{g-qq}). For a test area in the Canadian Rockies, the magnitudes of these corrections are up to 1.4 cm and 3 cm in magnitude respectively [Vaníček et al., 1999]. The transformation into Helmert gravity anomalies, $\Delta g^H(\Omega_P, r_P)$, is given by (e.g., Huang [2001, eq. (1)]):

$$\begin{aligned} \Delta g^H(\Omega_P, r_P) = & \Delta g(\Omega_P, r_P) + \delta A^l(\Omega_P, r_P) + \delta A^a(\Omega_P, r_P) + \\ & + \delta\gamma^l(\Omega_P, r_P) + \delta\gamma^a(\Omega_P, r_P) + \varepsilon_{\delta g}(\Omega_P, r_P) + \varepsilon_{g-qq}(\Omega_P, r_P). \end{aligned} \quad (1.19)$$

Once the Helmert cogeoid has been computed from Stokes's integration, it must be converted back to the real space. The transformation of the cogeoidal height, $N^H(\Omega_P)$, into the geoidal height is given by subtraction of the PITE and PIAE on height from the cogeoidal height (cf., Ellmann and Vaníček [2007, eq. (12)]):

$$N(\Omega_P) = N^H(\Omega_P) - \delta N^l(\Omega_P) - \delta N^a(\Omega_P). \quad (1.20)$$

1.3.5 Downward continuation of gravity anomalies

Once the gravity anomalies at the topographical surface have been transformed into the Helmert space, they must be reduced to the geoid level. Determining gravity anomalies above the geoid from those on the geoid is relatively straightforward. The field given by $r \cdot \Delta g(\Omega_P, r)$ is harmonic outside the geoid, so that if the values of $r_g(\Omega_P) \cdot \Delta g(\Omega_P, r_g[\Omega_P])$ are known on the geoid, the values of $r \cdot \Delta g(\Omega_P, r)$ external to the geoid can be found by solving *Dirichlet's problem* [Heiskanen and Moritz, 1967, section 1-16]. This is an instance of the first boundary value problem of potential theory (e.g., Kellogg [1929, section IX.4]), and is solved by a Fredholm integral of the first kind [Fredholm, 1900] called Poisson's integral (e.g., Heiskanen and Moritz [1967, eq. (6-74)]):

$$\Delta g(\Omega_P, r_P) = \frac{(r_g[\Omega']^2 (r_P^2 - [r_g(\Omega')]^2))}{4\pi r_P} \iint_{\Omega'} \frac{\Delta g(\Omega', r_g[\Omega'])}{\ell^3(\Omega_P, r_P; \Omega', r_g[\Omega'])} d\Omega', \quad (1.21)$$

where:

$$\ell(\Omega, r; \Omega', r') = \sqrt{r^2 + r'^2 - 2rr' \cos\psi[\Omega, \Omega']}, \quad (1.22)$$

or the straight line (Euclidean) distance between P and the running integration point, and $\psi(\Omega, \Omega')$ is the spherical angular distance between positions Ω and Ω' . To downward continue gravity anomalies to the geoid, we must solve the inverse problem: given

gravity anomalies on the topographical surface, determine the values on the geoid (e.g., Vaníček and Martinec [1994]).

While the downward continuation problem is well posed in the Hadamard sense [Hadamard, 1923, section 1.1], no continuous solution can be formulated mathematically, and so only a discrete solution is possible [Wong, 2002]. Written in a discrete form, in matrix-vector notation, the direct problem is (cf., Vaníček et al. [1996, eq. (12)]):

$$\Delta \mathbf{g}_s = \mathbf{B} \Delta \mathbf{g}_g, \quad (1.23)$$

where $\Delta \mathbf{g}_s$ is the vector of gravity anomalies at the topographical surface, $\Delta \mathbf{g}_g$ is the vector of gravity anomalies on the geoid, and \mathbf{B} is the matrix composed of integral kernels relating the two. The inverse operation, which provides values of gravity on the geoid given those on the topographical surface, is then given by:

$$\Delta \mathbf{g}_g = \mathbf{B}^{-1} \Delta \mathbf{g}_s. \quad (1.24)$$

Although a solution to eq. (1.24) always exists, finding the solution presents a significant numerical challenge due to frequent ill-conditioning, and some regularization is necessary to solve it [Martinec, 1996].

1.3.6 Determination of cogeoidal heights by Stokes's integration

Once Helmert gravity anomalies have been determined on the surface of the geoid, they are converted to disturbing potentials in the Helmert space, $T^H(\Omega_P, r_g[\Omega_P])$. The disturbing potential is the difference between the actual gravity potential on the geoid in the Helmert space, $W^H(\Omega_P, r_g[\Omega_P])$, and the normal potential, $U(\Omega_P, r_g[\Omega_P])$ (e.g., Heiskanen and Moritz [1967, section 2-13]). It can be converted into the cogeoidal height, $N^H(\Omega_P)$ using an approximation to Bruns's formula (Heiskanen and Moritz [1967, eq. (2-144)]; cf., Bruns [1878, p. 20]):

$$N^H(\Omega_P) \approx \frac{T^H(\Omega_P, r_g[\Omega_P])}{\gamma_0(\Omega_P)}. \quad (1.25)$$

The error in the approximation in eq. (1.25) is never more than 1.5 mm, and so it is negligible [Vaníček and Martinec, 1994].

The computation of disturbing potentials from gravity anomalies is an example of the third boundary-value problem of potential theory, in this case called the geodetic boundary value problem (e.g., Heiskanen and Moritz [1967, section 1-17]), expressed in the fundamental equation of physical geodesy [Heiskanen and Moritz, 1967, eq. (2-148)]:

$$\left. \frac{\partial T^H(r, \Omega)}{\partial n} \right|_{r=r_g(\Omega)} - \frac{1}{\gamma_0(\Omega)} \frac{\partial \gamma}{\partial n} T^H(\Omega, r_g[\Omega]) = -\Delta g^H(\Omega, r_g[\Omega]), \quad (1.26)$$

where n is the normal to the ellipsoidal surface. A highly accurate solution is found by applying the appropriate Green's function for a sphere, resulting in Stokes's integral [Stokes, 1849]. While this spherical formulation can cause errors that are significant by modern standards [Martinec and Grafarend, 1997], these errors are avoided if a higher-degree reference field is used for computing the low-frequency constituents of the disturbing potential, as is often the case in practice [Vaníček and Featherstone, 1998; Ardestani and Martinec 2002]. Stokes's integral for determining disturbing potential on the geoid from gravity anomalies on the geoid is given by (e.g., Heiskanen and Moritz [1967, eq. (2-161)]):

$$T^H(\Omega_p, r_g[\Omega_p]) = \frac{R}{4\pi} \iint_{\Omega'} \Delta g^H(\Omega', r_g[\Omega']) S(\psi[\Omega_p, \Omega']) d\Omega', \quad (1.27)$$

where (e.g., Heiskanen and Moritz, 1967, eq. (2-164)):

$$S(\psi) = \frac{1}{\sin(\psi/2)} - 6 \sin \frac{\psi}{2} + 1 - 5 \cos \psi - 3 \cos \psi \ln \left(\sin \frac{\psi}{2} + \sin^2 \frac{\psi}{2} \right), \quad (1.28)$$

where the variable ψ is a shorthand for $\psi(\Omega_p, \Omega')$. Eq. (1.27) may be substituted into eq. (1.25) to calculate the Helmert cogeoidal height directly (e.g., Heiskanen and Moritz [1967, eq. (2-165)]):

$$N^H(\Omega_p) = \frac{R}{4\pi\gamma_0(\Omega_p)} \iint_{\Omega'} \Delta g^H(\Omega', r_g[\Omega']) S(\psi[\Omega_p, \Omega']) d\Omega'. \quad (1.29)$$

Practical evaluation of eq. (1.29) is not simple because it strictly requires global integration, but reduced terrestrial Helmertized gravity anomalies are not available globally, and may only be available or available with sufficient quality locally [Vaniček and Sjöberg, 1991]. To overcome this problem, it is useful to replace the usual Stokes's kernel in eq. (1.28) with a kernel modified to reduce the weight of the contribution of distant gravity anomalies in the computation (e.g., Wong and Gore [1969]; Sjöberg [1984]; Vaniček and Kleusberg [1987]). Even using such a modified kernel, limiting the integration to a small “near zone” around the computation point causes considerable error. For this reason, precise geoid determination also uses a global geopotential model (GGM) to evaluate in spectral form the portion of the integral outside of the near zone, called the far zone contribution or the truncation error (e.g., Hernandez et al. [2002]).

The Stokes's kernel may also be written in a “spheroidal” form that omits certain spherical harmonic bands from the Stokes's integration [Vaniček and Sjöberg, 1991]. Using this formulation, the low-frequency components of the geoid are not evaluated from terrestrial data during Stokes's integration, and can be computed separately using spherical harmonic synthesis based on a GGM (e.g., Vaniček and Sjöberg [1991]). Thus, the long-wavelength accuracy of GGMs from satellite gravity potential observations can be exploited, while retaining the high accuracy of terrestrial observations at short wavelengths.

1.4 Review of developments in orthometric height and Stokes–Helmert geoid determination

1.4.1 Developments in determining orthometric heights from leveling

The original prescription for orthometric heights was formulated by Helmert [1890] based on the Poincaré-Prey gradient, and contains the first order approximation of the Bouguer shell effect and the first order effect of normal gravity. It is accurate to within a few decimetres in mountainous areas [Santos et al., 2006]. Strange [1982] has shown by a comparison with mean gravity from borehole gravimetry that Helmert’s method models the real mean gravity along the plumbline very well, and suggests that in most areas it is accurate to about 3 cm. Because it is straightforward and requires only the data already available from leveling operations, Helmert’s method remains useful for approximate heighting.

Due mainly to the unknown density distribution within topography, topographical modeling has been persistent barrier to improving the accuracy of orthometric heights (e.g., Rapp [1961]; Heiskanen and Moritz [1967]; Strange [1982]; Allister and Featherstone [2001]; Tenzer et al. [2005]). Methods for modeling the constant density effect of topography, including terrain effects, have been in place since the early 1900’s (e.g., Hayford and Bowie [1912]). Since the 1930’s, inclusion of terrain effects on gravity in orthometric height calculation (e.g., Niethammer [1932]; Mader [1954]; Krakiwsky [1965]; Sünkel [1986]) has increased orthometric height accuracy by several decimetres, or an order of magnitude, in mountainous areas. Although terrain effects relative to a Bouguer shell (as opposed to a plate) had been used for some time in

geophysical applications (e.g., Takin and Talwani [1966]), they were not used in orthometric height calculations until relatively recently (e.g., Featherstone et al. [2001]; Tenzer et al. [2005]; Santos et al. [2006]), and the plate model is still sometimes applied (e.g., Hwang and Hsiao [2003]).

Since Helmert [1890], the necessity of including density variation effects on height has been suggested by authors writing on orthometric heights (e.g., Rapp [1961]; Sünkel [1986]). Geophysical methods for inferring density models from surface data, and for forward modelling gravitational effects of density models, exist (e.g., Parasnis [1997]) and have been refined during the past century [Mooney, 2007]. Although Heiskanen and Moritz [1967, section 4-4] suggested that the anomalous density effects on orthometric height would not be larger than about 2.5 cm for heights of 1000 m, which was a very small error by the standards of their time, Strange [1982] pointed out that errors in orthometric heights do not just increase linearly with height and that the error might be as large as 22 cm for an elevation of 3000 m. Strange [1982] and Sünkel [1986] both recommended applying a density correction to orthometric height, suggesting that an approximate DDM be constructed based on a map of Bouguer gravity anomalies. When the density effect was first applied to orthometric corrections by Allister and Featherstone [2001], they used a laterally-varying density model created by Middleton et al. [1993] according partly to the recommendations of Strange [1982] and Sünkel [1986]. Contemporary efforts at the University of New Brunswick (Tenzer et al. [1995]; Santos et al. [2006]) use a laterally-varying DDM created by digitizing geological maps and assigning appropriate rock densities [Fraser et al., 1998], comparable to a procedure used by [Martinec, 1993] in geoid determination. In these efforts, including the density

effect improved heights by up to 7 cm in an area of the Canadian Rockies. Hwang and Hsiao [2003] used a similar method of DDM creation to evaluate orthometric corrections over Taiwan. Some of these authors mention the desirability of three-dimensional DDMs for evaluating the density correction (e.g., Hwang and Hsiao [2003], Tenzer et al. [2005]), but none discuss it in any concrete way. The benefit to orthometric heights of accurately modeling the whole three-dimensional variation of topographical density is expected to be only a few centimetres, even in extreme circumstances [Kingdon et al., 2006].

The main improvement in the non-topographical effects has been the inclusion of the NT geoid-generated gravity disturbance [Vaníček et al., 2004]. This effect on orthometric height has been exclusively modeled by the University of New Brunswick group, and can improve orthometric heights by up to a few decimetres (Tenzer et al. [2005]; Santos et al. [2006]).

A further minor improvement to Helmert heights is the inclusion of the second order effects of normal gravity and the Bouguer shell [Santos et al., 2006]. The result of these second order improvements are only 1.5 cm and -1.6 cm, respectively, for Mount Everest, and in most cases these corrections are negligible.

In addition to a theory containing all of the effects on rigorous orthometric heights, the past century has brought significant improvements in the numerical methods of evaluating these effects. Unlike the Bouguer shell effect, the integral mean of the terrain and density effects cannot be represented as a simple function of computation point height. Historically, various numerical methods have been applied for evaluating the terrain effect on mean gravity. Until recently the most accurate method was that of

Neithammer [1932], who calculated the effect as the average of terrain effects on gravity sampled at discrete intervals along the plumbline. Assuming the terrain effect to vary in a roughly linear fashion, Mader [1954] suggested using only the average of the effects at both ends of the plumbline [Mader, 1954]. Later studies verified that these two methods were similar (Heiskanen and Mortiz [1967, section 4-4]; Rapp [1961]), but that the Neithammer method was superior in terms of accuracy [Dennis and Featherstone, 2003]. The point became moot, however, with the realization that the integral mean gravity could be evaluated exactly by simply evaluating the difference in the terrain effect on gravity potential at both ends of the plumbline and dividing by height (e.g., Tenzer et al. [2005]; Santos et al. [2006]), which was more accurate than Neithammer's method and more quickly evaluated than Mader's method [Kingdon, 2005a].

There have been numerous developments in modeling the mass bodies generating the terrain and density effects, which are pertinent to both orthometric height and to geoid determination. Early analog efforts used Hammer charts [Hammer, 1939] to discretize terrain masses, following a method already used to evaluate the terrain effect for geophysical purposes [Hayford and Bowie, 1912]. Digital computing later made more complex models practical (e.g., Bott [1959]; Talwani and Ewing [1960]; Takin and Talwani [1966]; Paul [1974]), and some of these advances eventually found their way into geoid (e.g., Anderson [1976]; Vaníček et al. [1987]) and orthometric height (e.g., Sünkel [1986]) calculations. Advanced methods of topographical modeling used in geodesy include modeling topographical masses as discrete mass columns [Martinec, 1993], rectangular prisms (e.g., Mollweide [1813]; Bessel [1813]; Nagy [2000, 2002]), prisms with inclined (e.g., Smith [2000]) or bilinear (e.g., Tsoulis et al. [2003]) surfaces,

or tesseroids (e.g., Anderson [1976]; Seitz and Heck [2001]). A thorough listing of these methods is given by Heck and Seitz [2007]. The accuracy improvements from the most precise methods, while necessary for calculating the whole gravitational effect in geophysics, are not required to calculate topographical corrections to Helmert heights, nor to calculate the conversions to and from the Helmert space in Stokes-Helmert geoid modeling. The modeling errors will be very similar in the topographical effects on mean and surface gravity, so that when their difference is calculated according to eq. (1.6), these errors mostly cancel each other. The modeling errors in effects of real and condensed topography are likewise similar, and so cancelation likewise occurs when evaluating the DTE, PITE, etc.

1.4.2 Developments in the Stokes-Helmert method of geoid modeling

As with orthometric heights, the greatest unresolved challenge in geoid determination is accurately accounting for topographical effects without complete knowledge of the topographical density distribution. Within the Stokes-Helmert context, the transformation according to a constant density model comprised of a Bouguer shell and terrain has been investigated considerably (e.g., Martinec [1993]; Vaníček et al. [2001]; Novák et al. [2001b]). Borraß [1911] applied the earliest transformation of gravity observations to the Helmert space using a constant density model, and Lambert and Darling [1936] applied it along with Stokes's integration for geoid computations [Lambert, 1930]. The latter computations applied the DTE, considered as a specific form of isostatic reduction (e.g., Heiskanen and Moritz [1967, section 3-7]), but applied no other components of the transformation to Helmert space, nor the conversion of the

cogeoïd to the geoid. This approximate form was suitable for the accuracies of the time. For example, Lambert suggests that the DTE is often negligible because it is less than 1 m in most areas [Lambert, 1930]. The magnitude of the DTE may reach several metres in rugged mountains (e.g., Martinec [1993]; Novák [2000]).

Wichiencharoen [1982] first included the PITE in a geoid computation by the Stokes–Helmert method, and was followed by Vaniček et al. [1987]. The PITE can reach about a metre in magnitude in sufficiently rough topography, and so must be included for decimetre level accuracy (e.g., Martinec [1993]; Novák [2000]). The SITE is also included by Martinec [1993], and later by others (e.g., Novák [2000]; Ellmann and Vaniček [2007]).

The second most significant theoretical advance in DTE evaluation since Lambert's [1930] application has been the evaluation in spherical coordinates, described precisely in Vajda et al. [2004]. This was applied by Wichiencharoen [1982] when many other methods were still using planar coordinates (e.g., Vaniček et al. [1987]), and later became common for all topographical effect evaluations (e.g., Martinec [1993]; Vaniček and Martinec [1994]; Huang et al. [2001]; Ellmann and Vaniček [2007]).

The most significant theoretical advance in determining the topographical effects has been the inclusion of anomalous density effects in DTE evaluation. This began with Martinec [1993], who proposed a mathematical framework for including anomalous density effects in the DTE, PITE and SITE, using a laterally-varying DDM, ideally a DDM representing the mean density along each topographical column. An experiment to practically realize these corrections was performed in Martinec's 1993 report, and then in a more refined version by Martinec et al. [1995], in which a DDM was created for

Lake Superior in Canada by using the lake bathymetry to evaluate the average density in discrete topographical columns. This model assumes the lake water density to be 1000 kg/m^3 while the topographical density remains constant at 2670 kg/m^3 . The results showed that the total anomalous density effect ranged from -1.1 to 1.3 cm .

Additional efforts to calculate the anomalous density effects used a laterally-varying DDM created from surface geology maps (e.g., Fraser et al. [1998]). The first such computation was by Martinec [1993], who was followed by Pagiatakis et al. [1999], Tziavos and Featherstone [2001], Huang et al. [2001] and Kuhn [2003], all of whom found that including anomalous density affected solutions by at most one or two decimetres, in especially challenging test areas. The most accurate DDMs were those used by Martinec [1993, section 7.1] for part of Canada and Kuhn [2003] for a mountainous region of Europe, both of whom used a laterally-varying DDM constructed from sedimentary basin data as well as bedrock geology maps, providing a more accurate determination than other efforts of the average rock densities in topographical columns. The resulting anomalous density effects were below 1 decimetre, a magnitude comparable to other efforts. Notably, Kuhn discusses the superiority of a three-dimensionally varying DDM for geoid modeling, and provides some basic guidelines for how one might be obtained by geophysical methods, though he admits that such models do not exist and would be difficult to create.

Atmospheric effects have been included in geoid modeling generally since the 1970's (e.g., Anderson [1976]). In the Stokes-Helmert context, Vaníček et al. [1987] include the DAE, but not the PIAE, following the prescription of the International Association of Geodesy [1971]. Later efforts included both the DAE and the PIAE

(e.g. Vaniček and Martinec [1994]), and use updated atmospheric models (e.g., Sjöberg and Nahavandchi [2000]; Novák [2000]; Ellmann and Vaniček [2007]). The magnitude of the DAE is normally of the order of a few decimetres (Novák [2000]; Sjöberg and Nahavandchi [2000]), while the PIAE is no more than about a centimetre globally (e.g., Ellmann and Vaniček [2007]).

In addition to those involved in the transformations to and from the Helmert space, the Stokes–Helmert approach has other numerical difficulties. There is an open question of what parameters are suitable for Stokes’s integration in a given circumstance [Ellmann and Vaniček, 2007], although the numerical techniques of evaluating Stokes’s integration are fast and accurate (e.g., Huang et al. [2000]; Novák et al. [2001a]; Hirt et al. [2011]), as are the methods of spherical harmonic synthesis necessary for working with the reference field [Vaniček and Sjöberg, 1991].

The most challenging numerical problem in the Stokes-Helmert solution is the downward continuation of gravity anomalies to the geoid (e.g., Sun and Vaniček [1998]). This is especially a problem when using Helmert’s second condensation method that, while it minimizes the PITE and the problems with an unknown density distribution, results in a very rough gravity anomaly field [Heck, 2003] that must be carefully continued downward to the geoid. While more finely spaced gravity data can provide more accurate geoidal heights, as the resolution of gravity data increases the conditioning of the downward continuation problem becomes worse, especially for regions with large topographical heights [Martinec, 1996]. Ongoing efforts have sought to address these stability problems by regularization (e.g., Schwarz [1979]; Martinec et al. [1996]; Huang [2002]). Some recent investigations have also examined the behaviour

of the downward continuation using point vs. mean gravity anomalies (e.g., Huang [2002]; Sun [2005]; Goli [2010]; Vaníček and Santos [2010]).

1.4.3 Data sources for determination of orthometric heights and the geoid

Regarding the data used for determining orthometric heights, steady improvements in the accuracy of GNSS positioning have made it a feasible source of precise orthometric heights, provided that a suitable geoid model exists (Meyer et al. [2006]; Featherstone [2008]). This especially emphasizes the geodetic importance of an accurate geoid model, beyond its continuing importance to scientific studies (e.g., Vaníček and Christou [1993]; Vaníček et al. [2004]; Tapley et al. [2003]; Ellmann et al. [2005]).

In addition to improvements in GNSS observations, the sources of gravity and auxiliary data for gravimetric geoid determination have developed considerably in the past twenty years. Although terrestrial gravity measurement has seen little significant improvement, airborne gravity observation has become more accurate, allowing rapid acquisition of data over large areas [Olesen and Forsberg, 2007]. As a result, airborne data is extensively applied in geoid determination (e.g., NOAA/NGS [2007]).

Meanwhile, satellite missions have measured the gravitational potential field of the Earth to a high accuracy at higher resolutions than before, especially with the GRACE [Tapley et al., 2005] and GOCE [Rummel et al., 2009] projects. Satellite altimetry, which once provided relatively coarse gravity anomalies over oceans [Sandwell and Smith, 1997], is now capable of delivering gravity anomalies of much higher resolution and accuracy [Sandwell and Smith, 2009; Andersen et al., 2010], and has extended its reach to inland water bodies and coastal areas (e.g., Hwang and Hsu [2003]). This

promises to provide valuable data for lake waters, where large density contrasts exist and dense sampling of the gravity field is required, although the accuracy and resolution of satellite altimetry are ultimately limited by the difficulty in extracting the rough gravity anomaly field from smooth observations of a surface (the sea or a lake surface) approximately parallel to the geoid. Finally, spherical harmonic GGMs of improved accuracy have been developed using a combination of terrestrial data and new satellite gravity fields. Examples of these are EGM2008 [Pavlis et al., 2008] and EIGENGL04C [Förste et al., 2008].

DEM data has long been available, even to relatively high accuracy, in the form of topographical maps. However, these are now available over wider areas and at higher resolutions and precisions than before. This is especially important in geoid modeling, which requires consistent regional data sets with high local accuracy. Notable recent DEMs have been the SRTM data set [Werner, 2001] that covers much of the globe and the ASTER GDEM [Abrams et al., 2010] that covers almost the whole globe. Both of these, developed by NASA from radar interferometry observations, claim vertical accuracies of about 20 m and useful horizontal resolutions of about 3 arc-seconds, or 100 m. The ACE2 GDEM, based on SRTM data corrected by comparison to satellite altimetry heights for e.g., false returns due to forest cover, claims similar levels of accuracy, but with biases in some areas removed [Berry et al., 2010]. Also relevant to geoid determination are spherical harmonic models of squared heights, the most recent being the DEM2006.0 model used as a complement to EGM2008 [Pavlis et al., 2007], which are useful for performing topographical effect calculations in the spectral form.

Most of the laterally-varying DDMs already mentioned have not really satisfied the recommendation of Martinec for a DDM that represents the average value of gravity in a topographical column. In particular, the DDMs of Fraser et al. [1998] and Chiou [1997], which are based on geological maps of surface rock densities, are likely to be sufficiently accurate in most areas but inaccurate in areas of large elevation or in sedimentary basins. In such regions, the actual density may change significantly throughout the vertical profile. The DDM of Middleton et al. [1993] avoids this problem somewhat because it is based on geophysical data and thus representative of more than just the surface rock type. However, the results from geophysical data are likely to reflect densities of larger portions of the crust than just the relatively thin topography. The same problem limits the usefulness of global density models derived from geophysical operations, such as the CRUST 2.0 model [Bassin et al., 2000]. Because such models also delineate major density interfaces they may be useful for modeling effects of large sedimentary basins, and may also find use in modeling far zone density effects. Local investigations are able to provide relatively high resolution DDMs from geophysical data (e.g., Yen and Hsieh [2010]), but their vertical resolution is still rarely sufficient for geoid or orthometric height calculations. The most suitable DDMs to date have been those used by Martinec [1993] and Kuhn [2003], created from a geological bedrock map, but also modeling local sedimentary structures, which were likely to present the largest vertical deviations from the geological map values.

1.5 Significance of included articles

1.5.1 General comments on included articles

The six included articles are presented in almost their published form, except for minor grammar and typographical corrections. They are prefaced with explanatory notes where necessary, addressing deficiencies or points of contention in the articles.

While some effort has been made in this chapter sections to make the included articles accessible to readers in other disciplines, some esoteric content remains. For example, this dissertation commonly uses the Gal (1 Gal = 1 centimetre per second squared) as a unit of measurement, although SI units are now preferred in most fields. Also, we have chosen to specify position as an argument of terms depending on it, e.g. using $H(\Omega_P, r_P)$ to represent the height corresponding to the point P . This makes some expressions more cumbersome, especially for readers not already familiar with them, but we have preferred it because it is more transparent than the common alternative notation that uses the point name as a subscript (e.g. H_P).

Also along these lines, the significance of the included articles may be difficult to appreciate for those outside the discipline of geodesy. Why are we concerned with accuracies of better than one centimetre on top of a mountain? The main reason is because the techniques described would normally be applied to height control points, upon which other observations will be based. As a rule, control points must be significantly more accurate than the desired accuracy of observations based to them. For example, if a series of leveling observations is meant to have an accuracy of ± 10 cm,

the height control points upon which these are based should have accuracies of ± 5 cm or better.

There are a number of engineering applications common in mountainous regions for which very accurate heights are important. Two prominent examples are tunnel drilling and bridge building. Accurate height control minimizes the potential breakthrough errors in tunneling. It is an expensive mistake to correct if the machines drilling a tunnel from both ends of a mountain are offset from each other by a decimetre when they meet up in the middle. It is likewise expensive to repair a bridge when the two halves do not meet up correctly in the middle. Also, even though the effects described in the following articles are smaller at lower elevations, they may still be significant for some engineering tasks, e.g. ground deformation and subsidence monitoring, which require very precise height measurements.

1.5.2 Articles dealing with corrections to Helmert orthometric heights

The first two articles concern corrections to Helmert orthometric heights. The Chapter 2 article uses the test area in the Canadian Rocky Mountains, as shown in Figure 1.6, while the article in Chapter 3 uses a portion of this area.

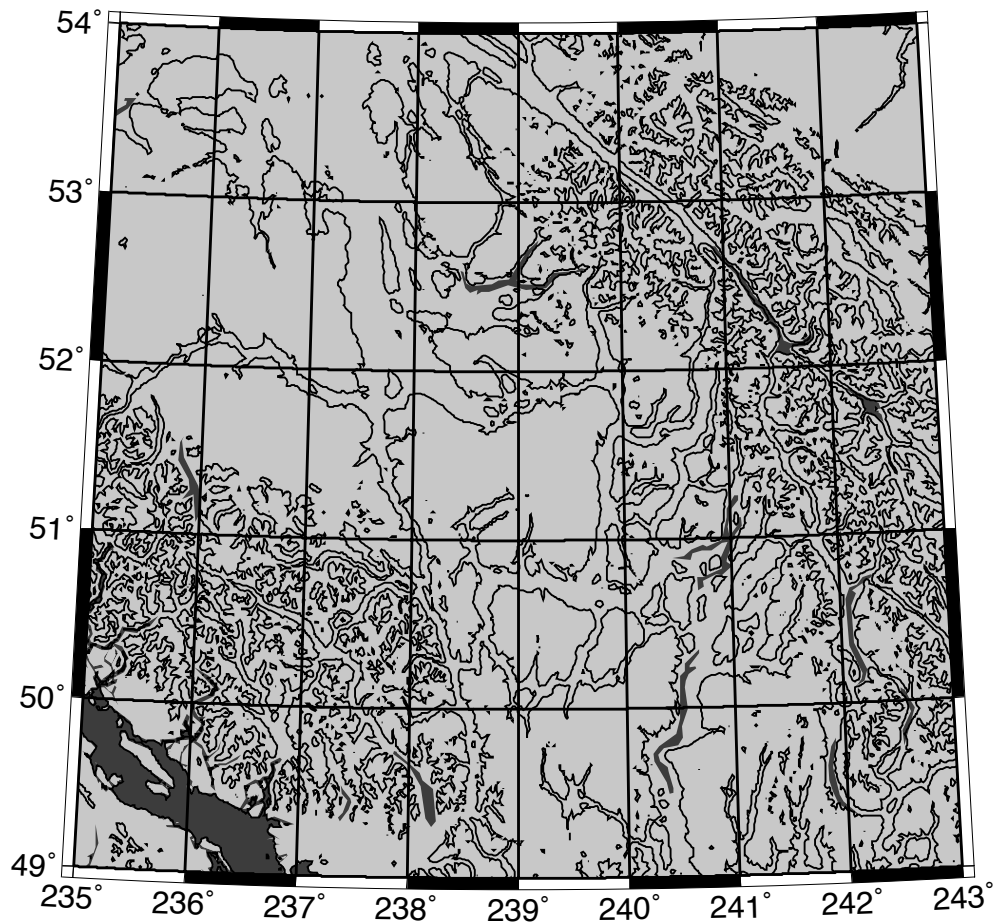


Figure 1.6. Base map of the test area for Chapters 2 and 3, with 1 km contours.

Chapter 2, “Toward an improved orthometric height system for Canada” [Kingdon et al., 2005b] is an article demonstrating, for an especially challenging area in the Canadian Rocky Mountains, an evaluation of the three main corrections needed to upgrade Helmert heights to rigorous orthometric heights. While Canada officially uses a normal-orthometric height system (the cited article erroneously claims otherwise), Helmert orthometric heights are commonly used in mountainous areas where high accuracy is needed, e.g. for using GPS and leveled heights to evaluate geoid models. Helmert

heights are also common elsewhere in the world, and so the article's findings are relevant to numerous other height systems.

The article shows results for the terrain correction, computed using publicly available DEMs; the anomalous density correction, using a DDM providing two-dimensionally varying anomalous densities drawn from geological maps; and the correction for the NT geoid-generated gravity disturbance, based on NT gravity anomalies on the geoid that were a byproduct of geoid determination. It demonstrates the feasibility of applying corrections to Helmert heights, and also shows that the magnitudes of the corrective terms are large enough that they should be taken seriously. It also shows that the density correction is quite small, even in an area of very large elevations, and that it tends to be smaller for lower elevations. This suggests that in most areas, the anomalous density effect will not prevent determination of heights with 1 cm accuracy.

Chapter 3, "Computationally efficient correction to Helmert orthometric heights for terrain and density effects" [Kingdon et al., 2012], an article currently in preparation, investigates more thoroughly the numerical methods required to evaluate the terrain and density corrections. Directed at a more general audience than the first article, it provides an accurate method for calculating the terrain and anomalous density corrections by discretizing the topography as a series of columns, rather than using a more complex approach, and also evaluating effects on mean gravity based on effects on potential at both ends of the plumbline. It further demonstrates that by this method Helmert heights can be corrected to rigorous orthometric heights efficiently and to better than 1 cm numerical accuracy, using only basic methods of topographical modeling and numerical integration.

1.5.3 Articles on errors in laterally-varying density models for geoid determination

The next two articles also deal with topographical effects, but in the context of the transformations to and from the Helmert space in geoid determination. Since the Bouguer shell and terrain contributions to the DTE, PITE and SITE have been addressed by other researchers, as has the anomalous density effect for laterally-varying densities, these articles deal with the remaining effect of the vertical variations of anomalous density, by investigating the difference between using a DDM that allows three-dimensional density variations, and one that uses only two-dimensional variations.

The article “Modeling topographical density for geoid determination” [Kingdon et al., 2009], comprising Chapter 4, first provides a thorough review of data sets and methodologies that might be useful for constructing three dimensional DDMs. Next, a mathematical framework is suggested for calculating the DTE, PITE and SITE on geoidal height for three-dimensional bodies of anomalous density. Methods are proposed for bodies bounded by simple surfaces (e.g. discs, which are bounded by two planes and a cylinder), and for bodies bounded by irregular surfaces (e.g. lake waters, which are bounded at the bottom by the lake bed and at the top by the lake surface). These methods are tested by comparison of the numerical result for a disc with the result from an analytical calculation, and they are found to be coarse methods but sufficient for their task. The numerical methods are applied in a series of simulations attempting to find the worst-case error in geoidal height that might result from neglecting vertical density variations in a DDM of the topographical masses. It is found that even in a very extreme

scenario, laterally-varying density models are able to provide a geoid accurate to within several centimetres.

To demonstrate the capability of the proposed methodology on real data, a calculation is carried out for Lake Superior in Canada. The lake is an example of an extreme density contrast delineated by an irregular surface, i.e. the lake bed, and has been used previously in studying anomalous density effects [Martinec et al., 1995]. The error in the geoid from omitting the three-dimensional density variations of the lake is found to be less than one centimetre, confirming that in most real world applications, laterally-varying DDMs can produce precise geoid results.

This article not only provides for the first time a complete methodology for calculating three-dimensional density effects within the Stokes-Helmert model, but also uses these methods to demonstrate that even existing DDMs can provide a geoid accurate to a few centimetres.

Chapter 5, “Effects of hypothetical complex mass-density distributions on geoidal height” [Kingdon et al., 2011a] briefly examines the extent to which adjacent bodies of anomalous density might cancel each other’s effects. In simulations for two arrays of discs, the DTE is reduced significantly by the presence of adjacent masses of lower density contrast, but not the PITE. This suggests that in some complex density distributions, the overall density effect may be smaller than what the simple examples of the previous article suggest.

1.5.4 Articles dealing with numerical and data issues

Next, an attempt is made to address the numerical problems of downward continuation in Chapter 6, “Poisson downward continuation by the relaxed Jacobi method” [Kingdon and Vaníček, 2011b]. The Jacobi iterative method is commonly applied to solve the downward continuation problem. It is conventionally applied with convergence tolerances based on a desired accuracy. In attempting to meet these requirements when the downward continuation problem is especially ill-conditioned, significant noise is added to the results. Instead of solving this problem by conventional regularization methods, this article suggests regularizing the downward continuation by relaxing the tolerance for the Jacobi method to a value reflecting the ill-conditioning of the problem, based on the condition number. The method is validated by testing in an area where the downward continuation problem is especially ill-conditioned, and it is found to work very well. This article provides a new, simple and efficient solution to one of the most challenging numerical problems of geoid determination.

The final article is provided in Chapter 7. Titled “Gravity Anomalies from retracked ERS and Geosat Altimetry over the Great Lakes: Accuracy Assessment and Problems” [Kingdon et al., 2007], it is the only article dealing with advances in data collection. This article presents a case study in the relatively new application of satellite altimetry to providing gravity anomalies over lake waters, made possible by the recent advances in accuracy and resolution of satellite altimetry missions. The altimetry result is able to resolve features of the gravity field that the GRACE satellite mission cannot, and provides accuracies comparable with some terrestrial methods, but is also sometimes subject to unknown errors and requires further refinement. The study is valuable as a

first assessment of the potential of satellite altimetry to provide cheap and readily available gravity anomalies over an area (over lakes) where they are often lacking. The study is also unique in its analysis of the ability of satellite altimetry to resolve gravitational effects of bathymetric features. When such features exist between the geoid and the lake surface, they contribute to topographical density effects in orthometric height determination.

Chapter 1 References

- Abrams, M., B. Bailey, H. Tsu, and M. Hato (2010). "The ASTER Global DEM." *Photogrammetric Engineering and Remote Sensing*, Vol. 76, No. 4, pp. 344–348.
- Allister, N., and W. Featherstone (2001). "Estimation of Helmert orthometric heights using digital barcode leveling, observed gravity and topographic mass-density data over part of Darling Scarp, Western Australia." *Geomatics Research Australasia*, No. 75, pp. 25–52.
- Anderson, E. (1976). "The Effect of Topography on Solutions of Stokes' Problem." Unisurv: Reports from the School of Engineering No. S14. University of New South Wales, Kensington, N.S.W., Australia.
- Andersen, O., P. Knudsen, and P. Berry (2010). "The DNSC08GRA global marine gravity field from double retracked satellite altimetry." *Journal of Geodesy*, Vol. 84, No. 3, pp. 191–199, doi: 10.1007/s00190-009-0355-9.
- Ardestani, V., and Z. Martinec (2002). "Geoid Determination Through Ellipsoidal Stokes Boundary-Value Problem by Splitting Its Solution to the Low-Degree and the High-Degree Parts." *Studia Geophysica et Geodaetica*, Vol. 47, No. 1, pp. 73–82, doi: 10.1023/A:1022299521920.
- Bassin, C., G. Laske, and G. Masters (2000). "The Current Limits of Resolution for Surface Wave Tomography in North America." *Eos, Transactions, American Geophysical Union*, Vol. 81, No. 48 (supplement), p. F897.
- Berry, P., R. Smith, and J. Benveniste (2010). "ACE2: the new Global Digital Elevation Model." *Gravity, Geoid and Earth Observation*, Ed. S. Mertikas. International Association of Geodesy International Symposium on "Gravity, Geoid and Earth Observation 2008", Chania, Crete, Greece, June 23–27, 2008. *International Association of Geodesy Symposia*, Vol. 135, Springer, New York, U.S.A., pp. 231–237, doi: 10.1007/978-3-642-10634-7_30.
- Bessel, F. (1813). "Auszug aus einem Schreiben des Herrn Prof. Bessel." *Zach's Monatliche Correspondenz zur Beförderung der Erd – und Himmelskunde*, Vol. 27, pp. 80–85.
- Bjerhammer, A. (1964). "A new theory of geodetic gravity." *Pure and Applied Mathematics and Physics, Transactions of the Royal Institute of Technology, Stockholm*, Vol. 27, No. 243. 75 pp.
- Borraß, E. (1911) "Bericht über der relativen Messungen der Schwerkraft mit Pendelapparaten in der Zeit von 1808 bis 1909: und über ihre Darstellung im

- Potsdamer Schweresystem.” *Comptes rendus des séances de la seizième conférence générale de l'Association géodésique internationale*, Ed. H. van de Sande Bakhuyzen. Association Géodésique Internationale, London and Cambridge, England, September 21–29, 1909. Rapport spécial sur les mesures relatives de la pesanteur, Vol. 3, Georg Reimer, Berlin, Germany.
- Bott, M. (1959). “The use of electronic digital computers for the evaluation of gravimetric terrain corrections.” *Geophysical Prospecting*, Vol. 7, No. 1, pp. 45–54, doi: 10.1111/j.1365-2478.1959.tb01452.x.
- Bruns, H. (1878) *Die Figur der Erde*. Königliches Preußischen Geodätischen Institut, Berlin, Germany.
- Chiou, Y. (1997). “The generation and application of the digital terrain density model of Taiwan Area.” M.Sc.E. thesis, Department of Civil Engineering, National Chiao Tung University, Hsinchu, Taiwan.
- Engelis, T., R. Rapp, and C. Tscherning (1985). “The precise computation of geoid undulation differences with comparison to results obtained from the Global Positioning System.” *Geophysical Research Letters*, Vol. 11, No. 9, pp. 821–824, doi: 10.1029/GL011i009p00821.
- Ellmann, A., P. Vaníček and M. Santos (2005). “Report on precise geoid determination for geo-referencing and oceanography.” Paper presented at the 2005 Geomatics for Informed Decisions (GEOIDE) Annual Scientific Conference, Québec City, Québec, Canada, 29–31 May.
- Ellmann, A., and P. Vaníček (2007). “UNB application of Stokes-Helmert's approach to geoid computation.” *Journal of Geodynamics*, Vol. 43, No. 2, pp. 200–213, doi:10.1016/j.jog.2006.09.019.
- Featherstone, W., M. Dentith, and J. Kirby (1998). “Strategies for the accurate determination of orthometric heights from GPS.” *Survey Review*, Vol. 34, No. 267, pp. 278–296.
- Featherstone, W., and D. Sproule (2006). “Fitting AusGeoid98 to the Australian height datum using GPS-leveling and least squares collocation: application of a cross-validation technique.” *Survey Review*, Vol. 38, No. 301, pp. 573–582.
- Featherstone, W. (2008). “GNSS-heighting in Australia: current, emerging and future issues.” *Journal of Spatial Science*, Vol. 53, No. 2, pp. 115–133, doi: 10.1080/14498596.2008.9635153.
- Flury, J. (2009). “On the geoid-quasigeoid separation in mountainous areas.” *Journal of Geodesy*, Vol. 83, No. 9, 829–847, doi: 10.1007/s00190-009-0302-9.

- Förste, C., R. Schmidt, R. Stubenvoll, F. Flechtner, U. Meyer, R. König, H. Neumayer, R. Biancale, J.-M. Lemoine and S. Bruinsma, S. Loyer, F. Barthelmes, and S. Esselborn (2008). "The GeoForschungsZentrum Potsdam/Groupe de Recherche de Gèodésie Spatiale satellite-only and combined gravity field models: EIGEN-GL04S1 and EIGEN-GL04C." *Journal of Geodesy*, Vol. 82, No. 6, pp. 331–346, doi: 10.1007/s00190-007-0183-8.
- Fraser, D., S. Pagiatakis, and A. Goodacre (1998). "In-situ rock density and terrain corrections to gravity observations." *Proceedings of the 12th Annual Symposium on Geographic Information Systems*, 6–9 April, 1998, Toronto, Ontario, Canada, 1998.
- Fredholm, E. (1900). "Sur une nouvelle méthode pour la résolution du problème de Dirichlet." *Öfversigt af Kongliga Svenska Vetenskaps-Akademiens Förhandlingar*, Vol. 131, pp. 39–46.
- Gauss, C. (1828). *Bestimmung des Breitenunterschiedes zwischen den Sternwarten von Göttingen und Altona : durch Beobachtungen am Ramsdenschen Zenithsector*. Vandenhoeck & Ruprecht, Göttingen, Germany.
- Goli, M., M. Najafi-Alamdari, and P. Vaniček (2010). "Numerical behaviour of the downward continuation of gravity anomalies." *Studia Geophysica at Geodaetica*, Vol. 55, No. 2, pp. 191–202, doi: 10.1007/s11200-011-0011-8.
- Hackney, R., and W. Featherstone (2003). "Geodetic versus geophysical perspectives of the 'gravity anomaly'." *Geophysical Journal International*, Vol. 154, No. 1, pp. 35–43, doi: 10.1046/j.1365-246X.2003.01941.x.
Erratum in Vol. 154, No. 2, p. 596, doi: 10.1046/j.1365-246X.2003.02058.x.
Corrigendum in Vol. 167, No. 6, p. 585, doi: 10.1111/j.1365-246X.2006.03035.x.
- Hadamard, J. (1923). *Lectures on Cauchy's Problem in Linear Partial Differential Equations*. Oxford University Press, London, England.
- Hammer, S. (1939). "Terrain Corrections for Gravimetric Stations." *Geophysics*, Vol. 4, No. 3, pp. 184–194, doi:10.1190/1.1440495.
- Hayford, J., and W. Bowie (1912). *The Effect of Topography and Isostatic Compensation upon the Intensity of Gravity*. Special Publication No. 10, United States Coast and Geodetic Survey, Government Printing Office, Washington, U.S.A.
- Heck, B. (2003). "On Helmert's methods of condensation." *Journal of Geodesy*, Vol. 77, No. 3–4, pp. 155–170, doi: 10.1007/s00190-003-0318-5.

- Heck, B., and K. Seitz (2007). "A comparison of the tesseroid, prism and point-mass approaches for mass reductions in gravity field modelling." *Journal of Geodesy*, Vol. 81, No. 2, pp. 121–136, doi: 10.1007/s00190-006-0094-0.
- Heiskanen W., and H. Moritz (1967). *Physical Geodesy*. Freeman, San Francisco, U.S.A.
- Helmert, F. (1884). *Die Physikalischen Theorieen*. Vol. II of *Die Mathematischen und Physikalischen Theorieen der Höheren Geodäsie*, B. G. Teubner, Leipzig, Germany.
- Helmert, F. (1890). *Die Schwerkraft im Hochgebirge insbesondere, in den Tyroler Alpen, in geodätischer und geologischer Beziehung*. Königliches Preußischen Geodätischen Institut, Berlin, Germany.
- Henning, W., E. Carlson, and D. Zilkoski (1998). "Baltimore County, Maryland, NAVD 88 CPS-derived orthometric height project." *Surveying and Land Information Systems*, Vol. 58, No. 2, pp. 97–113.
- Hernandez, N., M. Gomez, and P. Vaníček (2002). "The far zone contribution in spherical Stokes's integration." *Revista Cartografica*, Vols. 74–75, pp. 61–74.
- Hirt, C., W. Featherstone, and S. Claessens (2011). "On the accurate numerical evaluation of geodetic convolution integrals." *Journal of Geodesy*, Vol. 85, No. 8, pp. 519–538, doi: 10.1007/s00190-011-0451-5.
- Hotine, M. (1969). *Mathematical Geodesy*. U. S. Environmental Science Services Administration, Washington.
- Huang, J., P. Vaníček, and P. Novák (2000). "An alternative algorithm to FFT for the numerical evaluation of Stokes's integral." *Studia Geophysica et Geodaetica*, Vol. 44, No. 3, pp. 374–380, doi: 10.1023/A:1022160504156.
- Huang, J., P. Vaníček, S. Pagiatakis, and W. Brink (2001). "Effect of topographical density on the geoid in the Rocky Mountains." *Journal of Geodesy*, Vol. 74, No. 11–12, pp. 805–815, doi: 10.1007/s001900000145.
- Huang, J. (2002). *Computational Methods for the Discrete Downward Continuation of the Earth Gravity and Effects of Lateral Topographical Mass Density Variation on Gravity and the Geoid*. Ph.D. dissertation, Department of Geodesy and Geomatics Engineering Technical Report No. 216, University of New Brunswick, Fredericton, New Brunswick, Canada, 141 pp.
- Hwang, C., and Y.-S. Hsiao (2003). "Orthometric corrections from leveling, gravity, density and elevation data: a case study in Taiwan." *Journal of Geodesy*, Vol. 77, No. 5–6, pp. 279–291, doi: 10.1007/s00190-003-0325-6.

- Hwang, C., and H.-Y. Hsu (2003) "Marine Gravity Anomaly from Satellite Altimetry: a Comparison of Methods over Shallow Waters." In *Satellite Altimetry for Geodesy, Geophysics and Oceanography*, Eds. C. Hwang, C. Shum and J. Li. Vol. 126 of *International Association of Geodesy Symposia*, Springer, New York, U.S.A., pp. 59–66.
- International Association of Geodesy (IAG) (1971). "Geodetic Reference System, 1967." IAG Special Publication No. 3, IAG, Muenchen, Germany.
- International Organization for Standardization (ISO) (1975) "Standard Atmosphere", ISO 2533:1975, ISO, Geneva, Switzerland.
- Karl, J. (1971). "The Bouguer correction for the spherical Earth." *Geophysics*, Vol. 36, No. 4, pp. 761–762, doi: 10.1190/1.1440211.
- Kellogg, O. (1929). *Foundations of Potential Theory*. Springer, New York, U.S.A.
- Kingdon, R., P. Vaníček, M. Santos, A. Ellmann, R. Tenzer (2005a). "Corrections for the improvement of the Canadian height system." Paper presented at the 31st Canadian Geophysical Union Annual Scientific Meeting, Banff, Alberta, Canada, May 8–11.
- Kingdon, R., P. Vaníček, A. Ellmann, M. Santos, and R. Tenzer (2005b). "Toward an improved orthometric height system for Canada." *Geomatica*, Vol. 59, No. 3, pp. 241–249.
- Kingdon, R., A. Ellmann, P. Vaníček and M. Santos (2006). "The cost of assuming a lateral density distribution in corrections to Helmert orthometric heights." Paper presented at the American Geophysical Union 2006 Joint Assembly, Baltimore, Maryland, U.S.A., May 23–26.
- Kingdon, R., C. Hwang, Y-S. Hsiao, and M. Santos (2007). "Gravity Anomalies from retracked ERS and GeoSat Altimetry over the Great Lakes: Accuracy Assessment and Problems." *Terrestrial, Atmospheric and Ocean Sciences*, Vol. 19, No. 1–2, pp. 93–102, doi: 10.3319/TAO.2008.19.1-2.93(SA).
- Kingdon, R., P. Vaníček, and M. Santos (2009). "Modeling topographical density for geoid determination." *Canadian Journal of Earth Sciences*, Vol. 46, No. 8, pp. 571–585, doi: 10.1139/E09-018.
- Kingdon, R., P. Vaníček, and M. Santos (2011a). "Effects of hypothetical complex mass-density distributions on geoidal height." *Geodesy for Planet Earth*, Eds. S. Kenyon, M. Pacino and U. Marti. International Association of Geodesy IAG2009 "Geodesy for Planet Earth" Scientific Assembly, Buenos Aires, Argentina, 31

- August–4 September, 2009. *International Association of Geodesy Symposia*, Vol. 135, Springer, New York. (in press)
- Kingdon, R., and P. Vaniček (2011b). “Poisson downward continuation solution by the Jacobi method.” *Journal of Geodetic Science*, Vol. 1, No. 1, pp. 74–81, doi: 10.2478/v10156-010-0009-0.
- Kingdon, R., P. Vaniček, M. Santos, and A. Ellmann (2012). “Efficient correction of Helmert orthometric heights for terrain and density effects.” *Computations and Geosciences* (in preparation).
- Knudsen, P., R. Bingham, O. Andersen, and M.-H. Rio (2011). “A global mean dynamic topography and ocean circulation estimation using a preliminary GOCE gravity model.” *Journal of Geodesy*, “Online First”, doi: 10.1007/s00190-011-0485-8.
- Krakiwsky, E. (1965). “Heights.” M.Sc. thesis, Department of Geodetic Science and Surveying, Ohio State University, Columbus, U.S.A. 157 pp.
- Kuhn, M. (2003). “Geoid determination with density hypotheses from isostatic models and geological information.” *Journal of Geodesy*, Vol. 77, Nos. 1–2, pp. 50–65, doi: 10.1007/s00190-002-0297-y.
- Lambert, W. (1930). “The reduction of observed values of gravity to sea level.” *Bulletin Géodésique*, Vol. 26, No. 1, pp. 107–181, doi: 10.1007/BF03030029.
- Lambert, W., and F. Darling (1936). *Tables for Determining the Form of the Geoid and its Indirect Effect on Gravity*. Special Publication No. 199, U. S. Department of Commerce Coast and Geodetic Survey, United States Government Printing Office, Washington, District of Columbia, U.S.A.
- Lambin, J., R. Morrow, L.-L. Fu, J. Willis, H. Bonekamp, J. Lillibridge, J. Perbos, G. Zaouche, P. Vaze, W. Bannoura, F. Parisot, E. Thouvenot, S. Coutin-Faye, E. Lindstrom, and M. Mignogno (2010). “The OSTM/Jason-2 mission.” *Marine Geodesy*, Vol. 33, Supplement 1, pp. 4–25, doi: 10.1080/01490419.2010.491030.
- Listing, J. (1873). *Über unsere jetzige Kenntnis der Gestalt und Grosse der Erde, Nachrichten von der Königl Gesellschaft der Wissenschaften und der Georg-Augusts-Universität zu Göttingen aus dem Jahre 1873*, pp. 33–98, Verlag der Dieterichschen Buchhandlung, Göttingen, Germany.
- Mader, K. (1954). “Die orthometrische Schwerekorrektion des Präzisions-Nivellements in den Hohen Tauern.” *Österreichische Zeitschrift für Vermessungswesen*, Special issue 15.

- Martinec, Z., C. Matyska, E. Grafarend, and P. Vaníček (1993). "On Helmert's 2nd condensation method." *Manuscripta Geodaetica*, Vol. 18, No. 6, pp. 417–421.
- Martinec, Z. (1993). "Effect of lateral density variations of topographical masses in improving geoid model accuracy over Canada." Contract report for the Geodetic Survey of Canada, Ottawa, Ontario, Canada.
- Martinec Z., and P. Vaníček (1994a). "Direct topographical effect of Helmert's condensation for a spherical approximation of the geoid." *Manuscripta Geodaetica*, Vol. 19, No. 4, pp. 213–219.
- Martinec Z., and P. Vaníček (1994b). "Indirect effect of topography in the Stokes-Helmert technique for a spherical approximation of the geoid." *Manuscripta Geodaetica*, Vol. 19, No. 5, pp.257–268.
- Martinec, Z., P. Vaníček, A. Mainville, and M. Véronneau (1995). "The effect of lake water on geoidal heights." *Manuscripta Geodaetica*, Vol. 20, No. 3, pp. 193–203.
- Martinec, Z. (1996). "Stability investigations of a discrete downward continuation problem for geoid determination in the Canadian Rocky Mountains." *Journal of Geodesy*, Vol. 70, No. 11, pp. 805–828, doi: 10.1007/BF00867158.
- Martinec, Z., P. Vaníček, A. Mainville, and M. Véronneau (1996) "Evaluation of topographical effects in precise geoid determination from densely sampled heights." *Journal of Geodesy*, Vol. 70, No. 11, pp. 746–754, doi: 10.1007/BF00867153.
- Martinec, Z., and E. Grafarend (1997). "Solution to the Stokes boundary-value problem on an ellipsoid of revolution." *Studia Geophysica et Geodaetica*, Vol. 41, No. 2, pp. 103–129, doi: 10.1023/A:1023380427166.
- Meyer, T., D. Roman, and D. Zilkoski (2006). "What Does Height Really Mean? Part IV: GPS Orthometric Heighting." *Surveying and Land Information Science*, Vol. 66, No. 3, pp. 165–183.
- Middleton, M., S. Wilde, B. Evans, A. Long, and M. Dentith (1993). "A preliminary interpretation of deep seismic reflection and other geophysical data from the Darling Fault Zone, Western Australia." *Exploration Geophysics*, Vol. 24, No. 4, pp. 711–718, doi: 10.1071/EG993711.
- Mollweide, K. (1813). "Auflösung einiger die Anziehung von Linien Flächen und Köpern betreffenden Aufgaben unter denen auch die in der Monatliche Correspondenz Band 24, Seite 522, vorgelegte sich findet." *Zach's Monatliche Correspondenz zur Beförderung der Erd – und Himmelskunde*, Vol.27, pp. 26–38.

- Molodensky M. (1945). "Fundamental Problems of Geodetic Gravimetry." TRUDY Technical Report No. 42, Geodezizdat Novosibirskiy Institut Inzhenerov Geodezii, Aerofotos yemki i Kartografii (NIIGAiK), Moscow.
- Molodensky, M., V. Eremeev, and M. Yurkina (1962). *Methods for the study of the external gravitational field and figure of the Earth*. Translated from Russian by the Israeli Program for Scientific Translations, Jerusalem.
- Mooney, W. (2007). "Crust and Lithospheric Structure – Global Crustal Structure." In: *Seismology and Structure of the Earth*, Vol. 1 of *Treatise on Geophysics*, Ed. G. Schubert, Elsevier Science, Amsterdam, pp. 361–417.
- Moritz, H. (2000). "Geodetic Reference System 1980." *Journal of Geodesy*, Vol. 74, No. 1, pp. 128–162. doi: 10.1007/s001900050278.
- Nagy D., G. Papp, and J. Benedek (2000). The gravitational potential and its derivatives for the prism. *Journal of Geodesy*, Vol. 74, Nos. 7–8, pp. 552–560, doi: 10.1007/s001900000116.
- Nagy D., G. Papp, and J. Benedek (2002). "Corrections to 'The gravitational potential and its derivatives for the prism.'" *Journal of Geodesy*, Vol. 76, No. 8, p. 475, doi: 10.1007/s00190-002-0264-7.
- National Imaging and Mapping Agency (2000). "Department of Defense World Geodetic System 1984: Its Definition and Relationships With Local Geodetic Systems." NIMA Technical Report TR8350.2, 3rd Ed., Amendment 1, 4 July 1997, NIMA, Bethesda, Maryland, U.S.A.
- National Oceanographic and Atmospheric Administration (NOAA) and National Geodetic Survey (NGS) (2007). *The GRAV-D Project: Gravity for the Redefinition of the American Vertical Datum*. NOAA/NGS, Silver Spring, Maryland, U.S.A.
- Niethammer, T. (1932). *Nivellement und Schwere als Mittel zur Berechnung wahrer Meereshöhen*. Schweizerische Geodätische Kommission, Bern, Switzerland.
- Novák, P. (2000). *Evaluation of Gravity Data for the Stokes-Helmert Solution to the Geodetic Boundary-Value Problem*. Ph.D. dissertation, Department of Geodesy and Geomatics Engineering Technical Report No. 207, University of New Brunswick, Fredericton, New Brunswick, Canada, 133 pp.
- Novák, P., P. Vaníček, M. Véronneau, S. Holmes, and W. Featherstone (2001a). "On the accuracy of modified Stokes's integration in high-frequency gravimetric geoid determination." *Journal of Geodesy*, Vol. 74, No. 9, pp. 644–654, doi: 10.1007/s001900000126.

- Novák, P., P. Vaníček, Z. Martinec, and M. Véronneau (2001b). "Effects of the spherical terrain on gravity and the geoid." *Journal of Geodesy*, Vol. 75, Nos. 9–10, pp. 491–504, doi: 10.1007/s001900100201.
- Olesen, A., and R. Forsberg (2007). "Airborne Scalar Gravimetry for Regional Gravity Field Mapping and Geoid Determination." *Proceedings of the 1st International Symposium of the International Gravity Field Service: "Gravity Field of the Earth."* Ankara, Turkey, August 28–September 1, 2006. *Harita Dergisi*, Vol. 73, No. 18, pp. 277–282. Harita Genel Komutanlığı, Ankara, Turkey.
- Pagiatakis, S., D. Fraser, K. McEwen, A. Goodacre, and M. Véronneau (1999). "Topographic mass density and gravimetric geoid modelling." *Bollettino di Geofisica Teorica e Applicata*, Vol. 40, Nos. 3–4, pp. 189–194.
- Parasnis, D. (1997). *Principles of Applied Geophysics*. 5th ed., Chapman and Hall, New York, U.S.A.
- Paul, M. (1974). "The gravity effect of a homogeneous polyhedron for three dimensional interpretation." *Pure and Applied Geophysics*, Vol. 112, No. 3, pp. 553–561, doi: 10.1007/BF00877292.
- Pavlis, N., S. Holmes, S. Kenyon, and J. Factor (2008). "An Earth Gravitational Model to Degree 2160: EGM2008." Paper presented at the 2008 General Assembly of the European Geoscience Union (ESU), Vienna, Austria, April 13–18.
- Pavlis, N., J. Factor and S. Holmes (2007). "Terrain-related gravimetric quantities computed for the next EGM." *Proceedings of the 1st International Symposium of the International Gravity Field Service: "Gravity Field of the Earth."* Ankara, Turkey, August 28–September 1, 2006. *Harita Dergisi*, Vol. 73, No. 18, pp. 318–323. Harita Genel Komutanlığı, Ankara, Turkey.
- Picone, J., A. Hedin, D. Drob, and A. Aikin (2002). "NRL-MSISE-00 Empirical Model of the Atmosphere: Statistical Comparisons and Scientific Issues." *Journal of Geophysical Research*, Vol. 107, No. A12, p. 1468, doi:10.1029/2002JA009430.
- Pizzetti, P. (1894). "Sulla espressione della gravità alla superficie del geoide, supposto ellissoide." *Atti Della Reale Accademia Dei Lincei, Anno CCXCI*, Vol. 3, Series 5, pp. 166–172.
- Rapp, R. (1961). "The orthometric height." M.Sc. thesis, Department of Geodetic Science, Ohio State University, Columbus, U.S.A., 117 pp.
- Roman, D., and D. Smith (2002). "Recent investigations toward achieving a one centimeter geoid." *Gravity, Geoid and Geodynamics 2000*, Ed. M. Sideris. GGG2000 IAG International Symposium, Banff, Alberta, Canada July 31–August 4,

2000. *International Association of Geodesy Symposia*, Vol. 123, Springer, New York, U.S.A., pp. 285–290.
- Roman, D., Y. Wang, W. Henning, and J. Hamilton (2004). “Assessment of the New National Geoid Height Model, GEOID03.” *Surveying and Land Information Science* Vol. 64, No. 3, pp. 153–162.
- Rummel, R., T. Gruber, J. Flury, and A. Schlicht (2009). “ESA’s gravity field and steady-state ocean circulation explorer GOCE.” *Zeitschrift für Vermessungswesen*, Vol. 134, No. 3, pp. 125–130.
- Sandwell, D., and W. Smith (1997). “Marine gravity anomaly from Geosat and ERS-1 satellite altimetry.” *Journal of Geophysical Research*, Vol. 102, No. B5, pp. 10039–10054, doi:10.1029/96JB03223.
- Sandwell, D., and W. Smith (2009). “Global marine gravity from retracked Geosat and ERS-1 altimetry: Ridge segmentation versus spreading rate.” *Journal of Geophysical Research*, Vol. 114, No. B0, p. 1411, doi:10.1029/2008JB006008.
- Sansò, F., and R. Rummel (Eds.)(1997). *Geodetic Boundary Value Problems in View of the One Centimeter Geoid*. Springer, New York, U.S.A.
- Santos, M., P. Vaníček, W. Featherstone, R. Kingdon, A. Ellmann, B.A. Martin, M. Kuhn and R. Tenzer (2006). “Relation between the rigorous and Helmert’s definitions of orthometric heights.” *Journal of Geodesy*, Vol. 80, No. 12, pp. 691–704, doi: 10.1007/s00190-006-0086-0.
- Schwartz, K. (1979). “Geodetic improperly posed problems and their regularization.” *Bollettino di Geodesia e Scienze Affini*, Vol. 38, No. 3, pp. 389–416.
- Seitz, K. and B. Heck (2001). “Tesseroids for the calculation of topographic reductions.” Paper presented at the International Association of Geodesy 2001 Scientific Assembly, Budapest, Hungary, 2–7 September.
- Sjöberg, L. (1984). “Least squares modification of Stokes' and Vening Meinesz' formulas by accounting for the truncation and potential coefficient errors.” *Manuscripta Geodaetica*, Vol. 9, pp. 209–229.
- Sjöberg, L. (1995). “On the quasigeoid to geoid separation.” *Manuscripta Geodaetica*, Vol. 20, No. 3, pp. 182–192.
- Sjöberg, L., and H. Nahavandchi (2000). “The atmospheric effects in Stokes’ formula.” *Geophysical Journal International*, Vol. 140, No. 1, pp. 95–100, doi: 10.1046/j.1365-246x.2000.00995.x.

- Sjöberg, L. (2003). "A computational scheme to model the geoid by the modified Stokes' formula without gravity reductions." *Journal of Geodesy*, Vol. 77, Nos. 7–8, pp. 423–432, doi: 10.1007/s00190-003-0338-1.
- Smith, D. (2000). "The gravitational attraction of any polygonally shaped vertical prism with inclined top and bottom faces." *Journal of Geodesy*, Vol. 74, No. 5, pp. 414–420, doi: 10.1007/s001900000102.
- Somigliana, C. (1930). "Sul campo gravitazionale esterno del geoide ellissoidico." *Rendiconti Della Reale Accademia dei Lincei*, Vol. 6, pp. 237–243.
- Stokes, G. (1849). "On the variation of gravity on the surface of the Earth." *Transactions of the Cambridge Philosophical Society*, Vol. 8, pp. 672–695.
- Strange, W. (1982). "Evaluation of orthometric height accuracy using bore hole gravimetry." *Bulletin Géodésique*, Vol. 56, No. 4, pp. 300–311, doi: 10.1007/BF02525730.
- Strang van Hees, G. (1992). "Practical formulas for the computation of the orthometric, dynamic and normal heights." *Zeitschrift für Vermessungswesen*, Vol. 117, No. 11, pp. 727–734.
- Sun, W., and P. Vaníček (1998). "On some problems of the downward continuation of 5' x 5' mean Helmert's gravity disturbance." *Journal of Geodesy*, Vol. 72, Nos. 7–8, pp. 411–420, doi: 10.1007/s001900050180.
- Sun, W. (2005). "On Discrete Schemes in Downward Continuation of Gravity." *A Window on the Future of Geodesy*, Ed. F. Sansò. International Association of Geodesy General Assembly, Sapporo, Japan, June 30–July 11, 2003. *International Association of Geodesy Symposia*, Vol. 128, Springer, New York, U.S.A., pp. 512–517.
- Sünkel, H. (1986). "Digital height and density model and its use for orthometric height and gravity field determination for Austria." *Proceedings of the International Symposium on the Definition of the Geoid*, International Association of Geodesy, Florence, 26–30 May 1986. Istituto Geografico Militare Italiano, Florence, pp. 599–606.
- Takin, M., and M. Talwani (1966). "Rapid computation of the gravitation attraction of topography on a spherical Earth." *Geophysical Prospecting*, Vol. 14, No. 2, pp. 119–142, doi: 10.1111/j.1365-2478.1966.tb01750.x.
- Talwani, M., and M. Ewing (1960). "Rapid computation of gravitational attraction of three-dimensional bodies of arbitrary shape." *Geophysics*, Vol. 25, No. 1, pp. 203–225, doi: 10.1190/1.1438687.

- Tapley, B., D. Chambers, S. Bettadpur, and J. Ries (2003). "Large scale ocean circulation from the GRACE GGM01 Geoid." *Geophysical Research Letters*, Vol. 30, No. 22, p. 2163, doi:10.1029/2003GL018622.
- Tapley, B., J. Ries, S. Bettadpur, D. Chambers, M. Cheng, F. Condi, B. Gunter, Z. Kang, P. Nagel, R. Pastor, T. Pekker, S. Poole, and F. Wang (2005). "GGM02 An improved Earth gravity field model from GRACE." *Journal of Geodesy*, Vol. 79, No. 8, pp. 467–478, doi: 10.1007/s00190-005-0480-z.
- Tenzer, R., P. Vaníček, M. Santos, W. Featherstone, and M. Kuhn (2005). "The rigorous determination of orthometric heights." *Journal of Geodesy*, Vol. 79, Nos. 1–3, pp. 82–92, doi: 10.1007/s001-005-0445-2.
- Tsoulis, D., H. Wziontek, and S. Petrovic (2003). "A bilinear approximation of the surface relief in terrain correction computations." *Journal of Geodesy*, Vol. 77, Nos. 5–6, pp. 338–344, doi: 10.1007/s00190-003-0332-7.
- Tziavos, I., and W. Featherstone (2001). "First results of using digital density data in gravimetric geoid computation in Australia." *Gravity, Geoid and Geodynamics 2000*, Ed. M. Sideris. GGG2000 IAG International Symposium, Banff, Alberta, Canada July 31–August 4, 2000. *International Association of Geodesy Symposia*, Vol. 123, Springer, New York, U.S.A., pp. 335–340.
- Vajda P., P. Vaníček, P. Novák, and B. Meurers (2004). "On evaluation of Newton integrals in geodetic coordinates: Exact formulation and spherical approximation." *Contributions to Geophysics and Geodesy*, Vol. 34, No. 4, pp. 289–314.
- Vaníček, P., and C. Merry (1973). "Determination of the geoid from deflections of vertical using a least-squares surface fitting technique." *Bulletin Géodésique*, Vol. 109, No. 1, pp. 261–279, doi: 10.1007/BF02525574.
- Vaníček P., and E. Krakiwsky (1986). *Geodesy: The Concepts*. 2nd rev. ed., North-Holland Press, Elsevier Science Publishers, Amsterdam, The Netherlands.
- Vaníček, P., and A. Kleusberg (1987). "The Canadian geoid-Stokesian approach." *Manuscripta Geodaetica*, Vol. 12, No. 2, pp. 86–98.
- Vaníček, P., A. Kleusberg, R. G. Chang, H. Fashir, N. Christou, M. Hofman, T. Kling, and T. Arsenault (1987) "The Canadian Geoid." Final contract report for DSS contract No. 24ST.23244-4-4020 prepared by the Department of Surveying Engineering, University of New Brunswick, Fredericton, New Brunswick, Canada, for the Geodetic Survey of Canada, Energy, Mines and Resources Canada, Ottawa, Canada, 123 pp.

- Vaniček, P., and L. Sjöberg (1991). “Reformulation of Stokes’s theory for higher than second-degree reference field and modification of integral kernels.” *Journal of Geophysical Research*, Vol. 96, No. B4, pp. 6529–6539, doi: 10.1029/90JB02782.
- Vaniček, P., and N. Christou (Eds.)(1993). *Geoid and its geophysical interpretations*. CRC Press, Boca Raton, Florida, U.S.A.
- Vaniček, P., and Z. Martinec (1994). “Stokes-Helmert scheme for the evaluation of a precise geoid.” *Manuscripta Geodaetica* Vol. 19, No. 2, pp. 119–128.
- Vaniček, P., and W. Featherstone (1998). “Performance of three types of Stokes’s kernel in the combined solution for the geoid.” *Journal of Geodesy*, Vol. 72, No. 12, pp. 684–697, doi: 10.1007/s001900050209.
- Vaniček, P., J. Huang, P. Novák, M. Véronneau, S. Pagiatakis, Z. Martinec, and W. Featherstone (1999). “Determination of boundary values for the Stokes–Helmert problem.” *Journal of Geodesy*, Vol. 73, No. 4, pp. 180–192, doi: 10.1007/s001900050235.
- Vaniček, P., P. Novák, and Z. Martinec (2001). “Geoid, topography, and the Bouguer plate or shell.” *Journal of Geodesy*, Vol. 75, No. 4, pp. 210–215, doi: 10.1007/s001900100165.
- Vaniček, P., R. Tenzer, L. Sjöberg, Z. Martinec, and W. Featherstone (2004). “New views of the spherical Bouguer gravity anomaly.” *Journal of Geophysics International*, Vol. 159, No. 2, pp. 460–472, doi: 10.1111/j.1365-246X.2004.02435.x.
- Vaniček P., and M. Santos (2010). “Can mean values of Helmert’s gravity anomalies be continued downward directly?” *Geomatica*, Vol. 64, No. 2, pp. 245–251.
- Véronneau, M., R. Duval, and J. Huang (2006). “A gravimetric model as a vertical datum in Canada.” *Geomatica*, Vol. 60, No. 2, pp. 165–172.
- Völgyesi, L. (2005). “Local geoid determination based on gravity gradients.” *Acta Geodaetica et Geophysica Hungarica*, Vol. 36, No. 2, pp. 153–162, doi: 10.1556/AGeod.36.2001.2.3.
- Werner, M. (2001). “Shuttle Radar Topography Mission (SRTM), Mission overview.” *Frequenz*, Vol. 55, Nos. 3–4, pp. 75–79, doi: 10.1515/FREQ.2001.55.3-4.75.
- Wichiencharoen, C. (1982). “The indirect effects on the computation of geoid undulations.” Reports of the Department of Geodetic Science and Surveying, Report No. 336, Department of Geodetic Science and Surveying, Ohio State University, Columbus, Ohio, U.S.A.

- Wong, J. (2002). *On Picard Criterion and the Well-Posed Nature of Harmonic Downward Continuation*. M.Sc.E. thesis, Department of Geodesy and Geomatics Engineering Technical Report No. 213, University of New Brunswick, Fredericton, New Brunswick, Canada, 85 pp.
- Wunsch, C. (1993). "Physics of the ocean circulation." In *Satellite Altimetry in Geodesy and Oceanography*, Eds. R. Rummel and F. Sansò, Vol. 50 of *Lecture Notes in Earth Sciences*, Springer-Verlag, New York, pp. 10–98, doi: 10.1007/BFb0117926.
- Yen, H.-Y., and H.-H. Hsieh (2010). "A Study on the Compatibility of 3-D Seismic Velocity Structures with Gravity Data of Taiwan." *Terrestrial, Atmospheric and Ocean Sciences*, Vol. 21, No. 6, pp. 897–904, doi: 10.3319/TAO.2010.03.03.01(T).
- Zilkoski, D., and L. Hothem (1989). "GPS satellite surveys and vertical control." *Journal of Surveying Engineering*, Vol. 115, No. 2, pp. 262–281, doi: 10.1061/(ASCE)0733-9453(1989)115:2(262).

Chapter 2: Toward an improved orthometric height system for Canada

This article was published in *Geomatica*, a journal published by the Canadian Institute of Geomatics, in 2005. I developed the software and methods used in this article, performed the computations, and wrote the article. My coauthors provided guidance in the computation process, and in revising the manuscript for submission. The full citation for the article is:

Kingdon, R., P. Vaníček, A. Ellmann, M. Santos, and R. Tenzer (2005b). “Toward an improved orthometric height system for Canada.” *Geomatica*, Vol. 59, No. 3, pp. 241–249.

Note: The DTM data used in this publication is drawn from the Canadian Digital Elevation Database (CDED) data set. The reference is:

Canada, Natural Resources (2007). *Canadian Digital Elevation Data, Level 1 Product Specifications*. Edition 3.0, Centre for Topographic Information, Natural Resources Canada, Customer Support Group, Sherbrooke, Québec, Canada.

At the time of this article’s publication, I understood the DDM used in this article to have been produced by the Geological Survey of Canada. Since then I have learned that it was actually generated at UNB. The relevant reference is:

Fraser, D., S. Pagiatakis, and A. Goodacre (1998). “In-situ rock density and terrain corrections to gravity observations.” *Proceedings of the 12th Annual Symposium on Geographic Information Systems*, 6–9 April, 1998, Toronto, Ontario, Canada, 1998.

The NT gravity disturbances used here were also created at UNB, as a byproduct of geoid calculations. Though reasonably accurate, they were not final results, and were not otherwise published.

In sections 2.2 and 2.6, reference is made to the NT geoid-generated gravity disturbance being a result of the “geoid’s mass”. This expression refers to the masses contained within the geoid surface, excluding those whose effects are accounted for by the normal ellipsoid. Really, the NT gravity disturbance also includes the effects of masses exterior to the geoid (where it lies below the ellipsoid), which are counted both in the normal gravity effect and in the topographical effects. The redundant effects of these masses are removed when applying the NT disturbance, analogous to the accounting for absent topographical mass by the terrain effect. Thus, saying that the NT gravity disturbance results from the geoid’s mass in this paper is slightly misleading.

Chapter 2 Abstract

Heights in Canada are defined in the system of orthometric heights, according to a method proposed by Helmert in 1890. However, much development in the theory of heights has been done since then, leading to a more rigorous approach to orthometric heights. The new approach takes into account the effects of terrain roughness, laterally varying anomalous topographical density, and the NT geoid-generated gravity disturbance, which are not considered in the Helmert method.

This paper presents a calculation of corrections to Helmert orthometric heights, to update them to the more rigorous definition. The corrections for each effect, as well as a

total correction comprising all three effects, are evaluated for a Canadian test area comprising several types of terrain. The correction is found to reach decimetres in some mountainous areas.

2.1 Introduction

An understanding of heights is essential to the study of any field of geomatics, and the Canadian height system – called Helmert Orthometric Heights – is directly related to Earth's gravity field as well. This paper deals with the improvement of the Canadian height system, as a result of variations in Earth's gravity field; and in particular, with the determination of corrections to Helmert orthometric heights to account for these variations. Other errors, such as those involved in leveling operations for height determination, or inaccuracies in definition of the height datum, are not considered.

Orthometric height, geometrically, is the length of a (curved) plumbline intersecting the geoid – an equipotential surface having the same potential as mean sea level – at a right angle, and the corresponding point on the surface of the Earth. The heights in Canada were estimated by the 1928 adjustment of leveling networks, resulting in the Canadian Geodetic Vertical Datum 1928 (CGVD28). This readjustment used Helmert orthometric heights in its calculations, as did later incarnations such as the North American Vertical Datum 1988 (NAVD88) [Zilkoski et al., 1992].

Mathematically, the orthometric height, $H^o(\Omega)$ of a point is defined as its geopotential number divided by the mean gravity along the plumbline between that point and the geoid. The geopotential number, defined as the difference between the potential

on the geoid and the potential at a surface point, is determined from observed gravity and height differences between that point and mean sea level, realized at the surface of the Earth. The mean value of gravity along the plumbline, here shortened to *mean gravity*, is not so easily determined since the factors contributing to this value are difficult to quantify and require more complex mathematics for their evaluation. Traditionally, mean gravity has only been approximately calculated according to Helmert's method, which accounts for gravity generated by the ellipsoid, and approximates topography with a plate extending to infinity, known as a Bouguer plate. Since Helmert's method was introduced, however, the attempt to calculate mean gravity has undergone significant evolution. As pointed out in Tenzer et al. [2005], relevant developments are the inclusion of local terrain effects in the calculation (e.g., Niethammer [1932]; Mader [1954]), the introduction of effect of lateral anomalous density variations [Vaníček et al., 1995; Allister and Featherstone, 2001] and an examination of the effect of the geoid-generated gravity disturbance [Martin et al., 2003]. This paper presents an evaluation of corrections to Helmert orthometric heights required to account for these effects. Corrections calculated in a Canadian context are presented here, and an assessment of their behavior is carried out. The theoretical background is presented in Santos et al. [2006].

2.2 Corrections to Helmert orthometric heights

The Helmert method requires mean gravity along a plumbline as [Heiskanen and Moritz, 1967, eq. (4-24)]:

$$\bar{g}^H(\Omega) = g(r_t, \Omega) + 0.0424H(\Omega), \quad (2.1)$$

where $g(r_t, \Omega)$ is the value of gravity at the point at the surface of the Earth with spherical coordinates Ω and geocentric radius r_t , and $H(\Omega)$ is the orthometric height of the surface at the same point. This is based upon application of the Poincaré-Prey reduction to surface gravity, assuming a linear gravity gradient along the plumbline. It takes into account both normal gravity and the effect of a Bouguer plate having a constant density of 2670 kg/m^3 . However, as Santos et al. [2006] explain, these effects alone do not provide a sufficiently accurate calculation of mean gravity in all parts of Canada.

Mean gravity may be defined more rigorously as a sum of calculable effects. Those related to topography are shown in Figure 2.1, where the black hills and valleys represent the contribution of terrain roughness, and the columns of varying shades of grey represent lateral density variations, and their contribution. Vertical density variations and effects of atmospheric masses are not shown, since they are not considered herein.

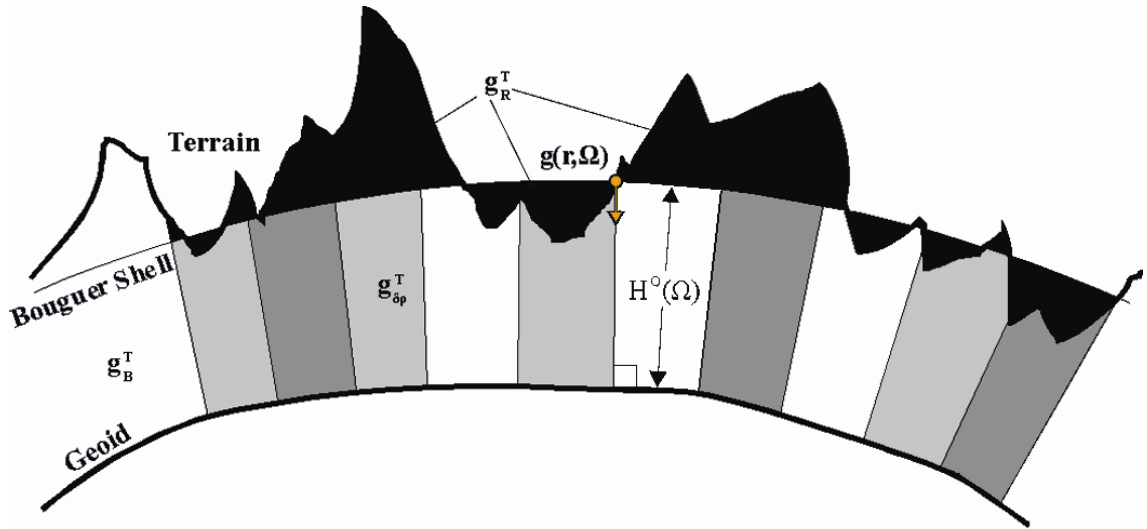


Figure 2.1: Components of gravity related to topography.

In addition to the contributions shown in Figure 2.1, gravity includes contributions not generated by topography. These are the gravity generated by the reference ellipsoid being used, and that generated by masses within the geoid. The latter exist in the no-topography (NT) space, a space where the topography of Earth has been removed, which is convenient for some calculations. It was introduced in Vaníček et al. [2004], which may be referred to for further explanation.

Mathematically, the total gravity may be written:

$$g(r, \Omega) \approx \gamma(r, \Omega) + \delta g^{NT}(r, \Omega) + g_B^T(r, \Omega) + g_R^T(r, \Omega) + g^{\delta p}(r, \Omega), \quad (2.2)$$

where $\gamma(r, \Omega)$ represents normal gravity (generated by mass within the geodetic reference ellipsoid, e.g., GRS-80 (e.g., Moritz [2000])); $\delta g^{NT}(r, \Omega)$ represents the geoid-generated

gravity disturbance (generated by the anomalous mass within the geoid); $g_B^T(r, \Omega)$ represents the effect on gravity of mass within a Bouguer shell of thickness $H^O(\Omega)$, assuming all mass has constant average crustal density; $g_R^T(r, \Omega)$ represents the effect on gravity of terrain variations, or roughness, above and below the Bouguer shell (i.e., hills and valleys) of constant average density; and $g^{\delta\rho}(r, \Omega)$ represents the effect on gravity of lateral density variations from constant average crustal density, within the topography.

Note that effects of atmospheric masses and of radial density variations are neglected throughout this paper. The effect of atmospheric masses is negligible because it is very small [Tenzer et al., 2005]. The density of air is around 1.25 kg/m^3 , which is less than 0.05% of average crustal density, resulting in a minimal effect of atmospheric masses on gravity. The effect of radial density variations has been neglected because it is difficult to quantify due to insufficient data on the radial distribution of density within the crust.

It follows from eq. (2.2) that gravity at a point on the surface, $g(r_t, \Omega)$ is rigorously defined as,

$$g(r_t, \Omega) \approx \gamma(r_t, \Omega) + \delta g^{NT}(r_t, \Omega) + g_B^T(r_t, \Omega) + g_R^T(r_t, \Omega) + g^{\delta\rho}(r_t, \Omega), \quad (2.3)$$

and mean gravity, $\bar{g}(r, \Omega)$, given by the integral mean of $g(r, \Omega)$, as,

$$\bar{g}(r, \Omega) \approx \bar{\gamma}(\Omega) + \overline{\delta g^{NT}}(\Omega) + \bar{g}_B^T(\Omega) + \bar{g}_R^T(\Omega) + \bar{g}^{\delta\rho}(\Omega); \quad (2.4)$$

where the bars over the terms represent integral mean quantities.

By substituting eq. (2.3) into the expression for mean gravity according to Helmert's method, eq. (2.1), for a constant crustal density of 2670 kg/m^3 , we obtain the following expanded expression for Helmert mean gravity:

$$\begin{aligned} \bar{g}^H(\Omega) \approx & \gamma(r_t, \Omega) + \delta g^{NT}(r_t, \Omega) + g_B^T(r_t, \Omega) + g_R^T(r_t, \Omega) + g^{\delta p}(r_t, \Omega) + \\ & + 0.0424H(\Omega). \end{aligned} \quad (2.5)$$

The correction to Helmert's mean gravity is then given by finding the difference between eq. (2.5) and the rigorous mean gravity given by eq. (2.4). In this operation, the contributions of normal gravity and gravity generated by mass within the Bouguer shell, along with the last term on the right-hand side of eq. (2.5), effectively cancel each other out [Santos et al., 2006]. Thus,

$$\begin{aligned} \varepsilon_{\bar{g}}(\Omega) = & \bar{g}(\Omega) - \bar{g}^H(\Omega) \\ = & \overline{\delta g^{NT}}(\Omega) - \delta g^{NT}(r_t, \Omega) + \\ & + \bar{g}_R^T(\Omega) - g_R^T(r_t, \Omega) + \\ & + \bar{g}^{\delta p}(\Omega) - g^{\delta p}(r_t, \Omega), \end{aligned} \quad (2.6)$$

and the only terms of the correction which must be calculated are those resulting from the mean and surface effects on gravity of terrain roughness, the laterally varying

density distribution, and the geoid-generated gravity disturbance. Once these terms have been calculated, the corresponding correction to Helmert orthometric heights may be determined using (cf., Heiskanen and Moritz [1967, chap 4]):

$$\varepsilon_{H^o}(\Omega) = -\frac{H^o(\Omega)}{\bar{g}(\Omega)} \varepsilon_{\bar{g}}. \quad (2.7)$$

Corrections thus calculated may then be applied to leveling benchmarks, or any orthometric heights defined in the Canadian height system.

2.3 The test area

Software has been written to calculate the corrections to Helmert orthometric heights for the three effects shown in eq. (2.6), and the source code is available from the primary author upon request. These calculations were performed using a regular grid of points 5' apart, to provide suitable resolution for plots of the area, within a test area stretching from 49° to 54° in latitude, and 235° to 243° east in longitude. This area was chosen because its characteristics produce extreme results for each of the three effects calculated. Although it only represents a small segment of Canada's land mass, it contains both rugged and flat terrain, and seashore; so that the nature of the effects in many other areas may be judged from the results.

Heights in the test area range from 0 m to 3227 m, and laterally varying densities, based on surface geology, range from 2490 kg/m³ to 2980 kg/m³. Since the average crustal density is 2670 kg/m³, assumed constant, this corresponds to laterally varying

anomalous densities between -180 kg/m^3 and 310 kg/m^3 . Geoid-generated gravity disturbances ranged from -266 mGal to -16 mGal . The distributions of height, anomalous density, and gravity anomalies are shown in Figures 2.2, 2.3 and 2.4, below.

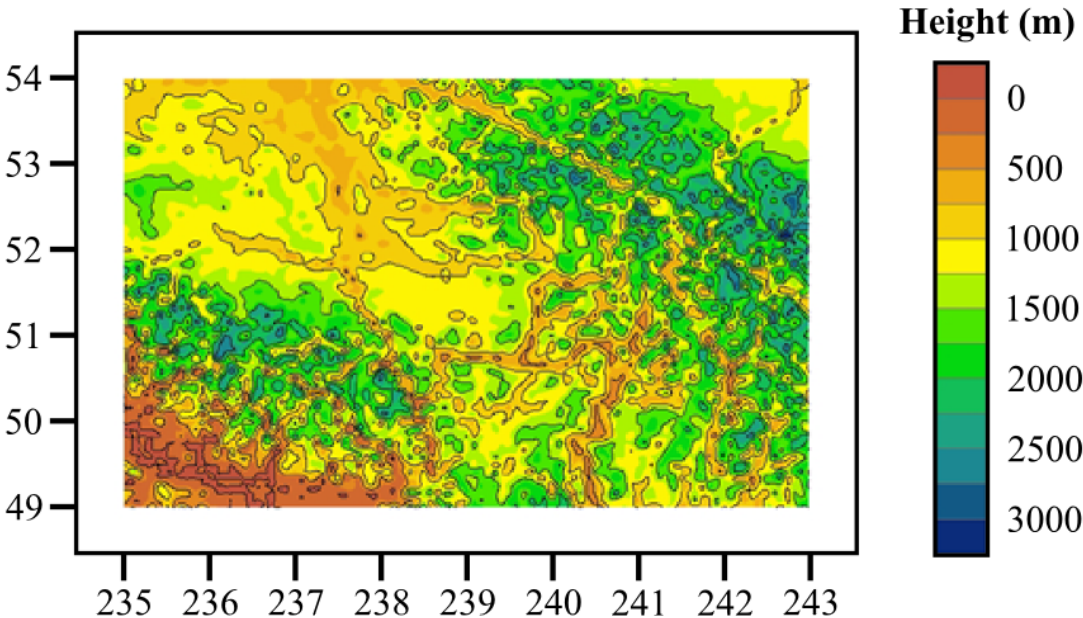


Figure 2.2: Orthometric heights within the test area, 500 m contours.

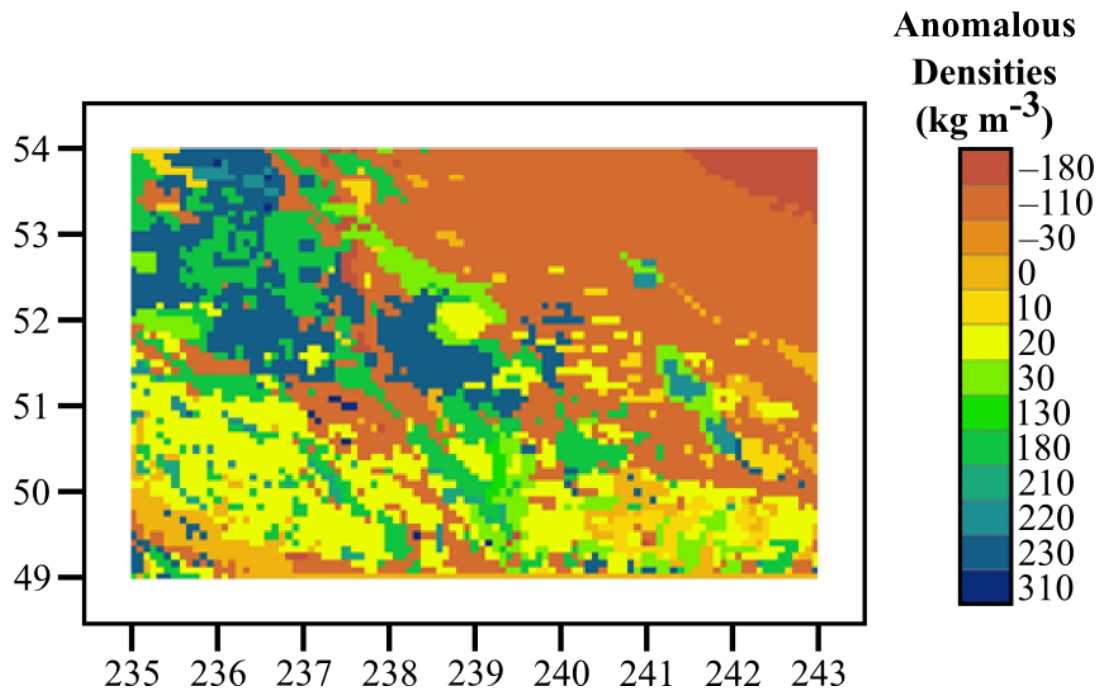


Figure 2.3: Laterally-varying anomalous densities within the test area, anomalous density indicated by tone. Data from the Geological Survey of Canada.

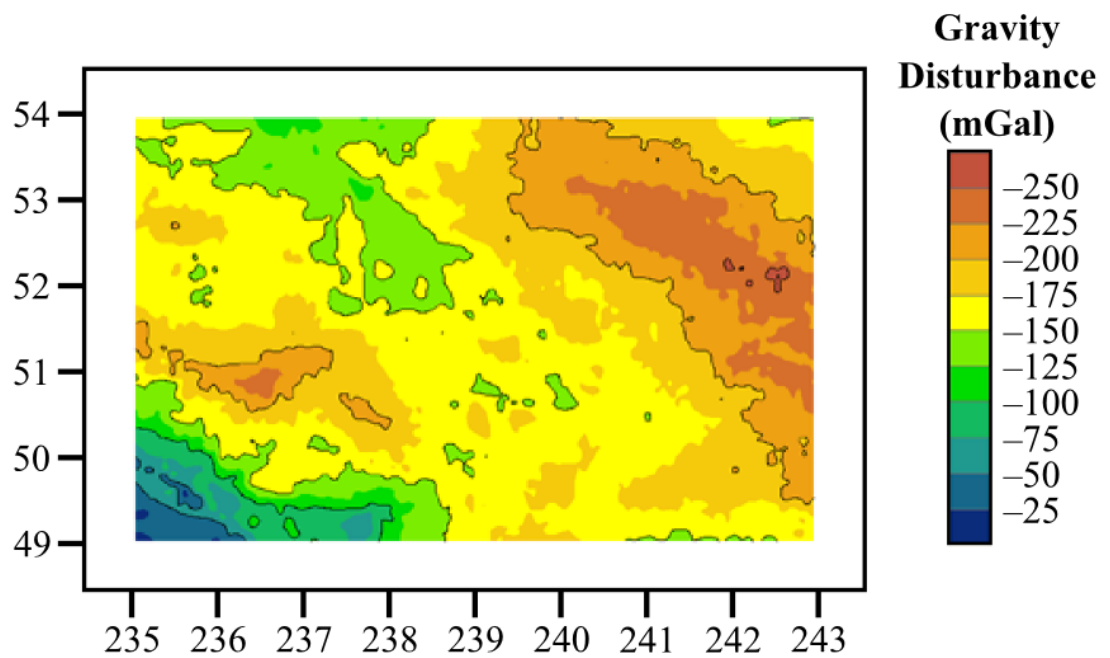


Figure 2.4: NT Geoid-generated gravity disturbances within the test area, 50 mGal contours.

2.4 The effect of terrain roughness

The effect of terrain roughness, sometimes called just “the terrain effect” on gravity may be evaluated by integration of effects of surplus mass above the Bouguer shell, and mass deficit below the Bouguer shell, indicated by the black shaded area in Figure 2.1.

The terrain effect on Helmert mean gravity may be evaluated either as a simple average of the effect on gravity at the Earth’s surface and on the geoid, according to the method of Mader [1954], or using an integral mean. If the integral mean approach is applied, it may be done using the Niethammer approach [1932], in which the integral mean is approximated by calculating the effects on gravity at a series of points along the plumbline and averaging these results. Alternatively, according to a recent method developed at the University of New Brunswick (U.N.B.), the contribution of terrain roughness to gravitational potential at the surface and on the geoid may be calculated, and divided by orthometric height, to determine an exact value of the effect on Helmert mean gravity (e.g., Tenzer et al. [2005, eq. (21)]). Although results from all three methods are similar, the present study confirms that the U.N.B. method for calculating effects on mean gravity is the most effective due to its speed and accuracy.

For the calculation of both effects, integration of mass surpluses and deficits is performed within a spherical cap of 3° , using an analytical solution for the radially integrated negative radial derivative of the Newton’s integral kernel, with the assumption that any masses outside of this area may be neglected in this calculation. The integral kernel is (e.g., Martinec [1998]):

$$N(r, \psi[\Omega, \Omega'], r') = \frac{r' \cos(\psi[\Omega, \Omega']) - r}{\ell^3(r, \psi[\Omega, \Omega'], r')}, \quad (2.8)$$

where r is the geocentric radius of the computation point, r' is the geocentric radius of the integration point, $\psi[\Omega, \Omega']$ is the spherical angle between the computation point and the integration point, and $\ell(r, \psi[\Omega, \Omega'], r')$ is the distance between the computation and integration points. The assumption that the effect of terrain beyond 3° is negligible is based on test computations with varying sizes of spherical cap over a test area. DEM data in three integration zones provides a basis for numerical integration. In the innermost zone, a $15'$ by $15'$ square centered on the computation point, $3''$ data is used. In the inner zone, a $200'$ square, $30''$ data is used. Within the rest of the spherical cap, $5'$ data are used. These parameters were all determined, like the radius of the spherical cap, by variation of each parameter for a test area. Furthermore, interpolation is performed to divide the central $3''$ cell into four $1.5''$ cells to make the integration more accurate. Integration is performed to determine both the effect on Helmert mean gravity, and the effect on surface gravity. Once these are found, they are subtracted according to eq. (2.6) to determine a correction to Helmert's mean gravity for terrain roughness. Note that the total effect on Helmert's mean gravity would have the opposite sign of this correction.

Values of this correction within the test area ranged from 106 mGal to -25 mGal, while the corresponding corrections to Helmert orthometric height, calculated according to eq. (2.9), ranged from 4.6 cm to -31.0 cm, and may be seen in Figures 2.5 and 2.6.

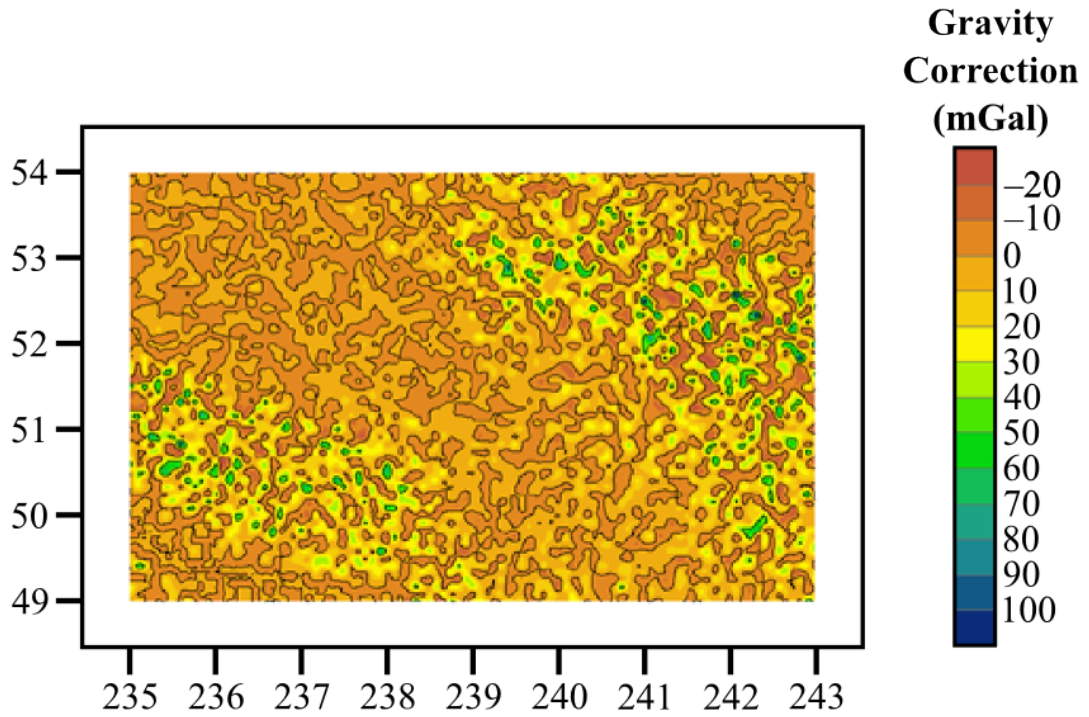


Figure 2.5: Correction to Helmert mean gravity for terrain roughness within the test area, 40 mGal contours.

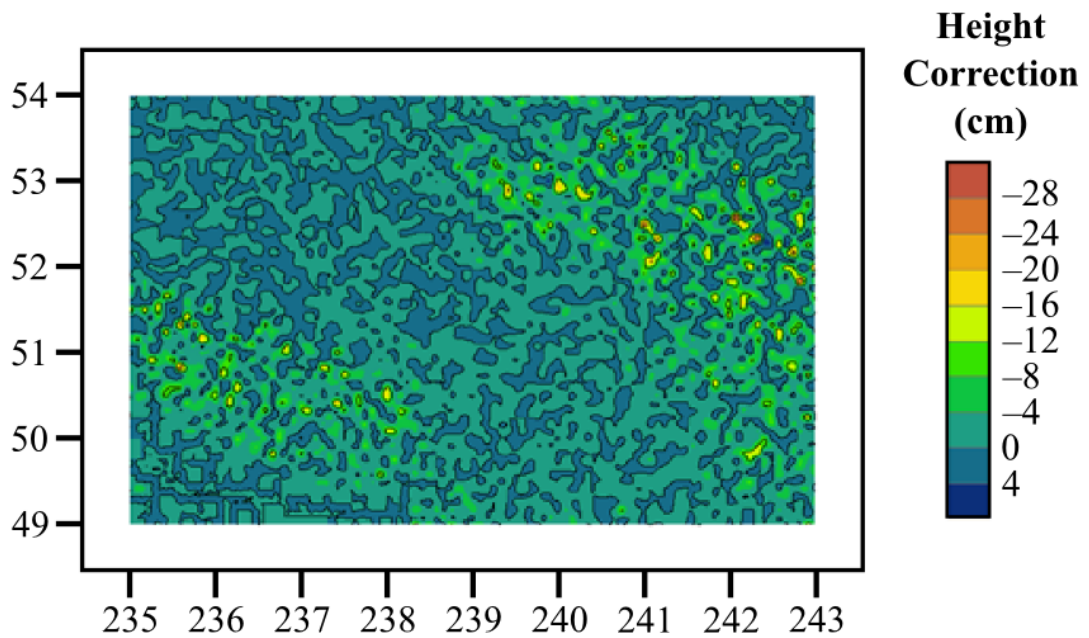


Figure 2.6: Correction to Helmert orthometric heights for terrain roughness within the test area, 10 cm contours.

Effects related to roughness should be expected to peak where the terrain does, and this behaviour is seen in Figures 2.5 and 2.6. While it may appear at first glance as though the correction follows the height of terrain almost exactly, Figure 2.6 shows that this is not the case. For example, notice that the valleys which are distinctly defined in the topographic map of Figure 2.1 are not easily distinguished in the corrections given in Figures 2.5 and 2.6. This behavior is expected, since the terrain effect on gravity is a function of roughness, rather than of height of the computation point. Also, notice that the terrain in the middle of the map, having a more gradual slope, produces lower correction values; while the values peak sharply in rough terrain. While greater heights may amplify the correction, rough terrain is also necessary for it to be significant.

2.5 The effect of laterally-varying anomalous density

The effects of the Bouguer shell and of terrain are both evaluated assuming constant topographical density, and thus do not include the effect of density variations. While sufficient data are not available to calculate the effect of radial density variations, the effect of lateral variations may be calculated, thus accounting to some extent for the influence of density variations.

The effect of lateral density variations on gravity is calculated by first obtaining a series of density values for polygons within the area, and then subtracting from these the average crustal density of 2670 kg/m^3 . This results in a series of density differences for the polygons, which may be thought of as columns of positive or negative density

anomalies, extending from the surface of the geoid to the Earth's surface, as indicated in Figure 2.1. For a more detailed description, see Huang et al. [2001].

To calculate exactly the effect of these anomalous density columns on gravity requires integration over the mass surpluses and deficits within these columns, using the same Newton kernel as for the terrain effect. Practically, however, the variations in height of these columns above and below the Bouguer shell – i.e., their influence on the terrain effect – may be neglected.

Integration was performed over two integration zones, the inner zone and the middle zone. Within the inner zone, which was 5' square, integration points were spaced 3" apart, and density anomaly values were interpolated to these points. Within the middle zone, which was 10' square, integration points were spaced 30" apart and were located in the center of cells of the input density data. As with the terrain effect calculations, these values were determined by varying one parameter while holding the others fixed.

Calculation of the effect on Helmert mean gravity may be performed using the same three methods as for calculation of the terrain roughness effect. However, the difference in results using these three methods is less than half a centimetre within the test area. Still, the U.N.B. method is preferred and was used for calculations, for the same reasons as with the terrain effect: speed, and accuracy.

The correction to Helmert mean gravity for laterally-varying anomalous density over the test area varied from 14 mGal to –24 mGal. Corresponding corrections to height, computed in a regular grid, varied from 6.5 cm to –4.5 cm, with both corrections correlated to both density and height. These results are also similar to those presented in Tenzer et al. [2003], whose corrections, calculated for Canadian leveling points, ranged

from 3.4 cm to -1.9 cm. Because the actual density in the test area was generally greater than average topographic density, the effect of the laterally-varying density distributions on height was positive. It is also noteworthy that the effect on mean gravity is very small, and might normally be negligible, the magnitude of the correction coming mainly from the effect on surface gravity. Results for the test area are shown in Figures 2.7 and 2.8.

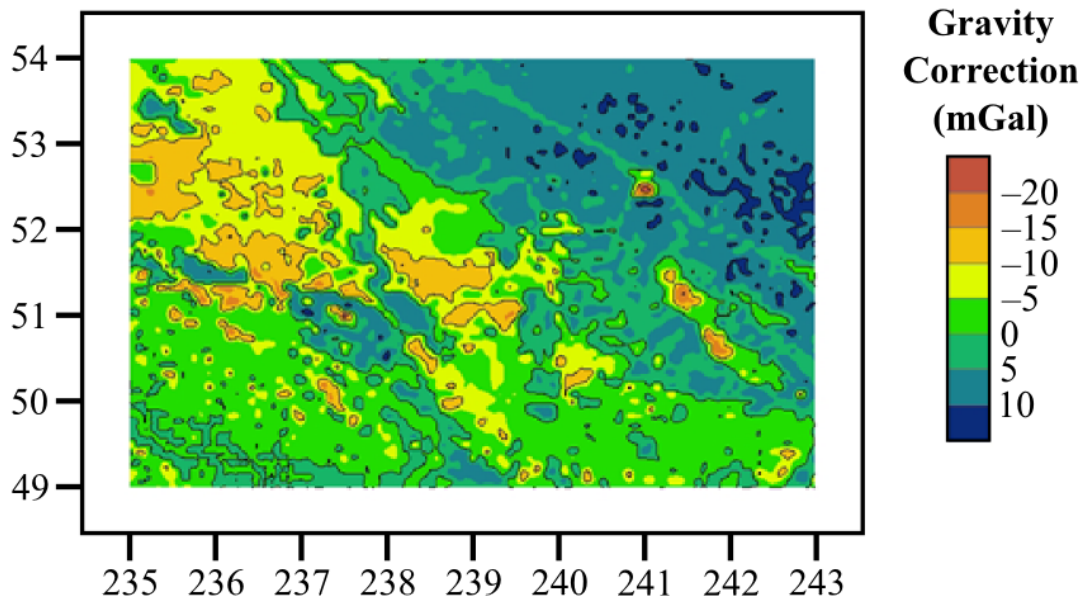


Figure 2.7: Correction to Helmert mean gravity for laterally-varying anomalous density within the test area, 10 mGal contours.

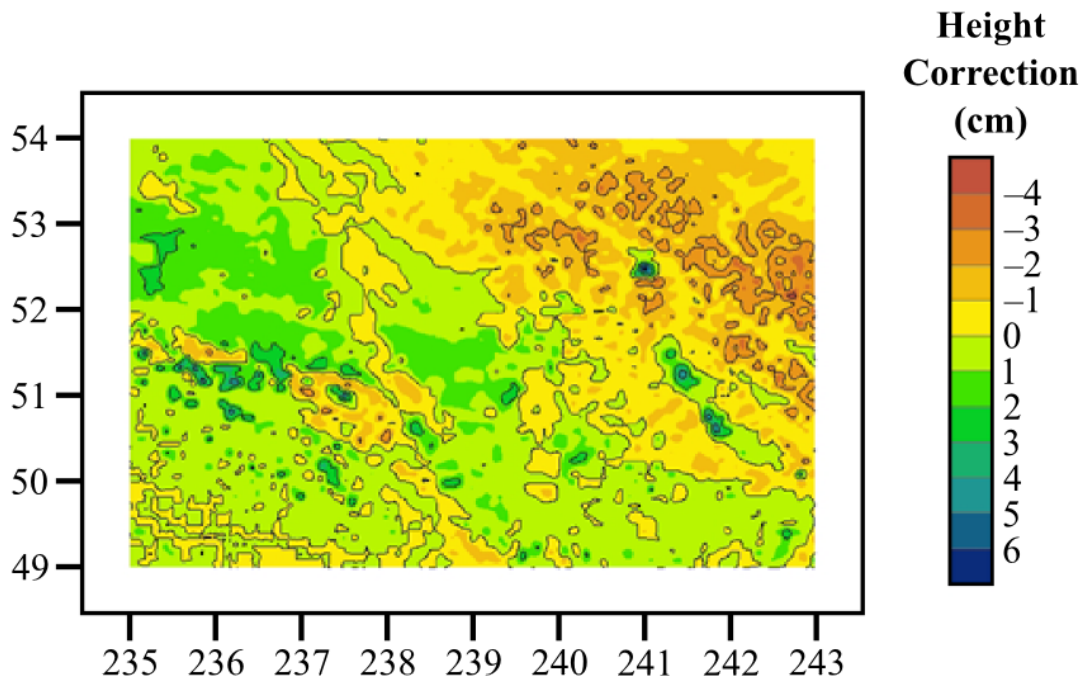


Figure 2.8: Correction to Helmert orthometric heights for laterally-varying anomalous density within the test area, 2 cm contours.

Figures 2.7 and 2.8 show a tendency for both the mean gravity and height corrections to peak where the terrain does, as with the terrain roughness effect; though the tendency is not so pronounced here. This is to be expected, since while the effect of lateral density variations within a Bouguer shell is a function of height, the lateral density variations amount to no more than about 10% of the average crustal density, so that their influence on gravity is relatively small. Also, the magnitude of this effect is generally small, in part because anomalous densities are significantly smaller than average topographical density.

2.6 The geoid-generated gravity disturbance

The geoid-generated gravity disturbance represents the effect of the geoid's mass on gravity. The effect on gravity at the surface may be found by upward continuation of the disturbance, referred to the geoid's surface, to the Earth's surface. This is done using Poisson's integral [Kellogg, 1929]. Radial integration, using this kernel, is performed over a spherical cap with radius of 7° from the computation point. Disturbances referred to the geoid may be found by removing the secondary indirect topographical effect from the NT gravity anomaly referred to the geoid [Tenzer et al., 2005]. Note, however, that this effect may also be calculated directly using downward continuation of gravity disturbances referred to the Earth's surface.

The upward continuation calculation used gravity disturbance data given in a regular grid with 5' spacing. Integration was done in two zones, with integration in a 10' square inner zone performed separately from that over the rest of the 7° spherical cap. In the inner zone, a planar approximation of distance was applied in evaluation of the Poisson kernel, and the 5' input data was interpolated to create a regular 30'' grid. The size of each zone was determined by varying its radius while holding that of the other zone constant. The 5' spacing simply reflects the available data, while the 30'' interpolation of data was determined by varying interpolation intervals until the effect on results from any finer interpolation was negligible.

The mean effect on gravity may either be approximated by upward continuation of the disturbance to a point halfway along the plumbline, or directly evaluated using an integral mean. In the latter case, a formula for the indefinite integral of the Poisson

kernel has been provided by Tenzer et al. [2005, eq. (9)], which is employed, slightly adapted to use a planar approximation of spherical distance in the inner zone, in calculation of the mean geoid-generated gravity disturbance. Both techniques produced results no more than 5 mm apart, but the results from the integral mean approach were accepted as more accurate [Martin et al., 2003].

Results for the correction to Helmert mean gravity over the test area vary from -66.1 mGal to 8.9 mGal, and for the correction to Helmert orthometric heights from -0.1 cm to 21.0 cm. As expected, the differences between gravity disturbances on the geoid, and mean or surface gravity disturbances, vary according to the height of the computation point. It also follows that the magnitude of corrections is correlated with height of the computation point, though it is also correlated with the magnitude of the geoid-generated gravity disturbances. Distribution of the results is shown in Figures 2.9 and 2.10, below.

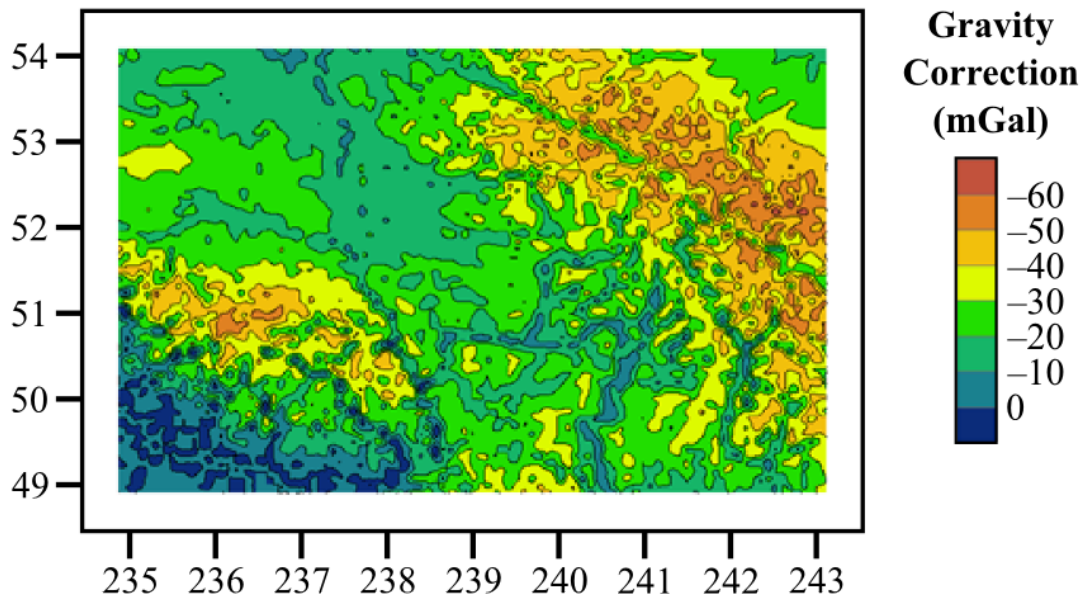


Figure 2.9: Correction to Helmert mean gravity for the geoid-generated gravity disturbance within the test area, 10 mGal contours.

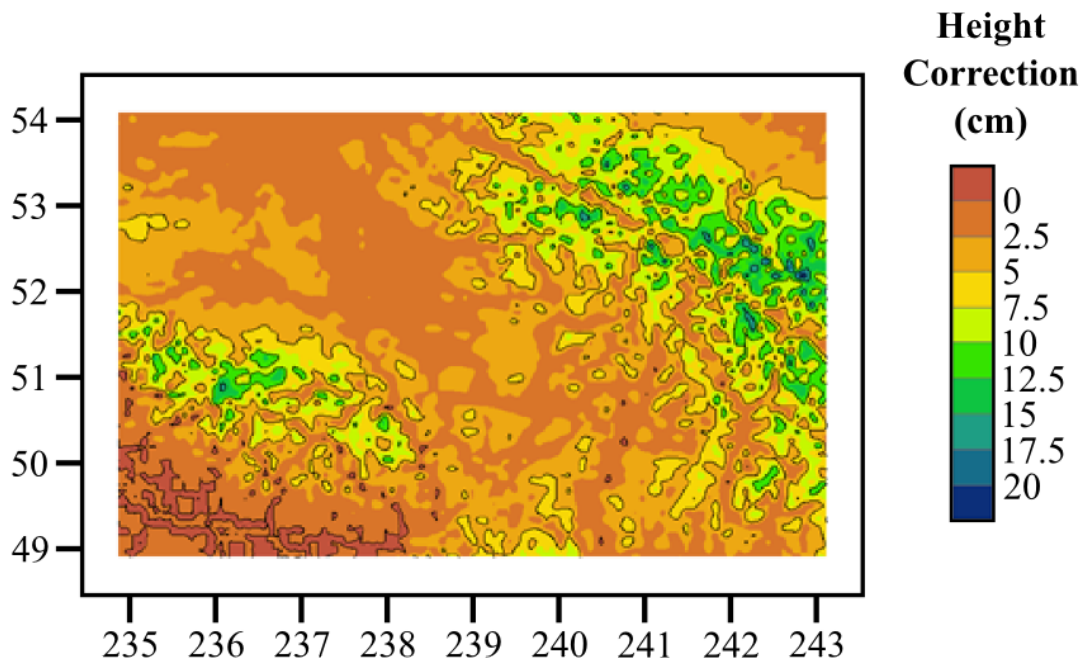


Figure 2.10: Correction to Helmert orthometric heights for the geoid-generated gravity disturbance within the test area, 5 cm contours.

2.7 Total corrections to Helmert orthometric height

These three corrections must be added together to determine a final correction to Helmert orthometric heights. The final correction to mean gravity ranges from -70.3 mGal to 58.4 mGal. These correspond to corrections to Helmert's orthometric height from -17.1 cm to 14.2 cm. In the final summation, the geoid-generated gravity disturbance effect and the terrain roughness effect often cancel each other within the test area, where the geoid-generated gravity disturbances are often negative. While the correction resulting from anomalous density occasionally works in the opposite direction to the terrain effect, in the highest parts of the test area – where the influence of the density correction is amplified – it works in the same direction as the terrain effect, making the overall correction larger. The corrections to gravity over the test area are given in Figure 2.11, below; and the corrections to height in Figure 2.12.

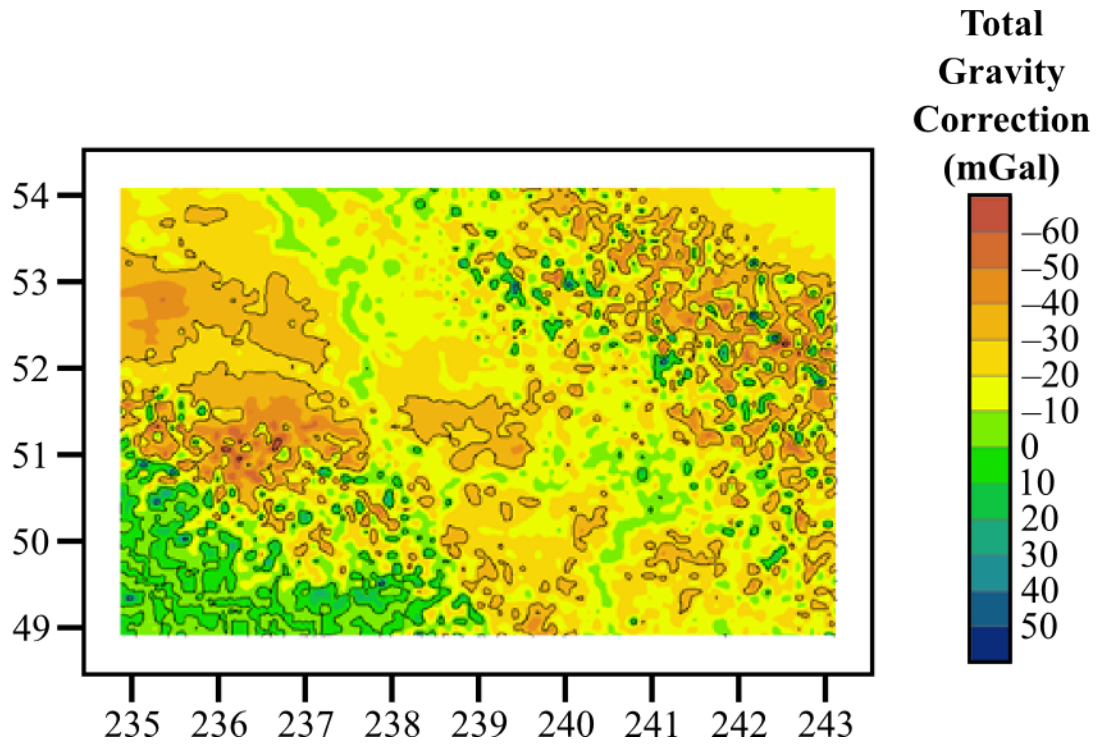


Figure 2.11: Total corrections to Helmert mean gravity for the spherical terrain effect, the effect of laterally-varying anomalous density, and the geoid-generated gravity disturbance, within the test area. 30 mGal contours.

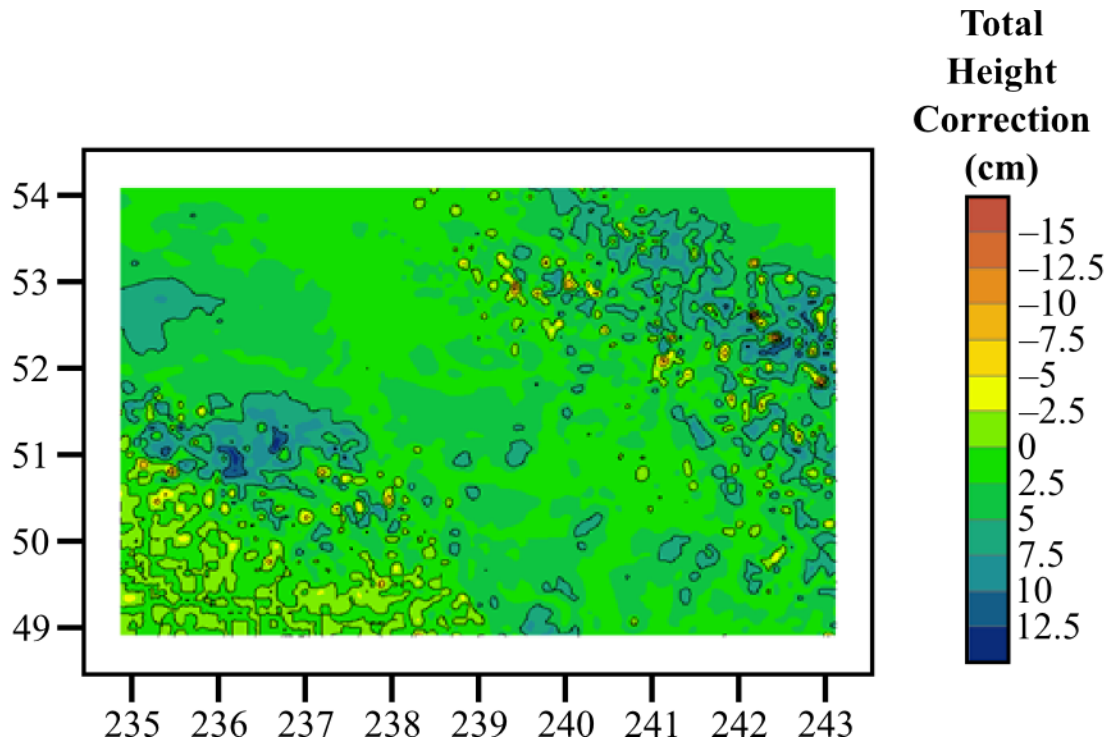


Figure 2.12: Total corrections to Helmert orthometric height for the spherical terrain effect, the effect of laterally-varying anomalous density, and the geoid-generated gravity disturbance within the test area. 5 cm contours.

Figure 2.11 shows that the correction to gravity has a tendency to peak in areas of rough terrain, where the main factor in these corrections – the terrain roughness effect – is at its greatest, and where the influences of height on the other two corrections is also at a maximum. While these gravity corrections may be the most effective means of seeing which effects have the greatest contribution to the final height corrections, it is the height corrections themselves that this paper sets out to describe. They are generally small, with a tendency to peak in rough terrain at high elevations. In most low-lying areas, the total correction is under 5 cm; while in more rugged areas it is as high as 17 cm in magnitude.

A summary of all contributions and total effects is provided in Table 2.1, below.

Table 2.1: Corrections to Helmert orthometric height for the spherical terrain effect, the effect of laterally-varying anomalous density, and the geoid-generated gravity disturbance within the test area.

Correction	Minimum	Maximum	Mean
Terrain roughness	-31.0 cm	4.6 cm	-1.3 cm
Laterally-varying anomalous density	-4.5 cm	6.5 cm	-0.1 cm
Geoid-generated gravity disturbance	-0.1 cm	21.0 cm	4.0 cm
Total correction	-17.1 cm	14.2 cm	3.7 cm

2.8 Summary and conclusions

Helmert’s standard method for determining orthometric height is not adequate to determine heights having accuracy less than 1 cm in all areas of Canada. In a test area in the Rocky Mountains, corrections for three effects were calculated: the effect of terrain roughness, the effect of laterally-varying anomalous density, and the geoid-generated gravity disturbance. The total correction reached a maximum of 17 centimetres in magnitude. If Canadian heights are to be considered rigorous, these effects must be taken into consideration – especially in mountainous areas, like the Rockies.

Chapter 2 Acknowledgements

First, we thank GSD (Geodetic Survey of Division of Natural Resources Canada) for supplying the topographic data used in these calculations. We would also like to thank the GEOIDE (GEOmatics for Informed DEcisions) Network of Centres of Excellence of Canada for their financial support of this research. Furthermore, we acknowledge

NSERC, the National Science and Engineering Council of Canada, for their funding of our research.

Chapter 2 References

- Allister, N., and W. Featherstone (2001). "Estimation of Helmert orthometric heights using digital barcode leveling, observed gravity and topographic mass-density data over part of Darling Scarp, Western Australia." *Geomatics Research Australasia*, No. 75, pp. 25–52.
- Heiskanen W., and H. Moritz (1967). *Physical Geodesy*. Freeman, San Francisco, U.S.A.
- Helmert, F. (1890). *Die Schwerkraft im Hochgebirge insbesondere, in den Tyroler Alpen, in geodätischer und geologischer Beziehung*. Königliches Preußischen Geodätischen Institut, Berlin, Germany.
- Huang, J., P. Vaníček, S. Pagiatakis, and W. Brink (2001). "Effect of topographical density on the geoid in the Rocky Mountains." *Journal of Geodesy*, Vol. 74, No. 11–12, pp. 805–815, doi: 10.1007/s001900000145.
- Kellogg, O. (1929). *Foundations of Potential Theory*. Springer, New York, U.S.A.
- Mader, K. (1954). "Die orthometrische Schwerekorrektion des Präzisions-Nivellements in den Hohen Tauern." *Österreichische Zeitschrift für Vermessungswesen*, Special issue 15.
- Martin, B.-A., C. MacPhee, R. Tenzer, P. Vaníček, and M. Santos, 2003. "Mean geoid-generated gravity disturbance along plumbline." Paper presented at the 29th Canadian Geophysical Union Annual Scientific Meeting, Banff, Alberta, Canada, May 10–14.
- Martinec, Z. (1998). *Boundary value problems for gravimetric determination of a precise geoid*. Vol. 73 of *Lecture notes in Earth Sciences*, Springer, Berlin.
- Moritz, H. (2000). "Geodetic Reference System 1980." *Journal of Geodesy*, Vol. 74, No. 1, pp. 128–162. doi: 10.1007/s0019000050278.
- Niethammer, T. (1932). *Nivellement und Schwere als Mittel zur Berechnung wahrer Meereshöhen*. Schweizerische Geodätische Kommission, Bern, Switzerland.
- Santos, M., P. Vaníček, W. Featherstone, R. Kingdon, A. Ellmann, B.A. Martin, M. Kuhn and R. Tenzer (2006). "Relation between the rigorous and Helmert's definitions of orthometric heights." *Journal of Geodesy*, Vol. 80, No. 12, pp. 691–704, doi: 10.1007/s00190-006-0086-0.

- Tenzer, R., and P. Vaníček, (2003). “The correction to Helmert’s orthometric height due to actual lateral variation of topographical density.” *Revista Brasileira de Cartografia*, Vol. 55, No. 2, pp. 44–47.
- Tenzer, R., P. Vaníček, M. Santos, W. Featherstone, and M. Kuhn (2005). “The rigorous determination of orthometric heights.” *Journal of Geodesy*, Vol. 79, Nos. 1–3, pp. 82–92, doi: 10.1007/s001-005-0445-2.
- Vaníček P., A. Kleusberg, Z. Martinec, W. Sun, P. Ong, M. Najafi, P. Vajda, L. Harrie, P. Tomášek, and B. ter Horst (1995). “Compilation of a precise regional geoid.” Final contract report prepared by the Department of Surveying Engineering, University of New Brunswick, Fredericton, New Brunswick, Canada for the Geodetic Survey Division, Natural Resources Canada, Ottawa, Canada, 25 pp.
- Vaníček, P., R. Tenzer, L. Sjöberg, Z. Martinec, and W. Featherstone (2004). “New views of the spherical Bouguer gravity anomaly.” *Journal of Geophysics International*, Vol. 159, No. 2, pp. 460–472, doi: 10.1111/j.1365-246X.2004.02435.x.
- Zilkoski, D., J. Richards, and G. Young (1992). “Results of the General Adjustment of the North American Datum of 1988.” *Surveying and Land Information Systems*, Vol. 52, No. 3, pp. 133–149.

Chapter 3: Computationally efficient corrections to Helmert orthometric heights for terrain and density effects

This article will be submitted to *Computers and Geosciences*, a journal published by the International Association of Mathematical Geosciences, for anticipated publication in 2012. As with the previous article, I developed the software and methods, performed the computations, and wrote the article. My coauthors provided guidance in the computation process, and in revising the manuscript for submission. The full citation for the article is:

Kingdon, R., P. Vaníček, M. Santos, and A. Ellmann (2012). “Efficient correction of Helmert orthometric heights for terrain and density effects.” *Computers and Geosciences* (in preparation).

Chapter 3 Abstract

The system of orthometric heights is the official height system in many countries, and thus it is the system used on maps and in engineering applications. It provides “heights above mean sea level”, based on the mean value of gravity between a computation point and the geoid. The original method of evaluating the mean gravity, attributed to Helmert [1890], has been progressively refined. Here we describe an implementation of the terrain and density corrections to Helmert heights, based on the rigorous theory

described by Santos et al. [2006]. The computation requires evaluation of a 3-dimensional volume integral for each effect. We efficiently evaluate these integrals by using effects on potential to evaluate effects on mean gravity, reducing the dimensionality of the integration to 2, using simplified integration kernels, and by choosing optimal cell spacing for each of 5 integration zones. By applying this methodology, we are able to evaluate the terrain and density corrections for 3,721 points in the Canadian Rocky Mountains in only 33 minutes. We find that the speed of our computation is improved mostly by the use of potentials to evaluate effects on mean gravity, and by reduction of the integration dimensionality to 2. Omitting the former approach increases computation time by 116%, and omitting the latter approach by 59%. Also, we find that choice of integration zone sizes and resolutions has a significant effect on computational efficiency.

Conforming to our expectations, the terrain correction in the test area reaches 31.0 cm in magnitude, is predominantly negative, and is largest for high elevations. The density correction reaches only 6.2 cm in magnitude, has alternating signs depending on local density anomalies, and is also correlated with topography. The terrain correction is found to cancel up to 50% of the Bouguer shell effect for points at high elevations, which could be attributed to isostasy.

3.1 Introduction

For precise heighting in North America, two height systems are commonly used: geodetic (also incorrectly called ellipsoidal) heights, which measure heights

geometrically from some reference ellipsoid (e.g., GRS-80 [Moritz, 2000]) up and orthometric heights (e.g., NAVD88 [Zilkowski et al., 1992]). Orthometric heights are intimately related to the Earth's gravity field. The orthometric height of a point is the distance along the (slightly curved) plumbline between a point of interest and the geoid, the equipotential surface that approximates mean sea level [Heiskanen and Mortiz, 1967, chapter 4]. These are the heights used on maps and in engineering practice, while geodetic heights, which are easily determined by satellite systems such as the GPS, are used as an intermediate quantity. The realization of an orthometric height system within a country consists of national benchmarks with orthometric heights determined through a series of precise leveling and gravity observations. As a result, precise orthometric heights have to be evaluated at benchmark points located irregularly along leveling lines, rather than, e.g., on a regular grid.

Mathematically, the orthometric height $H^O(\mathbf{x}_P)$ at a point P with three-dimensional coordinates indicated by coordinate triplet \mathbf{x}_P is given by [Heiskanen and Moritz, 1967, eq. (4-21)]:

$$H^O(\mathbf{x}_P) = \frac{C(\mathbf{x}_P)}{\bar{g}(\mathbf{x}_P)}, \quad (3.1)$$

where $C(\mathbf{x}_P)$ is the geopotential number at P , and $\bar{g}(\mathbf{x}_P)$ is the mean value of gravity along the plumbline from P to the geoid. The geopotential number of the point of interest is the difference in gravity potential between the geoid and the point of interest, and is computed by geodetic leveling in conjunction with surface gravity observation

[Heiskanen and Moritz, 1967, section 4-1]. The mean gravity, $\bar{g}(P)$, is defined as the integral mean of gravity along the plumbline, given by the following formula

[Heiskanen and Moritz, 1967, Eq. 4-22]:

$$\bar{g}(\mathbf{x}_p) = \frac{1}{H^o(\mathbf{x}_p)} \int_{z=0}^{H^o(\mathbf{x}_p)} g(\mathbf{x}') dz, \quad (3.2)$$

where \mathbf{x}' is the coordinate triplet of an integration point lying on the plumbline, and dz represents a portion of the distance along the plumbline, from the geoid. Although values of gravity along the plumbline can be measured directly using borehole gravimetry (e.g., Strange [1982]), allowing a more direct determination of the mean gravity, this is not a practicable solution in the context of orthometric heights. Therefore, the mean gravity is instead calculated based on some model of the Earth's gravity field (e.g., Helmert [1890]; Niethammer [1932]; Allister and Featherstone [2003]).

Mean gravity may be considered as the sum of effects induced by masses above the geoid surface, and those induced by other masses [Tenzer et al., 2005]. Masses above the geoid comprise those contained between the geoid and the surface of the Earth, known as topographical masses, and the atmospheric masses above the surface of the Earth. The contributions of topographical and atmospheric masses to the mean gravity may be directly evaluated through Newton integration, based on some models of their mass density. The atmospheric effects are very small and can be considered negligible

[Tenzer et al., 2005], while the topographical effects are significant and will be the focus of this paper.

Non-topographical masses generate the normal (ellipsoid generated) gravity, and the deviations from normal gravity called the NT geoid-generated gravity disturbance (cf., Vaníček et al. [2004]). The contributions of normal gravity can be evaluated to a high precision in a straightforward manner, and much of their effect is already accounted for in historical models. As a matter of fact, if we decide to consider the normal gravity alone, we would be dealing with mean normal gravity along the normal plumbline. Heights defined in such a manner are the normal heights (e.g., Heiskanen and Moritz [1967, section 4-4]). The calculations for the geoid-generated gravity disturbance are more involved. The curious reader is directed to Tenzer et al. [2005] for further discussion of these effects, or to Santos et al. [2006] for discussion of the corresponding corrections to orthometric heights. Note that the corrections to orthometric heights referred to in Santos et al. [2006], and in this document, are not to be confused with the “orthometric correction” that can be applied to levelled height differences to convert them into orthometric height differences.

The model most widely used to calculate mean gravity is attributed to Helmert [1890], and is usually formulated as (Heiskanen and Mortiz [1967, eq. (4-24)]):

$$\bar{g}^H(\mathbf{x}_p) = g(\mathbf{x}_p) + 0.0424H^O(\mathbf{x}_p), \quad (3.3)$$

where the resulting mean gravity value is given in mGal for $H^O(\mathbf{x}_p)$ in metres.

In this prescription, that uses the Poincaré-Prey gravity gradient, a linear function of height is added to the observed surface gravity to find the mean gravity. Since the value of gravity varies by at most several hundred milligals between the Earth's surface and the geoid, the additional term is much smaller than the observed gravity, and the observed gravity is a good initial approximation of the mean gravity. Viewed in this way, the rightmost term in eq. (3.3) may be considered a first order correction to bring the mean gravity estimated by surface gravity nearer to the actual mean gravity value. For large heights, using this correction improves accuracy by several metres. In the case of Mount Everest, with a height of approximately 8.8 km, adding Helmert's first order correction to mean gravity improves the height determination by about 3.3 m, or about 0.04% of the total height. Although orthometric height is not yet available when applying eq. (3.3), using the leveled height instead introduces an error of at most 1.5 mm; thus using the leveled height instead of orthometric height in eq. (3.3) is an acceptable alternative.

While the first order correction given in eq. (3.3) accounts for most of the difference between mean gravity and surface gravity, it has not proven adequate to meet increasing requirements for precise orthometric heights. Consequently, repeated attempts have been made since the early 1900's to improve upon Helmert's recommendations by adding further corrective terms to account for higher than first order gravitational effects [Niethammer, 1932; Mader, 1954; Allister and Featherstone, 2001; Hwang and Hsiao, 2003; Tenzer et al., 2005; Kingdon et al., 2006]. These efforts have mainly dealt with improving modelling of topographical effects, whose precise calculation is the topic of this paper. We will show how to efficiently and accurately implement the rigorous

second order topographical corrections for the terrain and density effects discussed by Santos et al. [2006]. Furthermore, to make as practical an evaluation as possible, we will show an efficient way to evaluate these corrections at arbitrary points, so that it can be applied directly to benchmark heights.

3.2 Framework for calculating topographical corrections

3.2.1 General form of second order corrections to mean gravity

We have said that the prescription in eq. (3.3) is attributed to Helmert. In its original version, it is represented by the following formula (Heiskanen and Mortiz [1967, eq. (4-26)]):

$$\bar{g}^H(\mathbf{x}_p) = g(\mathbf{x}_p) - \left(\frac{1}{2} \frac{\partial \gamma}{\partial h} + 2\pi G \rho_0 \right) H^o(\mathbf{x}_p), \quad (3.4)$$

where γ is the normal gravity, h is the geodetic height; ρ_0 is the mean topographical density of 2670 kg m^{-3} ; and G is Newton's gravitational constant, equal to $6.67 \times 10^{-11} \text{ m}^3 \text{ kg}^{-1} \text{ s}^{-2}$. In eq. (3.4), the first order correction to mean gravity has been separated into the two bracketed terms. The first bracketed term represents the first order effect of normal gravity based on the normal gravity gradient, a non-topographical correction that will not be dealt with here. The second term accounts for the first order effect of the topographical masses on gravity along the plumbline. The correction is first order in that

is considers the linear components of the gravitational effects, and so it corresponds to the first order terms in the power series expansions for surface and mean gravity. Thus, Helmert's correction may be seen as a linearized version of the rigorous correction. While these first order corrections provide accuracies of a metre or better in most circumstances (the correction for an elevation of 1000 m is only 4.3 cm), modern applications require centimetre-level accuracy.

The corrective terms in eq. (3.4), and the higher order corrective terms we will discuss, are derived in the same general way. For a given effect E , on gravity at point P , $g^E(\mathbf{x}_P)$, with corresponding effect on mean gravity along the plumbline below P , $\bar{g}^E(\mathbf{x}_P)$, the corrective term (to be added to a less accurate approximation of mean gravity) is:

$$c_{\bar{g}}^E(\mathbf{x}_P) = \bar{g}^E(\mathbf{x}_P) - g^E(\mathbf{x}_P). \quad (3.5)$$

The correction to height corresponding to eq. (3.5) is based on the Taylor series expansion for orthometric height, expanded about a less accurate orthometric height. For a correction to Helmert orthometric height, the Taylor series is:

$$H^O(\mathbf{x}_P) = H^H(\mathbf{x}_P) - \frac{H^H(\mathbf{x}_P)}{\bar{g}^H(\mathbf{x}_P)} c_{\bar{g}^H}^E(\mathbf{x}_P) + \frac{H^H(\mathbf{x}_P)}{[\bar{g}^H(\mathbf{x}_P)]^2} [c_{\bar{g}^H}^E(\mathbf{x}_P)]^2 - \dots, \quad (3.6)$$

which leads to the correction to Helmert orthometric height

$$\begin{aligned}
c_{H^H}^E(\mathbf{x}_p) &= H^O(\mathbf{x}_p) - H^H(\mathbf{x}_p) = -\frac{H^H(\mathbf{x}_p)}{\bar{g}^H(\mathbf{x}_p)} c_{\bar{g}}^E(\mathbf{x}_p) + \frac{H^H(\mathbf{x}_p)}{[\bar{g}^H(\mathbf{x}_p)]^2} [c_{\bar{g}}^E(\mathbf{x}_p)]^2 - \dots \\
&\approx -\frac{H^H(\mathbf{x}_p)}{\bar{g}^H(\mathbf{x}_p)} c_{\bar{g}}^E(\mathbf{x}_p).
\end{aligned} \tag{3.7}$$

which can be evaluated to an accuracy of up to 6 mm or 0.2% of the total height using normal gravity and leveled height instead of mean gravity and orthometric height.

Three second-order corrections are not included in the topographical part of Helmert's approach. These are the corrections for the second and higher order effects of the Bouguer shell, the effect of variations in height of topography relative to the Bouguer shell (called terrain), and the effect of density variations relative to the assumed constant density of ρ_0 . The first of these is directly evaluated according to Santos et al. [2006, eq. (27)]. The evaluation of the other two will be discussed in the next section.

3.2.2 Evaluation of terrain and topographical density corrections using Newton integrals

In order to evaluate the terrain and topographical density corrections to mean gravity, we must determine the effect of the terrain and the mass density variations on both surface

gravity and on mean gravity. Both effects can be determined by Newton integration over the volumes of topographical mass. For a given effect E induced by volume of mass v^E , the effect on gravity is given by:

$$\mathbf{g}^E(\mathbf{x}_P) = -G \iiint_{v \in v^E} \rho(\mathbf{x}_{P'}) \frac{\partial N(\mathbf{x}_P; \mathbf{x}_{P'})}{\partial z} dv, \quad (3.8)$$

where $N(P;P')$ is the Newton kernel given by (e.g., Martinec [1993, eq. (2.2)]):

$$N(\mathbf{x}_P, \mathbf{x}_{P'}) = L(\mathbf{x}_P, \mathbf{x}_{P'})^{-1}, \quad (3.9)$$

L is the straight line distance between the computation point \mathbf{x}_P and the integration point $\mathbf{x}_{P'}$, $\rho(\mathbf{x}_{P'})$ is the density at point P' of the mass inducing E , and dv is the volume element. The effect E on mean gravity, based on eq. (3.2), is given by (cf., Tenzer et al. [2005, eq. (2)]):

$$\bar{\mathbf{g}}^E(\mathbf{x}_P) = \frac{1}{H^O(\mathbf{x}_P)} \int_{z=0}^{H^O(\mathbf{x}_P)} \mathbf{g}^E(\mathbf{x}') dz. \quad (3.10)$$

Considering the relationship between gravitational potential and gravity, eq. (3.10) can also be written [Tenzer et al. 2005, eq. (18)]:

$$\bar{g}^E(\mathbf{x}_P) = \frac{V^E(\mathbf{x}_{P_0}) - V^E(\mathbf{x}_P)}{H^O(\mathbf{x}_P)}, \quad (3.11)$$

where V^E is the effect of the masses in v^E on gravitational potential, and P_0 is the point on the geoid along the plumbline below P . $V^E(\mathbf{x}_P)$ can be calculated by the volume integral:

$$V^E(\mathbf{x}_P) = G \iiint_{v \in v^E} \rho(\mathbf{x}_{P'}) N(\mathbf{x}_P; \mathbf{x}_{P'}) dv. \quad (3.12)$$

The application of eq. (3.11) to calculate the effect on mean gravity is unique to the UNB approach to rigorous orthometric heights as introduced by Tenzer et al. [2005]. Previously, the effects on mean gravity were calculated either as the average of gravitational effects at both ends of the plumbline [Mader, 1954], or as the average of the gravitational effects at discrete intervals along the plumbline [Niethammer, 1932]. Mader and Niethammer originally employed these methods to calculate terrain effects, using eq. (3.8). Because it more closely approximated the integral mean, Niethammer's method is considered more accurate than Mader's [Dennis and Featherstone, 2003]. The method used in eq. (3.11), however is faster and more exact than Niethammer's method, and about as fast and much more accurate than Mader's [Kingdon et al., 2006].

We substitute eqs. (3.8) and (3.10) to (3.12) into eq. (3.5) to write a single expression for the correction to mean gravity:

$$c_{\bar{g}}^E(\mathbf{x}_P) = G \iiint_{v \in v^E} \rho(\mathbf{x}_{P'}) \left[\frac{N(\mathbf{x}_{P_0}; \mathbf{x}_{P'}) - N(\mathbf{x}_P; \mathbf{x}_{P'})}{H^O(\mathbf{x}_P)} + \frac{\partial N(\mathbf{x}_P; \mathbf{x}_{P'})}{\partial z} \right] dv. \quad (3.13)$$

We may further directly evaluate the correction to height by substituting eq. (3.13) into eq. (3.7), providing the general formula for a correction to height for any effect E :

$$c_H^E(\mathbf{x}_P) = \frac{G}{\bar{g}(\mathbf{x}_P)} \iiint_{v \in v^E} \rho(\mathbf{x}_{P'}) \left[N(\mathbf{x}_P; \mathbf{x}_{P'}) - N(\mathbf{x}_{P_0}; \mathbf{x}_{P'}) - H^O(\mathbf{x}_P) \frac{\partial N(\mathbf{x}_P; \mathbf{x}_{P'})}{\partial z} \right] dv. \quad (3.14)$$

3.2.3 Application for terrain and density effects

We will evaluate the integral in eq. (3.14) using the spherical approximation of the geocentric geodetic coordinate system [Moritz, 1980, p. 349]. Horizontal positions in this system are indicated by the direction Ω consisting of geodetic latitude, φ , and longitude, λ ; however, the eccentricity of the ellipsoid is removed so that these are treated as spherical coordinates for distance calculations [Vajda et al., 2004]. We have deviated from the usual spherical approximation in which the major semi-axis of the ellipsoid is replaced by the mean radius of the ellipsoid. Instead, following Tenzer et al. [2005] and Santos et al. [2006], we have replaced the geocentric radius of the geoid at every point with the mean radius of the ellipsoid, which for the GRS-80 ellipsoid, is $R = 6371008.7714$ m. Since the major semi-axis of the GRS-80 ellipsoid deviates from the mean radius by about 7 km, and the geoid only deviates from the ellipsoid by up to a few

hundred metres [Vaniček and Krakiwsky, 1986, chapter 7], this implementation is admissible. The error in the topographical corrections induced by using this form of the spherical approximation is expected to be less than 1 mm [Santos et al., 2006]. Under the spherical approximation, the distance between two points is given by:

$$L(\mathbf{x}_P; \mathbf{x}_{P'}) = (r^2 + r'^2 - 2rr' \cos \psi[\Omega, \Omega'])^{1/2}, \quad (3.15)$$

where $r = R + H^O(P)$, $r' = R + H^O(P')$, Ω and Ω' represent the horizontal positions of P and P' , and $\psi[\Omega, \Omega']$ is the spherical geocentric angle between P and P' , given by (e.g. Heiskanen and Moritz [1967, eq. 1-72]):

$$\cos \psi[\Omega, \Omega'] = \cos \varphi \cos \varphi' + \sin \varphi \sin \varphi' \cos(\lambda - \lambda'). \quad (3.16)$$

We first apply the general formula in eq. (3.14) for the case of the terrain correction, which we will indicate by the superscript T . The shaded region in Figure 3.1 indicates the mass deficiencies and excesses with respect to the Bouguer shell that cause the terrain effect.

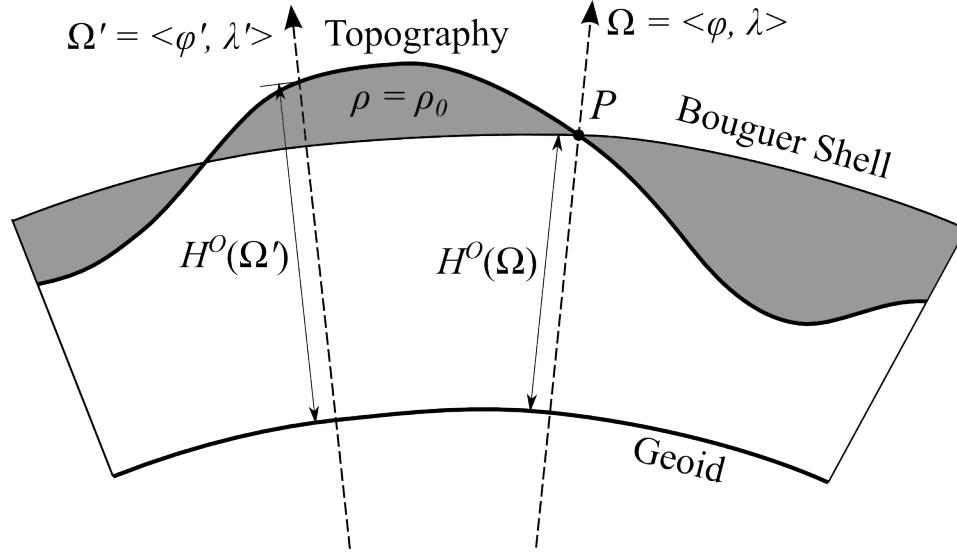


Figure 3.1: Masses causing the terrain effect on gravity.

The density of the terrain is considered equal to ρ_0 , the density assigned to the Bouguer shell. Equation (3.14) applied for the terrain correction, using spherical coordinates, is given by (cf., Santos et al. [2006, eqs. (43), (51) and (52)]):

$$\begin{aligned}
 c_H^T(r, \Omega) &= \\
 &= \frac{G\rho_0}{\bar{g}(r, \Omega)} \int_{\lambda'=0}^{2\pi} \int_{\varphi'=-\pi/2}^{\pi/2} \int_{r'=R}^{r'=R+H^0(P_t[\Omega'])} K(r, \Omega; r', \Omega') r'^2 dr' \sin(\varphi) d\varphi' d\lambda', \quad (3.17)
 \end{aligned}$$

where $P_t(\Omega)$ is the point where the direction Ω intersects the topographical surface, $P_t(\Omega')$ is the corresponding point for Ω' , and $K(r, \Omega; r', \Omega')$ is the integration kernel from eq. (3.13), written in spherical coordinates:

$$K(r, \Omega; r', \Omega') = N(r, \Omega; r', \Omega') - N(R, \Omega; r', \Omega') - H^o(r, \Omega) \frac{\partial N(r, \Omega; r', \Omega')}{\partial r}. \quad (3.18)$$

The density effect integral is over the variations in topographical density relative to ρ_0 . Because high-resolution knowledge of three dimensional topographical density variations is extremely limited except in specific areas [Kuhn, 2003; Kingdon et al., 2009], a simplified model of topographical density consisting of only horizontal density variations is adopted. Realization of such a model, with a suitable accuracy, is more achievable than that of a three-dimensional model. Furthermore, influence of the third dimension of density variations ignored in the two-dimensional model is expected to be at most several centimetres, and usually significantly less than that [Kingdon et al., 2006], so it may be considered a third order effect. The anomalous two dimensional (horizontally-varying) mass density model that causes the density effect, is shown in Figure 3.2.

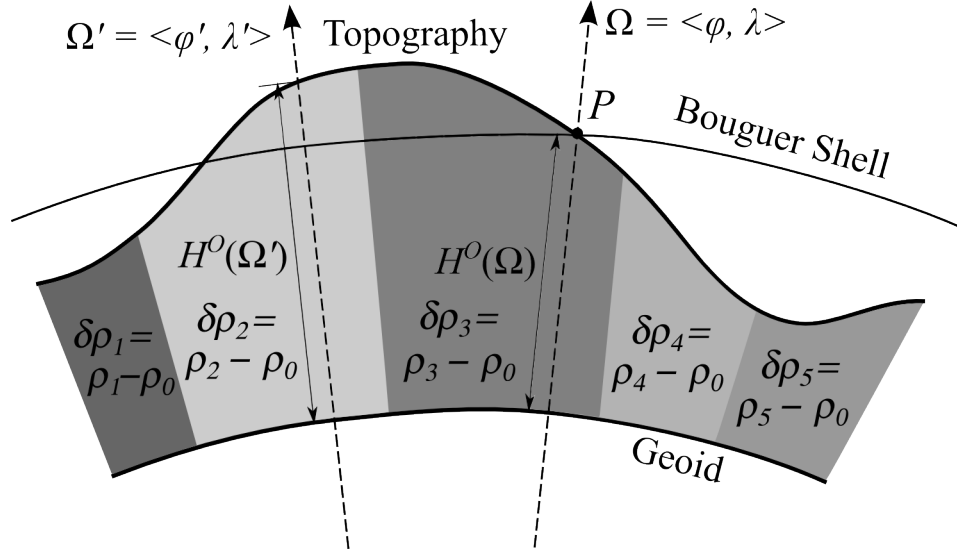


Figure 3.2: Masses inducing the density effect on gravity modeled as horizontally varying only.

Under this model, the anomalous density at the horizontal coordinate Ω is given by:

$$\delta\rho(\Omega) = \rho(\Omega) - \rho_0. \quad (3.19)$$

The effects of the density variations will be indicated by the superscript D . Applying the density model given by eq. (3.19) in eq. (3.14), and integrating over all anomalous topographical density yields (cf., Santos et al. [2006, eqs. (53) to (55)]):

$$c_H^D(r, \Omega) = \frac{G}{\bar{g}(r, \Omega)} \int_{\lambda'=0}^{2\pi} \int_{\varphi'=-\pi/2}^{\pi/2} \delta\rho(\Omega') \int_{r'=R}^{r'=R+H^0(P_1[\Omega'])} K(r, \Omega; r', \Omega') r'^2 dr' \sin(\varphi) d\varphi' d\lambda'. \quad (3.20)$$

Because of limitations on density data coverage, the integral in eq. (3.20) cannot be evaluated over the whole globe and is only carried out over a spherical cap of limited extent, represented here by Ω_0 . For some circumstances, or if the highest accuracy is not required, the same limitation may be applied to the integration region of the terrain effect.

3.3 Approach to numerical integration

3.3.1 Reduction of integral dimensionality

Much has been written on evaluating gravitational effects of rock masses, usually by division of those masses into cells whose individual effects can be calculated analytically and then summed (e.g., Talwani and Ewing [1960]; Smith [2000]; Tsoulis et al. [2003]). Most of these methods are awkward to apply in our situation, because they do not use spherical approximations of topography and are usually designed with local integration in mind. Also, while very accurate, they are time consuming to compute.

We need a method that will work for global integration in the spherical approximation, and we do not require high accuracy since we are calculating second order corrections. Two methods are especially suitable for our situation: a method used by Martinec [1993] that performs analytical integration in the vertical direction prior to using standard two dimensional integration techniques for the horizontal integration; and one described by e.g., Heck [2007], who uses analytical integration over tesseroids (a spherical analog to prisms, described by Anderson [1976]). The former method requires

less computation time than the tesseroid method, for only slightly less accuracy, and is our method of choice.

Martinec [1993] provides exact formulas for the analytical integral with respect to r' of the Newton kernel and its vertical derivative. We apply his results here to reduce the dimensionality of our integrals to two. For the “vertical” integral of the Newton kernel, we have written Martinec’s result as the integral between two surfaces a and b , defined by radii $r_a(\Omega')$ and $r_b(\Omega')$ (cf., Martinec [1993, eq. (2.20)], citing a more general form from Gradshteyn and Ryzhik [1980, paragraphs 2.261 and 2.264]),:

$$\begin{aligned} \tilde{N}(r, \Omega; r_a, r_b, \Omega') &= \int_{r'=r_a(\Omega')}^{r_b(\Omega')} N(r, \Omega; r', \Omega') r'^2 dr' = \frac{(r_b + 3r \cos \psi) L(r, \Omega; r_b, \Omega')}{2} - \\ &- \frac{(r_a + 3r \cos \psi) L(r, \Omega; r_a, \Omega')}{2} + \\ &+ \frac{r^2 (3 \cos^2 \psi - 1)}{2} \ln \left| \frac{r_b - r \cos \psi + L(r, \Omega; r_b, \Omega')}{r_a - r \cos \psi + L(r, \Omega; r_a, \Omega')} \right|. \end{aligned} \quad (3.21)$$

For the integral of the radial derivative of the Newton kernel, he gives [1993, eq. (2.22)]:

$$\begin{aligned} \frac{\partial \tilde{N}(r, \Omega; r_a, r_b, \Omega')}{\partial r} &= \int_{r'=r_a(\Omega')}^{r_b(\Omega')} \frac{\partial N(r, \Omega; r', \Omega')}{\partial r} r'^2 dr' = \frac{(r_b^2 + 3r^2) \cos \psi + r_b r (1 - 6 \cos^2 \psi)}{L(r, \Omega; r_b, \Omega')} - \\ &- \frac{(r_a^2 + 3r^2) \cos \psi + r_a r (1 - 6 \cos^2 \psi)}{L(r, \Omega; r_a, \Omega')} + \end{aligned}$$

$$+r(3\cos^2\psi - 1)\ln\left|\frac{r_b - r\cos\psi + L(r,\Omega;r_b,\Omega')}{r_a - r\cos\psi + L(r,\Omega;r_a,\Omega')}\right|. \quad (3.22)$$

Based on eqs. (3.21) and (3.22), we can write the radial integral of the integration kernel in eq. (3.18):

$$\begin{aligned} \tilde{K}(r,\Omega;r_a,r_b,\Omega') &= \int_{r'=r_a(\Omega')}^{r_b(\Omega')} K(r,\Omega;r',\Omega')r'^2 dr' = \\ \tilde{N}(r,\Omega;r_a,r_b,\Omega') - \tilde{N}(R,\Omega;r_a,r_b,\Omega') - H^o(r,\Omega) &\frac{\partial\tilde{N}(r,\Omega;r_a,r_b,\Omega')}{\partial r}. \end{aligned} \quad (3.23)$$

Considering that eq. (3.23) will be evaluated using height data on a two-dimensional grid, it is not convenient to reduce the dimensionality of the integration any further than we have above. Reduction to one dimensional integrals has been used for topographical effects in the past [Jiang and Duquenne, 1997; Hwang and Hsiao, 2003], but it has been applied with an integration kernel in planar form, or as a locally symmetrical approximation of the spherical kernel, whereas we are interested in an integration with a spherical kernel and beyond the region where a planar approximation is appropriate.

According to eq. (3.23), for each effect we calculate we must evaluate eq. (3.21) twice and eq. (3.22) once for each integration point. Even considering only a global integration with cells spaced 1° apart, this entails 64,800 kernel evaluations for each computation point. Since our cells will be spaced more closely than 1° , the number of evaluations will be significantly higher. Equations (3.21) and (3.22) can be evaluated in

a more compact way, as described in Appendix I, which we have followed in our numerical evaluations.

Equation (3.23) contains a weak (removable) singularity, occurring when $\psi \rightarrow 0$ (i.e., when $\Omega' \rightarrow \Omega$) and when either $r_a = r$ or $r_b = r$ [Martinec, 1993]. The singularity is easily resolved in the case of the terrain correction, using the same methods employed by Martinec [1993] and others in geoid determinations, but the removal for the density effect is more involved. Our treatment of the singularity is described in Appendix II, and results in treating the central cell contributions for both effects separately from the rest of the numerical integration.

3.3.2 Approach to numerical integration

We are constrained in our numerical integration to evaluate integrands on the regular grid where digital elevation model heights are given, preventing us from using Monte Carlo or adaptive mesh methods. Because our digital elevation model (DEM) and digital density model (DDM) data refer to cell centers, the values of the integrand are not known at the boundaries of our integration domain, and an open Newton-Cotes formula is required. The Newton-Cotes formulas prescribe ways of representing the integrand between sampling points in numerical integration, and are well explained in Press et al. [2007] and many other textbooks dealing with numerical integration. In our case, our data spacing confines us to a specific Newton-Cotes formula called the extended midpoint rule [Press et al., 2007, section 4.1], which is analogous to the Riemann concept of the integral, and allows us to sample the integrand at cell centers. Since we

have removed the singularities in eq. (3.23) from the domain of numerical integration, we need not worry about the mesh selection for the Newton-Cotes formulas. The error that might be incurred by using the extended midpoint rule, which is a very simple approximation of the behavior of the integrand, is minimized by using mean heights and average rock densities in our evaluation, since these both represent relatively smoothly varying fields.

The extended midpoint rule for a two-dimensional integral in a grid of N by N points, written for our particular kernel function, is (cf., Press et al. [2007, eq. (4.1.19)]):

$$\iint_{\Omega' \in \Omega} f(\Omega') d\Omega' = \sum_{i=0}^{n-1} \sum_{j=0}^{n-1} f(\Omega_{ij}) \Delta\Omega_{ij} + O\left(\frac{1}{n^2}\right), \quad (3.24)$$

where $f(\Omega_{ij})$ is the value of the integrand at the i th latitude, φ_i , and j th longitude, λ_j , in the grid; and $\Delta\Omega_{ij}$ is the area of the cell centered at this point. In geocentric spherical coordinates $\Delta\Omega_{ij} = \cos(\varphi_i) \Delta\varphi \Delta\lambda$. For the terrain correction:

$$f(\Omega_{ij}) = \tilde{K}(r, \Omega; R + H^o(P_t[\Omega]), R + H^o(P_t[\Omega']), \Omega'), \quad (3.25)$$

and for the density correction:

$$f(\Omega_{ij}) = \delta\rho(\Omega') \tilde{K}(r, \Omega; R + H^o(P_t[\Omega]), R + H^o(P_t[\Omega']), \Omega'). \quad (3.26)$$

The error in eq. (3.23) could be improved upon using techniques such as Romberg integration [Press et al., 2007], but the accuracy improvement is unnecessary and so the additional computational expense is unwarranted.

While values of the integrand must be sampled on a regular grid following the format of our DEM data, we can use horizontal averaging of DEM heights to reduce the resolution of this grid far from the computation point and improve the speed of our computation. A more substantial problem occurs near to the computation point, where the integration kernel must be sampled at a higher resolution than the DEM points allow. In this case, we interpolate the DEM as necessary to evaluate the integrands at a suitable spacing.

In the subsequent computations, we will use a DEM containing 3" mean heights given by version 2 of the NASA Shuttle Radar Topography Mission (SRTM) topographical data [Farr et al., 2007]. To provide for higher resolution near to the computation point and lower resolution far from it, we divide the integration region into 5 integration zones, as shown in Figure 3.3.

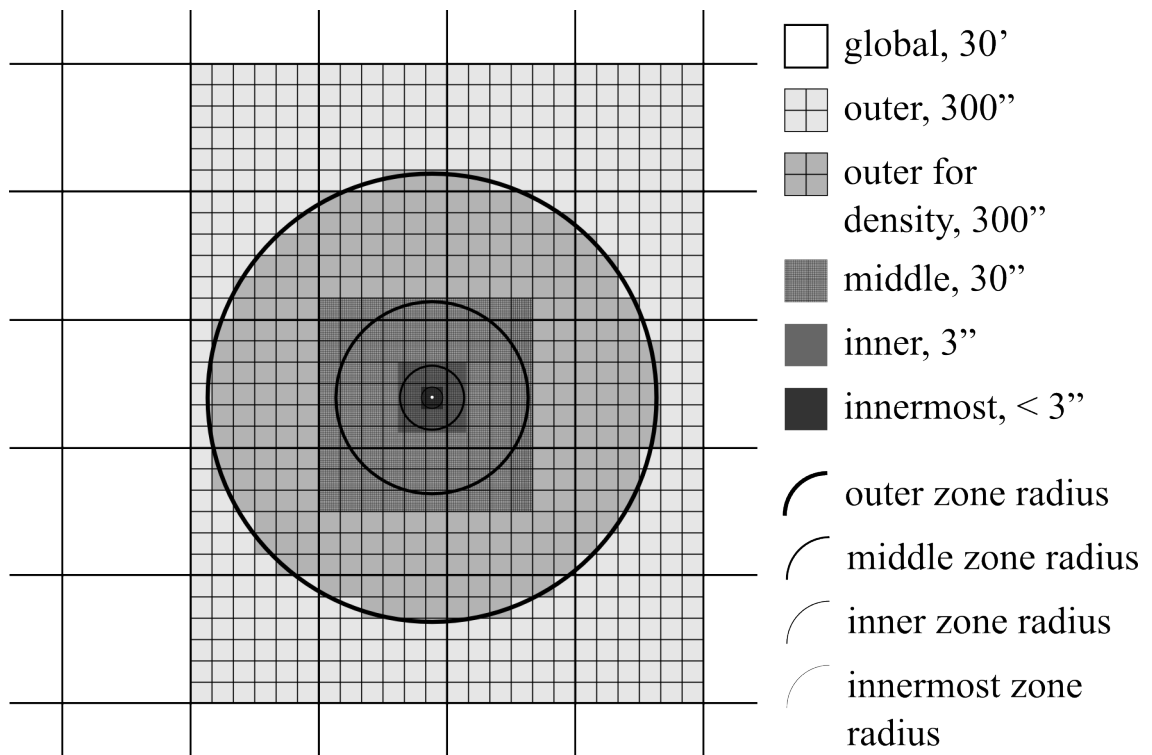


Figure 3.3: Arrangement of integration zones about a computation point.

In the inner zone, we use the 3'' DEM heights directly, and we use interpolated heights in the innermost zone. In the middle zone, a 30'' spacing is used, with heights determined by averaging the 3'' DEM over each 30'' cell. Beyond that is the outer zone, where a similar averaging process provides heights sampled at 300''. Integration over the rest of the globe is carried out using 30' heights taken from NASA's global JGP95E height model [Lemoine et al., 1998], since the SRTM data set does not cover the whole globe. The 30'', 300'' and 30' DEMs are created before the calculation of the height corrections, and stored as data files to be read when needed. Boundaries of integration zones and the spacing of points in the innermost zone are chosen such that the calculation can be performed as quickly as possible with no significant loss of accuracy.

These parameters are determined empirically, as described in Section 3.4, and are expected to be less stringent for the density effect than for the terrain effect since the relatively small masses of anomalous density are expected to have less overall effect than the terrain masses. Also, in some circumstances the global integration may not be applied even for the terrain effect, although the spacing of integration points in the global zone is so sparse that omitting it makes little difference to computational efficiency.

For evaluating density effects, we use a Canadian digital density model (DDM) created by digitizing geological maps (e.g., Kingdon et al. [2005]; cf. the work of Huang et al. [2001] in geoid determination) that models horizontal rock densities. Our DDM has a 30'' resolution, with cell centers corresponding to the 30'' DEM, and covers all of Canada and the northern part of the United States. For integration in the innermost and inner zones the density data is interpolated, and it is averaged for integration in the outer zone.

Since the DDM is not global, we cannot integrate over the whole globe when calculating the density effect. Fortunately, the density variations distant from the computation point are similar in effect to homogeneous masses of mean crustal density, and the anomalous density effect of distant masses tends toward zero. Because of this we are able to capture the density effect sufficiently by integrating over a relatively small cap. The method of determining what size of integration cap is necessary to adequately capture the density effect is described in Section 3.4.

Apart from the outer zone cap used for evaluating density effects, the integration zones in Figure 3.3 extend beyond the indicated integration radii. To ensure seamless

transitions between the 5 integration zones, the zone boundaries for each zone are defined so they correspond with cell boundaries, given by straight line segments, of the outlying zone. Thus, they usually extend beyond the defined zone radius. This is especially the case since the computation points are not defined on a grid, as they might be for, e.g., geoid calculations. Leveling benchmarks, where orthometric height corrections are required, are not expected to correspond with cell boundaries.

Where DEM interpolation is necessary, we use bilinear interpolation. The interpolation need not be very rigorous since the requirement for higher resolution heights in the innermost zone is only such that the Newton kernel can be sampled at a sufficient horizontal resolution. Also, we are using mean heights which vary more smoothly than point heights. For interpolation of the density model, we use an inverse distance squared interpolation, since the density values are not expected to vary linearly between DDM points.

3.3.3 Computation overview

Because we need results at leveling points rather than over a grid, the calculation is performed for one computation point at a time. First, an ASCII file containing point name, latitude, longitude and height (Helmert or levelled) for each computation point is read to determine the spatial extent of the points. Next, data sufficient to cover the computation area is loaded from the 30', 300'', 30'' DEMs, as well as the 30'' DDM. Even for large leveling campaigns data at these resolutions consume little memory, so they can be held in RAM for the duration of the computation.

Once the lower resolution DEM files are loaded, the algorithm runs through the file of leveling points, in each case reading the record for a computation point, loading the required 3" DEM data, performing the numerical integration to determine the terrain and density corrections, and appending the result to an output file. An overview of the process is given in the flow chart in Figure 3.4.

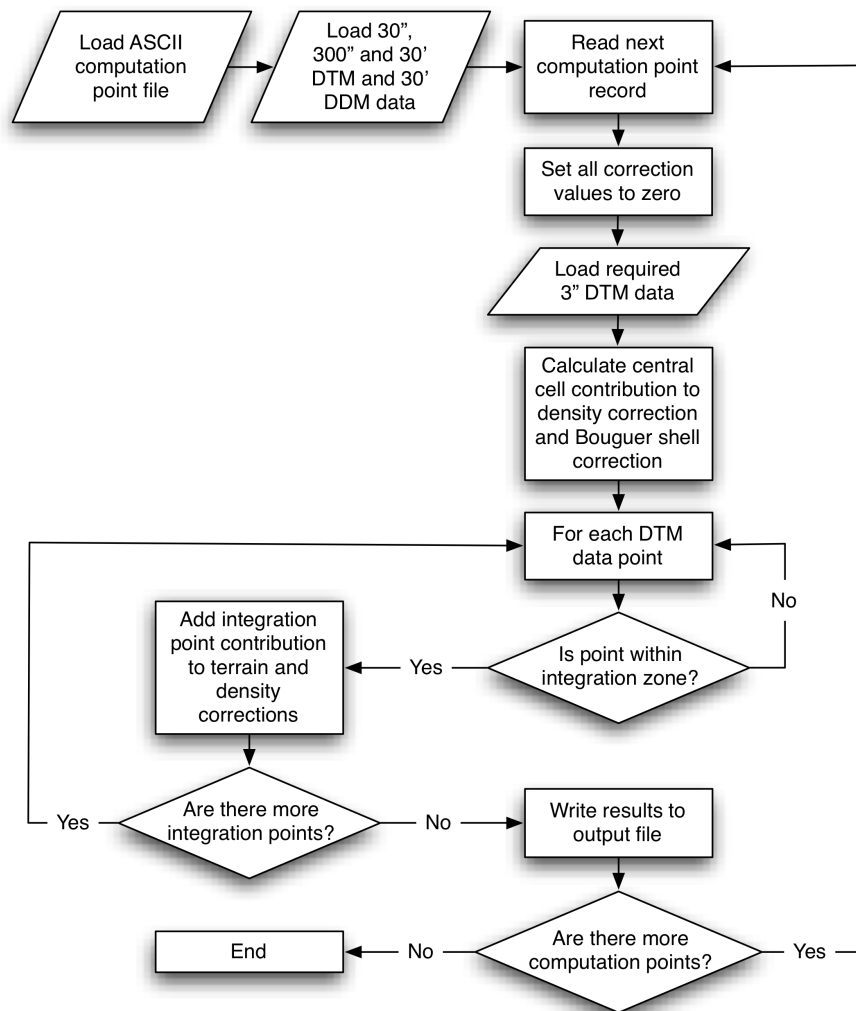


Figure 3.4: Flow chart of computation.

The required 3" DEM files, each by default covering a $1^\circ \times 1^\circ$ area, are read separately for each point, first because storing such high resolution data over the whole extent of a leveling network might consume a great deal of RAM, and second because, especially with conventional (not solid state) hard disks, reading data covering the whole area from disk would significantly increase running time.

The numerical integration is performed in 5 separate loops, one for each integration zone, the density effect being omitted from the global integration loop and only evaluated for points within a spherical cap in the outer zone integration loop. When the calculation for a computation point finishes, the point name, latitude, longitude, terrain correction and density correction are written to an output file.

3.4 Results

3.4.1 Testing integration zone parameters using a "tower" scenario

We now determine the zone boundaries and innermost zone resolution necessary to accurately evaluate the topographical corrections to Helmert heights. To do this, we use an artificial "tower" scenario, in which the computation point is 9000 m high, while all other topography is at sea level. The terrain correction in this scenario is equal to the correction induced by a spherical Bouguer shell (cf., Vaniček et al. [2001]). By performing the integration in a tower scenario numerically, and comparing it to the exact result, we can estimate the error in our numerical evaluation of the terrain correction for any set of zone radii and innermost zone spacing.

Since the density of the masses causing the terrain correction is over 3 times larger than the largest anomalous densities ($\sim 800 \text{ kg/m}^3$ for unconsolidated sediments, which have densities of $\sim 1900 \text{ kg/m}^3$, e.g., Parasnis [1997]), we expect that any kernel sampling providing suitable accuracy for the terrain correction will also provide suitable accuracy for the density correction.

We begin determining zone parameters by setting larger initial zone sizes and finer innermost zone resolution than we expect are necessary. The initial zone resolutions and initial radii and are shown in Table 3.1.

Table 3.1: Integration parameters before refinement.

Zone	Resolution	Initial Radius
innermost	0.03 arc-seconds	30 arc-seconds
inner	3 arc-seconds	30 arc-minutes
middle	30 arc-seconds	2°
outer	5 arc-minutes	6°
global	30 arc-minutes	180°

Applying these parameters in the tower scenario, with the computation point height set to 8800 m and all DEM heights set to zero, reveals a difference of only 8.5 mm, or 0.096%, between the numerical integration result and the exact result. This is very reasonable, considering the extreme scenario we are simulating.

We next begin increasing the spacing in the innermost integration zone, until the numerical result changes by 0.5 mm. After that, we reduce each zone radius, one at a time, ensuring that the result does not change by more than 0.5 mm. Thus, we seek integration parameters that will provide an accuracy within 2.5 mm of the initial result.

By following this procedure, we have determined the new integration limits and resolutions shown in Table 3.2.

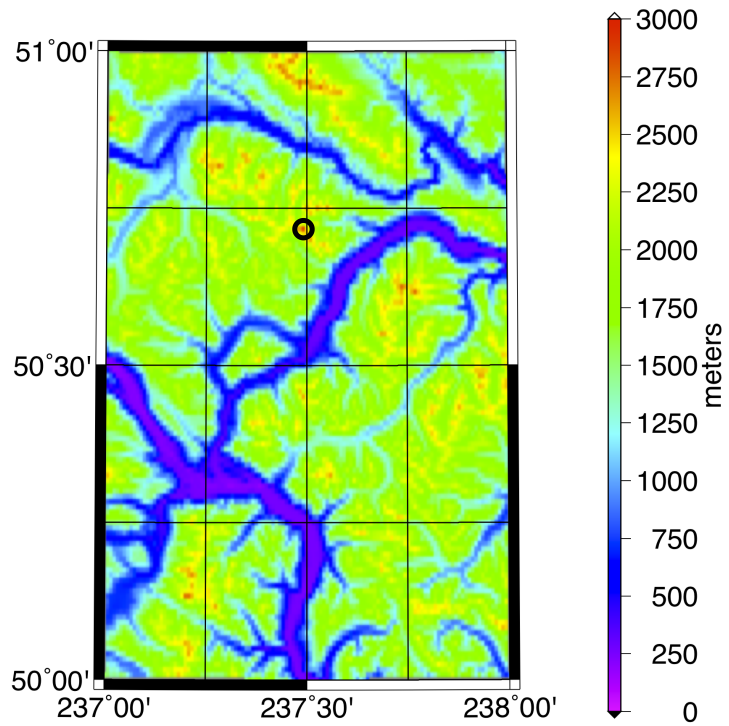
Table 3.2: Integration parameters sufficient to accurately sample the integration kernel for the terrain effect.

Zone	Resolution	Final Radius
innermost	0.12 arc-seconds	6 arc-seconds
inner	3 arc-seconds	25 arc-minutes
middle	30 arc-seconds	1°
outer	5 arc-minutes	3°
global	30 arc-minutes	180°

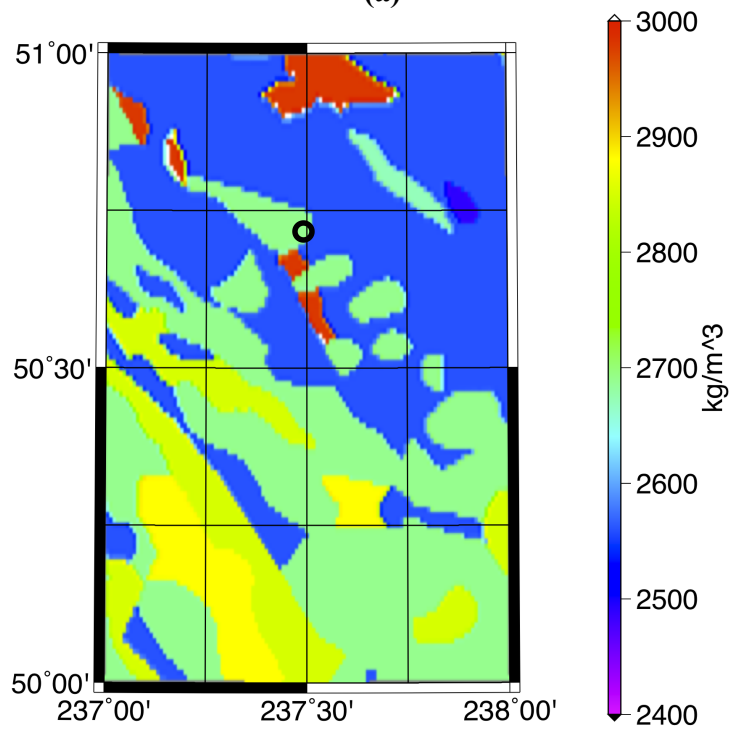
Using these parameters, the final accuracy for the tower scenario is 9.3 mm, or 0.106%, indicating that we have not lost significant accuracy by our choice of integration parameters. In real world cases, which are not as extreme as this simulation, it is likely possible to decrease the zone radii to retain accuracy while improving efficiency; i.e., the presented parameters are erring on the side of caution. We have not investigated the possibility of using smaller zone radii here.

3.4.2 Canadian test area

For the next stage in our evaluation, we will be using a test area in the Canadian Rockies, from 50° to 51° north latitude, and 237° to 238° east longitude. The heights in this area range from 194 m to 2875 m, and are shown in Figure 3.5a. The rock densities range from 2490 kg/m³ to 2980 kg/m³, which is almost the full range of densities within the entire DDM. These are shown in Figure 3.5b.



(a)



(b)

Figure 3.5: Heights (a) and rock densities (b) in the test area. Computation point at 50°43'00' N and 237°29'30" E indicated by black circle.

We will first use this test area to determine a suitable boundary of the outer zone for the density correction calculations. The outer zone must be large enough to include all density anomalies that may have a significant influence (more than 1mm) on the density effect at the computation point.

We begin by selecting a point in the test area having large elevation and located near to significant density contrasts – in this case, we have selected the point at 50°43'00' N and 237°29'30" E, which has a height of 2875 m, the highest in the test area. The point is indicated by the dark circles in Figures 3.5a and 3.5b. The density at this point is 2690 kg/m³, though within a 5 arc-minutes radius there are densities spanning the whole range present in the test area. For our computation point, we calculate the density correction using outer zone radii from 1° to 30°. Figure 3.6 shows the percent difference in the density effect for each choice of outer zone radius.

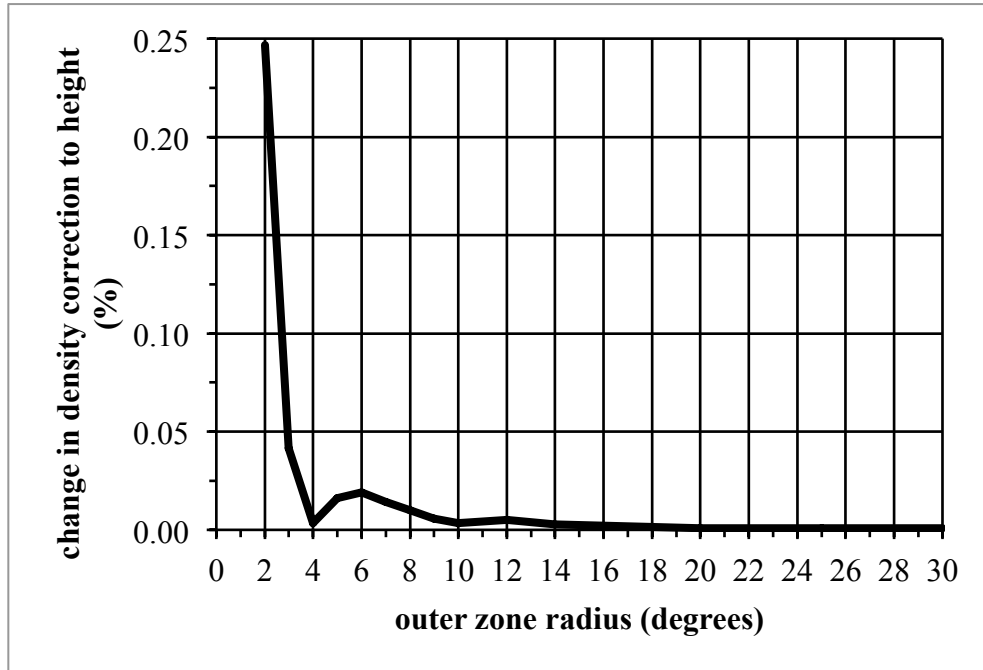


Figure 3.6: Density correction for values of outer zone radius incremented by 1°.

The largest possible topographical correction on Earth is close to 8.83 m (based on the Bouguer shell correction for Mount Everest), and the maximum density contrasts are about 800 kg/m^3 , or 30% of the assumed representative density value. Therefore, we expect the density correction will never exceed 2.65 m. In this case, a relative error of 0.05 % in the density correction calculation will result in at most a 1.3 mm error in the result. Figure 3.6 shows that even in the most extreme case in our region, an outer zone radius of 3° is sufficient to guarantee less than a 0.05% error, and so a 3° radius is expected to be suitable for our task.

The single point computation also gives some indication of the contribution of each integration zone to the final terrain and density corrections. The zonal contributions for

this case are shown in Table 3.3. The total terrain correction is 30.0 cm, and the total density correction is -0.3 cm, a ratio of two orders of magnitude.

Table 3.3: Zonal contributions to the terrain and density effects, for 6" innermost zone radius, 25' inner zone radius, 1° middle zone radius, and 3° outer zone radius.

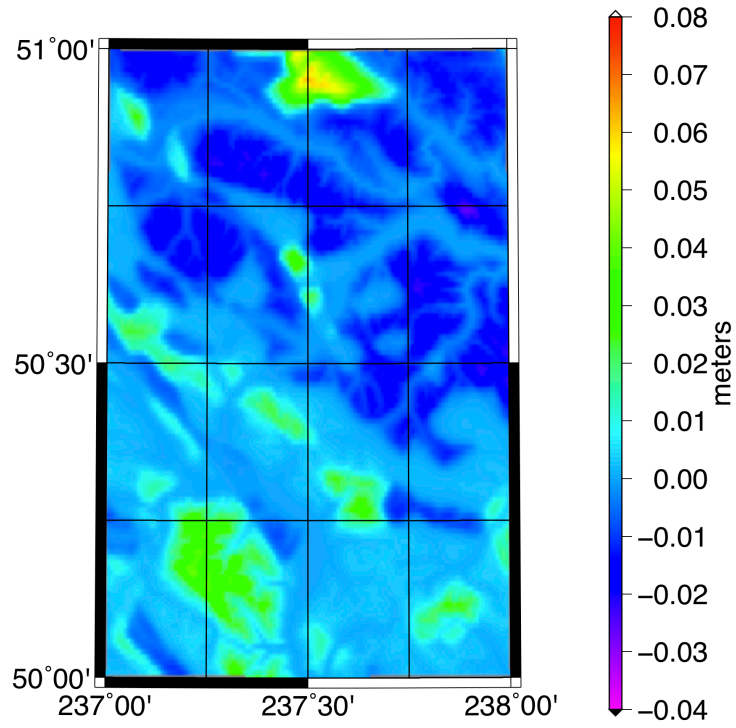
zone	contribution to terrain correction		contribution to density correction	
	cm	%	cm	%
innermost	-1.06	3.46	0.05	-18.07
inner	-27.81	90.50	-0.27	98.50
middle	-1.00	3.26	0.01	-2.28
outer	-0.57	1.86	-0.06	21.81
global	-0.28	0.91	n/a	n/a

The overall density correction is very small because of the placement of the computation point on the boundary between two anomalous density bodies of opposite sign. We see that the inner zone contains by far the greatest contribution to the terrain correction. This is because on one hand the innermost zone is small and the Bouguer shell approximation is very good near to the computation point; and on the other hand because masses outside the inner zone are distant enough that their effects are small. The largest contributions to the density correction are also in the inner zone, again because the innermost zone is relatively small, but also because the innermost zone is dominated by two contrasting density anomalies whose effects somewhat cancel each other. Even so, the contribution of the innermost zone is proportionally larger than that for the terrain correction, since these anomalies do not cancel each other completely. The variations in zonal contributions for the density correction depend heavily on the size of density

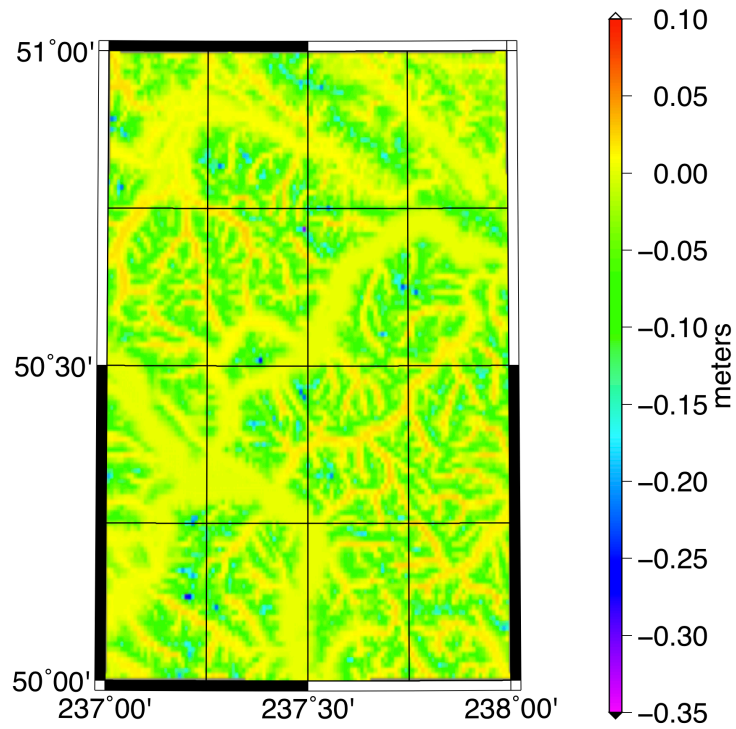
anomalies in each zone, and whether these anomalies are such that this kind of cancellation occurs.

3.4.3 Magnitude of the corrective terms

Having validated our method and determined suitable parameters for the integration zones, we now provide results for the terrain and density corrections on a grid over our test area. Figure 3.7a shows the terrain correction and 3.7b the density correction evaluated at a grid of points, with 30" x 30" spacing, covering our test area.



(a)



(b)

Figure 3.7: Density (a) and terrain (b) corrections to orthometric height.

The statistics of the terrain and density correction are given in Table 3.4.

Table 3.4: Statistics of the terrain and density corrections to orthometric height.

statistic	terrain correction [cm]	density correction [cm]
minimum	-30.96	-2.63
maximum	2.90	6.19
mean	-2.77	-0.03
standard deviation	4.06	1.07
R.M.S.	4.92	1.07
range	33.86	8.82

In our test area the terrain correction ranges from -2.90 cm to -30.96 cm, and has its largest magnitudes in mountainous areas, as we might expect. By contrast, the density effect never exceeds 6.2 cm. The density effect is largest at large elevations and in the presence of large density anomalies, also as expected. The magnitudes and behaviors of the terrain and density corrections are consistent with our preliminary evaluations [Santos et al., 2006; Kingdon et al. 2005].

3.4.4 Improvements in computation time

Two features improve the speed of our approach relative to other methods of orthometric height correction. First, the use of gravity potential, according to eq. (3.10), to calculate effects on mean gravity, rather than the Niethammer method. Second, reduction of the dimensionality of integration to 2, using eqs. (3.20) and (3.21). Our optimal choice of

integration parameters is also important, although it does not distinguish our approach from others.

To examine what improvement these give, we have run the computation for our test area excluding each improvement, now using a cell spacing of 1'. This results in 3,721 evaluation points, more than we would expect in a leveling network. For comparisons with the Niethammer method and with numerical integration in the radial direction, we use a discretization step of 250m, which allows comparable accuracy to the exact results. Also, to show what effect the choice of optimal integration parameters has, we run the computation with both the initial and final set of integration parameters. The computation time for each segment of the program under these variations is shown in Table 3.5.

Table 3.5: Computation time with and without various modifications.

method	total time [mm:ss]
all improvements	33:32
Niethammer instead of gravity potential	105:59
3D instead of 2D numerical integration	53:24
initial rather than final integration parameters	138:26

All of these computations were run on a 2.3 GHz quad core Intel i7 processor with 8 GB of 1333 MHz RAM, and with a solid state hard disk that makes the file loading times as quick as possible. The computation speed could be improved further by parallel processing. Also, note that with a conventional hard disk, the time required for file loading might be significantly higher.

The results show that for a realistic number of evaluation points (~ 3700), the terrain and density corrections can be evaluated accurately by most methods in less than 1 hour. Only the Niethammer method takes longer than this. Thus, the use of effects on potential to evaluate mean gravity effects is the most significant improvement in our approach. Reduction of the dimensionality of the integral to 2 also has a significant effect on the computation time. Like the Niethammer method, radial numerical integration requires several kernel evaluations for each computation point. However, it consumes less time than the Niethammer method, since the kernels being evaluated are more simple.

Using the Niethammer method requires 116% more computation time, and using numerical integration in the radial direction requires 59% more time. If we run the computation using our initial set of parameters, it requires 213% more time, indicating the importance of properly choosing these parameters, and the benefit of dividing the integration area into multiple zones.

3.5 Conclusions

Effects on mean gravity may be efficiently calculated based on the difference in effects on gravity potential at both ends of the plumbline, according to eq. (3.10). Using the traditional Niethammer method with 250 m spacing, sufficient to achieve similar accuracy to our method, requires 116% more computation time than using effects on gravity potential. The calculation is further accelerated by reducing the dimensionality of the volume integration to 2, and using the radial integrals of the relevant kernels supplied by Martinec [1993] in eqs. (3.20) and (3.21), without which the computation

would require 59% more time. With these two improvements, the computation for over 3,500 input points may be completed in well under an hour, a reasonable computation time for any practical applications.

By our choice of integration zone parameters, we were able to achieve a numerical integration accuracy of 0.113% determined using a tower scenario. To achieve this accuracy, we used 30' data for global integration, 300'' data within 3° of the computation point, 30'' data within 1° of the computation point, 3'' data within 25' of the computation point, and 0.12'' data within 6'' of the computation point. These parameters were determined by starting with zone sizes somewhat larger, and resolutions somewhat higher than required, and then progressively reducing these while ensuring that the error in our tower scenario was increased by less than 5 mm. Using our initial testing parameters would have required 213% more computation time, illustrating the importance choice of these parameters in computation efficiency. During our testing, we found that with the final choice of integration parameters, the inner zone, containing 3'' data, contributes 91% of the magnitude of the terrain effect for a rigorous sample point, and 99% to the density effect.

To demonstrate our method, we generated results over an area in the Canadian Rocky Mountains spanning from 50° to 51° latitude and 237° to 238° longitude, with heights up to 2875 m and density anomalies from -180 kg/m^3 to 310 kg/m^3 . In this region, the topographical correction ranged from -31.0 cm to 2.9 cm , with a mean value of -2.77 cm . The largest values coincided with the highest computation points, which should be expected. The density correction ranged from -2.6 cm to 6.2 cm , with a mean

value of 0.0 cm. The signs corresponded with the signs of the density anomalies, and magnitudes were determined mainly by topographical heights.

Chapter 3 References

- Allister, N., and W. Featherstone (2001). "Estimation of Helmert orthometric heights using digital barcode leveling, observed gravity and topographic mass-density data over part of Darling Scarp, Western Australia." *Geomatics Research Australasia*, No. 75, pp. 25–52.
- Anderson, E. (1976). "The Effect of Topography on Solutions of Stokes' Problem." Unisurv: Reports from the School of Engineering No. S14. University of New South Wales, Kensington, N.S.W., Australia.
- Dennis, M., and W. Featherstone (2003). "Evaluation of orthometric and related height systems using a simulated mountain gravity field." *Gravity and Geoid 2002*, Ed. I. Tziavos. 3rd Meeting of the International Gravity and Geoid Commission, Thessaloniki, Greece, August 26–30, 2002. Department of Surveying and Geodesy, Aristotle University of Thessaloniki, Thessaloniki, Greece, pp. 389–394.
- Farr, T., P. Rosen, E. Caro, R. Crippen, R. Duren, S. Hensley, M. Kobrick, M. Paller, E. Rodriguez, L. Roth, D. Seal, S. Shaffer, J. Shimada, J. Umland, M. Werner, M. Oskin, D. Burbank, and D. Alsdorf (2007). "The Shuttle Radar Topography Mission." *Reviews of Geophysics*, Vol. 45, No. RG2004, doi: 10.1029/2005RG000183.
- Gradshteyn, I., and I. Ryzhik (1980). *Table of Integrals, Series and Products*. 2nd revised edition, Ed. A. Jeffrey. Academic Press, New York, U.S.A.
- Heck, B., and K. Seitz (2007). "A comparison of the tesseroid, prism and point-mass approaches for mass reductions in gravity field modelling." *Journal of Geodesy*, Vol. 81, No. 2, pp. 121–136, doi: 10.1007/s00190-006-0094-0.
- Heiskanen W., and H. Moritz (1967). *Physical Geodesy*. Freeman, San Francisco, U.S.A.
- Helmert, F. (1890). *Die Schwerkraft im Hochgebirge insbesondere, in den Tyroler Alpen, in geodätischer und geologischer Beziehung*. Königliches Preußischen Geodätischen Institut, Berlin, Germany.
- Huang, J., P. Vaníček, S. Pagiatakis, and W. Brink (2001). "Effect of topographical density on the geoid in the Rocky Mountains." *Journal of Geodesy*, Vol. 74, No. 11–12, pp. 805–815, doi: 10.1007/s001900000145.
- Hwang, C., and Y.-S. Hsiao (2003). "Orthometric corrections from leveling, gravity, density and elevation data: a case study in Taiwan." *Journal of Geodesy*, Vol. 77, No. 5–6, pp. 279–291, doi: 10.1007/s00190-003-0325-6.

- Jiang, Z., and H. Duquenne (1997). "On fast integration in geoid determination." *Journal of Geodesy*, Vol. 71, No. 2, pp. 59–69, doi: 10.1007/s001900050075.
- Kingdon, R., P. Vaníček, A. Ellmann, M. Santos, and R. Tenzer (2005). "Toward an improved orthometric height system for Canada." *Geomatica*, Vol. 59, No. 3, pp. 241–249.
- Kingdon, R., A. Ellmann, P. Vaníček and M. Santos (2006). "The cost of assuming a lateral density distribution in corrections to Helmert orthometric heights." Paper presented at the American Geophysical Union 2006 Joint Assembly, Baltimore, Maryland, U.S.A., May 23–26.
- Kingdon, R., P. Vaníček, and M. Santos (2009). "Modeling topographical density for geoid determination." *Canadian Journal of Earth Sciences*, Vol. 46, No. 8, pp. 571–585, doi: 10.1139/E09-018.
- Kuhn, M. (2003). "Geoid determination with density hypotheses from isostatic models and geological information." *Journal of Geodesy*, Vol. 77, Nos. 1–2, pp. 50–65, doi: 10.1007/s00190-002-0297-y.
- Lemoine, F., S. Kenyon, J. Factor, R. Trimmer, N. Pavlis, D. Chinn, C. Cox, S. Klosko, S. Luthcke, M. Torrence, Y. Wang, R. Williamson, E. Pavlis, R. Rapp and T. Olson (1998). "The development of the joint NASA GSFC and the National Imagery and Mapping Agency (NIMA) Geopotential Model EGM96." NASA Technical Paper No. TP-1998-206861, NASA, Goddard Space Flight Center, Greenbelt, Maryland, U.S.A.
- Mader, K. (1954). "Die orthometrische Schwerekorrektion des Präzisions-Nivellements in den Hohen Tauern." *Österreichische Zeitschrift für Vermessungswesen*, Special issue 15.
- Martinec, Z. (1993). "Effect of lateral density variations of topographical masses in improving geoid model accuracy over Canada." Contract report for the Geodetic Survey of Canada, Ottawa, Ontario, Canada.
- Moritz, H. (2000). "Geodetic Reference System 1980." *Journal of Geodesy*, Vol. 74, No. 1, pp. 128–162. doi: 10.1007/s001900050278.
- Nagy D., G. Papp, and J. Benedek (2000). The gravitational potential and its derivatives for the prism. *Journal of Geodesy*, Vol. 74, Nos. 7–8, pp. 552–560, doi: 10.1007/s001900000116.
- Niethammer, T. (1932). *Nivellement und Schwere als Mittel zur Berechnung wahrer Meereshöhen*. Schweizerische Geodätische Kommission, Bern, Switzerland.

- Parasnis, D. (1997). *Principles of Applied Geophysics*. 5th ed., Chapman and Hall, New York, U.S.A.
- Press, W., S. Teukolsky, W. Vetterling, and B. Flannery (2007). *Numerical Recipes: The Art of Scientific Computing*. 3rd ed., Cambridge University Press, New York, U.S.A.
- Santos, M., P. Vaníček, W. Featherstone, R. Kingdon, A. Ellmann, B.A. Martin, M. Kuhn and R. Tenzer (2006). "Relation between the rigorous and Helmert's definitions of orthometric heights." *Journal of Geodesy*, Vol. 80, No. 12, pp. 691–704, doi: 10.1007/s00190-006-0086-0.
- Smith, D. (2000). "The gravitational attraction of any polygonally shaped vertical prism with inclined top and bottom faces." *Journal of Geodesy*, Vol. 74, No. 5, pp. 414–420, doi: 10.1007/s001900000102.
- Strange, W. (1982). "Evaluation of orthometric height accuracy using bore hole gravimetry." *Bulletin Géodésique*, Vol. 56, No. 4, pp. 300–311, doi: 10.1007/BF02525730.
- Talwani, M., and M. Ewing (1960). "Rapid computation of gravitational attraction of three-dimensional bodies of arbitrary shape." *Geophysics*, Vol. 25, No. 1, pp. 203–225, doi: 10.1190/1.1438687.
- Tenzer, R., P. Vaníček, M. Santos, W. Featherstone, and M. Kuhn (2005). "The rigorous determination of orthometric heights." *Journal of Geodesy*, Vol. 79, Nos. 1–3, pp. 82–92, doi: 10.1007/s001-005-0445-2.
- Tsoulis, D., H. Wziontek, and S. Petrovic (2003). "A bilinear approximation of the surface relief in terrain correction computations." *Journal of Geodesy*, Vol. 77, Nos. 5–6, pp. 338–344, doi: 10.1007/s00190-003-0332-7.
- Vajda P., P. Vaníček, P. Novák, and B. Meurers (2004). "On evaluation of Newton integrals in geodetic coordinates: Exact formulation and spherical approximation." *Contributions to Geophysics and Geodesy*, Vol. 34, No. 4, pp. 289–314.
- Vaníček, P., P. Novák, and Z. Martinec (2001). "Geoid, topography, and the Bouguer plate or shell." *Journal of Geodesy*, Vol. 75, No. 4, pp. 210–215, doi: 10.1007/s001900100165.
- Vaníček, P., R. Tenzer, L. Sjöberg, Z. Martinec, and W. Featherstone (2004). "New views of the spherical Bouguer gravity anomaly." *Journal of Geophysics International*, Vol. 159, No. 2, pp. 460–472, doi: 10.1111/j.1365-246X.2004.02435.x.

Zilkoski, D., J. Richards, and G. Young (1992). "Results of the General Adjustment of the North American Datum of 1988." *Surveying and Land Information Systems*, Vol. 52, No. 3, pp. 133–149.

Chapter 3 Appendix I: Simplified integration kernels

To evaluate eq. (3.23) in an efficient manner, we calculate the following eight values for each integration point:

$$(p_1)_a^r = r_a(\Omega') / r, \quad (3.A1)$$

$$(p_2)_b^r = r_b(\Omega') / r, \quad (3.A2)$$

$$(p_3)_a^r = \sqrt{1 + (p_1)_a^r [(p_1)_a^r - 2(p_5)]}, \quad (3.A3)$$

$$(p_4)_b^r = \sqrt{1 + (p_2)_b^r [(p_2)_b^r - 2(p_5)]}, \quad (3.A4)$$

$$(p_5) = \cos(\psi[\Omega, \Omega']), \quad (3.A5)$$

$$(p_6) = 3(p_5), \quad (3.A6)$$

$$(p_7) = (p_5)(p_6) - 1, \quad (3.A7)$$

$$(p_8)_{a,b}^r = \ln \left| \frac{(p_2)_b^r - (p_5) + (p_4)_b^r}{(p_1)_a^r - (p_5) + (p_3)_a^r} \right|. \quad (3.A8)$$

Substituting these into eq. (3.22) yields:

$$\begin{aligned}
\tilde{K}(r, \Omega; r_a, r_b, \Omega') = & 0.5r^2[(p_4)_b^r[(p_2)_b^r + (p_6)] - (p_3)_a^r[(p_1)_a^r + (p_6)] + (p_7)(p_8)_{a,b}^r] - \\
& -0.5R^2[(p_4)_b^R[(p_2)_b^R + (p_6)] - (p_3)_a^R[(p_1)_a^R + (p_6)] + (p_7)(p_8)_{a,b}^R] + \\
& (r - R)r \left[\frac{(p_5)[3 + (p_2)_b^r[(p_2)_b^r - 6(p_5)]] + (p_2)_b^r}{(p_4)_b^r} - \right. \\
& \left. - \frac{(p_5)[3 + (p_1)_a^r[(p_1)_a^r - 6(p_5)]] + (p_1)_a^r}{(p_3)_a^r} + (p_7)(p_8)_{a,b}^r \right]. \tag{3.A9}
\end{aligned}$$

Notice that the first and third term on the right hand side of eq. (3.A9) both have the same values for p_1 to p_8 . Thus, these only need to be computed once and used to evaluate both terms. Also, p_5 to p_7 only need to be calculated once per integration point.

In the case of the terrain correction, $r_a = R + H^O(P_i[\Omega])$ and $r_b = R + H^O(P_i[\Omega'])$. In the case of the density correction, $r_a = R$, and r_b is the same as for the terrain correction. Because both corrections share the same value for r_b , it is beneficial to evaluate the terrain and density corrections simultaneously, so that (p_2) , (p_4) , and the terms in Eq. (A9) involving these parameters need only be calculated once for both corrections.

If we use eqs. (3.21) to (3.23) to evaluate the terrain and density corrections, for each integration point we must evaluate 144 multiplications, 22 divisions, 12 square roots and 6 logarithms. Using eqs. (3.A8) and (3.A9), we evaluate only 52 multiplications, 14 divisions, 6 square roots, and 4 logarithms.

Chapter 3 Appendix II: Removal of Newton kernel singularities

The kernel in eq. (3.25) is plotted in Figure A1 for $r = R + H^{max}$, $r_a = R$ and $r_b = r$, and $H^{max} = 8,800$ m. The plot shows kernel value with respect to ψ , the solid spherical angle between the computation and integration points.

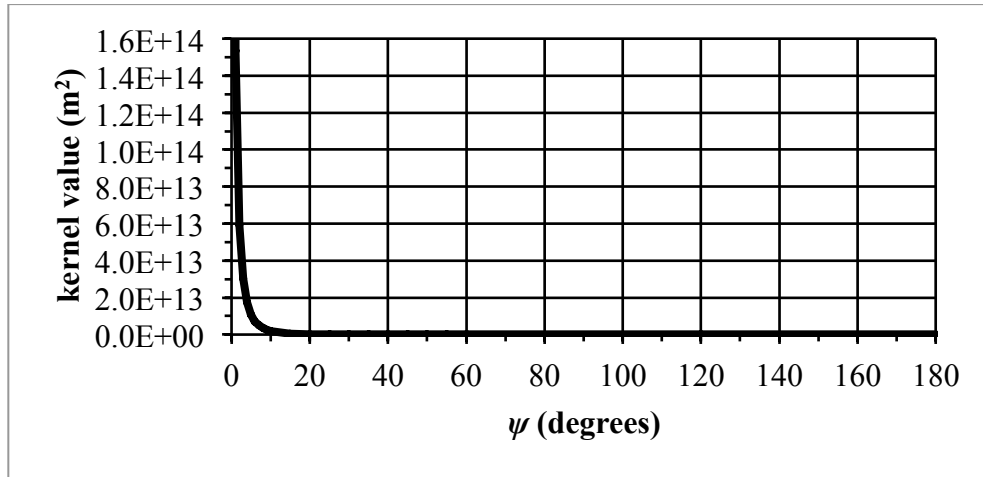


Figure 3.A1: Radially integrated integration kernel with respect to distance from the computation point, for $r = R + H^{max}$, $r_a = R$ and $r_b = r$, and $H^{max} = 8,800$ m. Note the logarithmic vertical axis.

The value of the kernel decreases rapidly near to the computation point, but more gradually as distance from the computation point increases. It is symmetrical for constant height, and increases rapidly to a singularity at the computation point.

The singularity is a weak singularity [Martinec, 1993], occurring when $\psi \rightarrow 0$ (i.e., when $\Omega' \rightarrow \Omega$) and when either $r_a = r$ or $r_b = r$. The singularity is easily avoided in the evaluation of the terrain correction, since the height of terrain equals to 0 at the point $\Omega' = \Omega$. Thus the contribution of the point $\Omega' = \Omega$ to the terrain correction is equal to zero and the point may simply be omitted from the integration domain [Martinec, 1993]. The

treatment for the density correction is more complicated, since the contribution at $\Omega' = \Omega$ is not equal to zero.

For the density correction, numerical integration is performed in the usual way over most of the integration region, excluding the cell containing the computation point, where the singularity occurs. Over the central cell, the integration is performed analytically. Since the Newton kernel and its derivative are only weakly singular, their surface integral is bounded [Martinec, 1993, eq. (2.10)], and thus the integral of our kernel over the central cell is also bounded. However, attempting to integrate the Newton kernel in spherical coordinates over a tesseroidal region (such as our central cell) requires evaluation of elliptic integrals. Although approximate methods exist to solve these integrals, they are inaccurate near to the computation point [Heck, 2007]. To overcome this problem, we reformulate the kernel using planar coordinates, meaning that in the neighbourhood of the point of singularity we calculate distances according to the planar formula:

$$L^p(P; P') = ([R\psi]^2 + H^2)^{1/2} = ([x - x']^2 + [y - y']^2 + H^2)^{1/2}, \quad (3.A10)$$

where the superscript p indicates a quantity in the Cartesian coordinate system, $P = \langle x, y, z \rangle$, $x = R\lambda\cos(\varphi)$, $y = R\varphi$, $z = H^O(P)$, $x' = R\lambda'\cos(\varphi')$, $y' = R\varphi'$, and $z' = H^O(P')$.

Based on eq. (3.A10), we can formulate our kernel from eq. (3.18) in planar coordinates, which evaluates to:

$$K^p(P;P') = \frac{1}{\sqrt{[R\psi]^2 + [H^o(P) - H^o(P')]^2}} - \frac{1}{\sqrt{[R\psi]^2 + [H^o(P')]^2}} - \frac{[H^o(P)]^2}{([R\psi]^2 + [H^o(P) - H^o(P')]^2)^{3/2}}. \quad (3.A11)$$

Integrating over a prismoidal region corresponding closely to the central cell yields the central cell contribution:

$$C_H^D(x, y, z = H^o[P]) = \frac{G\delta\rho(\Omega)}{\bar{g}} (H^o[P])^2 \int_{z'=0}^{H^o(P)} \int_{y'=y_s}^{y_n} \int_{x'=x_w}^{x_e} K^p(P, P') dx' dy' dz', \quad (3.A12)$$

where x_w and x_e are the western and eastern boundaries of the central cell, and y_s and y_n are the southern and northern boundaries.

The prismoidal region of integration shown in eq. (3.A12) does not correspond exactly to the tesseroidal shape of the central cell in spherical coordinates, but considering the small size of the central cell (at most about 100m wide), we consider this a reasonable approximation. The analytical integrals of the Newton kernel and its radial derivative have been calculated exactly by Nagy [2000, eq. (8)], and can be used to evaluate eq. (3.A12). After evaluating the vertical component of the integral, the result is:

$$\begin{aligned}
C_H^D(x, y, z = H^O[P]) = & \frac{G}{g} \left\| (x' - x)(y' - y) \ln \left(\frac{L^P(P_0, P')^2}{[L^P(P, P') - H][L^P(P, P') + H]} \right) - \right. \\
& -H^O(P) \left[(y' - y) \ln \left(\frac{x' - x + L^P[P_0; P']}{x' - x + L^P[P; P']} \right) + (x' - x) \ln \left(\frac{y' - y + L^P[P_0; P']}{y' - y + L^P[P; P']} \right) \right] + \\
& \left. +H^O[P] \arctan \left(\frac{[x' - x][y' - y]}{H^O[P]L^P[P; P']} \right) \right] \Bigg|_{y=y_s}^{y_n} \Bigg|_{x=x_w}^{x_e} . \tag{3.A13}
\end{aligned}$$

The values of x_w , x_e , y_s and y_n will vary with each computation point, and since the computation points are not spaced at even grid intervals they will not be placed symmetrically around the computation point. By evaluating the central cell contribution to the density correction using eq. (3.A13), we avoid the kernel singularity.

Chapter 4: Modeling topographical density for geoid determination

This article was published in the *Canadian Journal of Earth Sciences*, a journal of the National Research Council Research Press, in a 2009 special issue on Geodesy. I did the mathematical developments, background research, software development and computations, and wrote the full text of the article. My coauthors provided guidance in the computation process, and in revising the manuscript for submission. The full citation for the article is:

Kingdon, R., P. Vaníček, and M. Santos (2009). “Modeling topographical density for geoid determination.” *Canadian Journal of Earth Sciences*, Vol. 46, No. 8, pp. 571–585, doi: 10.1139/E09-018.

Note: The title of the article, “Modeling topographical density for geoid determination”, may mislead readers to believe we have created a model of an actual topographical density distribution. While we have done so in a very limited way (for Lake Superior), the intent is really to introduce a new type of topodensity model (three dimensional), and compare it to the most accurate current model type (two dimensional), in terms of geoid determination accuracy.

Also, in the introduction to the article, section 4.1 of the current document, Vaníček et al. [1999] is cited as an example of geoid determination that uses topographical density models. This is the incorrect citation; the citation should be Huang et al. [2001].

Chapter 4 Abstract

In geoid computation, effects of real three-dimensional topographic masses on the Earth's gravity field must be accurately quantified and, in the Stokes–Helmert scheme, replaced with effects of those masses condensed on the geoid. The most comprehensive modern schemes for evaluation of topographical effects account for terrain effects, use a spherical model of topography, and incorporate two-dimensionally varying models of topographical mass density. In this contribution, we employ a three-dimensionally varying model of topographical density. We use Newton's integration to determine the direct topographical effect (DTE) on gravity and primary indirect topographical effect (PITE) on gravity potential. Lastly, we apply Stokes's integration to calculate the DTE, PITE, and secondary indirect topographical effect (SITE) on geoidal height. We focus here on validation of our results and demonstration of our software's capabilities. We present results for the simple geometrical shape of a disc under various rotations and for the anomalous density of lake waters. Effects on geoidal height for these simulations reach centimetre level, up to 2.2 cm in magnitude. For a simulation of the effects of neglected mass anomalies of the lakes, we find results reaching 0.8 cm in magnitude. We examine the behavior of our results as calculated using various step sizes for

numerical integration and by comparing numerical results with analytical results for the specific case of a disc. These results show that the maximum percent error of our results is about 23.5% for the DTE on gravity and 7.6% for the PITE on gravity potential.

4.1 Introduction

The geoid, an equipotential surface approximating mean sea level, is a common reference surface for height systems. It is given by its vertical separation from a reference geocentric biaxial ellipsoid that best fits to the figure of the Earth, such as the GRS-80 ellipsoid [Moritz, 1984]. This separation can be determined by gravimetric, geometric, or other means; here, we discuss one specific gravimetric approach: the Stokes–Helmert technique (e.g., Vaníček and Martinec [1994]). This method applies the theorem of Stokes [1849] for estimation of the geoid based on gravity observations at the geoid level but assumes no masses are present above the geoid, where gravity observations are made. To achieve this condition, the Stokes technique is applied after replacing the topographical masses (between the geoid and the Earth’s surface) by an infinitesimally thin layer of horizontally varying density at or below the geoid surface. This method was originally proposed by Helmert [1884]. In the Stokes–Helmert technique, this condensation layer is located at the geoid surface, which is known as Helmert’s second condensation method. The effect of this change in mass distribution on gravity is called a direct topographical effect (DTE). Note that there is also a corresponding direct atmospheric effect (DAE), which we do not deal with here. Application of the Stokes technique to gravity anomalies that reflect this new mass

distribution produces a surface that is very close to the geoid and is called the co-geoid. A corrective term, which is called the primary indirect topographical effect (PITE), must be applied to the co-geoid to get the final geoid.

Any topographical effect can be calculated by finding the difference between the effect of condensed masses and the effect of real masses. Determination of the topographical effects thus requires an accurate knowledge of the mass–density distribution within topography. The most comprehensive current evaluations of topographical effects on the geoidal height account for terrain effects, use a spherical (rather than planar) approximation of topography to determine distances, and incorporate two-dimensionally (2-D; laterally) varying models of topographical mass–density (e.g., Vaníček et al. [1999]). A laterally varying mass–density model is often used to approximate the Earth’s real three-dimensional (3-D) density anomalies because it is difficult and expensive to determine the distribution of density within topography in a given area; and even where information about the distribution is known, it is not precise [Martinec 1993; Kuhn 2003].

For this investigation, we are interested only in the density structure of topographical masses, since effects of any masses deeper than the geoid are already accounted for in the Stokes–Helmert geoid solution. We are thus interested in knowledge of the density distribution in at most the upper 10 km of the Earth’s crust and normally <1 km. Investigations into the structure of the Earth’s crust have been ongoing over the past century using various methods [Mooney, 2007]. Seismic reflection among these methods is the most relevant active seismic method of locating density interfaces in the upper crust, including the topography. Currently, seismic reflection provides horizontal

and vertical accuracies as good as 50 m, though interfaces determined to this precision are not available globally [Mooney 2007]. Seismic wide-angle reflection and refraction are less precise, usually applying forward modeling (e.g., Zelt [1999]) and occasionally inverse methods (e.g., Zelt and Smith [1992]) to determine crustal structures. Among the passive seismic methods, local seismic tomography allows construction of a 3-D image of the upper crust (e.g., Salah and Zhao [2003]), with horizontal resolutions of up to 25 km and vertical resolutions of several kilometres. Seismic methods are especially valuable in conjunction with deep (3–12 km) borehole sampling, which provides in situ measurements of seismic velocity and density and can act as a control for density or seismic modeling (e.g., Smithson et al. [2000]). Gravity studies (e.g., Tiberi et al. [2003]) complement seismic investigations for determination of crustal density structures, although they do not provide sufficient accuracy for our methods. Geological mapping is a further useful source of information on the near-surface crustal density structure [Mooney, 2007].

There have been some applications of these techniques to constructing regional and global crustal geology models, usually with a focus on the whole crust and even the upper mantle (e.g., Mooney et al. [1998]; Bassin et al. [2000]; Pasyanos et al. [2004]). These applications consist of a series of geological boundaries between layers having different geological characteristics but are usually directed at an understanding of the whole crust and below. The earliest global model was the 3SMAC model invented by Soller et al. [1982] that provided $2^\circ \times 2^\circ$ cells, giving density and seismic information. More recently, the CRUST 2.0 global model has been produced [Bassin et al. 2000], which represents crustal structure according to a series of seven layers with thicknesses

given in a $2^\circ \times 2^\circ$ grid. Although this model is not specifically a model of topographical density, it may be useful for calculation of topographical density effects, since it includes layers describing sediment thickness, and sediment represents one of the key density anomalies within topography. Kuhn [2003] has outlined a method for determining a 3-D density model specifically for geodetic purposes by interpretation of results of seismic surveys, borehole data, and geological maps, but such a model has not yet been implemented. Instead, for geodetic calculations, a laterally varying model based on surface topographical densities derived from geology maps is normally used (e.g., Huang et al. [2001]).

We set aside for the time being the problem of determining exactly the real topographical mass–density distribution and, instead, try to estimate the potential loss in accuracy of geoidal heights by using a 2-dimensionally varying, rather than 3-dimensionally varying model of topographical density (hereafter called a 2-D model and a 3-D model). Through this investigation, we hoped to determine whether evaluation of effects of 3-D density models is worthwhile. We did this by creating hypothetical but realistic density distributions and calculating their effects on geoidal height. In these calculations, we followed roughly the approach of Martinec [1998], with some generalization, where necessary, to determine effects of the topographical density accounted for in a 3-D model but unaccounted for in a 2-D model. In terms of the Stokes–Helmert scheme, we evaluated the contribution of anomalous density unaccounted for in 2-D models on the DTE on gravity and the PITE on gravity potential. From these, the corresponding DTE, PITE, and secondary indirect topographical effect

(SITE) on geoidal height can be determined by applying Stokes' integration to the individual effects (e.g., Heiskanen and Moritz [1967]; Vaníček and Kleusberg [1987]).

In this contribution, we focus mainly on validating our application of the Newton integral for calculating effects of 3-D anomalous density on gravity and gravity potential. We limit ourselves to two families of simulations: density distributions defined by simple geometrical figures and those defined by a single density contrast. We primarily discuss results for the former application, only demonstrating our capacity to generate results with the latter, as we are attempting as a first step to understand the behaviour and potential order of magnitude of neglected 3-D density effects on a simple level before turning to more complex distributions. Also, applying distributions based on simple shapes allows us to easily compare some results with an analytical determination in spherical coordinates. Once our software has effectively met this first benchmark, we can rely more heavily on its results for more complex distributions.

This paper first describes the key points of our methodology. We begin by describing the key mathematical aspects of our approach to indicate its relation to and distinction from other density effect calculations. We conclude our discussion of methodology by describing how the technique has been implemented in our numerical calculation software, `Rad_Eff_Geoid.c`. Thereafter, we present some preliminary results to demonstrate the capability of the software, followed by results of our validation attempts.

4.2 Methodology

4.2.1 Modeling of topographical density

Our 3-D model of topographical density represents density variation within topography by a series of surfaces, each representing a particular density contrast. For example, if we wish to model the topographical density of a region including a lake, our model consists of a horizontal surface at a height of zero (corresponding to the geoid), a surface given by the height of the lakebed, and a surface given by the height of the topography (or the lake surface, over the lake). The densities of the volumes between the layers are then specified. In the case of a lake, the density in the region above the geoid surface but below the topographical and lakebed surfaces might be assigned the commonly assumed average crustal density ($\bar{\rho}$) of 2670 kg/m^3 . The density in the region above the lakebed and geoid surfaces but below the topographical surface, i.e., the lake waters, would have a density of about 1000 kg/m^3 . Thus, the anomalous density in the latter region would be -1670 kg/m^3 .

More intricate arrangements of surfaces are also possible, though distributions based on more than two input surfaces have not been implemented in the current version of our software. We have implemented density distributions defined by simple geometrical figures. For example, we may define a disc as a body of anomalous density bounded by a cylinder and two planes. We assign the disc a large anomalous density, e.g., 660 kg/m^3 , typical of a density contrast between basalt and sandstone [Parasnis 1997]. Density distributions thus defined provide the region over which our Newton integration is carried out.

4.2.2 The Newton kernel and its radial derivative for calculation of effects on gravity and gravity potential

The following derivations are performed in a spherical coordinate system, considered to have its origin at the geocentre, and illustrated in Figure 4.1 with **C** indicating the coordinate system origin.

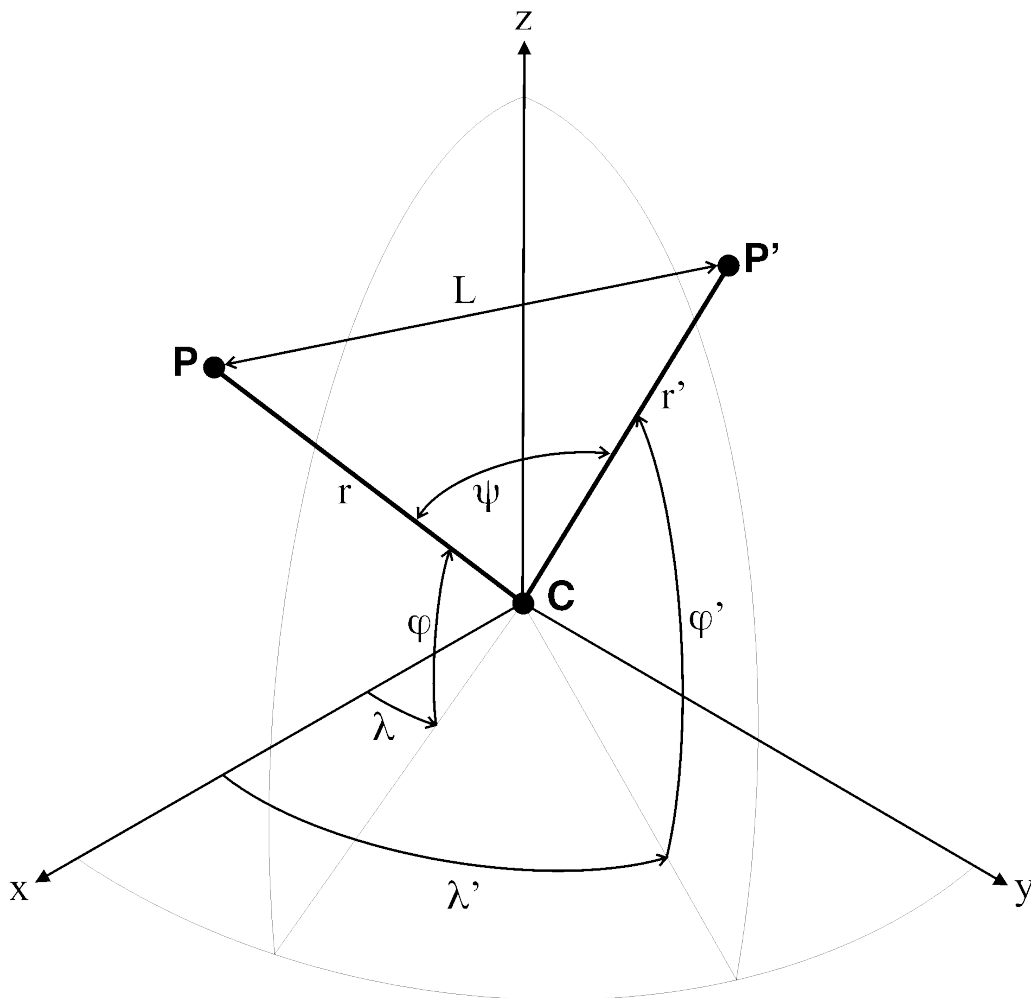


Figure 4.1: Spherical coordinate system for evaluation of Newton integrals. See text for definition of parameters.

We use the coordinates $(r, \Omega = (\varphi, \lambda))$ to represent the geocentric radius, latitude, and longitude of a point of interest P , also called the computation point. The coordinates $(r', \Omega' = (\varphi', \lambda'))$ represent the coordinates of the running point in integration, P' . The term $\psi(\Omega, \Omega')$ represents the spherical solid angle between these two points given by:

$$\cos \psi(\Omega, \Omega') = \cos \varphi \cos \varphi' + \sin \varphi \sin \varphi' \cos(\lambda - \lambda'). \quad (4.1)$$

We normally refer to it simply as ψ for the sake of conciseness.

We also introduce $L(r', r, \psi)$, the straight line (Euclidian) distance between the point of interest and the integration point:

$$L(r', r, \psi) = \sqrt{r'^2 + r^2 - 2r'r \cos \psi}. \quad (4.2)$$

The gravitational potential $V(r, \Omega)$ resulting from a density distribution $\rho(r', \Omega')$ over a region $(r' \in [r_g(\Omega'), r_t(\Omega')] \cap \Omega' \in \Omega_0)$, is given by integration of the Newton kernel,

$L^{-1}(r', r, \psi)$, over that region (e.g., Martinec [1998, eq. (1.5)]):

$$V(r, \Omega) = G \iint_{\Omega' \in \Omega_0} \int_{r'=r_g(\Omega')}^{r_t(\Omega')} L^{-1}(r, r', \psi) \rho(r', \Omega') r'^2 dr' d\Omega', \quad (4.3)$$

where G is the Newton's gravitational constant; $r_g(\Omega')$ and $r_t(\Omega')$ represent the geocentric radii of the geoid and topographical surfaces at the integration point, respectively; and $r_t(\Omega') = r_g(\Omega') + H_t(\Omega')$, where $r_g(\Omega')$ may be given by a geoid model and $H_t(\Omega')$ from a terrain model. For all applications described here, Ω_0 is defined by a spherical cap of constant radius centered on the computation point.

The gravity, $A(r, \Omega)$, resulting from a mass distribution is then given by the integral over the radial derivative of the inverse of eq. (4.2) multiplied by the density, which follows Martinec [eq. (3.6), 1998]:

$$A(r, \Omega) = G \iint_{\Omega' \in \Omega_0} \int_{r'=r_g(\Omega')}^{r_t(\Omega')} \frac{\partial L^{-1}(r, r', \psi)}{\partial r} \rho(r', \Omega') r'^2 dr' d\Omega'. \quad (4.4)$$

Equations (4.1) to (4.4) are applied for a density distribution representing anomalous density as well. In that case, we replace $\rho(r', \Omega')$ with:

$$\delta\rho(r', \Omega') = \rho(r', \Omega') - \bar{\rho}, \quad (4.5)$$

where we deal with anomalies relative to some prescribed constant density $\bar{\rho}$ or:

$$\delta\rho(r', \Omega') = \rho(r', \Omega') - \bar{\rho}(\Omega'), \quad (4.6)$$

where we deal with anomalies relative to a laterally varying density distribution $\bar{\rho}(\Omega')$.

In the case of eq. (4.5), the reference density value, ρ_0 , is defined such that the sum of anomalous densities (usually globally) is expected to be zero. In the case of eq. (4.6), although ideally the sum of anomalous density values along any topographical column should equal to zero, e.g., by assigning to $\bar{\rho}(\Omega')$, the mean density value along the column, there is usually not sufficient information to meet this condition. Instead, the density value of rock at the topographical surface is often assigned to the whole column. We consider anomalies defined according to eq. (4.6) hereafter.

4.2.3 Mathematical representation of 3-D density and condensed density models

For any integration point, with horizontal coordinate Ω' , we can represent the radial distribution of density as a piecewise function. Let us take the simple example of a lake, as in the section “Modeling of topographical density”. Let the density of topography outside the lake be ρ_0 and the density of the lake water be ρ_1 . We deal with three surfaces here: the geoid surface; the lower bound of the region we are concerned with, defined by $r_g(\Omega')$; the surface of the topography and the surface of the lake, defined by $r_t(\Omega')$, and the lake bed with geocentric radius $r_b(\Omega')$. In this case, for any point Ω' , we write:

$$\rho(r', \Omega') = \begin{cases} \rho_0, & r' \in [r_g(\Omega'), r_t(\Omega')] \cap \Omega' \notin \Omega_b \\ \rho_0, & r' \in [r_g(\Omega'), r_t(\Omega')] \cap r' \leq r_b(\Omega') \cap \Omega' \in \Omega_b \\ \rho_1, & r' \in [r_g(\Omega'), r_t(\Omega')] \cap r' > r_b(\Omega') \cap \Omega' \in \Omega_b \\ 0, & \text{elsewhere} \end{cases}, \quad (4.7)$$

where Ω_b represents the region covered by the lake, over which $r_b(\Omega')$ is defined. In some cases, we may have more complicated parameters. For example, if we deal with a model defined by a rectangular prism under some rotations, we have six planes to deal with in addition to $r_g(\Omega')$ and $r_t(\Omega')$.

When we are dealing with anomalous densities, we must change somewhat the formulation of eq. (4.7). If the prescription in eq. (4.5) is used, then instead of eq. (4.7), we represent the anomalous density distribution within Ω_b by:

$$\delta\rho(r',\Omega') = \begin{cases} \rho_0 - \bar{\rho}, & r' \in [r_g(\Omega'), r_t(\Omega')] \cap r' \leq r_b(\Omega') \\ \rho_1 - \bar{\rho}, & r' \in [r_g(\Omega'), r_t(\Omega')] \cap r' > r_b(\Omega') \\ 0, & \text{elsewhere} \end{cases} . \quad (4.8)$$

If density differences are used and $\rho(\Omega')$ is the laterally varying density (computed from surface horizontal density variations, as is often the practice, e.g., Tziavos and Featherstone [2000]; Huang et al. [2001]), then it reads:

$$\delta\rho(r',\Omega') = \begin{cases} \rho_0 - \rho_1, & r' \in [r_g(\Omega'), r_t(\Omega')] \cap r' \leq r_b(\Omega') \\ 0, & \text{elsewhere} \end{cases} . \quad (4.9)$$

Since we can determine the radial distribution of anomalous density at any integration point, we can also determine the resulting anomalous condensation density at any integration point. We do this by applying the general formula (e.g., Martinec [1998, eq. (2.3)]):

$$\delta\sigma(\Omega') = \frac{1}{r_g^2(\Omega')} \int_{r'=r_g(\Omega')}^{r_i(\Omega')} \delta\rho(r', \Omega') r'^2 dr' . \quad (4.10)$$

where $\delta\sigma(\Omega')$ is the condensation density at coordinate Ω' . Since for any value of Ω' the density can be written as a piecewise constant function, the integral in eq. (4.10) can be written in a more general form for any series of surfaces:

$$\delta\sigma(\Omega') = \frac{1}{r_g^2(\Omega')} \sum_{i=0}^{n-1} \int_{r'=r_i(\Omega')}^{r_{i+1}(\Omega')} \delta\rho_{i,i+1} r'^2 dr' = \frac{1}{r_g^2(\Omega')} \sum_{i=0}^{n-1} \delta\rho_{i,i+1} \frac{[r_{i+1}^3(\Omega') - r_i^3(\Omega')]}{3}, \quad (4.11)$$

where $r_i(\Omega')$ is a radius vector of any surface contained within the topography at Ω' , $\delta\rho_{i,j}$ is the anomalous density between surfaces i and j , n is the number of surfaces present in the topography including the geoid and topographical surface, $r_0(\Omega') = r_g(\Omega')$, and $r_n(\Omega') = r_t(\Omega')$. In our situation, where at most four surfaces are concerned, evaluating $\delta\sigma(\Omega')$ using eq. (4.11) is trivial.

4.2.4 Calculations of 3-D anomalous density effects on geoid and gravity

Prescriptions for the evaluation of the DTE, PITE, and SITE are given in a variety of sources (e.g., Martinec and Vaníček [1994a, 1994b]; Sjöberg and Nahavandchi [1999]); most notably in Martinec [1998] whom we follow closely here.

The DTE is simply the difference between the effect of the anomalous density of real topography and that of the condensed topography on surface gravity:

$$\delta A_{\delta\rho}(\Omega) = A_{\delta\rho}^t(\Omega) - A_{\delta\rho}^c(\Omega), \quad (4.12)$$

where $\delta\rho$ indicates that we are dealing with 3-D anomalous density effects (not to be confused with the $\delta\rho$ subscript sometimes used to denote effects of laterally varying anomalous density). $A_{\delta\rho}^t(\Omega)$ is the effect of real topography on gravity and can be found using eq. (4.4):

$$A_{\delta\rho}^t(\Omega) = A_{\delta\rho}(r^t(\Omega), \Omega) = G \iint_{\Omega' \in \Omega_0} \int_{r_g^t(\Omega')}^{r_t(\Omega')} \frac{\partial L^{-1}(r, r', \Psi)}{\partial r} \Big|_{r=r^t(\Omega)} \delta\rho(r', \Omega') r'^2 dr' d\Omega', \quad (4.13)$$

while the effect of the condensed layer, $A_{\delta\rho}^c(\Omega)$, is found by taking the limit of eq. (4.4)

as $r_i(\Omega') \rightarrow r_g(\Omega')$, which yields:

$$\begin{aligned} A_{\delta\rho}^c(\Omega) &= \lim_{r_i(\Omega') \rightarrow r_g(\Omega')} A_{\delta\rho}(r'(\Omega), \Omega) = \\ &= G \iint_{\Omega' \in \Omega_0} \frac{\partial L^{-1}(r, r_g(\Omega'), \psi)}{\partial r} \Big|_{r=r'(\Omega)} \delta\sigma(\Omega') r_g^2(\Omega') d\Omega'. \end{aligned} \quad (4.14)$$

The values of $\delta A_{\delta\rho}(\Omega)$ can be determined, depending on the information available about anomalous density structures, by numerical integration, analytical integration, or some combination of both. In the context of this study, we have performed all integration numerically in the horizontal direction but analytically in the vertical direction along a given column of topography. Having calculated $\delta A_{\delta\rho}(\Omega)$, we may determine the corresponding DTE on geoidal height through the Stokes's integration. The Stokes' integration, in conjunction with Bruns's formula, may be used to convert a field of effects on gravity into their effect on geoidal height. The formulation for Stokes' integration to determine the DTE on geoidal height as a result of a topographical effect is given by [Martinec, 1993, eq. (4.5)]:

$$\delta N_{DTE, \delta\rho}(\Omega) = \frac{R}{4\pi\gamma} \iint_{\Omega' \in \Omega_0} S(\psi) \delta A_{\delta\rho}(\Omega') d\Omega', \quad (4.15)$$

where R is the mean radius of the Earth, γ is the normal gravity at the point Ω , and $S(\psi)$ is the Stokes kernel given by (e.g., Vaniček and Krakiwsky [1986]):

$$S(\psi) = 1 + \frac{1}{\sin[\psi / 2]} - 6 \sin[\psi / 2] - 5 \cos \psi - 3 \cos \psi \ln(\sin[\psi / 2] + \sin^2[\psi / 2]). \quad (4.16)$$

The PITE is the difference between the effects of mass anomalies of real and condensed topography on gravity potential at the geoid:

$$\delta V_{\delta\rho}(\Omega) = V_{\delta\rho}^t(\Omega) - V_{\delta\rho}^c(\Omega); \quad (4.17)$$

Here, we use eq. (4.3) to evaluate the term $V_{\delta\rho}^t(\Omega)$:

$$V_{\delta\rho}^t(\Omega) = V_{\delta\rho}(r_g(\Omega), \Omega) = G \iint_{\Omega' \in \Omega_0} \int_{r'=r_g(\Omega')}^{r_t(\Omega')} L^{-1}(r_g(\Omega), r', \psi) \delta\rho(r', \Omega') r'^2 dr' d\Omega'. \quad (4.18)$$

and the limit of eq. (4.17) as $r_t(\Omega') \rightarrow r_g(\Omega')$ to find $V_{\delta\rho}^c(\Omega)$:

$$V_{\delta\rho}^c(\Omega) = \lim_{r_t(\Omega') \rightarrow r_g(\Omega')} V_{\delta\rho}(r_t(\Omega'), \Omega) = G \iint_{\Omega' \in \Omega_0} L^{-1}(r_g(\Omega), r_g(\Omega'), \psi) \sigma(\Omega') r_g^2(\Omega') d\Omega'. \quad (4.19)$$

For each point where the PITE on gravity potential is evaluated, the PITE on geoidal height may also be evaluated according to Bruns's formula [Martinec, 1993, eq. (4.6)]:

$$\delta N_{PITE,\delta\rho}(\Omega) = \frac{\delta V_{\delta\rho}(\Omega)}{\gamma}. \quad (4.20)$$

The PITE on gravity is further given by:

$$\delta A_{PITE,\delta\rho}(\Omega) = \frac{2}{R} \delta V_{\delta\rho}(\Omega), \quad (4.21)$$

By Stokes's integration of the PITE on gravity over a large area, we may determine the SITE on geoidal height [Martinec, 1993, eq. (4.7)]:

$$\delta N_{SITE,\delta\rho}(\Omega) = \frac{1}{2\pi\gamma} \iint_{\Omega' \in \Omega_0} S(\psi) \delta V_{\delta\rho}(\Omega') d\Omega'. \quad (4.22)$$

4.2.5 Numerical evaluation of the DTE, PITE, and SITE

Throughout our numerical evaluations, we consider that $r_g(\Omega') = r_g(\Omega) = R$, i.e., we employ a spherical approximation. This is common in similar calculations, e.g., of laterally varying anomalous density effects on geoidal height (e.g., Martinec [1993]; Huang et al. [2001]). Although we have not rigorously tested its validity, here we consider the approximation still appropriate as we only perform a first estimation of 3-D

anomalous density effects.

Horizontal numerical integration is required for eqs. (4.13), (4.14), (4.18), and (4.20). All numerical integration is performed using spherical coordinates φ' and λ' , with the areal element $d\Omega' = \sin\varphi' d\varphi' d\lambda'$. Testing has shown that the local density bodies we are modeling (most <100 km wide and <1 km thick, i.e. thicker than most topography) do not have a significant effect beyond 3° from the computation point, so integration is limited to a 3° cap. The cap is divided into four circular zones centered on the computation point: the middle zone, inner zone, innermost zone, and a zone comprising only the near vicinity of the computation point. The sizes and resolutions of these zones may be modified in the option file of our software. Through testing, we have determined suitable resolutions and sizes for each of these zones, as indicated in Table 4.1.

Table 4.1: Integration zone sizes and resolutions.

Zone	Radius (arcseconds)	Resolution (arcseconds)
Middle	7200	300
Inner	3600	30
Innermost	1080	3
Central	1.5	1

These radii were determined by increasing each until the change in the results was negligible. So, for example, starting with a middle zone radius of 3600 arcseconds, we then increased it by intervals of 1800 arcseconds until the difference in results after a particular increase was negligible (less than 1 cm). We determined that the difference in results was negligible when increasing the radius from 5400 to 7200 arcseconds, so we considered 7200 arcseconds a sufficient radius.

Equations (4.13) and (4.18), which appear to require a 3-D numerical integration, can be reduced to only 2-D integrations by taking advantage of the aforementioned behavior of $\delta\rho(r',\Omega')$ as a piecewise constant function of argument Ω' . Analogous to the development of eq. (4.11), we can write, e.g., eq. (4.13) as:

$$\int_{r'=R}^{r_i(\Omega')} \frac{\partial L^{-1}(r,r',\psi)}{\partial r} \Big|_{r=r'(\Omega)} \delta\rho(r',\Omega') r'^2 dr' = \sum_{i=0}^{n-1} \delta\rho_{i,i+1} \frac{\partial \widetilde{L}^{-1}(r,r',\psi)}{\partial r} \Big|_{r'=r_i}^{r_{i+1}} \Big|_{r=r'(\Omega)}, \quad (4.23)$$

where, as provided by Martinec [1993, eq. (2.22)]:

$$\begin{aligned} \frac{\partial \widetilde{L}^{-1}(r,r',\psi)}{\partial r} &= \frac{(r'^2 + 3r^2)\cos\psi + (1 - 6\cos^2\psi)rr'}{\ell(r,r',\psi)} + \\ &+ r(3\cos^2\psi - 1)\ln|r' - r\cos\psi + \ell(r,r',\psi)|. \end{aligned} \quad (4.24)$$

Similarly, for eq. (4.17) we can write:

$$\int_{r'=R}^{r_i(\Omega')} L^{-1}(R,r',\psi) \delta\rho(r',\Omega') r'^2 dr' = \sum_{i=0}^{n-1} \delta\rho_{i,i+1} \widetilde{L}^{-1}(R,r',\psi) \Big|_{r'=r_i}^{r_{i+1}}. \quad (4.25)$$

and according to Martinec [1993, eq. (2.20)]:

$$\begin{aligned} \widetilde{L}^{-1}(r, r', \psi) = \\ = \frac{(r' + 3r \cos \psi)}{2} \ell(r, r', \psi) + \frac{r^2 (3 \cos^2 \psi + 1)}{2} \ln |r' - r \cos \psi + \ell(r, r', \psi)|. \end{aligned} \quad (4.26)$$

Thus, numerical integration is only necessary to carry out horizontally.

In cases where the topographical density distribution is given by a surface or series of surfaces, the accuracy of determination of eqs. (4.13) and (4.18) could theoretically be further improved by representing the surface as a polyhedral body. The integration over a polyhedral body of constant density can be carried out analytically in all three dimensions in a Cartesian coordinate system (e.g., Paul [1974]) and even over a polyhedral body of linearly varying density [Pohánka, 1998]. Previous studies have shown that the polyhedral representation provides an improvement in the case of terrain effect calculations (e.g., Tsoulis [2001]) when applied in a local planar coordinate system. Unfortunately, this analytical integration over polyhedrons has not yet been developed in spherical coordinates; and, since the development cannot be done over relatively simple prismoidal bodies [Heck and Seitz 2007], it may be impossible. We have not investigated the possibility of using the analytical integration in, e.g., a global Cartesian coordinate system. While the existing developments could be applied for calculating effects of real topography using polyhedral models and may be useful for validation in the future, we are aware of no formulation for corresponding effects of condensed topography. Since this is only our first attempt at modeling 3-D density

effects, we have not attempted these developments. We also were unable to apply an analytical integration over each (prismoidal) cell in the 3-D integration of eqs. (4.13) and (4.18). While Nagy et al. [2000] provided formulas for this approach in a rectangular coordinate system, the horizontal integration over a cell cannot be carried out analytically in a spherical coordinate system, so numerical integration is necessary [Heck and Seitz 2007].

Determination of the geocentric radii of density interfaces for each cell was done differently for both types of simulations our software is capable of. Where a single density interface is used, depths to the interface are read from an input file, e.g., a bathymetric model. The geocentric radius of the interface at any integration point is determined by $r_b(\Omega') = r_t(\Omega') - D_b(\Omega')$, where $D_b(\Omega')$ is the lake depth at the integration point, derived by bilinear interpolation of depths from the input file. The values of the densities above and below the interface are given in an option file, and these values are assigned to different segments according to the conditions from eqs. (4.8) or (4.9). Where a geometrical figure is used to delineate a region of anomalous density, the determination of densities and density interfaces is more complicated.

The last but not least problem with numerical implementation is the behavior of the Newton kernel and its integrals and derivatives when the integration point is near to the computation point. We deal here with four different kernels: (1) the Newton kernel used in eq. (4.19), (2) its radial derivative used in eq. (4.14), (3) the integral of the Newton kernel with respect to the radius of the integration point used in eq. (4.26), and (4) the integral of the radial derivative of the Newton kernel with respect to the radius of the

integration point used in eq. (4.24). All these kernels have a point of singularity where $\psi = 0$ and $r = r'$. For our application, this condition is easily resolved for the kernel in (2), since the computation point and integration point are always on the topographical surface and geoid, respectively, so that this condition is only met when the height of the computation point is zero. In such situations, there can be no anomalous density at that point anyway (there is no topography), so the value of the kernel at the point of singularity is exactly zero. For kernel (1), the singularity always occurs. Since r is always equal to r' over the region of integration, the singularity occurs where $\psi = 0$, a point that must be included in any integration, since it represents the value at the center of the spherical integration cap. For (3), the singularity only occurs when $\psi = 0$ and the top of the anomalous density body coincides with the topographical surface, since this is the only situation where r may equal r' . This singularity is easily removed in the case where anomalous density is considered relative to laterally varying surface density, since in the case of the density anomaly, whenever the body representing the density structure intersects the topographical surface its density is the surface density, and the anomalous density of the body itself is zero. Likewise, (4) can only be singular where $\psi = 0$ and the density body intersects the geoid.

These singularities are easily removed in terrain and 2-D anomalous density effect calculations. When used to calculate terrain effects, for example, it is clear that the terrain has the same height as the Bouguer shell does at the computation point (i.e., the central cell has zero contribution to the terrain effect). Therefore, regardless of the singularity of the Newton kernel, the central cell contains no terrain, so the contribution

of the central cell to the integration is zero [Martinec, 1998]. When dealing with laterally varying anomalous density, the contribution of a Bouguer shell of density equal to the anomalous density in the central cell can be added to the Newton integral to account for the contribution of the singularity point and take the integral without that differential neighbourhood of that point. Thus, at the central point, the anomalous density relative to this shell is zero and, again, the singularity is removed [Martinec, 1998].

Although a similar approach could be applied for 3-D density effects, we have simply arranged our integration points for this work so that they do not correspond exactly with the computation point and the singularity does not occur. We recognize that this is not a rigorous way of dealing with the immediate neighbourhood of the singularity, but we consider our approach sufficient for a first effort.

Numerical Stokes' integration is required to evaluate eqs. (4.15) and (4.22). The integration is performed over a spherical cap of 4° radius with cell size of 3 arcseconds ($3600 \text{ arcseconds} = 1^\circ$), following the general procedure given in Heiskanen and Moritz (1967). The singularity of the Stokes kernel in the central cell is removed, as suggested by Vaniček and Krakiwsky [1986].

4.2.6 Criteria for verification of results

For the purposes of this investigation, we tested our results for effects on gravity and gravity potential only. Our Stokes' integration contains no novel adaptations whereas our Newton integration does and is thus the focus of verifications.

We propose three methods to validate the results of our computations: (1) examine the sequence of our results while the cell size used in numerical integration decreases,

(2) compare with entirely analytical results for specific cases where such results can be found, and (3) compare with other similar efforts. Here, we apply only (1) and (2), since we know no other efforts which use directly a 3-D model of topographical density, while previous efforts similar to some of our simulations exist. The work of Martinec et al. (1995) on lake water effects, for example, does not use a 3-D model directly but, instead, uses a 3-D model based on bathymetry to create a 2-D laterally varying density model by averaging densities along the plumbline in each topographical column. The resulting 2-D model is then used in later calculations.

The testing in method (1) is done by first increasing the size of the innermost integration zone to approximately 3° in radius, normally the size of the middle zone. This is much larger than it really needs to be. Then, the radii of other integration zones are also made equal to 3° so that they are skipped in the numerical evaluation. Thus, all cells used in integration have the same size, and the whole 3° spherical cap is covered. Next, the resolution of the innermost zone is varied from coarse to fine. As the resolution increases, we expect to see the results converge toward some particular value. If they do, then the results are at least consistent with each other.

Testing by method (2) provides a comparison with exact results in specific cases. The test we apply here is a comparison with an exact result for the DTE on gravity and PITE on gravity potential at a computation point on the axis of a spherical disc. The spherical disc is defined by the intersection of a cone, and a spherical shell with its center at the apex of the cone. We examined the effect of a disc of a given size, oriented with its axis vertical but with its mass center at various heights above the geoid.

To calculate exactly the PITE of the disc, we integrated eqs. (4.18) and (4.19) setting $r = R$ over the region of a disc with a given density. We integrated in a geocentric spherical coordinate system to simplify the integration – the primary axis is made coincident with the axis of the disc – so that when the dummy point of integration is at the computation point, $\psi = 0$. This provides the effect of real topography on gravity potential at the geoid:

$$V'_{\delta\rho}(\Omega = \Omega_c) = \pi G \delta\rho_D \left[\frac{2}{3} \frac{L_{g,u}^3 - L_{g,l}^3 - r_u^3 + r_l^3}{R} + r_u^2 - r_l^2 + \cos(\psi_D) \left(L_{g,u} [r_u - R \cos(\psi_D)] - L_{g,l} [r_l - R \cos(\psi_D)] + R^2 \sin^2(\psi_D) \ln \left| \frac{r_u - R \cos(\psi_D) + L_{g,u}}{r_l - R \cos(\psi_D) + L_{g,l}} \right| \right) \right], \quad (4.27)$$

where r_l is the geocentric radius of the lower boundary of the disc, r_u is the geocentric radius of the upper boundary, ψ_D is the solid angle from the center of the disc to the edge, $\delta\rho_D$ is the anomalous density of the disc, and Ω_c is the spherical coordinates of the axis of symmetry of the disc. For conciseness, we have written straight-line distances using the convention $L_{p,q} = L(r_p, r_q, \psi_D)$. Where the term r_g is required to evaluate a distance, it is set to $r_g = R$.

For the effect of condensed topography on gravity potential at the geoid:

$$V^c_{\delta\rho}(\Omega = \Omega_c) = 2\pi G \delta\sigma_D R \sqrt{2(1 - \cos\psi_D)}, \quad (4.28)$$

where $\delta\sigma_D$ is the condensation density resulting from the anomalous density of the disc. By taking the derivatives of eq. (4.27), we can also find the effect of real topography on gravity at the topographical surface:

$$A_{\delta\rho}^t(\Omega = \Omega_c) = 2\pi G\delta\rho_D \left[L_{t,u} \left(\sin^2(\psi_D) - \frac{r_u}{r_t} \cos(\psi_D) \right) - L_{t,l} \left(\sin^2(\psi_D) - \frac{r_l}{r_t} \cos(\psi_D) \right) - \frac{L_{t,u}^3 - L_{t,l}^3 + r_u^3 - r_l^3}{3r_t^2} + r_t \cos(\psi_D) \sin^2(\psi_D) \ln \left| \frac{L_{t,u} + r_u - r_t \cos(\psi_D)}{L_{t,l} + r_l - r_t \cos(\psi_D)} \right| \right], \quad (4.29)$$

where $r_t = r_t(\Omega_c)$. By taking the derivative of eq. (4.26), we find the effect of condensed topography on gravity at the topographical surface:

$$A_{\delta\rho}^c(\Omega = \Omega_c) = -2\pi G\delta\sigma_D \frac{r_g^2}{r_t^2} \left(\frac{r_g - r_t \cos\psi_D}{\ell_{g,t}} - 1 \right). \quad (4.30)$$

From these results, we find the DTE and PITE for Ω_c using eqs. (4.12) and (4.17), respectively.

We evaluate the differences between the results from these analytical formulas and numerical determinations for the particular case of Ω_c to find an absolute determination of the error of our numerical approach in these particular cases, which we take as an

indicator of how well our approach might behave in other situations. Since this only provides absolute errors for one set of situations, the resulting error estimates are not applicable for other simulations as anything more than an indicator of what we might expect the errors in those cases to be.

4.3 Results and discussion

4.3.1 Results demonstrating the capability of simulation software

We present here two sets of results. First, as an example of a simulation of the effect of a simple density distribution, we present the effect on geoidal height of a disc, representing a realistic density contrast, in topography of uniform height. From these results, we are able to observe some characteristics of the behavior of anomalous density effects. We finally provide an example of the 3-D anomalous density effect of a lake, again in smooth topography, as an example of the effect of a density distribution given by a single density interface.

For the first simulation, we consider a density distribution given by a disc embedded in topography uniformly 2000 m thick. The disc itself is 40 km in diameter and 500 m thick. We have assigned it a density of 660 kg/m^3 , a typical anomalous density for, e.g., a disc of basalt embedded in sandstone (e.g., Parasnis [1997]). If the center of the disc is 500 m deep, it produces the DTE and PITE shown in Figure 4.2, both of which show results over a 1° by 1° area.

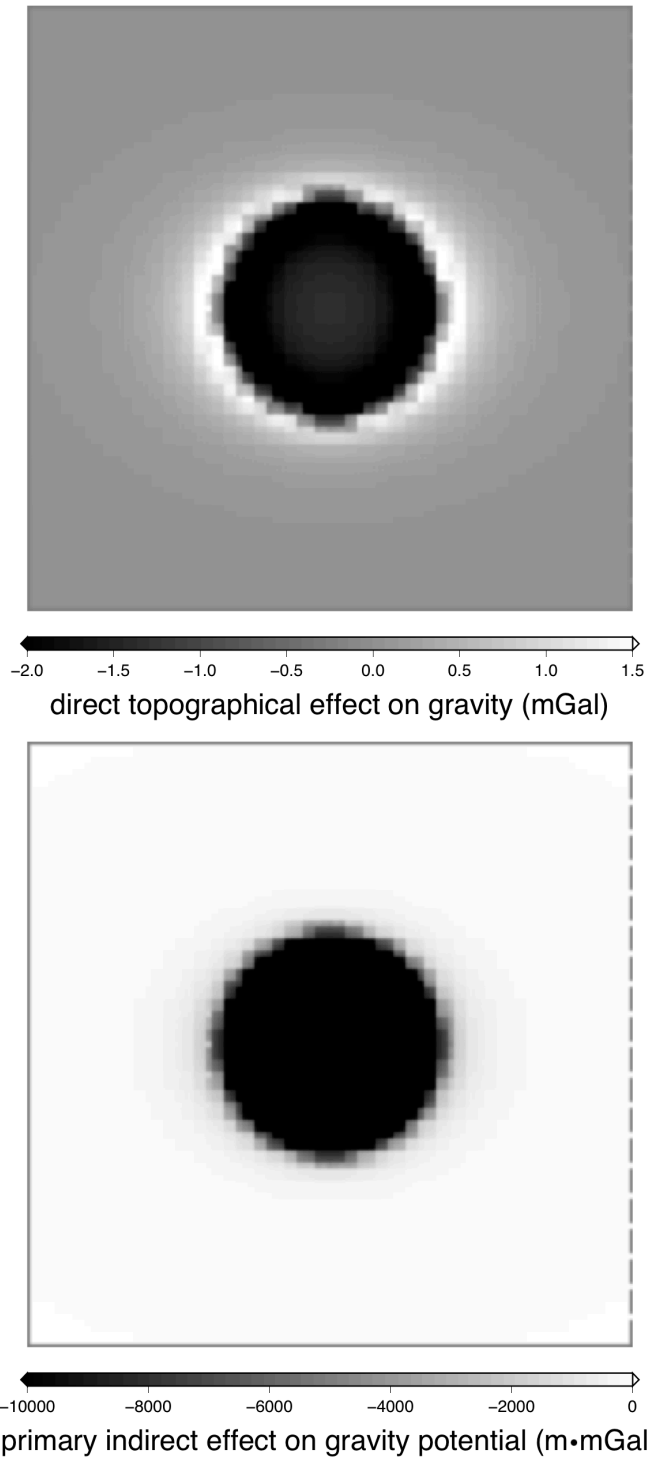


Figure 4.2: DTE on gravity and PITE on gravity potential, resulting from a disc 500 m thick, 40 km in diameter, with anomalous density of 660 kg/m^3 , with center 500 m deep, and embedded in 2000 m thick topography.

Notice that, with the DTE, the minimum of ~ -4 mGal ($1 \text{ Gal} = 1 \text{ cm} \cdot \text{s}^{-2}$) is not at the center of the disc but in a ring around the center. This is because the DTE is the difference between a contribution of real topography to surface gravity and a slightly smoother contribution of condensed topography to surface gravity. The difference is almost constant near the projected center of the disc; but within the disc, moving away from its center, the contribution of real topography decreases more slowly than that of condensed topography so that the difference between the two grows. However, around the edge of the disc the contribution of real topography diminishes rapidly, whereas the contribution of condensed topography diminishes more slowly. Thus, the difference between the two grows smaller and eventually changes sign, resulting in a ring of positive values surrounding the disc. The maximum result of 1.8 mGal occurs in this ring.

The same trend is not visible for the PITE, which has a minimum of ~ -19000 mGal at the disc center. Unlike the DTE, the magnitude of the PITE always decreases with distance from the disc center, since in the contribution of real topography decreases more rapidly than the contribution of condensed topography but is never less in magnitude than the contribution of condensed topography. For the same reason, the difference between the two contributions converges to zero, which is then the maximum value of the PITE.

Next, we examine the effects resulting from this disc if it is rotated by certain angles around its west–east axis. In this case, we present results from discs rotated by 0.5° , 1° , and 5° . Here, we give the DTE and PITE on geoidal height. Also, the center of the disc is now situated at a depth of 1000 m. The SITE in these and all of our simulations so far is

negligible. We further show the net effect on geoidal height resulting from both DTE and PITE. Results for the DTE, PITE, and total effect are given in Figure 4.3, all of which show results over a 1° by 1° area.

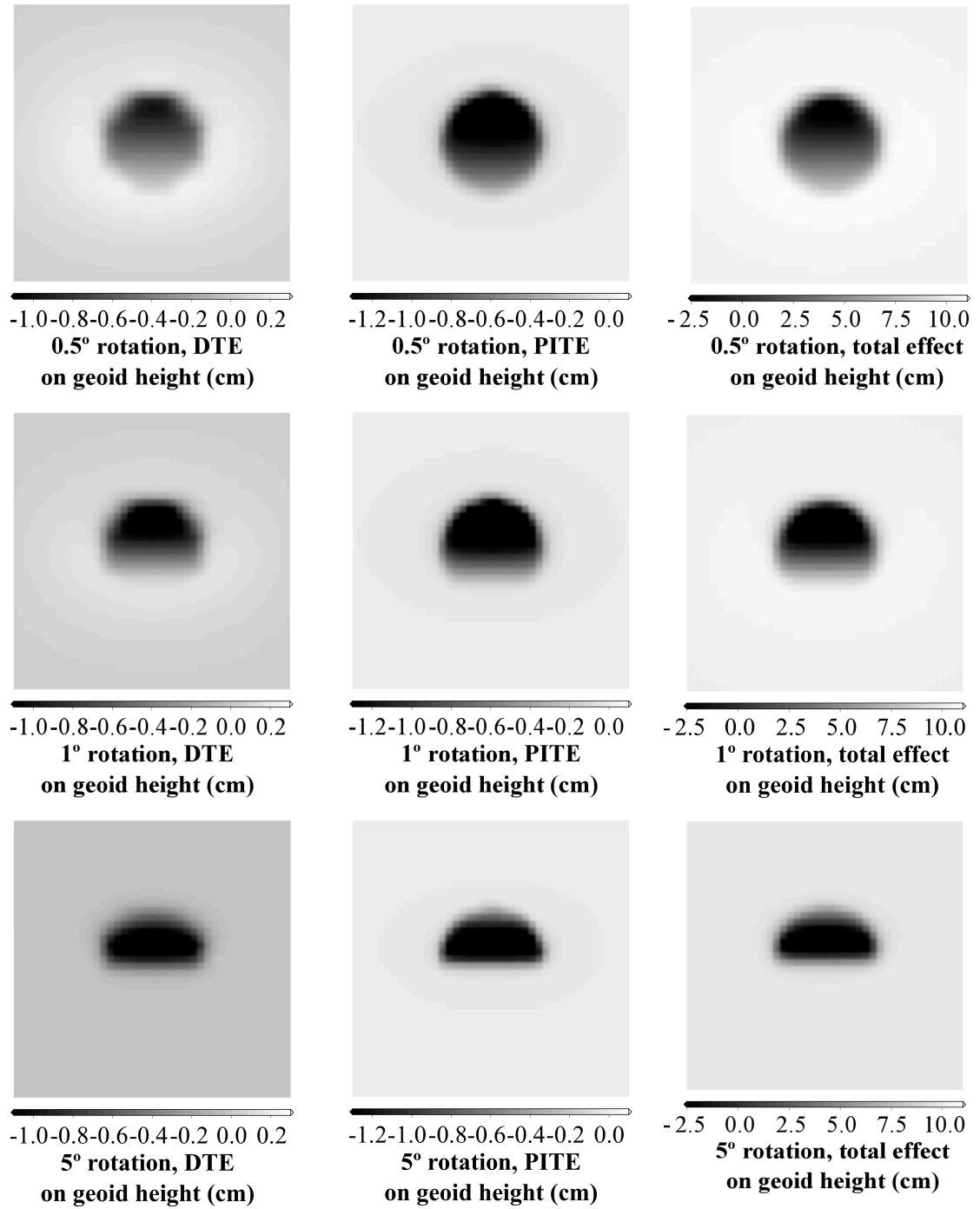


Figure 4.3: DTE, PITE, and the total effect of anomalous density on geoidal height for discs 500 m thick, 40 km in diameter, with anomalous density of 660 kg/m³, with centers 1000 m deep, embedded in 2000 m thick topography, and rotated to 0.5°, 1°, and 5° from horizontal.

First, notice that, when the disc is nearly horizontal, the maximum value of the DTE on height is over the center of the disc. This is in contrast to the case with the DTE on gravity and is a result of the smoothing effect of Stokes' integration used to determine the DTE on height. Also, the DTE and PITE tend to be larger where mass anomalies are distributed closer to the topographical surface. This is because both the DTE and PITE represent a difference between contributions of mass on the geoid and at the topographical surface, and these contributions are most different when the mass in real topography is distributed farther from the geoid. For this reason, the maximum values correspond to the part of the disc tilted toward the surface and the minimum to the part tilted toward the geoid. In terms of magnitude, in the case where magnitudes are largest – where the disc is rotated to 5° from the horizontal – the DTE ranges from -0.2 to 1.0 cm whereas the PITE ranges from 0 to 1.2 cm. However, due to the rotation of the discs, the DTE and PITE do not cancel each other where the positive effects are greatest. Thus, the total effect ranges from -0.2 to 2.2 cm, which indicates that such a density body would have a significant effect on precise geoid determinations. These values are smaller in magnitude for other simulations. For comparison, Huang et al. [2001], using a 2-D density model in the Canadian Rocky Mountains, calculated anomalous density effects on the DTE ranging from -5.1 to 2.6 cm, the PITE ranging from -2.5 to 1.7 cm, and a total effect ranging from -7.0 to 2.8 cm. Huang et al. find that these effects are $<10\%$ of the effects calculated using a heterogeneous model of topographical density.

For our second simulation, we examine the 3-D anomalous density effects generated by Lake Superior. We make some simple assumptions in this simulation. First, we consider all topography to have a thickness (height) of 183 m, about the average height

of the surface of Lake Superior. We also assume that the density of all topography in the area is 2670 kg/m^3 , a common value for the average crustal density. The depths of the lake bed are given by a bathymetric dataset prepared by Schwab and Sellers [1996].

We consider here the anomalous density relative to a laterally varying distribution, with densities equal to the density at the topographical surface. This is coherent with laterally varying density distributions based on densities from geology maps. Thus, the laterally varying anomalous density is situated between the bed of the lake and the geoid (where the lake bed is above the geoid). The results of the simulation are given in Figure 4.4.

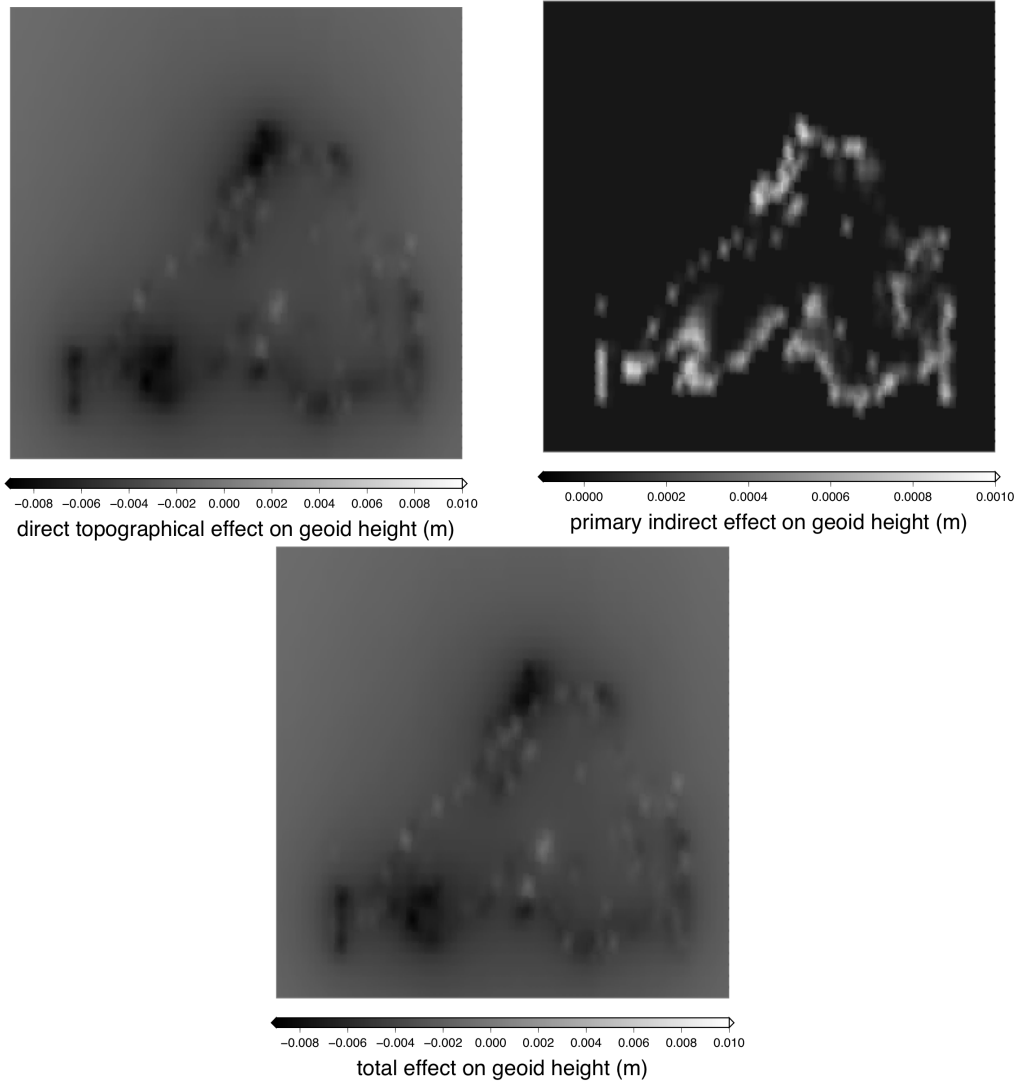


Figure 4.4: Effects of 3-D anomalous density of Lake Superior on geoidal height.

We present only results for the DTE and PITE on geoidal height, because the SITE is negligible. We also present the total effect of the DTE plus the PITE. The results are distributed from latitudes of 46°N to 50°N and from longitudes of 264°E to 274°E.

We notice especially here that the DTE on height is smoother than the PITE on height owing to smoothing of the DTE in Stokes' integration. We also notice that, though there are some peaks in the PITE, the PITE is generally about an order of

magnitude smaller than the DTE, so the effects of the DTE are still dominant in the total effect. The DTE ranges from -8 to 9 mm whereas the PITE is always positive and has a maximum magnitude of only 0.9 mm. Due to the small size of the PITE, the net effect is almost identical to the DTE.

4.3.2 Verification of results

Here, we apply the first of our suggested tests of our results. Since all vertical integration is analytical, only the horizontal integration in eqs. (4.13), (4.14), (4.18), and (4.19) is performed numerically. Thus, as the horizontal integration step is decreased, the results should approach an exact result. If the results do not converge, there is some problem with our approach. Note that while the analytical results provide a more accurate estimation in this particular case, the analytical result cannot yet be extended to any figure in spherical coordinates.

To visualize this test, we calculate the DTE on gravity and PITE on gravity potential for the projection of the center of a disc on the topographical surface and geoid, respectively, as the depth of the disc is varied. We model a disc similar to the one used previously in the text but only 200 m thick. The height of the center of the disc is varied from a height of 100 to 1900 m. Note that, at 1900 m, the top of the disc would actually be coincident with the surface of topography, a situation that cannot possibly occur when considering anomalous density relative to a laterally varying distributions based on surface geology. Here, we allow this situation to occur, so we can more fully examine the behavior of our results. Plots of the DTE and PITE against the height of the disc center for various horizontal integration step sizes are given in Figure 4.5.

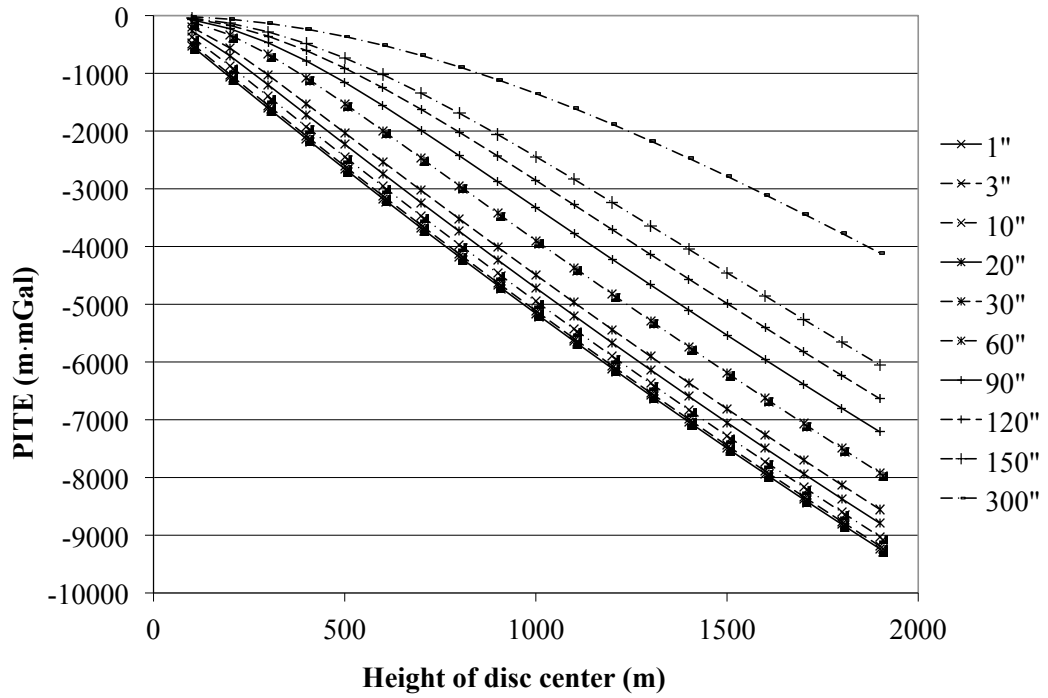
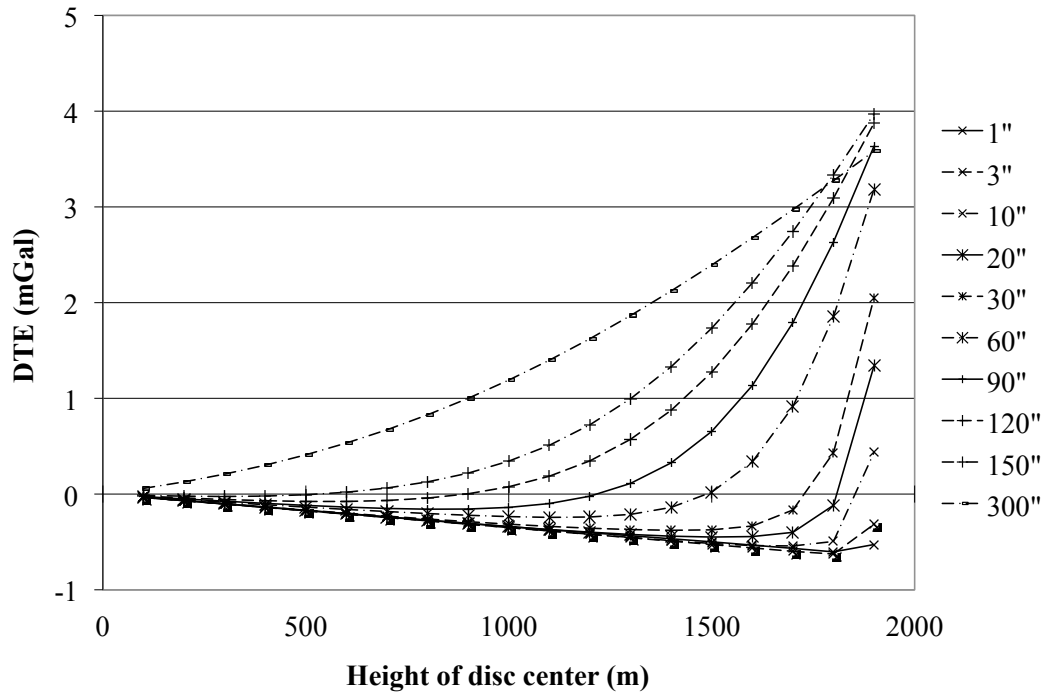


Figure 4.5: DTE and PITE against height to disc center for discs 200 m thick, 40 km in diameter, with anomalous density of 660 kg/m^3 , embedded in 2000 m thick topography, with varying heights to disc center, and with varying horizontal integration intervals.

We see that the results in both cases do converge as the integration step is decreased. In the case of the DTE, the 3 and 1 arcsecond lines are almost coincident except for a disc lying just under the surface. At that point, the DTE shows a slight increase for both. The same increase is much more noticeable for larger integration steps, and so is also apparently an artifact of the numerical integration. In the case of the PITE, the results converge very nicely to almost coincident lines. This indicates that our results are at least consistent with each other – at a given height, they converge to a single value. However, we must verify that they are approaching the correct result.

As an exact standard by which we may test our results, we apply eqs. (4.27) to (4.30) to determine exactly the DTE on gravity and the PITE on gravity potential generated by the disc discussed in this section. A comparison of the best 1 arcsecond numerical integration results with the fully analytical result available for the particular case of a disc is shown in Figure 4.6.

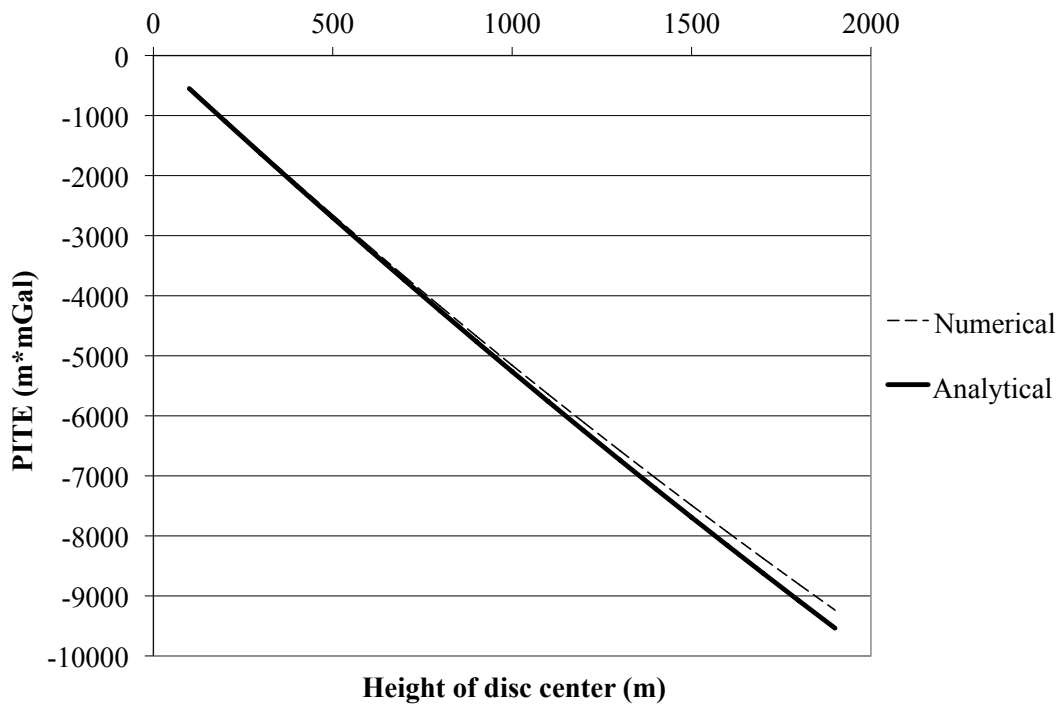
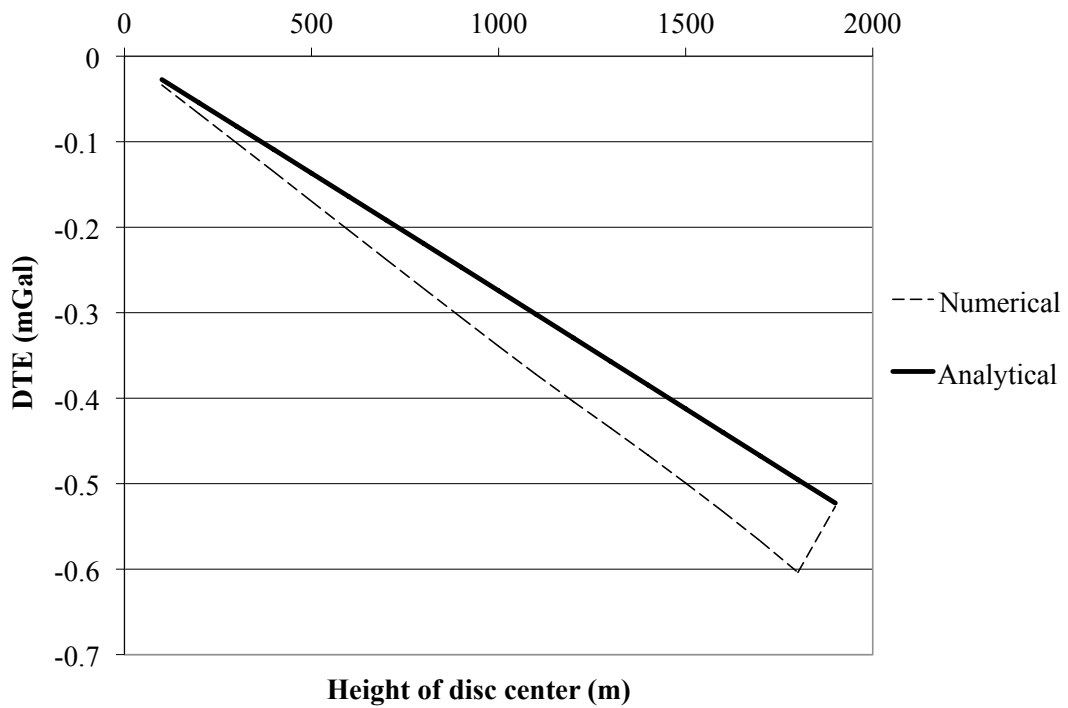


Figure 4.6: DTE and PITE against height to disc center for discs 200 m thick, 40 km in diameter, with anomalous density of 660 kg/m^3 , embedded in 2000 m thick topography, and with varying heights to disc center, from both analytical and numerical integration with 1 arcsecond step.

We see that the DTE from both results are nearly linear, but the numerical result decreases more quickly than the analytical result. Thus, the errors in the DTE grow as the depth of the density anomaly decreases. Although the sharp increase in the numerical result here makes it nearly coincident with the analytical result for a disc just below the topographical surface, we know from our previous comparison that this increase is an artifact of the numerical integration, so the coincidence of the two results at that point is only a fortunate canceling of errors, which does not usually occur.

For analysis of these results, we mainly discuss the percent differences between analytical and numerical results. This is expedient because it represents differences between the results in a way easily extrapolated to a crude estimate of errors for results in general or of errors in effects on geoidal height. For example, if we know the difference between the numerical and analytical results in this particular case, where an analytical result is available for comparison and reaches a maximum of 20%, we might guess that, e.g., our aforementioned lake simulation result has an error of 20% of the maximum effect of 9 mm, or about 2 mm. Of course, this is a crude way of estimating errors, since results of other simulations may behave very differently from those for a disc. However, it is currently our only indication of absolute error in the results.

Considering only the situations where the disc does not touch the topographical surface, the maximum percentage error in the DTE is 19% for a 1 arcsecond integration step. In other simulations, we have been able to achieve errors as large as 24%; but we are not especially concerned about these, since the error is proportionally larger for

thinner discs. For example, if we perform a simulation as shown in Figure 4.6a, but with a 400 m thick disc, we find the maximum percent error in the simulation is only 16%, whereas the maximum magnitude of results is 0.9 mGal. We find the greatest percent error (23.5%) for a disc 200 m thick and 30 km wide, and also in 2000 m thick topography. Thus, the formations with greatest influence on the DTE are also those whose effects, determined numerically, have the smallest relative error. This is also the width of disc that results in the smallest magnitude of DTE.

In the case of the PITE, both results are again nearly linear, but the numerical result here decreases more slowly than the analytical result with height of the disc center. Thus, again, the error in the PITE grows as depth to the disc decreases.

The percent error in the PITE is consistently much smaller than that in the DTE, reaching a maximum in this simulation of 4% for a disc near to the geoid. Note that the percent error in the PITE is smallest for narrower discs and when the bottom of the disc is near to the geoid. Unlike the DTE, the PITE is greatest for thicker discs. The largest percent error we have found for the PITE is for a disc 5 km wide and 1900 m thick, with its bottom at the geoid, and in 2000 m thick topography, which yields an error of 7.6%.

We summarize in Table 4.2 the worst errors we have been able to find in our results by comparison with an analytical result for a disc. For all of these situations, the simulations take place in 2000 m thick topography.

Table 4.2: Worst case errors to date for DTE and PITE, determined by comparison with an analytical result for a disc having density contrast of 660 kg/m^3 in 2000 m thick topography.

Quantity	DTE	PITE
Analytical result	-0.67 mGal	-38239 m · mGal
Numerical result	-0.82 mGal	-35317 m · mGal
Difference	-0.16 mGal	2922 m · mGal
% error	23.5	7.6
Disc width (km)	30	5
Disc thickness (m)	200	1900
Depth to disc center (m)	200	1050

These results suggest maxima for our DTE and PITE results for the disc simulation and also some general principles for the sort of distributions where our numerical results might have lower accuracy. Considering that the maximum error for the DTE is just over 20%, which decreases with an increase in DTE, we consider this sufficient validation of our approach for initial estimates of the order of magnitude of 3-D anomalous density effects.

4.4 Conclusions

Previous attempts to account for topographical density effects on geoidal height have modeled topographical density using a 2-D laterally varying model. Since in reality topographical density also varies vertically, the 2-D model cannot account for all topographical density effects on geoidal height. We attempt to remedy this problem by modeling topographical density instead using surfaces representing topographical

density interfaces. We calculate the DTE on gravity and PITE on gravity potential for any distribution by using Newton integration over a topographical density distribution defined by one or more interfaces within a spherical cap. In the Newton integration, we use the analytical radially integrated Newton kernel and its radial derivative to determine effects of density between interfaces, where it is piecewise constant. We then apply Stokes' integration to determine the DTE, PITE, and SITE on geoidal height.

In this paper, we present results for the effects of a horizontal disc, for a disc rotated by various degrees along its longitudinal axis, and for the vertical density anomalies of Lake Superior. In all cases, we assume smooth topography and reasonable density contrasts and consider anomalous density relative to a laterally varying density distribution. Total density effects of the disc on geoidal height reach 2.2 cm in magnitude when it is rotated by 5° while those for the lake reach 0.9 cm in magnitude. We observe that the DTE and PITE both have their greatest magnitude for masses near to the topographical surface and add rather than cancel each other for any of our disc simulations. In the case of the lake, the effects are generally opposite but do not significantly cancel each other out, since the PITE is considerably smaller than the DTE.

We also attempt to validate our results by examining the behavior of the DTE on gravity and PITE on gravity potential for the point at the center of a disc at various depths in topography. We found that as we decrease the horizontal integration step, the results in both cases converge but do not converge exactly to a purely analytical result for the effect of the disc at these points. In our simulations, we found that the numerical DTE result is greater in magnitude than the analytical result, with a maximum error of 23.5%. However, the greatest percent errors for this effect occur where the magnitudes

of the effect are smallest; and, in the worst case, we have found the error is only 0.16 mGal in magnitude. Greater DTE errors occur where the mass is concentrated near the topographical surface but in a small volume. The numerical PITE result is consistently of lower magnitude than the analytical result, with maximum percent error of 7.6%. In the case of the PITE, the greatest errors occur for discs near the geoid when mass is great and the discs are small. Thus, for distributions having large effects, we expect the error in our calculation of those effects is considerably smaller than the magnitudes suggested here.

Future efforts will include more thorough treatment of the singularity of the Newton kernel as applied in a 3-D density modeling context and investigation and mitigation of the errors we have detected in our numerical results. However, with our efforts so far, we can suggest that 3-D anomalous topographical density may have centimetre-level contributions to the geoidal height in some situations. Whether those situations are common is yet to be seen.

Chapter 4 Acknowledgements

We are grateful to the reviewers of this manuscript and the Associate Editor J.-C.

Mareschal of *Canadian Journal of Earth Sciences*, whose comments have made the final product much more approachable and complete. This research was funded mainly by a scholarship from the National Sciences and Engineering Research Council (NSERC).

Chapter 4 References

- Bassin, C., G. Laske, and G. Masters (2000). "The Current Limits of Resolution for Surface Wave Tomography in North America." *Eos, Transactions, American Geophysical Union*, Vol. 81, No. 48 (supplement), p. F897.
- Heck, B., and K. Seitz (2007). "A comparison of the tesseroïd, prism and point-mass approaches for mass reductions in gravity field modelling." *Journal of Geodesy*, Vol. 81, No. 2, pp. 121–136, doi: 10.1007/s00190-006-0094-0.
- Heiskanen W., and H. Moritz (1967). *Physical Geodesy*. Freeman, San Francisco, U.S.A.
- Helmert, F. (1884). *Die Physikalischen Theorieen*. Vol. II of *Die Mathematischen und Physikalischen Theorieen der Höheren Geodäsie*, B. G. Teubner, Leipzig, Germany.
- Huang, J., P. Vaníček, S. Pagiatakis, and W. Brink (2001). "Effect of topographical density on the geoid in the Rocky Mountains." *Journal of Geodesy*, Vol. 74, No. 11–12, pp. 805–815, doi: 10.1007/s001900000145.
- Kuhn, M. (2003). "Geoid determination with density hypotheses from isostatic models and geological information." *Journal of Geodesy*, Vol. 77, Nos. 1–2, pp. 50–65, doi: 10.1007/s00190-002-0297-y.
- Martinec, Z. (1993). "Effect of lateral density variations of topographical masses in improving geoid model accuracy over Canada." Contract report for the Geodetic Survey of Canada, Ottawa, Ontario, Canada.
- Martinec, Z. (1998). *Boundary value problems for gravimetric determination of a precise geoid*. Vol. 73 of *Lecture notes in Earth Sciences*, Springer, Berlin.
- Martinec Z., and P. Vaníček (1994a). "Direct topographical effect of Helmert's condensation for a spherical approximation of the geoid." *Manuscripta Geodaetica*, Vol. 19, No. 4, pp. 213–219.
- Martinec Z., and P. Vaníček (1994b). "Indirect effect of topography in the Stokes-Helmert technique for a spherical approximation of the geoid." *Manuscripta Geodaetica*, Vol. 19, No. 5, pp.257–268.
- Martinec, Z., P. Vaníček, A. Mainville, and M. Véronneau (1995). "The effect of lake water on geoidal heights." *Manuscripta Geodaetica*, Vol. 20, No. 3, pp. 193–203.

- Mooney, W., G. Laske, and T. Masters (1998). "CRUST 5.1: A global crustal model at $5^\circ \times 5^\circ$." *Journal of Geophysical Research*, Vol. 103, No. B1, pp. 727–747. doi:10.1029/97JB02122.
- Mooney, W. (2007). "Crust and Lithospheric Structure – Global Crustal Structure." In: *Seismology and Structure of the Earth*, Vol. 1 of *Treatise on Geophysics*, Ed. G. Schubert, Elsevier Science, Amsterdam, pp. 361–417.
- Moritz, H. (1984). "Geodetic reference system 1980." *Bulletin Géodésique*, Vol. 58, No. 3, pp. 388–398 doi: 10.1007/BF02519014.
- Nagy D., G. Papp, and J. Benedek (2000). The gravitational potential and its derivatives for the prism. *Journal of Geodesy*, Vol. 74, Nos. 7–8, pp. 552–560, doi: 10.1007/s001900000116.
- Parasnis, D. (1997). *Principles of Applied Geophysics*. 5th ed., Chapman and Hall, New York, U.S.A.
- Pasyanos, M., W. Walter, M. Flanagan, P. Goldstein, and J. Battacharyya (2004). "Building and testing an a priori geophysical model for Western Eurasia and North Africa." *Pure and Applied Geophysics*, Vol. 161, No. 2, pp. 235–281, doi:10.1007/s00024-003-2438-5.
- Paul, M. (1974). "The gravity effect of a homogeneous polyhedron for three dimensional interpretation." *Pure and Applied Geophysics*, Vol. 112, No. 3, pp. 553–561, doi: 10.1007/BF00877292.
- Pohánka, V. (1998). "Optimum expression for computation of the gravity field of a polyhedral body with linearly increasing density." *Geophysical Prospecting*, Vol. 46, No. 4, pp. 391–404, 10.1046/j.1365-2478.1998.960335.x.
- Salah, M., and D. Zhao (2003). "3-D seismic structure of Kii peninsula in southwest Japan: evidence for slab dehydration in the forearc." *Tectonophysics*, Vol. 364, Nos. 3–4, pp. 191–213, doi:10.1016/S0040-1951(03)00059-3.
- Schwab, D., and D. Sellers (1996). "Computerized bathymetry and shorelines of the Great Lakes." NOAA Data Report ERL GLERL-16, Great Lakes Environmental Research Laboratory, Ann Arbor, Michigan, U.S.A.
- Sjöberg, L., and Nahavandchi, H. (1999). "On the indirect effect in the Stokes–Helmert method of geoid determination." *Journal of Geodesy*, Vol. 73, No. 2, pp. 87–93, doi:10.1007/s001900050222.

- Smithson, S., F. Wenzel, Y. Ganchin, and I. Morozov (2000). "Seismic results at Kola and KTB deep scientific boreholes: velocities, reflections, fluids, and crustal composition." *Tectonophysics*, Vol. 329, Nos. 1–4, pp. 301–317, doi:10.1016/S0040-1951(00)00200-6.
- Soller, D., R. Ray, and R. Brown (1982). "A new global crustal thickness model." *Tectonics*, Vol. 1, No. 2, pp. 125–149, doi:10.1029/TC001i002p00125.
- Stokes, G. (1849). "On the variation of gravity on the surface of the Earth." *Transactions of the Cambridge Philosophical Society*, Vol. 8, pp. 672–695.
- Tiberi, C., M. Diament, J. Déverchère, C. Petit-Mariani, V. Mikhailov, S. Tikhotsky, and U. Achauer (2003). "Deep structure of the Baikal rift zone revealed by joint inversion of gravity and seismology." *Journal of Geophysical Research*, Vol. 108, No. B3, p. 2133, doi:10.1029/2002JB001880.
- Tsoulis, D. (2001). "Terrain correction computations for a densely sampled DEM in the Bavarian Alps." *Journal of Geodesy*, Vol. 75, Nos. 5–6, pp. 291–307, doi:10.1007/s001900100176.
- Tziavos, I., and W. Featherstone (2001). "First results of using digital density data in gravimetric geoid computation in Australia." *Gravity, Geoid and Geodynamics 2000*, Ed. M. Sideris. GGG2000 IAG International Symposium, Banff, Alberta, Canada July 31–August 4, 2000. *International Association of Geodesy Symposia*, Vol. 123, Springer, New York, U.S.A., pp. 335–340.
- Vaniček P., and E. Krakiwsky (1986). *Geodesy: The Concepts*. 2nd rev. ed., North-Holland Press, Elsevier Science Publishers, Amsterdam, The Netherlands.
- Vaniček, P., and A. Kleusberg (1987). "The Canadian geoid-Stokesian approach." *Manuscripta Geodaetica*, Vol. 12, No. 2, pp. 86–98.
- Vaniček, P., and Z. Martinec (1994). "Stokes-Helmert scheme for the evaluation of a precise geoid." *Manuscripta Geodaetica* Vol. 19, No. 2, pp. 119–128.
- Vaniček, P., J. Huang, P. Novák, M. Véronneau, S. Pagiatakis, Z. Martinec, and W. Featherstone (1999). "Determination of boundary values for the Stokes–Helmert problem." *Journal of Geodesy*, Vol. 73, No. 4, pp. 180–192, doi:10.1007/s001900050235.
- Zelt, C., and R. Smith (1992). "Seismic traveltime inversion for 2-D crustal velocity structure." *Geophysical Journal International*, Vol. 108, No. 1, pp. 16–34, doi:10.1111/j.1365-246X.1992.tb00836.x.

Zelt, C. 1999. Modelling strategies and model assessment for wide- angle seismic traveltime data. *Geophysical Journal International*, Vol. 139, No. 1, pp. 183–204, doi:10.1046/j.1365-246X.1999.00934.x.

Chapter 5: Effects of hypothetical complex mass-density distributions on geoidal height

This article was based on a presentation at the International Association of Geodesy (IAG) assembly in Buenos Aires, Argentina in 2009, and was published in the *Proceedings of the 2009 IAG Scientific Assembly* in 2011. I performed the computations and wrote the article. My coauthors provided guidance in revising the manuscript for submission. The full citation for the article is:

Kingdon, R., P. Vaníček, and M. Santos (2011a). "Effects of hypothetical complex mass-density distributions on geoidal height." *Geodesy for Planet Earth*, Eds. S. Kenyon, M. Pacino and U. Marti. International Association of Geodesy IAG2009 "Geodesy for Planet Earth" Scientific Assembly, Buenos Aires, Argentina, 31 August–4 September, 2009. *International Association of Geodesy Symposia*, Vol. 135, Springer, New York. (in press)

Chapter 5 Abstract

Geoid computation according to the Stokes-Helmert scheme requires accurate modelling of the variations of mass-density within topography. Current topographical models used in this scheme consider only horizontal density variations, although in reality density varies three-dimensionally. Insufficient knowledge of regional three-dimensional density distributions prevents evaluation from real data. In light of this deficiency, we attempt to estimate the order of magnitude of the error in geoidal heights caused by neglecting the

depth variations by calculating, for artificial but realistic mass-density distributions, the difference between results from 2D and 3D models.

Our previous work has shown that for simulations involving simple mass-density distributions in the form of planes, discs or wedges, the effect of mass-density variation unaccounted for in 2D models can reach centimetre-level magnitude in areas of high elevation, or where large mass-density contrasts exist. However, real mass-density distributions are more complicated than those we have modeled so far, and involve multiple structures whose effects might mitigate each other. We form a more complex structure by creating an array of discs that individually we expect to have a very significant effect, and show that while the contribution of such an array to the direct topographical effect on geoidal height is sub centimetre (0.85 cm for our simulation), the resulting primary indirect topographical effect may reach several centimetres or more (5 cm for our simulation).

5.1 Introduction

Forward modeling of gravitational effects of three-dimensionally varying density distributions has a long history. Evaluation of the Newton kernel over three-dimensionally varying mass distributions is an important task in geophysics and geodesy. Early attempts decompose crustal masses into prisms, over which the Newton integral is evaluated analytically, to determine either the effect of the masses on gravity [Mollweide, 1813] or gravity potential [Bessel, 1813]. More complex representations of crustal density bodies model crustal masses as polyhedrons [Paul, 1974] or tesseroids

[Seitz and Heck, 2001], and may allow vertical density variation within the bodies (e.g., Pohánka [1998]). In terms of geodesy, recent efforts have relied heavily on forward modeling of crustal mass effects, most prominently in creating synthetic gravity models (e.g., Baran et al. [2006]) useful for testing geoid computation techniques. However, three dimensional crustal density effects have not yet been incorporated in Stokes-Helmert geoid modeling.

The Stokes-Helmert method of geoid modeling requires determination of effects of all topographical masses, i.e. crustal masses above the geoid. These calculations have traditionally used a constant value of topographical density (e.g., Vaniček and Kleusberg [1987]), but numerous investigations have shown that to obtain a precise geoid the effects of density variations within topography must also be calculated (e.g., Martinec [1993]; Pagiatakis et al. [1999]; Huang et al. [2001]). These efforts have almost exclusively focused on horizontal density variations. Since the actual topographical density varies with depth, two dimensional topographical density models (2D DDMs) cannot exactly model the real density distribution. Martinec [1993] suggests a method of dealing with three-dimensionally varying density by averaging density in each topographic column to derive a laterally-varying density distribution, and this approach is applied by Martinec et al. [1995] to find effects of lake waters on the geoid. However, in most situations the information required to construct a 2D DDM using averaged data along columns of topography is not available, and so some other method is used, such as assigning surface density values to a whole column of topographical density [Huang et al., 2001], or applying Monte Carlo methods [Tziavos and Featherstone, 2001].

Investigation into effects of three-dimensionally varying density has been limited, because a three dimensional topographical density model (3D DDM) has not yet been developed with a high enough resolution and over a large enough area to be suitable for geoid modeling [Kuhn, 2003]. This is because the 3D density structure of the topography is known to a high resolution only over small areas (for local geophysical studies or prospecting), or to very coarse resolutions over large areas (e.g., the CRUST 2.0 model developed by Bassin et al. [2000]). A more complete discussion on the difficulties of creating a 3D density model for geodetic purposes is given in Kingdon et al. [2009].

Despite the lack of suitable 3D DDMs for geoid modeling, we can still guess some things about the shortcomings of 2D DDMs. Kingdon et al. [2009] recently showed that in the presence of a single body of topographical density not accounted for in the 2D DDM, using only a 2D DDM might introduce errors of up to several centimetres in areas of high topography. In reality, topography does not contain only a single body of anomalous density, but is a complex arrangement of bodies of varying densities. Thus, effects of a single body might be mitigated by the effects of the bodies around it.

In this effort, we try to discover whether in extreme cases adjacent density bodies mitigate each other's effects on the geoid. If effects of adjacent masses cancel each other even in a hypothetical situation created so that they are unlikely to do so, it is unlikely that the less extreme situations existing in reality will be of any concern. However, if the effects of the adjacent masses remain significant then more work is necessary to define situations where 3D DDMs are needed. Once we know what constitutes a distribution

where 3D DDMs are needed, will we be ready to choose some real data sets where these situations exist, for further testing.

Our investigation is done within the framework of the Stokes-Helmert scheme of geoid modeling, following the methodology discussed in section 5.2. Section 5.3 will show and discuss our results using this methodology, and finally we will present the conclusions derived from our results and make recommendations for future work in section 5.4.

5.2 Methodology

5.2.1 3D density modeling in the Stokes-Helmert context

Stokes-Helmert geoid computation requires a model of topographical density both for calculating the transformation of gravity anomalies to the Helmert space (called the Direct Topographical Effect or DTE), and for calculating the transformation of the Helmert co-geoid back to the real space (the Primary Indirect Topographical Effect or PITE) after the Stokes integration [Martinec et al., 1994a, 1994b]. Existing models normally consider topography of constant density, ρ_0 (usually 2670 kg m^{-3}), and may additionally include lateral variations of density, $\overline{\delta\rho}$ with respect to ρ_0 . For our modeling, we will consider the variation of topographical density from the laterally varying values, in a three dimensional sense. We label this anomalous topographical density $\delta\rho$. It can be considered as a residual density term, such that:

$$\rho(r, \Omega) = \rho_0 + \overline{\delta\rho}(\Omega) + \delta\rho(r, \Omega), \quad (5.1)$$

where r is the geocentric radius of a point where density is being represented, and Ω is a geocentric direction, representing the point's geocentric latitude and longitude

Each of the transformations required in the Stokes-Helmert method comprise an evaluation of the difference between the effect of real and of condensed anomalous topographical density at the location of each gravity anomaly. Here, we follow the approach outlined in Kingdon et al. (2009), which is a generalization of the approach given by Martinec (1998), and uses Helmert's second condensation method (Martinec and Vaniček 1994a,b). The DTE on gravity is calculated by the integral formula:

$$\begin{aligned} \varepsilon_{DTE}^{\delta\rho}(r, \Omega) = & \iint_{\Omega' \in \Omega_0} \frac{\partial}{\partial r} \left[\int_{r'=r_g(\Omega')}^{r_t(\Omega')} \delta\rho(r', \Omega') K(r, \Omega; r', \Omega') r'^2 dr' - \right. \\ & \left. - \delta\sigma(\Omega') K(r, \Omega; r_g[\Omega'], \Omega') r_g^2(\Omega') \right] d\Omega', \end{aligned} \quad (5.2)$$

where $\varepsilon_{DTE}^{\delta\rho}$ is the DTE on gravity at a point, and $\delta\rho$ is the anomalous density given by a 3D DDM for the integration point at coordinates r', Ω' . $r_t(\Omega')$ and $r_g(\Omega')$ are the surface of the topography and the geoid, respectively. The function $K(r, \Omega; r', \Omega')$ is the Newton kernel, equal to the inverse distance between the computation and integration points.

The PITE on gravitational potential, $\varepsilon_{PITE}^{\delta\rho}(r_g(\Omega), \Omega)$, is calculated by the formula:

$$\varepsilon_{PITE}^{\delta\rho}(r_g[\Omega], \Omega) = \iint_{\Omega' \in \Omega_0} \left[\int_{r'=r_g(\Omega')}^{r_i(\Omega')} \delta\rho(r', \Omega') K(r_g[\Omega], \Omega; r', \Omega') r'^2 dr' - \delta\sigma(\Omega') K(r_g[\Omega], \Omega; r_g[\Omega'], \Omega') r_g^2(\Omega') \right] d\Omega' . \quad (5.3)$$

Notice that the DTE for a particular computation point is evaluated at the topographical surface, since it is applied to gravity anomalies at the topographical surface. The PITE is evaluated for a point on the geoid surface, which we approximate for the evaluation of the Newton kernels as a sphere of radius $R = 6\,371$ km, the mean radius of the Earth. The condensation density referred to in these formulas is calculated for a 3D DDM according to:

$$\delta\sigma(\Omega) = \frac{1}{R^2} \int_{r'=r_g(\Omega)}^{r_i(\Omega)} r'^2 \delta\rho(r', \Omega) dr' . \quad (5.4)$$

For our investigation, we convert the effects in eqs. (5.2) and (5.3) into effects on geoidal heights. In the case of the DTE, the effect can be computed by applying Stokes integration to the DTE on gravity:

$$\delta N_{DTE}^{\delta\rho}(\Omega) \doteq \frac{1}{4\pi\gamma(\Omega)} \iint_{\Omega' \in \Omega_0} S(\psi[\Omega, \Omega']) \varepsilon_{DTE}^{\delta\rho}(\Omega') d\Omega', \quad (5.5)$$

where $\delta N_{DTE}^{\delta\rho}(\Omega)$ is the DTE on geoidal height, $\gamma(\Omega)$ is the normal gravity on the surface of the reference ellipsoid, and $S(\psi[\Omega, \Omega'])$ is the Stokes kernel.

In the case of the PITE, the effect on geoidal height is found by applying Bruns's formula:

$$\delta N_{PITE}^{\delta\rho}(\Omega) = \frac{\varepsilon_{PITE}^{\delta\rho}(\Omega)}{\gamma(\Omega)}. \quad (5.6)$$

These effects on geoidal height allow us to compare the effects of masses to some meaningful tolerance to determine whether they are significant. In this case, where we are looking for a 1 cm geoid, we will consider any effect over 0.5 cm significant.

5.2.2 Numerical considerations

The Newton kernel and its integrals and derivatives in eqs. (5.2) and (5.3) can be computed numerically in various ways. For our computation, we use the prismoidal method as summarized by Nagy et al. [2000, 2002] for integration near to the computation point, and 2D numerical integration [Martinec, 1998] farther from the computation point.

Applying the prismoidal method to a 3D DDM, the anomalous topographical masses are divided into blocks, and the integral of the Newton kernel in planar coordinates is evaluated over each block analytically. The same procedure was applied in a slightly different context by Kuhn [2003]. This formulation captures very well the behavior of the Newton kernel near to the computation point, and in that region is superior to 2D numerical integration [Heck and Seitz 2007], even though the 2D integration normally uses the more accurate spherical expression of the Newton kernel. The accuracy improvement from evaluating the kernel analytically near to the computation points outweighs the accuracy benefit of using a spherical formulation [Nagy, 2000]. The prismoidal formula is inherently faster than other analytical methods such as the polyhedral method, and is also faster than the tesseroïdal method near to the computation point. The tesseroïdal method is very fast when only the zero-order and second-order terms of its Taylor series representation are used, but these do not provide sufficient accuracy near to the computation point [Heck and Seitz 2007].

Comparison of the planar Newton kernels used in the prismoidal approach and the spherical Newton kernels shows that the kernels used to evaluate the DTE are more than 1 % different beyond 5 arc-minutes from the computation point, and that those used to

evaluate the PITE are more than 1 % different beyond 15 ° from the computation point. Fortunately, even for integration points within these ranges of the computation point, the 2D numerical integration provides identical results to the slower prismatic approach, and so these differences are moot.

The 2D integration employs the radial integrals of the Newton kernel developed by Martinec [1998] to perform the radial integration of the Newton kernel over the vertical anomalous density variations in a given topographical column, discretized as segments of the column, thus evaluating the radial component of the 3D integral analytically. The horizontal integration is performed by summing the radial integral over each particular column, and then summing the products of the values of the integrands of eqs. (5.2) and (5.3) at the cell centers with the cell areas. The 2D horizontal integration is suitable beyond about 5 arc-minutes of the computation point for the DTE, and beyond 1 ° of the computation point for the PITE. For our evaluations of the PITE, we use the prismatic formula within 5 ° of the computation point, to take greater advantage of its superior accuracy near the computation point. For the DTE, we use the prismatic formula only within 5 arc-minutes of the computation point. Beyond these limits, 2D integration is used.

With both of the methods we have chosen above, a discretization error is present since the actual mass distribution of the topography is represented as a series of rectangular prisms of varying height. Such discretization errors will be present unless the topographical density model exactly reflects the topographical density distribution, and are difficult to quantify since their behavior changes for different mass distributions. For example, discs of different size will have different discretization errors. We can decrease

the error by using a smaller cell or prism size in our integration procedures. By testing we have found that for the discs used here a resolution of 1 x 1 arc-second is sufficient. Using a higher resolution than 1 x 1 arc-second did not significantly change the results (<0.01 mGal), while going from 1 x 1 arc-second to 3 x 3 arc-second step affected the results by up to 0.21 mGal.

To validate our computational procedures in this investigation, we have tested our numerical integration for the case of a single disc of anomalous density, against results from analytical formulas for the DTE on gravity and PITE on gravity potential at the center of the disc, similar to the approach of Heck and Seitz [2007]. This is the point where the PITE caused by the disc is greatest, and a point where the DTE is very large. In the test, we find errors of up to 18 % in the numerical integration for the DTE and 5 % for the PITE in extreme cases, but normally less than 5 % for the DTE and 1 % for the PITE. The larger errors occur when the disc is very small, and consequently do not indicate a large magnitude of overall error. In terms of magnitude, the largest errors in the DTE are only 0.4 mGal, and in PITE on geoidal height only 0.5 mm. Errors in DTE and PITE were usually less than 0.15 mGal and 0.3 mm in magnitude respectively. We consider such errors admissible for determining the order of magnitude of differences between results from 3D DDMs and 2D DDMs.

5.2.3 Proposed tests

Our question is: can the effect on geoidal height of an anomalous density body, unaccounted for by a 2D DDM, be mitigated by the presence of adjacent bodies of different anomalous density? To investigate this, we take two extreme cases, each

involving an array of anomalous masses. In case A, we choose masses that individually are known to have a particularly large DTE, and investigate the effect of the conglomerate of these masses on geoidal height. In case B, we choose masses known to have a large PITE. In each case, we integrate three dimensionally over the masses considered unaccounted for in a 2D DDM, so that the results of the integration will give us the deficiency of the 2D DDM. If the effects mitigate each other significantly, it is an indicator that we can expect the same in any less extreme case.

In both cases A and B, we use an array of vertical cylinders as our density model. The upper part of the cylinders are assigned alternating density contrasts of positive or negative 600 kg m^{-3} , considered anomalous relative to a laterally-varying density model. The anomalous density outside the cylinders is zero; i.e., the 2D DDM is considered accurate outside of the cylinders.

Our past work on individual mass bodies has shown that the DTE and PITE are greatest when:

1. the topography involved is thick,
2. anomalous density is distributed away from the geoid, and
3. there is a large density contrast.

Regarding the horizontal size of the bodies, for the PITE the larger the body the greater its effect will be, although the rate at which the effect increases becomes very low for bodies beyond about 110 000 m wide. Therefore, we use a width of 110 000 m for the discs in case B. Of course, the largest PITE would be for a spherical shell, but such a model would not allow us to test whether adjacent masses mitigate each other, and so we have instead used a disc that induces much of the effect that a spherical shell of the same

thickness would, but whose effect still might be mitigated by adjacent discs of opposite anomalous density.

For the DTE, by contrast, there is a range of disc widths of about 3300 m where the effect is greatest. This is because the DTE is the difference between the effect of a real anomalous mass on gravity at a computation point, and the effect of the anomalous mass condensed onto the geoid. At about 3300 m from the computation point, for the case of a disc as tested here, these effects become similar, and thereafter the condensed density of a given mass has a greater effect on gravity at the computation point than its real density, so that the overall DTE becomes smaller. Thus, we use 3300 m as the disc diameter for case A.

In order to accommodate items 1 and 2 in the list above, we choose flat topography 2000 m thick, and use discs extending from the surface of the topography to 500 m depth. These can be thought of as anomalous masses relative to a 2D DDM that accurately portrays the density below the masses. An illustration of our model, including possible cylinder densities that might result in the $\pm 600 \text{ kg m}^{-3}$ anomalous densities used in our experiment, is given in Figure 5.1.

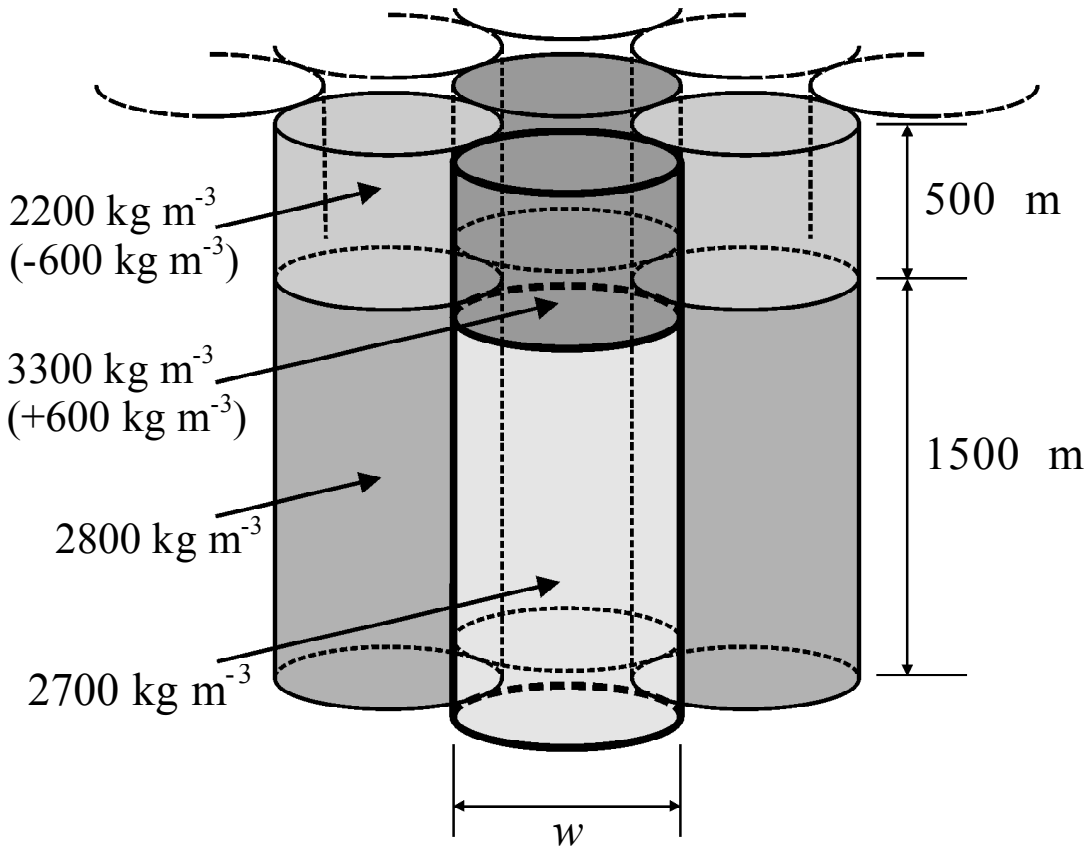


Figure 5.1: Topographical density distribution used for testing. $w = 3300 \text{ m}$ for DTE tests, and $w = 110\,000 \text{ m}$ for PITE tests.

We calculate results over a 1° by 1° area for our case A simulation, and a 2° by 2° area for our case B simulation, both described in section 5.3 below. We use a radius of 2° for Stokes integration, and so our array of cylinders in case A extended over a 5° by 5° area to capture most of their effect.

5.3 Results

5.3.1 Case A

The DTE on gravity for case A, as described in section 5.2.3, is given in Figure 5.2.

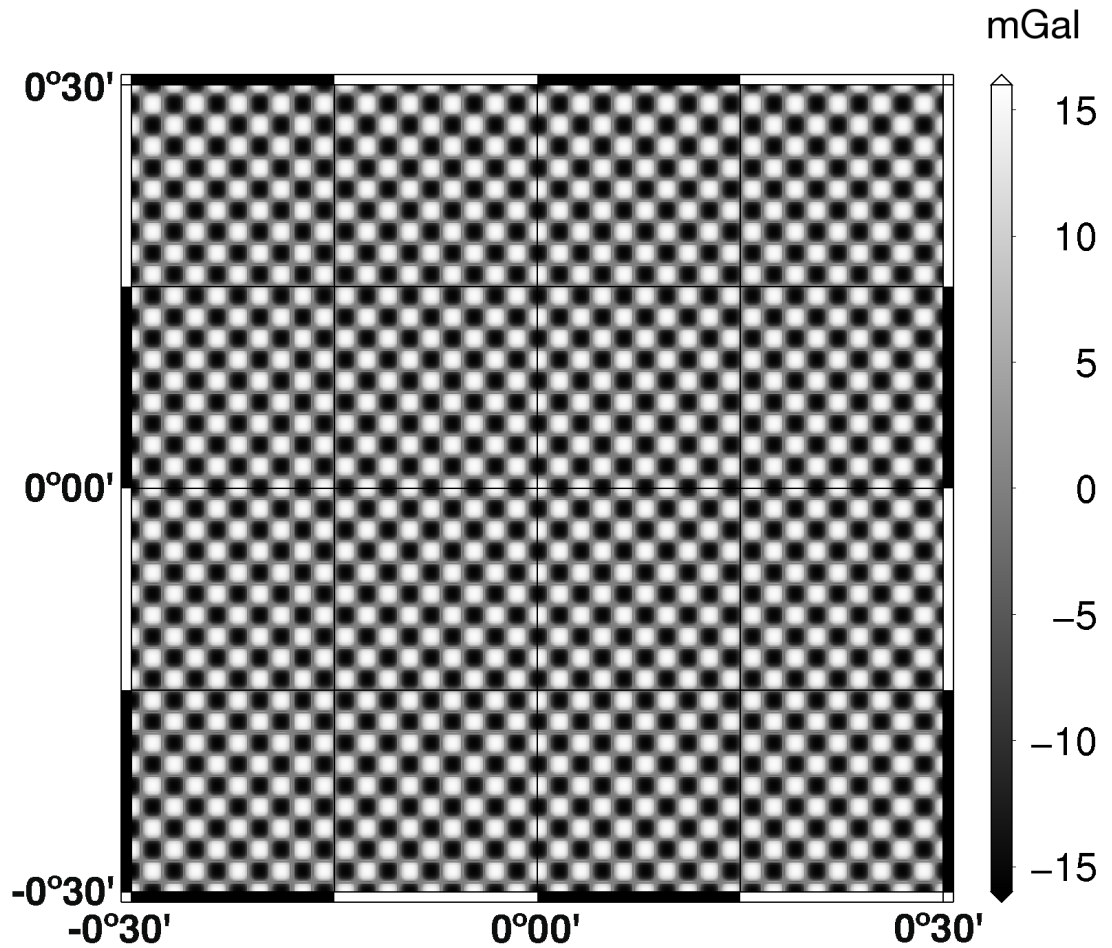


Figure 5.2: DTE on gravity for case A.

The adjacent density anomalies do not significantly mitigate each other's effects on the DTE, which reaches ± 16 mGal. This is not surprising, since the derivative of the Newton kernel, used to calculate these effects, decreases very rapidly with distance from

the source masses. However, we are ultimately interested in the DTE on geoidal height, resulting from the Stokes integration (given by eq. (5.5)) over the DTEs on gravity, and shown in Figure 5.3.

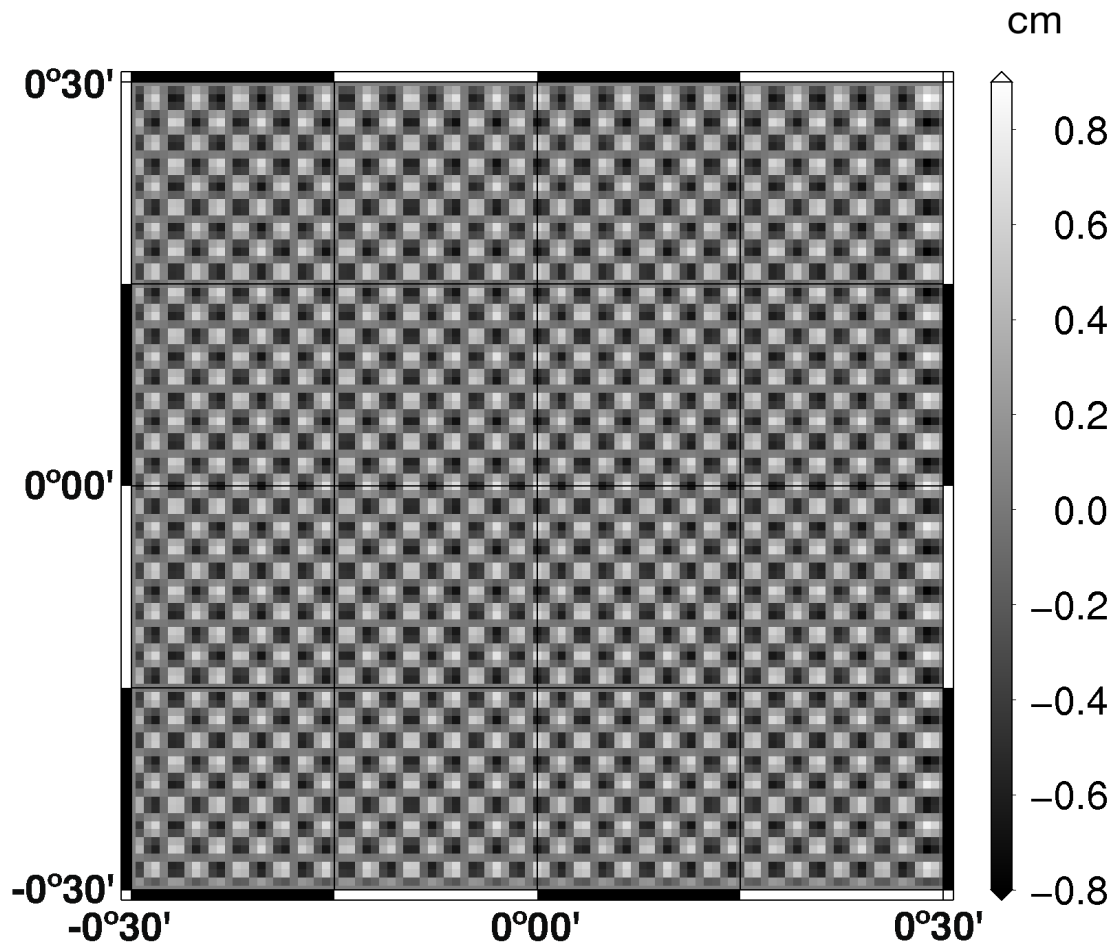


Figure 5.3: DTE on geoidal height for case A.

Under the smoothing influence of the Stokes kernel, the adjacent masses attenuate each other's contributions to the DTE on the geoidal height, which reaches about ± 0.85 cm. This may not be the case for density anomalies with greater horizontal extent, since in such cases the Stokes integral would do less to mitigate the effects of the

anomaly on gravity at its center, where the effect is largest. It thus remains to find the maximum effect that masses can have in a simulation like our own.

5.3.2 Case B

The PITE on gravity for case B, as described in section 5.2.3, is given in Figure 5.4.

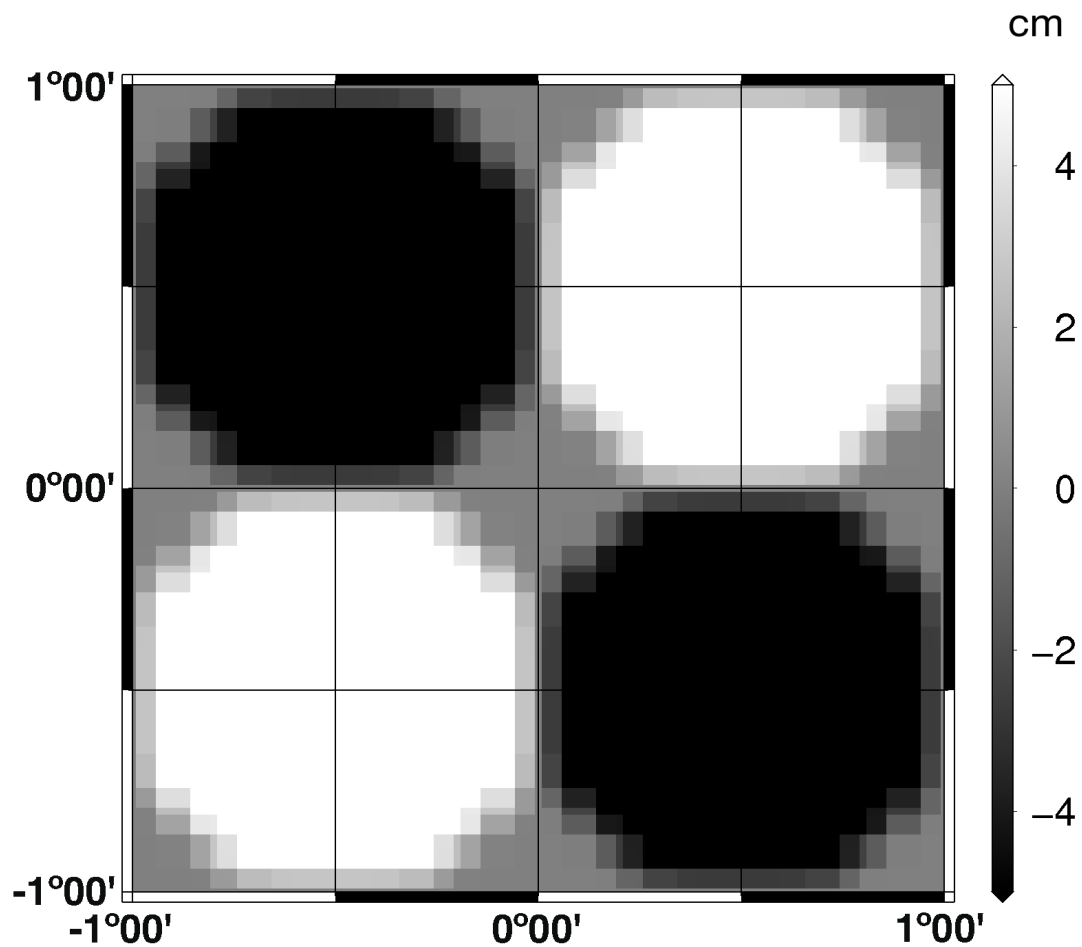


Figure 5.4: PITE on geoidal height for case B.

We see that for such large cylinders, the effect of adjacent cylinders of opposite anomalous density is minimal. Here the effects reach ± 5 cm, but for larger discs the

magnitude would be somewhat greater and the attenuation even less significant, since it is hardly significant even for the discs tested here. It is thus likely that the PITE will only increase for wider cylinders.

5.4 Conclusions

The DTE on gravity and the PITE on geoidal height for the anomalous masses (not modeled in 2D DDM) in our simulations are not significantly diminished by the presence of adjacent anomalous masses, even when there is an extreme density contrast. The PITE still reaches about 5 cm, and the DTE reaches about 16 mGal. This demonstrates that the error in the PITE resulting from only using a 2D DDM may be large even in the presence of adjacent mass anomalies.

The DTE on geoidal height resulting from using a 2D DDM is significantly diminished by the presence of adjacent masses, though it still approaches the 1 cm level. However, this is entirely a result of Stokes integration, which was not considered in the development of our extreme case scenarios. With this in mind, larger bodies of anomalous density that still have a significant impact on the DTE on gravity may produce significantly larger effects on geoidal heights.

Chapter 5 References

- Baran, I., M. Kuhn, S. Claessens, W. Featherstone, S. Holmes, and P. Vaníček (2006). "A synthetic Earth gravity model designed specifically for testing regional gravimetric geoid determination algorithms." *Journal of Geodesy*, Vol. 80, No. 1, pp. 1–16, doi: 0.1007/s00190-005-0002-z.
- Bassin, C., G. Laske, and G. Masters (2000). "The Current Limits of Resolution for Surface Wave Tomography in North America." *Eos, Transactions, American Geophysical Union*, Vol. 81, No. 48 (supplement), p. F897.
- Bessel, F. (1813). "Auszug aus einem Schreiben des Herrn Prof. Bessel." *Zach's Monatliche Correspondenz zur Beförderung der Erd – und Himmelskunde*, Vol. 27, pp. 80–85.
- Heck, B., and K. Seitz (2007). "A comparison of the tesseroid, prism and point-mass approaches for mass reductions in gravity field modelling." *Journal of Geodesy*, Vol. 81, No. 2, pp. 121–136, doi: 10.1007/s00190-006-0094-0.
- Huang, J., P. Vaníček, S. Pagiatakis, and W. Brink (2001). "Effect of topographical density on the geoid in the Rocky Mountains." *Journal of Geodesy*, Vol. 74, No. 11–12, pp. 805–815, doi: 10.1007/s001900000145.
- Kingdon, R., A. Ellmann, P. Vaníček and M. Santos (2006). "The cost of assuming a lateral density distribution in corrections to Helmert orthometric heights." Paper presented at the American Geophysical Union 2006 Joint Assembly, Baltimore, Maryland, U.S.A., May 23–26.
- Kuhn, M. (2003). "Geoid determination with density hypotheses from isostatic models and geological information." *Journal of Geodesy*, Vol. 77, Nos. 1–2, pp. 50–65, doi: 10.1007/s00190-002-0297-y.
- Martinec, Z. (1993). "Effect of lateral density variations of topographical masses in improving geoid model accuracy over Canada." Contract report for the Geodetic Survey of Canada, Ottawa, Ontario, Canada.
- Martinec Z., and P. Vaníček (1994a). "Direct topographical effect of Helmert's condensation for a spherical approximation of the geoid." *Manuscripta Geodaetica*, Vol. 19, No. 4, pp. 213–219.
- Martinec Z., and P. Vaníček (1994b). "Indirect effect of topography in the Stokes-Helmert technique for a spherical approximation of the geoid." *Manuscripta Geodaetica*, Vol. 19, No. 5, pp.257–268.

- Martinec, Z., P. Vaníček, A. Mainville, and M. Véronneau (1995). "The effect of lake water on geoidal heights." *Manuscripta Geodaetica*, Vol. 20, No. 3, pp. 193–203.
- Martinec, Z. (1998). *Boundary value problems for gravimetric determination of a precise geoid*. Vol. 73 of *Lecture notes in Earth Sciences*, Springer, Berlin.
- Mollweide, K. (1813). "Auflösung einiger die Anziehung von Linien Flächen und Köpern betreffenden Aufgaben unter denen auch die in der Monatliche Correspondenz Band 24, Seite 522, vorgelegte sich findet." *Zach's Monatliche Correspondenz zur Beförderung der Erd – und Himmelskunde*, Vol.27, pp. 26–38.
- Nagy D., G. Papp, and J. Benedek (2000). The gravitational potential and its derivatives for the prism. *Journal of Geodesy*, Vol. 74, Nos. 7–8, pp. 552–560, doi: 10.1007/s001900000116.
- Nagy D., G. Papp, and J. Benedek (2002). "Corrections to 'The gravitational potential and its derivatives for the prism.'" *Journal of Geodesy*, Vol. 76, No. 8, p. 475, doi: 10.1007/s00190-002-0264-7.
- Pagiatakis, S., D. Fraser, K. McEwen, A. Goodacre, and M. Véronneau (1999). "Topographic mass density and gravimetric geoid modelling." *Bollettino di Geofisica Teorica e Applicata*, Vol. 40, Nos. 3–4, pp. 189–194.
- Paul, M. (1974). "The gravity effect of a homogeneous polyhedron for three dimensional interpretation." *Pure and Applied Geophysics*, Vol. 112, No. 3, pp. 553–561, doi: 10.1007/BF00877292.
- Pohánka, V. (1998). "Optimum expression for computation of the gravity field of a polyhedral body with linearly increasing density." *Geophysical Prospecting*, Vol. 46, No. 4, pp. 391–404, 10.1046/j.1365-2478.1998.960335.x.
- Seitz, K. and B. Heck (2001). "Tesseroids for the calculation of topographic reductions." Paper presented at the International Association of Geodesy 2001 Scientific Assembly, Budapest, Hungary, 2–7 September.
- Tzaivos, I. N. and W. E. Featherstone (2001). "First results of using digital density data in gravimetric geoid computation in Australia." *Gravity, Geoid and Geodynamics 2000*, Ed. M. Sideris. GGG2000 IAG International Symposium, Banff, Alberta, Canada July 31–August 4, 2000. *International Association of Geodesy Symposia*, Vol. 123, Springer, New York, U.S.A., pp. 335–340.
- Vaníček, P., and A. Kleusberg (1987). "The Canadian geoid-Stokesian approach." *Manuscripta Geodaetica*, Vol. 12, No. 2, pp. 86–98.

Chapter 6: Poisson downward continuation solution by the Jacobi method

This article was published in the first issue of the *Journal of Geodetic Science*, an open access journal created by Lars Sjöberg of the Royal Institute of Technology in Sweden. I developed the central concept of the journal, with advice from my coauthors, performed the computations and wrote the article. My coauthors provided further guidance in revising the manuscript for submission. The full citation for the article is:

Kingdon, R., and P. Vaníček (2011b). “Poisson downward continuation solution by the Jacobi method.” *Journal of Geodetic Science*, Vol. 1, No. 1, pp. 74–81, doi: 10.2478/v10156-010-0009-0.

Chapter 6 Abstract

Downward continuation is a continuing problem in geodesy and geophysics. Inversion of the discrete form of the Poisson integration process provides a numerical solution to the problem, but because the **B** matrix that defines the discrete Poisson integration is not always well conditioned the solution may be noisy in situations where the discretization step is small and in areas containing large heights. We provide two remedies, both in the context of the Jacobi iterative solution to the Poisson downward continuation problem. First, we suggest testing according to the upward continued result from each solution,

rather than testing between successive solutions on the geoid, so that choice of a tolerance for the convergence of the iterative method is more meaningful and intuitive. Second, we show how a tolerance that reflects the conditioning of the \mathbf{B} matrix can regularize the solution, and suggest an approximate way of choosing such a tolerance. Using these methods, we are able to calculate a solution that appears regular in an area of Papua New Guinea having heights over 3200 m, over a grid with 1 arc-minute spacing, based on a very poorly conditioned \mathbf{B} matrix.

6.1 Introduction

A continuous plague in geodesy and geophysics is the problem of downward continuation of gravity. That is, the determination of the values of the field below the surface of the Earth from observations of gravity field on one surface. While various methods may be used for this process, we will discuss only the theoretically exact solution by the inversion of Poisson integration.

Downward continuation can be considered the inverse operation of Poisson integration, which itself is a solution to the first boundary problem of potential theory: given values of a potential field on a sphere, that is harmonic outside the sphere, Poisson integration provides values of the field anywhere outside the sphere [MacMillan, 1930]. In our case, the field will be the anomalous gravity field in the Helmert space, as described by Vaníček et al. [1996], multiplied by the geocentric radius. Considering the geoid as a spherical surface allows us to apply Poisson integration, valid for computation

points external to the geoid, according to the formula [Heiskanen and Moritz, 1967]:

$$\Delta g^h(r, \varphi, \lambda) = \frac{R^2(r^2 - R^2)}{4\pi r} \int_{\varphi'=-\pi/2}^{\pi/2} \int_{\lambda'=0}^{2\pi} \frac{\Delta g^h(R, \varphi', \lambda')}{\ell^3(r, \varphi, \lambda; R, \varphi', \lambda')} \cos \varphi' d\varphi' d\lambda', \quad (6.1)$$

where $\Delta g^h(r, \varphi, \lambda)$ is the Helmert gravity anomaly at a point with geocentric spherical latitude φ , longitude λ and radius r . The symbol R stands for the mean radius of the Earth, used here to approximate the radius of the geoid in the geocentric spherical coordinate system where the calculation is performed. We assume the value to be $R=6371008.7714$ m, i.e., equal to the mean radius of the GRS-80 ellipsoid (Moritz, 1980). $\Delta g^h(R, \varphi, \lambda)$ is the Helmert gravity anomaly at an integration point on the geoid with geocentric spherical latitude φ and longitude λ . Finally, $\ell(r, \varphi, \lambda; R, \varphi', \lambda')$ is the distance between the computation and integration points, also calculated in a geocentric spherical coordinate system.

The integral in eq. (6.1) is a Fredholm integral of the 1st kind [Fredholm, 1900]. It can be evaluated numerically in a discrete form for a set of N points, each point P_i having coordinates $(r_i, \varphi_i, \lambda_i)$, by:

$$\begin{aligned} \forall i \in 1, 2, \dots, N : \Delta g_i^h(r_i, \varphi_i, \lambda_i) = \\ = \frac{R^2(r_i^2 - R^2)}{4\pi r_i} \sum_{j=1}^M \frac{\Delta g_j^h(R, \varphi_j, \lambda_j)}{\ell^3(r_i, \varphi_i, \lambda_i; R, \varphi_j, \lambda_j)} \cos \varphi_j \Delta \varphi \Delta \lambda, \end{aligned} \quad (6.2)$$

where M is the number of points used for discrete representation of the gravity anomalies on the geoid, $\Delta g_j^h(R, \varphi_j, \lambda_j)$ is the gravity anomaly for the point P_j on the geoid having latitude φ_j and longitude λ_j , $\Delta\varphi$ is the step size in the latitudinal direction and $\Delta\lambda$ is the step size in the longitudinal direction. In matrix-vector notation, eq. (6.2) can be written as [Vaníček et al., 1996]:

$$\Delta \mathbf{g}^t = \mathbf{B} \Delta \mathbf{g}^g, \quad (6.3)$$

where $\Delta \mathbf{g}^t$ is a vector of gravity anomalies of length N , containing all point anomalies Δg_i^h on the terrain; $\Delta \mathbf{g}^g$ is a vector of gravity anomalies of length M , containing all point anomalies Δg_j^h on the geoid, and the N by M matrix \mathbf{B} is composed of elements b_{ij} given by (cf., Vaníček et al. [1996]):

$$b_{ij} = \frac{R^2(r_i^2 - R^2)}{4\pi r_i} \frac{1}{\ell^3(r_i, \varphi_i, \lambda_i; R, \varphi_j, \lambda_j)} \cos \varphi_j \Delta\varphi \Delta\lambda. \quad (6.4)$$

Usually, $N = M$, and the horizontal coordinates of the locations of the $\Delta \mathbf{g}^g$ vector correspond to the locations of the $\Delta \mathbf{g}^t$ vector. This results in a square \mathbf{B} matrix with the maximum value in each row and column being along the main diagonal, an arrangement which will be assumed in the following developments.

Note that the discretization given by eq. (6.2), which relates point values on the geoid to point values on the Earth surface, is not the only possible way to discretize the Poisson integration. In addition to the "point-point" approach given by eq. (6.2), there are the "point-mean", "mean-mean", and "mean-point" discretizations, according to what representation of the field is used on each surface where it is considered – the meaning of these descriptors should be self-evident. These alternative approaches result in different formulations of the elements of the **B** matrix and a different interpretation of the elements of $\Delta\mathbf{g}^t$ and $\Delta\mathbf{g}^g$. Eq. (6.3) and the developments presented here are valid for any of the four formulations, and for the calculations in this paper a point-mean scheme will be used, where the output is mean Helmert gravity anomalies, averaged over each cell on the geoid, and the elements of the B matrix are given by (cf., Vaníček et al. [1996]):

$$b_{ij} = \frac{R^2(r_i^2 - R^2)}{4\pi r_i} \frac{1}{n} \sum_{k=1}^n \frac{1}{\ell^3(r_i, \varphi_i, \lambda_i; R, \varphi_{j,k}, \lambda_{j,k})} \cos \varphi_{j,k} \Delta\varphi \Delta\lambda, \quad (6.5)$$

which represents an average of n kernel values calculated at each point P_k with coordinates $\varphi_{j,k}, \lambda_{j,k}$. The averaging points are usually given on a regular grid within each cell, and the cell dimensions are equal to $\Delta\varphi$ and $\Delta\lambda$. The other 3 formulations for the **B** matrix are discussed in [Vaníček and Santos, 2012].

While eq. (6.3) allows us to calculate $\Delta \mathbf{g}^f$ given $\Delta \mathbf{g}^g$, we really want to perform the inverse operation. We want gravity anomalies on the geoid based on values at the Earth's surface, i.e., we want to use the following equation:

$$\Delta \mathbf{g}^g = \mathbf{B}^{-1} \Delta \mathbf{g}^f. \quad (6.6)$$

Fredholm's integral equations of first kind, such as eq. (6.1), are inherently unstable. Even though the problem of downward continuation is "well posed" in the Hadamard sense [Wong, 2002], the system of linear equations formed as a numerical equivalent to the Fredholm integral may be ill-conditioned (see, e.g., Martinec, 1996). Under some circumstances, the system may be almost singular, meaning that the inverse \mathbf{B}^{-1} may be very difficult to obtain, a situation that some people solve by adopting one regularization scheme or another (e.g., Schwartz [1978]; Goli et al. [2010]). Under these circumstances, no exact iterative solution can be found but a non-iterative solution can. The LU decomposition is the most efficient non-iterative numerical method for calculating $\mathbf{B}^{-1} \Delta \mathbf{g}^f$ exactly, since it does not require a complete inversion of the \mathbf{B} matrix [Press et al., 2002]. However, it is still very time consuming because it goes through the decomposition of a potentially very large \mathbf{B} matrix. For a typical example, using gravity anomalies given at 5 arc-minute spacing over a 2° by 2° region requires an \mathbf{B} matrix with 576 rows and 576 columns (one for each integration/computation point).

6.2 The theory

An approximate iterative solution seems to be the direction to choose. The most intuitively attractive iterative approach is the Jacobi iterative method (e.g., Young [1971]), which may be formulated as [Vaníček et al., 1996]:

$$\Delta \mathbf{g}^{g(k)} = \Delta \mathbf{g}^f + (\mathbf{I} - \mathbf{B}) \Delta \mathbf{g}^{g(k-1)}, \quad (6.7)$$

where $\Delta \mathbf{g}^{g(k)}$ is the k -th iteration of $\Delta \mathbf{g}^g$, $\Delta \mathbf{g}^{g(k-1)}$ is the previous, $(k-1)$ -st iteration, and the usual initial estimate of $\Delta \mathbf{g}^g$ is $\Delta \mathbf{g}^{g(0)} = \Delta \mathbf{g}^f$. Our formulation here is slightly different from the standard formulation by Jacobi which uses the diagonal elements of the \mathbf{B} matrix instead of \mathbf{I} and therefore has a slightly faster rate of convergence [Press, 2002]. We have chosen the above form (eq. (6.7)) since it is conducive to testing the convergence of the solution using the methods we prescribe.

The ill-conditioning of \mathbf{B} increases with the maximum height of the evaluation points in the area of interest, and with decreasing the step size of the grid of integration points on the geoid. An upper bound, κ_{max} , of the condition number of the \mathbf{B} matrix is given, according to Martinec [1996], by:

$$\kappa_{max} = \left(\frac{r_{max}}{R} \right)^{\pi/\Delta\Omega} = \left(1 + \frac{H_{max}}{R} \right)^{\pi/\Delta\Omega} \approx 1 + \frac{\pi}{\Delta\Omega} \frac{H_{max}}{R}, \quad (6.8)$$

where H_{max} is the maximum value of height for $i = 1, 2, \dots, N$, and $\Delta\Omega$ is the step size of the grid of input gravity anomalies, considered equal in both the latitudinal and longitudinal directions. Thus, for the area with heights over 3200 m in Papua-New Guinea (used for our computations here) and input Helmert anomalies on the topography spaced 1 arc-minute apart, the upper bound on the condition number is over 227. The practical result of such a high condition number is that the numerical precision of the solution is worse than that of the input. Note also that the condition number may be higher than that predicted by eq. (6.8), which relies on a definition of the condition number that uses the eigenvalues of the \mathbf{B} matrix rather than its singular values. The definition that uses eigenvalues is only valid when the \mathbf{B} matrix is a normal matrix, which is rarely the case.

As an approximate rule, the loss of precision is equivalent to the base 10 logarithm of the condition number (e.g., Cheney and Kincaid [2008]), so that for a condition number of 1 there is no loss of precision, while for a condition number of 227 the loss of precision is up to 2 or 3 digits. So for gravity anomalies on the topography known with a precision of 0.01 mGal, the output gravity anomalies on the geoid may have a precision as low as 10 mGal, and any attempt to increase the precision of the output, for example by further iterations in the Jacobi method, will only add spurious noise to the result. Thus, it is reasonable to terminate the iterative process as soon as the best attainable result is reached.

A traditional approach to test whether an iterative solution has converged is to test the difference between the solutions from two successive iterations (e.g., Young [1971]). So, indicating the k -th difference being tested by the vector $\delta^{g(k)}$, we would have:

$$\delta^{g(k)} = \Delta \mathbf{g}^{g(k)} - \Delta \mathbf{g}^{g(k-1)}. \quad (6.9)$$

Since the process generating $\Delta \mathbf{g}^{g(k)}$ is convergent in the L_I norm [Vaníček et al., 1996], we know that the accuracy improvement from any subsequent iterations will be less than $\delta^{g(k)}$, and the process can be considered to have converged in L_I when $\|\delta^{g(k)}\|_{L_I}$ is smaller than some prescribed tolerance. If the L_I norm is used, a statement like “the errors will not exceed 0.1 mGal” can be substantiated. If the maximum value in $\delta^{g(k)}$ has a magnitude less than 0.1 mGal, it is presumed that including additional iterations would not change any value in $\Delta \mathbf{g}^g$ by more than 0.1 mGal.

The difficulty in applying eq. (6.9) is with choosing an adequate tolerance. We might assign a tolerance prescribing the desired accuracy for our $\Delta \mathbf{g}^{g(k)}$ determination. However, we may choose a desired accuracy higher than what the numerical apparatus is able to deliver. Also, even if the tolerance we set can be achieved by the numerical apparatus, there is no guarantee that our result will achieve the desired accuracy. In an ill-conditioned system, an exact solution will be very noisy, and as such will be very difficult to interpret.

An alternative to using eq. (6.9) is, at each step, to compare iterations of gravity anomalies on the topography, $\Delta \mathbf{g}^{t(k)}$, using the already calculated \mathbf{B} matrix:

$$\Delta \mathbf{g}^{t(k)} = \mathbf{B} \Delta \mathbf{g}^{g(k)}. \quad (6.10)$$

The testing is then done on the difference between the gravity anomalies on the topographical surface determined from the k -th solution ($\Delta \mathbf{g}^{t(k)}$), and the input anomalies on the topographical surface ($\Delta \mathbf{g}^t$):

$$\delta^{t(k)} = \Delta \mathbf{g}^{t(k)} - \Delta \mathbf{g}^t. \quad (6.11)$$

If we use $\delta^{t(k)}$ as defined by eq. (6.11), then we are no longer testing for convergence based on the desired accuracy of the result. Instead, we are testing whether the gravity anomalies arising from the k -th solution are distinguishable from those used as input. Assuming the system is well conditioned, this is done by comparing the L1 norm of $\delta^{t(k)}$ to a tolerance reflecting the precision of the input data. Thus, if the input data has a precision of 0.01 mGal, we might suppose that we have derived results of the best possible quality when they produce input values less than 0.005 mGal different from the originals. In an ill conditioned system, where $\Delta \mathbf{g}^{t(k)}$ is imprecise because of imprecise values of $\Delta \mathbf{g}^{g(k)}$, it may be impossible to reproduce the input gravity anomalies to such a precision [Wong, 2002]. However, the choice of half the precision of the input data as a tolerance will still produce a result compatible with an exact solution of eq. (6.6), since

exact solution methods are likewise blind to the effect of the ill-conditioned \mathbf{B} matrix (e.g., Young [1971]).

This change in approach is important mainly because it gives a context for choosing tolerances. It is only expected to have a significant effect on results in cases where the convergence is very rapid. In fact:

$$\delta^{g(k)} = \delta^{t(k-1)}, \quad (6.12)$$

so that, for any given tolerance, testing using the geoid gravity anomalies always requires one additional iteration.

If we use a $\delta^{t(k)}$ calculated by eq. (6.11) or (6.12), and a tolerance consistent with the precision of our input data, we will be able to produce an iterative solution as close to the exact solution of the system of equations as the precision of our input data allows. However, if the system of equations is especially ill-conditioned then we will still produce noisy results. This can be avoided by taking the possible error in $\Delta \mathbf{g}^{g(k)}$ into account in choosing our tolerance for $\delta^{t(k)}$.

If the tolerance chosen is consistent with the conditioning of the system of equations, the best possible solution under the circumstances may be reached. Thus, the choice of tolerance may be regarded as a regularization of the solution. If the result seems unwarrantedly rough, the tolerance applied may be too stringent, and can be varied until a reasonably smooth result is obtained. This refinement of the tolerance choice is

equivalent to tuning the tolerance so that it properly reflects what the system of equations and input data are actually able to deliver.

As a rough attempt at defining a suitable tolerance a-priori, we can apply the rule described above, which says that the order of magnitude of the loss of precision due to ill conditioning is roughly equal to the logarithm of the condition number. If we take p as the L_1 norm of the vector of precision of the input data (e.g., 0.01 mGal), we can choose an approximate tolerance, T , based on:

$$T = p\kappa, \tag{6.13}$$

where κ is the condition number of the system of equations. If the system is well conditioned, then eq. (6.13) provides a tolerance close to the precision of the input, suitable for testing $\|\delta^{(k)}\|_{L_1}$. If the conditioning is poor, eq. (6.13) scales the tolerance according to the expected loss of precision in the result.

In the following, we will test the methods discussed above on “real data” from an area of high mountains in Indonesia, based on a portion of the AusSEGM synthetic gravity field [Baran et al., 2006]. The next section will describe these results.

6.3 Results and discussion

6.3.1 Test area and data sets

We have performed three experiments to illustrate the points above. All cover the same area, from 147.5° to 148.5° longitude and -9° to -10° degrees latitude, using data from

147° to 149° longitude and -8.5° to -10.5° latitude, to avoid any edge effects (as described by Sun and Vaníček [1996]). This involves 14,400 input data points on a grid with 1 arc-minute spacing. The large number of data points magnifies the differences in computation time for different solution methods. The maximum point height in the test area, which includes some large mountains in Indonesia, is above 3,200 metres. This corresponds, according to eq. (6.8) to an upper bound for the condition number of the \mathbf{B} matrix of about 227, although we have estimated the actual condition number of the \mathbf{B} matrix, based on the L_1 norms of \mathbf{B} and \mathbf{B}^{-1} , to be 1347. We therefore expect significant numerical instability in the downward continuation process, allowing us to assess how well different solutions deal with the numerical instability.

The input gravity data for the tests will be Helmertized gravity anomalies based on the AusSEGM synthetic data set [Baran et al., 2006]. The input Helmert anomalies are given in Figure 6.1.

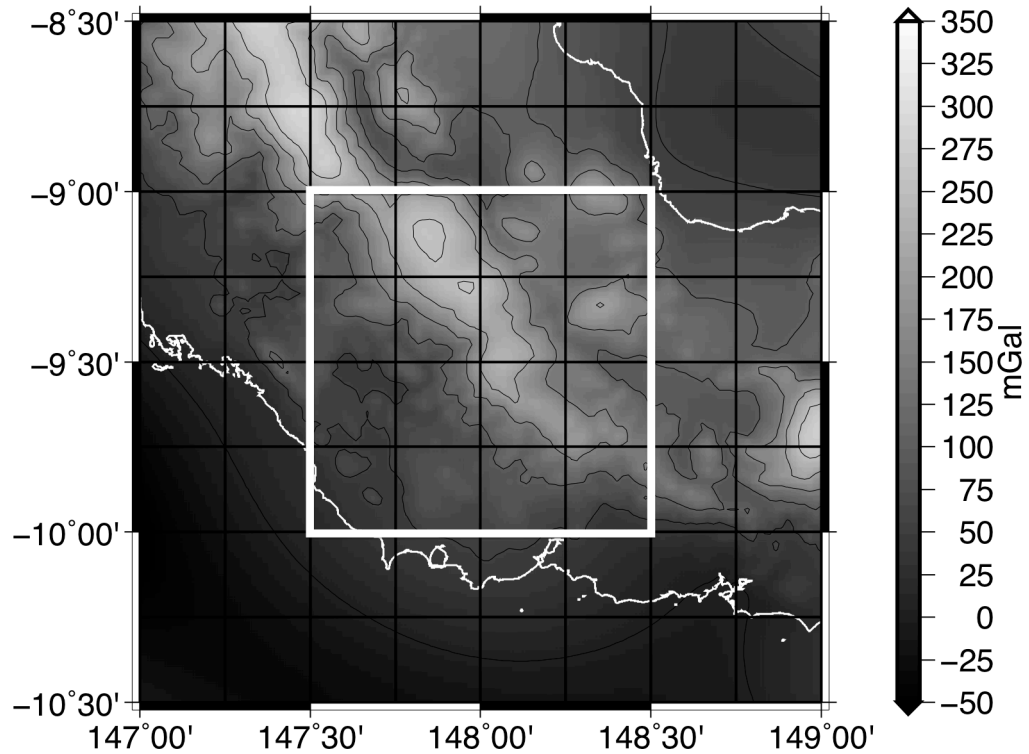


Figure 6.1: Helmert gravity anomalies over the study area.

While Figure 6.1 shows gravity anomaly data over the whole input area, the white square indicates the computation area. All input gravity anomalies are given in mGal to two decimal places, and lacking other information about their accuracy we assume they have a precision of 0.005 mGal. The values in this area range from -54.0 mGal to 290.0 mGal.

Heights are taken from the digital elevation model (DEM) accompanying the AusSEGM data set, and are shown in Figure 6.2. They range from 0 m to over 3200 m.

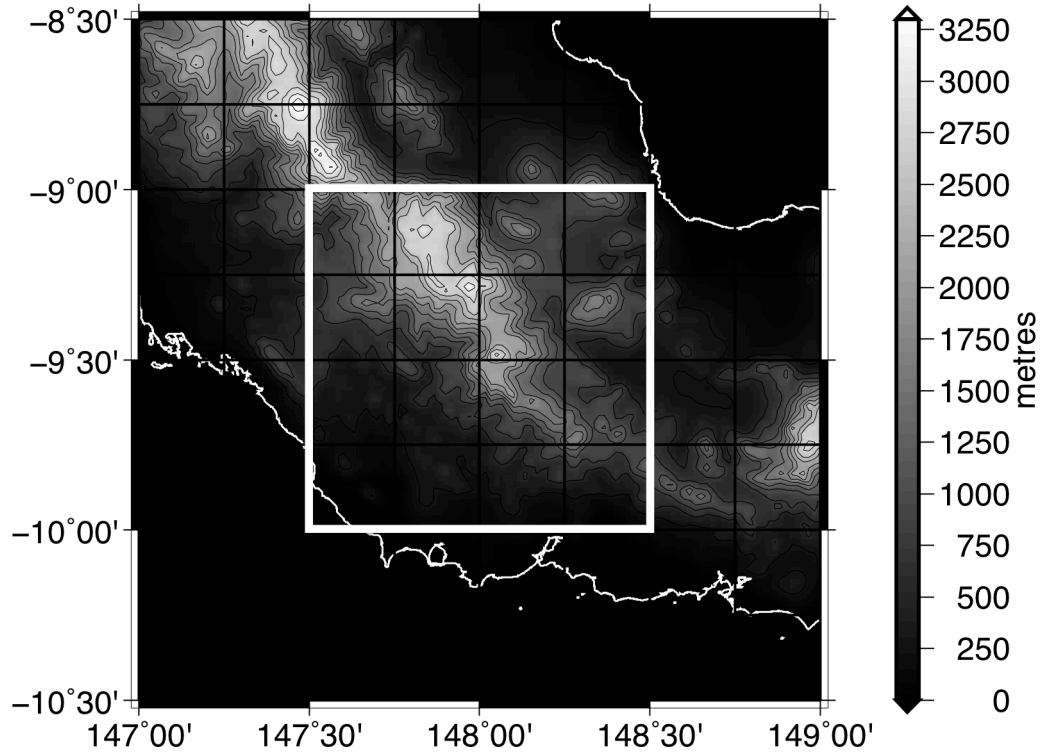


Figure 6.2: Heights of topography over the study area.

By using synthetic data, we will ensure that the comparisons of solution methods are affected as little as possible by errors in the input data. The influence of data errors on downward continuation is not a focus of this study.

6.3.2 Comparison of three methods for solving the downward continuation

First, we test whether our use of the $\delta^{(k)}$ vector, given by eq. (6.11), allows us to properly assess convergence of the Jacobi iterative process, so as to obtain a result congruous with an exact solution. To do this, we have performed downward continuation over our test area using LU decomposition, which provides an algebraically

exact solution, and the Jacobi iterative method with convergence testing based on $\|\delta^{t(k)}\|_{L_I}$, and also $\|\delta^{g(k)}\|_{L_I}$.

In this test, the $\|\delta^{t(k)}\|_{L_I}$ will be required to meet a tolerance of 0.005 mGal, equivalent to half the nominal precision of the input values. In other words, the iterative process will cease when the downward continued anomalies generate surface gravity anomalies indistinguishable in the L_I norm from the input data on the level of one half of the maximum data error. In this case, the result should be very close to the solution by LU decomposition.

The $\|\delta^{g(k)}\|_{L_I}$ will be required to meet the same tolerance, allowing us to verify eq. (6.12), and examine the additional computational cost of using $\delta^{t(k)}$ instead of $\delta^{g(k)}$, which requires an extra multiplication by the \mathbf{B} matrix for each iteration. If eq. (6.12) is correct, the extra multiplication need not be carried out in normal calculations, since $\delta^{t(k)}$ can just be calculated based on $\delta^{g(k+1)}$ – and thus the computational cost of each method would be almost the same.

The result for the calculation using the Jacobi method and testing $\|\delta^{t(k)}\|_{L_I}$ is given in Figure 6.3. The results from LU decomposition and from testing $\|\delta^{g(k)}\|_{L_I}$ are almost identical to Figure 6.3, and so they are not plotted. Additionally, Table 6.1 provides statistics and computation times for each result. All computation times indicated below are for running computations on the ACENet parallel grid computing system.

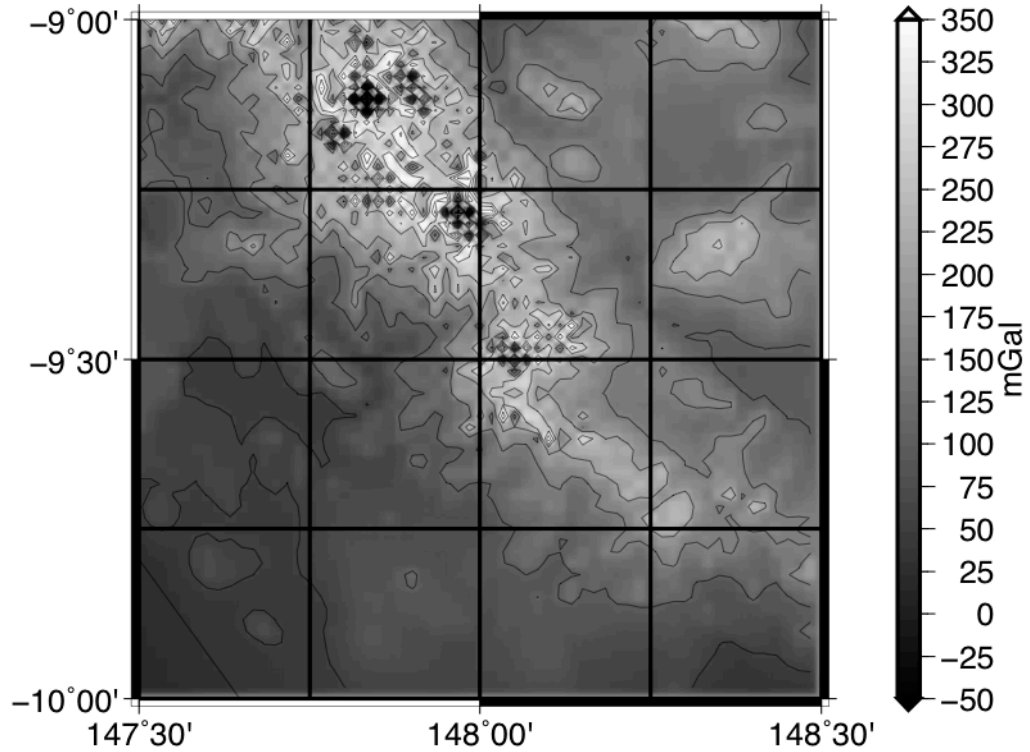


Figure 6.3: Result for Δg^g from Jacobi iterative approach based on norm of the δ^t vector.

Table 6.1: Statistics of results from three computation methods.

Method	LU decomposition	Jacobi testing δ^g	Jacobi testing δ^t
Minimum [mGal]	-291.65	-291.54	-291.54
Maximum [mGal]	1331.33	1331.23	1331.23
Mean [mGal]	127.24	127.42	127.42
Std. deviation [mGal]	79.26	79.01	79.01
No. of iterations	n/a	4684	4683
Processing time [mm:ss]	208:08	36:11	52:09

The similarity of all three results indicates that the tolerance of 0.005 mGal does lead to an iterative result commensurate with the exact result. Furthermore eq. (6.12) is verified since the method using $\delta^{g(k)}$ required exactly one more iteration than that using

$\delta^{(k)}$, to meet the same tolerance. The time required per iteration was about 0.46 seconds for the $\delta^{g(k)}$ method and 0.67 seconds for the $\delta^{t(k)}$ method. Thus the $\delta^{t(k)}$ method, implemented as it was here, is relatively slow, and values of $\delta^{t(k)}$ should be calculated by eq. (6.12) in normal practice.

As expected, all three results are very spiky. This does not mean the iterative solutions were unsuccessful – they achieved their purpose by converging to a result very close to the LU decomposition result. However, because of the ill conditioning of the \mathbf{B} matrix, we have tried to achieve a better agreement between the generated surface anomalies and the input surface anomalies than we possibly can.

6.3.3 Comparison of Jacobi results using varying tolerances

Next, we show how by varying the tolerances for the L_1 norm, both when testing the surface gravity anomalies and geoid gravity anomalies, the computational noise in the downward continuation solution can be reduced. The results given are for the "downward continuation effect", or the difference between the surface (as shown in Figure 6.1) and downward continued gravity anomalies, given by:

$$\boldsymbol{\varepsilon}^{(k)} = \Delta \mathbf{g}^{g(k)} - \Delta \mathbf{g}^t, \quad (6.14)$$

This presentation is used to best indicate the noisiness of the different results and their characteristic features. Figure 6.4 and Table 6.2 give four results based on tolerances of

0.05 mGal, 0.5 mGal, 5 mGal and 50 mGal, as well as the statistics of the surface gravity anomalies in the area for comparison.

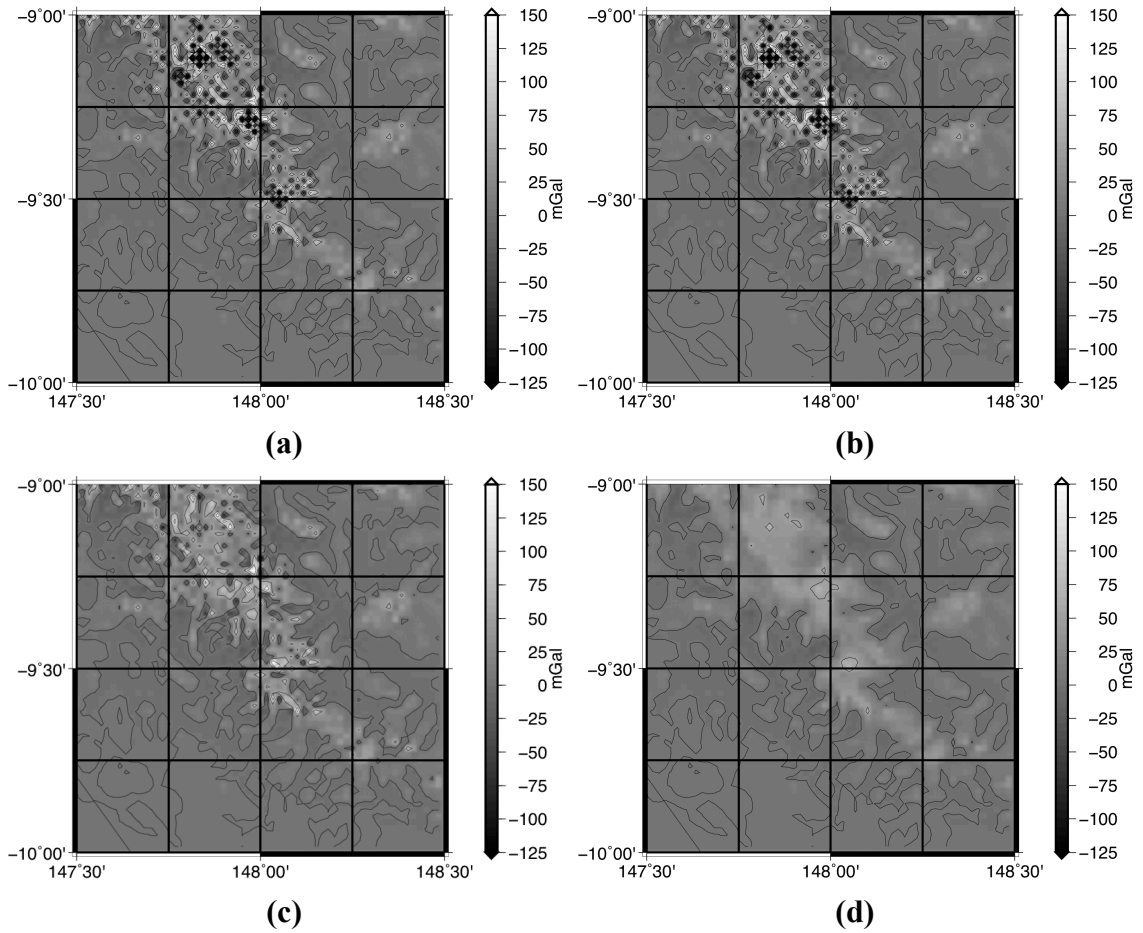


Figure 6.4: Downward continuation effect from the Jacobi iterative method with testing of the δ^l vector with (a) 0.05 mGal, (b) 0.5 mGal, (c) 5 mGal and (d) 50 mGal tolerances.

Table 6.2: Statistics of the downward continuation effect for the Jacobi iterative method with testing of the δ' vector using various tolerances.

	Jacobi results for anomalies on geoid				Surface anomalies
	0.05	0.5	5	50	n/a
Tolerance [mGal]					
Minimum [mGal]	-291.18	-268.91	15.52	15.52	15.52
Maximum [mGal]	1330.82	1303.08	558.79	332.55	261.43
Range [mGal]	1662.00	1571.99	543.27	317.03	245.91
Std. deviation [mGal]	78.99	78.27	68.77	66.40	57.21
No. of iterations	4683	1066	47	3	n/a
Processing time [mm:ss]	32:35	15:37	5:19	4:56	n/a

In all cases we have used the method of testing based on the L_1 norm of the δ' vector. The figures and statistics confirm the smoothing effect of choosing a less stringent tolerance. The spikes evident in the solution for a 0.05 mGal tolerance, which has a standard deviation of 78.99 mGal and range of 1662.00 mGal, are diminished in the solutions that use a 0.5 mGal and 5 mGal tolerance. They are absent in the solution using the 50 mGal tolerance, where the standard deviation has dropped to 66.40 mGal and the range to 317.03 mGal. Since the extreme positive and negative spikes are surely spurious, this suggests that a suitable tolerance will be somewhere between 5 mGal and 50 mGal – since the 5 mGal solution shows questionable spikes, which disappear in the 50 mGal solution.

As expected, the number of iterations and time consumed drop significantly as the tolerance is relaxed, although the drop is less pronounced once the tolerance exceeds about 1 mGal. The relationship between the choice of the tolerance and the number of iterations, for our computation area, is shown in a semi-logarithmic graph in Figure 6.5.

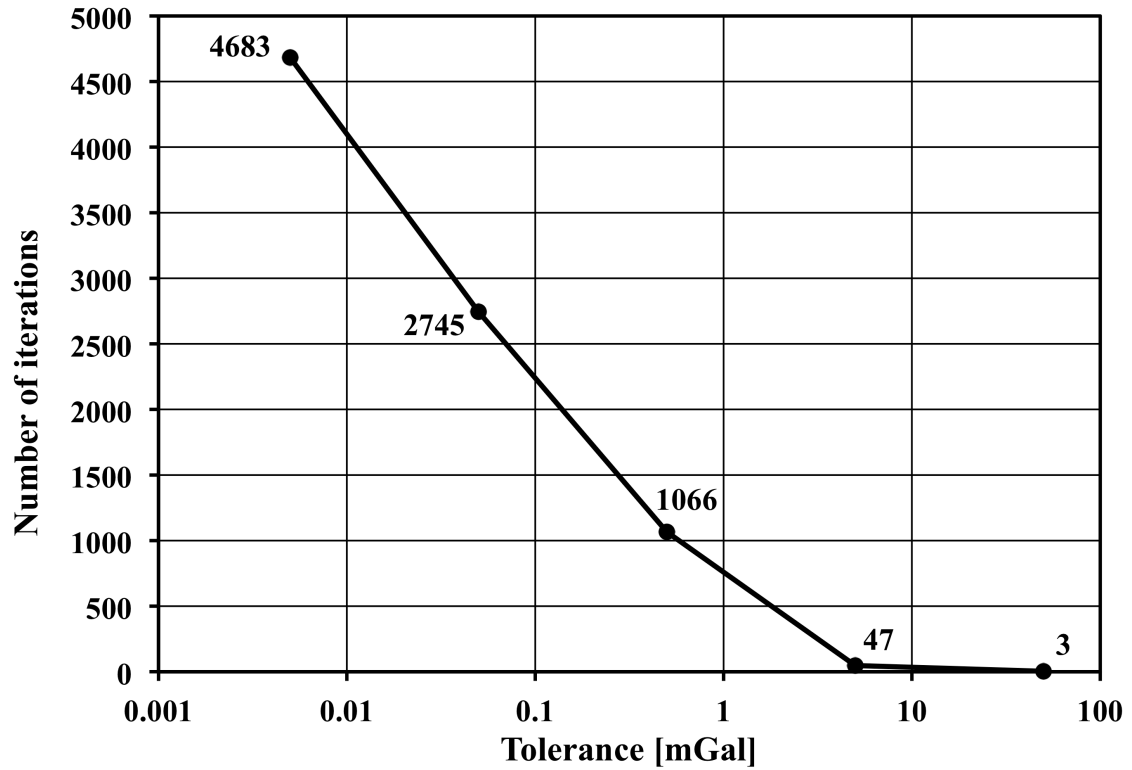


Figure 6.5: Number of iterations of the Jacobi method vs. tolerance chosen for convergence testing.

The impressive decrease in computation time with the relaxation of the Jacobi tolerance shows that in addition to regularizing the solution and producing a better result, using a suitable tolerance will also significantly improve computation speed.

6.3.4 Testing the choice of tolerance based on the condition number

Finally, we have applied Eq. (13) to our situation, using our estimate of the condition number based on the L_1 norms of 1347, and an assumed precision of the input data of 0.005 mGal, and come up with a tolerance of 6.7 mGal. This number is in the range we

might guess for the best tolerance, based on the results in section 6.3.3. If we use this tolerance in our calculations, we find the result shown in Figure 6.6.

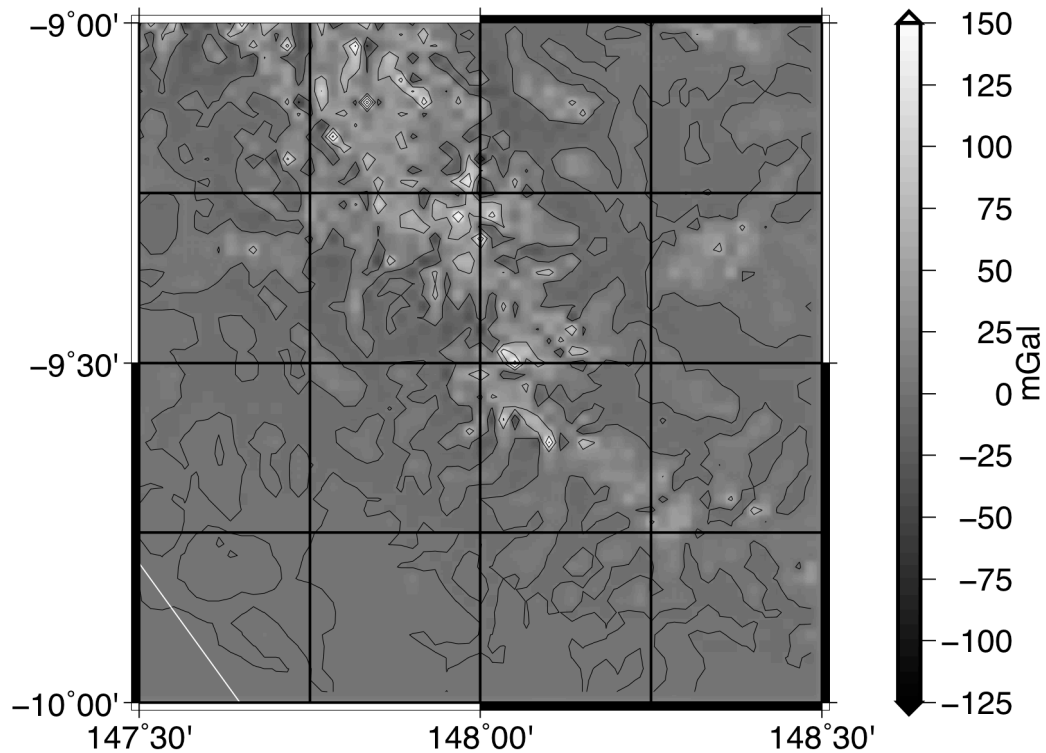


Figure 6.6: Downward continuation effect of Jacobi method using a tolerance of 6.7 mGal.

As with any attempt at regularization, we can do little to verify this result, apart from saying that it appears to behave as we expect it to. The gravity anomalies on the geoid are rougher than those at the topographical surface, but do not have any significant spikes, and do not have extreme ranges such as we have seen when using tolerances of 0.5 mGal or less. Thus, the tolerance chosen according to eq. (6.13) at least produces a reasonable result. There are still some smaller spikes in the solution, and so eq. (6.13) may provide too stringent of a tolerance, at least when based on the L_1 norm when

estimating of the condition number. If the condition number is estimated according to the L_2 or L_∞ norm, or determined exactly by singular value decomposition, it will be higher and the tolerance provided by eq. (6.13) will be less stringent. Also, eq. (6.13) would be slow to implement in practical computations due to the time consumption involved in finding the condition number, or even one of the more specific estimates of it. Thus, a better method of finding the most suitable tolerance would help in practical applications.

6.4 Conclusions

The results have shown first that testing downward continuation according to the L_1 norm of gravity anomalies (the largest absolute value in the vector of values) at the topographical surface, rather than on the geoid, provides a solution commensurate with the theoretically exact LU decomposition solution and also with the traditional method of testing gravity anomalies on the geoid. Testing of anomalies on the surface should be preferred because it allows a more meaningful choice of tolerance criteria and because in cases where convergence is rapid, testing the fit of anomalies at the geoid level leads to truncating the iterations one iteration too soon and this may result in a significant difference in the results. The vector of differences for testing, however, should be determined by eq. (6.12), to provide a faster calculation than eq. (6.11).

We have also shown that by relaxing the L_1 tolerances in the Jacobi method from those required to get the exact solution, we can regularize the downward continuation solution and significantly decrease computation time. While a better prescription can

probably be found, our proposal for the choice of a relaxed tolerance based on the condition number of the \mathbf{B} matrix, according to eq. (6.13), yields a reasonable result. It certainly provides a better result than the solution with a higher tolerance or the “exact” solution by LU decomposition.

It seems to us, that the described approach to downward continuation of gravity anomalies from the Earth surface to the geoid makes good physical sense. It also produces results that appear more transparent from the mathematical point of view, and that would be evaluated faster than by using some regularization methods.

Chapter 6 References

- Baran, I., M. Kuhn, S. Claessens, W. Featherstone, S. Holmes, and P. Vaníček (2006). “A synthetic Earth gravity model designed specifically for testing regional gravimetric geoid determination algorithms.” *Journal of Geodesy*, Vol. 80, No. 1, pp. 1–16, doi: 0.1007/s00190-005-0002-z.
- Cheney, W., and D. Kincaid (2008). *Numerical Mathematics and Computing*. Thomson Brooks/Cole, New York.
- Fredholm, E. (1900). “Sur une nouvelle méthode pour la résolution du problème de Dirichlet.” *Öfversigt af Kongliga Svenska Vetenskaps-Akademiens Förhandlingar*, Vol. 131, pp. 39–46.
- Goli, M., M. Najafi-Alamdari, and P. Vaníček (2010). “Numerical behaviour of the downward continuation of gravity anomalies.” *Studia Geophysica at Geodaetica*, Vol. 55, No. 2, pp. 191–202, doi: 10.1007/s11200-011-0011-8.
- Heiskanen W., and H. Moritz (1967). *Physical Geodesy*. Freeman, San Francisco, U.S.A.
- MacMillan, W. (1930). *The Theory of Potential*. Dover Publications Inc., New York, U.S.A.
- Martinec, Z. (1996). “Stability investigations of a discrete downward continuation problem for geoid determination in the Canadian Rocky Mountains.” *Journal of Geodesy*, Vol. 70, No. 11, pp. 805–828, doi: 10.1007/BF00867158.
- Moritz, H. (1980). “Geodetic Reference System 1980.” *Bulletin Géodésique*, Vol 54, No. 3, pp. 395–405, doi: 10.1007/BF02521480.
- P Press, W. (2002). *Numerical Recipes in C++: The Art of Scientific Computing*. Cambridge University Press, New York, U.S.A.
- Schwartz, K. (1978). “Geodetic improperly posed problems and their regularization.” Lecture Notes of the Second International School of Advanced Geodesy, Erice, Sicily, Italy.
- Sun, W., and P. Vaníček (1996). “On the discrete problem of downward Helmert's gravity continuation.” *Proceedings, Session G7, European Geophysical Society XXI General Assembly*, Eds. I. Tziavos and M. Vermeer. The Hague, The Netherlands, May 6–10, 1996. Reports of the Finnish Geodetic Institute, Vol. 96, No. 2, pp. 29–34.

- Vaniček, P., W. Sun, P. Ong, Z. Martinec, P. Vajda, and B. ter Horst (1996). “Downward continuation of Helmert's gravity.” *Journal of Geodesy*, Vol. 71, No. 1, pp. 21–34, doi: 10.1007/s001900050072.
- Vaniček P., and M. Santos (2012). “Can mean values of Helmert’s gravity anomalies be continued downward directly?” *Geomatica*, Vol. 64, No. 2, pp. 245–251.
- Wong, J. (2002). *On Picard Criterion and the Well-Posed Nature of Harmonic Downward Continuation*. M.Sc.E. thesis, Department of Geodesy and Geomatics Engineering Technical Report No. 213, University of New Brunswick, Fredericton, New Brunswick, Canada, 85 pp.
- Young, D. (1971). *Iterative solution of large linear systems*. Academic Press, New York, U.S.A.

Chapter 7: Gravity anomalies from retracked ERS and Geosat altimetry over the Great Lakes: accuracy assessment and problems

This article was published in the journal *Terrestrial, Atmospheric and Ocean Sciences*, a publication of the Chinese Geoscience Union. The concept for the paper was developed with Dr. Chienway Hwang, in preparation for a conference in Beijing, and the paper is a result of some further research. The computations were performed by myself with some assistance from the third author, Dr. Yu-Shen Hsiao. I wrote the manuscript, while my coauthors provided helpful comments and especially clarifications in the section on calculation of gravity anomalies from satellite altimetry. The full citation for the article is:

Kingdon, R., C. Hwang, Y-S. Hsiao, and M. Santos (2007). "Gravity Anomalies from retracked ERS and GeoSat Altimetry over the Great Lakes: Accuracy Assessment and Problems." *Terrestrial, Atmospheric and Ocean Sciences*, Vol. 19, No. 1–2, pp. 93–102, doi: 10.3319/TAO.2008.19.1-2.93(SA).

Note: The standard deviation in comparisons with the EIGEN-GL04C model is treated as an RMS error in the article, though not in the interpretation of its results elsewhere in this dissertation. The treatment in this chapter is incorrect, since the RMS error is a different quantity from the standard deviation.

We have not described in depth the way that the covariance matrices used in this article were calculated. This has been omitted, apart from a brief description following eq. (7.4), because it is an involved procedure and secondary to the main point of the article. As indicated in the discussion following eq. (7.4), additional details can be found in Tscherning and Rapp [1974].

Chapter 7 Abstract

Lake waters are a useful area for investigating the response of the Earth gravity field to topographical density variations, since lake beds represent large density contrasts between water and rock. However, our ability to investigate relations between lake bathymetry and the gravity field is limited because of relatively sparse gravity data coverage over most lake surfaces, and the inability of satellite-derived gravity fields to capture the high frequency response to density effects. Satellite altimetry may provide an alternate method to determine a dense gravity field at surfaces of large inland lakes. We calculate satellite altimetry derived free-air (FA) anomalies over the Great Lakes in Canada, and evaluate them in terms of resolution and accuracy. The anomalies are compared to those calculated from the EIGEN-GL04C gravity field, derived from terrestrial and GRACE satellite data, to test for bias; and to those from shipborne or airborne observations (where available) to test the accuracy of their determination of the high frequency component of the gravity field. Our results show that accuracies may reach less than 10 mGal, both in terms of bias and higher frequency effects, but are often

tens of milligals. Furthermore, we find that altimetry does provide a higher resolution gravity field than satellite-derived gravity fields, and so if the accuracy can be improved in later efforts it will be a useful tool for investigations of topographical density effects of lake waters.

7.1 Introduction

The study of Earth's gravity field, and the response of the gravity field to topographical density variations, has important implications in physical geodesy. One of these areas, and one not yet well explored, is the effect of topographical density variations on geodetic methods of height determination. Both geoid determination and orthometric heights depend directly on the behavior of Earth's gravity field, which in turn depends to a significant extent on the variations in crustal density near to the surface. While these effects have been approximated using a model of laterally-varying density (e.g., Huang et al. [2001]; Hwang et al. [2003]; Kingdon et al. [2006]), the effects of density viewed as a three-dimensionally varying quantity are not well known. However, any study of the effect of these variations requires sufficient knowledge of the gravity field in a study area. One of the key study areas for investigations of three-dimensional topographical density effects is the pronounced density contrasts existing at the bed of lakes.

Bathymetry can readily provide a three-dimensional model of these interfaces where available, but this is only useful if the gravity field around and over lakes is known to a sufficiently high resolution. While gravity anomalies can be computed from shipborne or airborne gravity data, in many areas these data are sparse. Also, while satellite gravity

data, e.g., from GRACE, may furnish a long-wavelength field over lakes, high frequency density affects are indistinguishable in this signal, and so a higher resolution field is preferred if available.

Procedures for calculating gravity anomalies using satellite altimetry results and least squares collocation over oceans are well established (e.g., Sandwell and Smith [1997]; Hwang et al. [2003]; Sandwell and Smith [2005]). These same procedures have been extended to inland water bodies (e.g., Hwang et al. [1998]). Errors in either case result from (1) corruption of waveforms by land interference and multi-returns from lake bottom for points in shallow waters near to shore, (2) errors in wet tropospheric corrections resulting from bad radiometer data, (3) error due to tidal effects, and (4) sea state bias. Over lakes, however, we expect (1) to have more influence than over oceans because lake waters are overall more shallow. (2) and (4) should be similar for both, while (3) should be slightly less in lakes since even in large lakes tidal influences are less than in oceans. Fortunately, the errors resulting from (1) are slightly diminished in the case of larger lakes, which are also the lakes most likely to have a significant effect on the gravity field. Furthermore, they can be mitigated in deep lakes by omitting satellite altimetry results near to shore (where waveforms are more erratic), and by including onshore gravity observations as part of the input to a least squares collocation procedure used to determine gravity anomalies (cf. Hwang et al. [2003]). In some cases, altimetry data have been extended to extrapolate information about density distributions over larger water bodies for some time now, in determinations of bathymetry from satellite altimetry results. Examples of such work are Smith and Sandwell [1994], Hwang [1999] and Vergos and Sideris [2002]. Thus, the relationship between density

distributions and gravity, determined from satellite altimetry, is well established. What we hope to discover is whether such relationships can be investigated using satellite altimetry data for the topographical density distribution represented by lake waters.

In this study, we attempt to calculate free-air gravity anomalies at a $1' \times 1'$ resolution, better than that currently attainable from GRACE results alone, over the Great Lakes in Canada, with a view to finding sufficiently dense gravity anomalies for density investigations. The gravity anomalies are calculated using both Topex/Poseidon and ERS-1/Geosat derived height anomalies, in combination with free-air anomalies from terrestrial gravity data gathered from the United States Geological Survey's database, and the Geological Survey of Canada's database. These are used as input to a least squares collocation, using the program `colloc.f` written by Prof. Chienway Hwang, and the output is examined by comparison with the GRACE-derived gravity field EIGEN-GL04C [Flechtner, 2006] and shipborne/airborne results to assess the accuracy of the gravity field determined from satellite altimetry.

7.2 Methodology

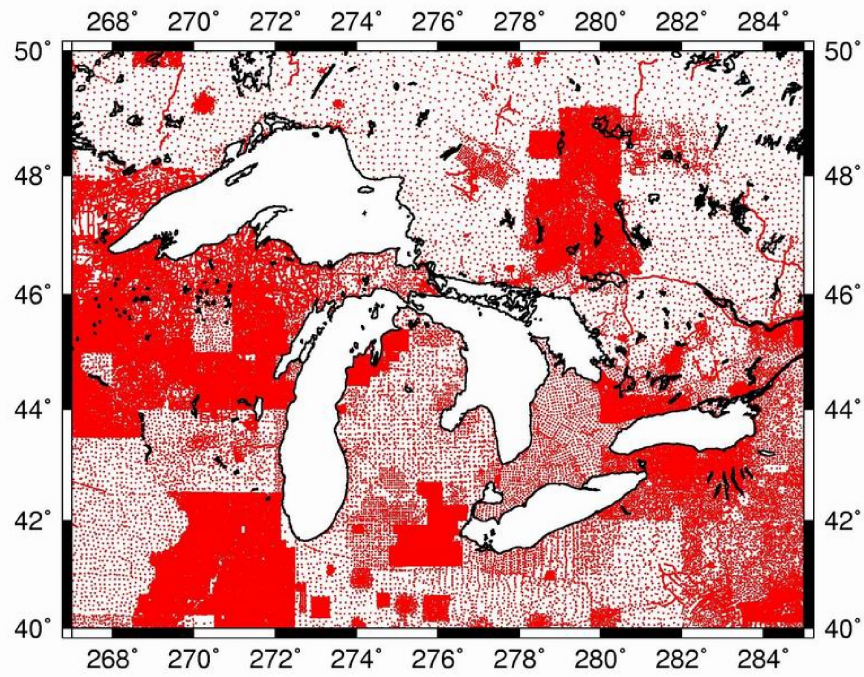
7.2.1 Preparation of terrestrial gravity data

Terrestrial gravity data for Canada and the United States are freely downloadable from the Geological Survey of Canada and the National Geological Survey. Each agency provides files containing gravity point names, coordinates, dates and times of collection, raw gravity values, and standard deviations. Once complete data sets of raw gravity observations were downloaded, data beyond 0.5 degrees of latitude and longitude from

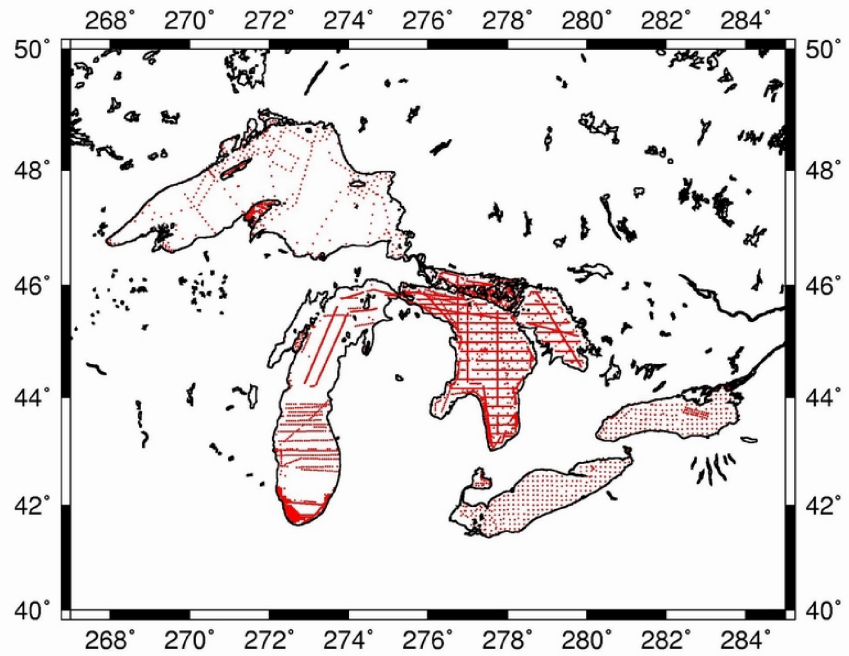
the Great Lakes were removed using MATLAB software, as were those assigned standard deviations greater than 3 mGal. A visual inspection was used to verify that the data at least appeared to represent a continuous surface.

The remaining data points were converted into free air anomalies according to Hofmann-Wellenhof and Moritz [2005, eq. 3-100]. Thereafter, the data set was exported from MATLAB and separated into free-air anomalies over lakes, to be used for later comparison with results; and terrestrial free-air anomalies, to be used as input for least squares collocation.

Finally, the terrestrial free-air anomalies were filtered using the box median filter included with the Generic Mapping Tools (GMT) [Wessel and Smith, 1999] to decimate it to a 1 arc-minute resolution. This filter divides input data into cells of user specified size, and removes from each cell all but the median data point. It was applied because our terrestrial gravity data was too dense, resulting in unnecessarily slow calculations and erratic behavior of our least squares collocation algorithm. Final data set coverage is shown in Figure 7.1.



(a)



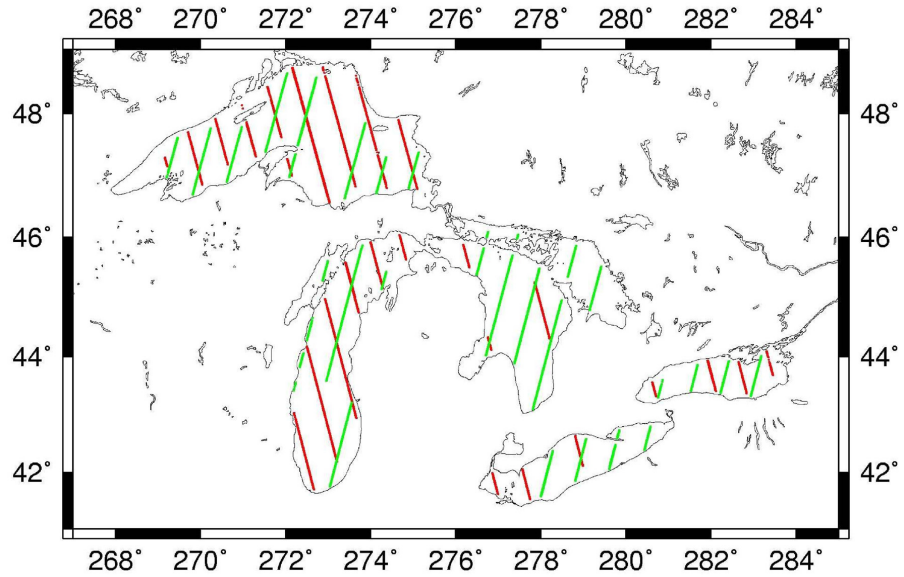
(b)

Figure 7.1: Terrestrial (a) and shipborne/airborne (b) gravity coverage around the Great Lakes.

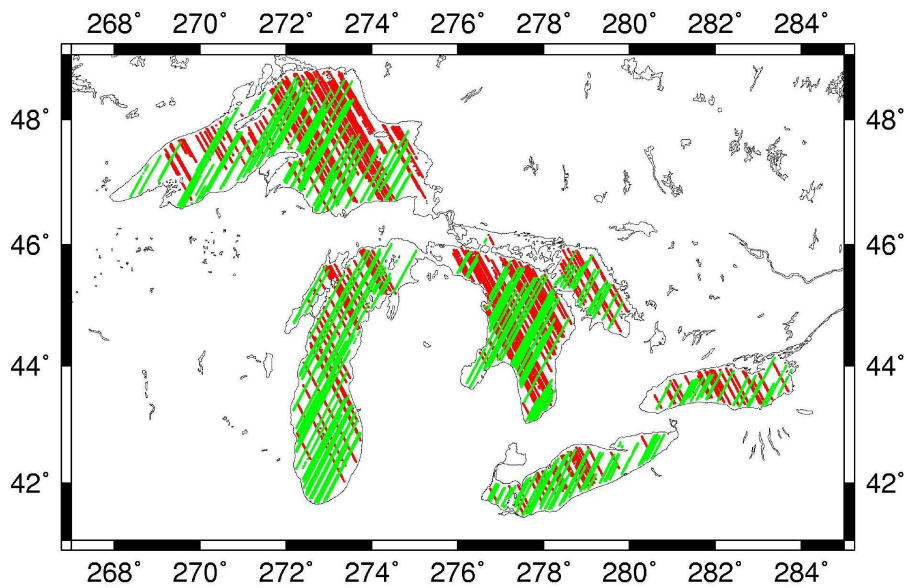
7.2.2 Preparation of ERS-1/GM and Geosat/GM data

ERS-1/GM and Geosat/GM data at a 5 Hz (1.4 km) sampling rate were retracked following the method of Sandwell and Smith [2005], to minimize the error in surface slope and to decouple it from wave height error. This is especially important because we use height gradients to derive gravity anomalies. Furthermore, Sandwell and Smith's method has proven useful in coastal areas, which are analogous to lake waters.

Because we expect altimetry results over lakes to contain some anomalous results not related to the mean lake surface, the retracked altimetry data was filtered for outliers by comparison of the observed heights with geoidal heights derived from the EIGEN-GL04C gravity field. Outlier testing was carried out using the sample standard deviation and sample mean for these differences, allowing for a bias between the altimetry results and the EIGEN-GL04C field. Pope's tau test was applied to create a confidence interval around the sample mean, and points where the difference fell outside of this interval were considered outliers. This filtering assumes that the surface of the lake follows a geopotential surface. Figure 7.2 shows data coverage before filtering, and Figure 7.3 shows the outliers found.

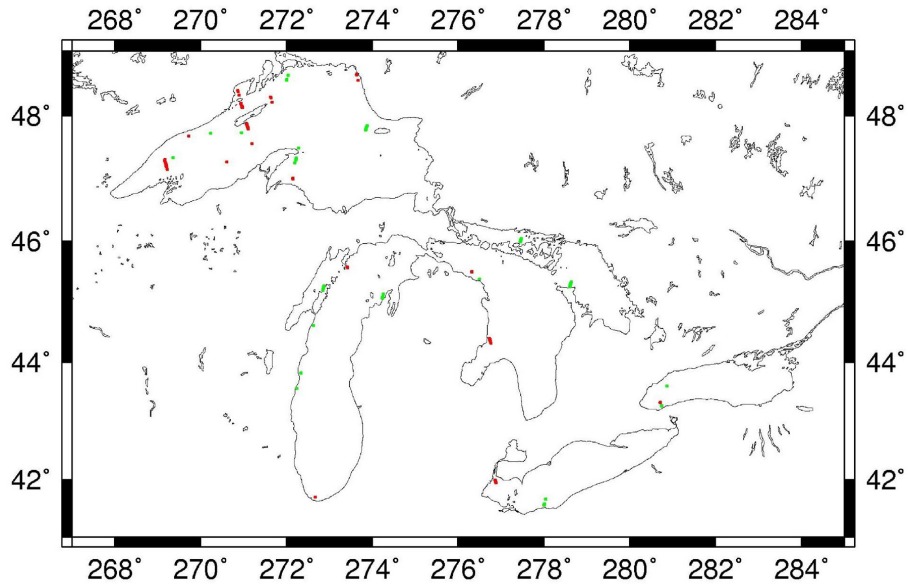


(a)

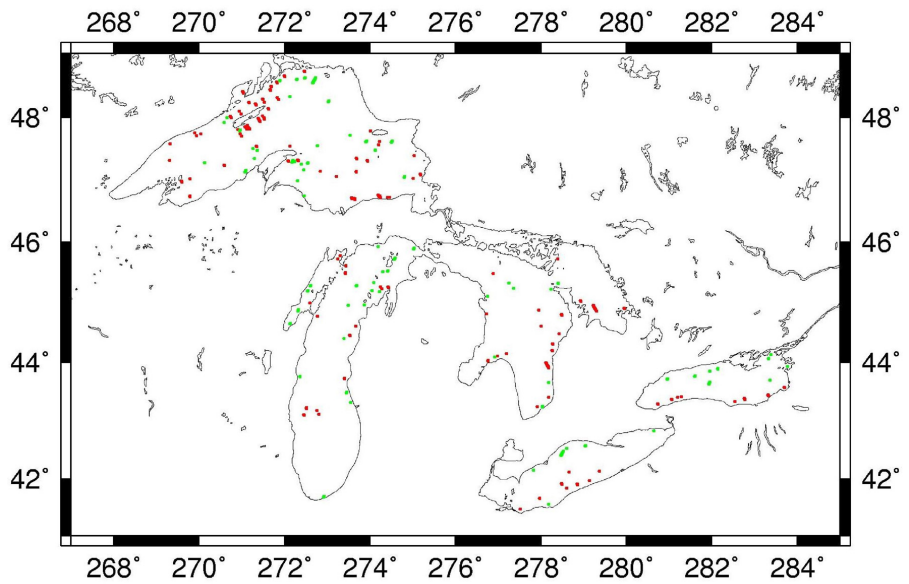


(b)

Figure 7.2: ERS-1/GM (a) and Geosat/GM (b) data coverage for the Great Lakes.



(a)



(b)

Figure 7.3: ERS-1/GM (a) and Geosat/GM (b) outliers for the Great Lakes.

It is evident from Figure 7.2 that ERS-1/GM data alone do not offer better coverage than airborne or shipborne data. Geosat/GM data are necessary to improve upon the

coverage from shipborne or airborne data. Also, a relatively small number of altimetry observations are removed as outliers, justifying our assumption that the lake surface coincides with a geopotential surface.

While many outliers are near to the shore, some occur near the middle of the lakes. Comparison of these with bathymetry reveals that they are often associated with formations on the lakebeds. These formations could influence the lake surface either by their interaction with water currents (which can be quite strong in the Great Lakes), or by the way they affect the gravity field. In the latter case they may represent interesting phenomena for topographic density effect investigations, although without shipborne or airborne data – which are relatively sparse over the Great Lakes, as Figure 7.1b shows – it is difficult to distinguish between these effects.

We can say that any local bathymetric formation would have to be quite large to have a noticeable effect on altimeter-derived gravity. For example, suppose a very optimistic sensitivity of altimeter results to gravity field variations of 3 mGal. This is suggested in Hwang and Hsu [2003] as the current best possible accuracy of altimetry-based gravity anomalies, based on results of e.g., Sandwell and Smith [1997], Andersen et al. [2001] and Hwang et al. [2002]. In order to cause an effect on the gravity field of this magnitude, a bathymetric formation would have to be very large. One possibility of many would be a 50m high, 460 m wide, hemi-ellipsoidal formation of average crustal density (2670 kg m^{-3}) at a depth of 100m below the lake. Such a formation would be too small to have a distinguishable effect on a satellite-derived gravity field, such as the EIGEN-GL04C field used for outlier testing. However, it could affect the lake surface

heights at up to two along track points, which might according to our testing be mistakenly considered outliers.

Finally, along track height gradients are calculated from the satellite altimetry-derived heights. Again assuming the lake surface to be an equipotential surface, these are considered to be the same as the geoid gradients, e . They are calculated according to:

$$e = \frac{\Delta h}{\Delta d}, \quad (7.1)$$

where Δh is the height difference between two along-track points, and Δd is the distance between the points.

7.2.3 Calculation of gravity anomalies from terrestrial and satellite altimetry data

A remove-compute-restore technique is applied to calculate gravity anomalies. In this procedure, effects of a global geopotential model are removed from both the geoid gradients e and the terrestrial gravity anomalies Δg . This is done according to

$$e_{res} = e - e_{ref}, \text{ and} \quad (7.2)$$

$$\Delta g_{res}^{land} = \Delta g - \Delta g_{ref}. \quad (7.3)$$

In eq. (2), for geoid gradients, e_{ref} represents the gradients derived from a geopotential model – in our case, EIGEN-GL04C expanded to degree 360 – and e_{res} represents the residual geoid gradient. Likewise with eq. (3), Δg_{ref} represents the EIGEN-GL04C gravity anomaly, and Δg_{res}^{land} the residual gravity anomaly. These residual quantities are then used as input for least squares collocation to calculate residual gravity anomalies over the lakes. The collocation is formulated thus:

$$\Delta g_{res} = \begin{pmatrix} C_{ge} & C_{gg} \end{pmatrix} \begin{pmatrix} C_{ee} + D_e & C_{eg} \\ C_{ge} & C_{gg} + D_g \end{pmatrix}^{-1} \begin{pmatrix} e_{res} \\ \Delta g_{res}^{land} \end{pmatrix} \quad (7.4)$$

where C_{ge} is the covariance matrix relating gravity to geoid gradients, C_{gg} is the gravity-gravity covariance matrix, and C_{ee} is the geoid gradient-geoid gradient covariance matrix. The terms D_g and D_e represent noise in the gravity and geoid gradient observations. The output of the collocation could be at any suitable resolution, but in our case a resolution of 1' x 1' was chosen.

The covariance functions needed in the least squares collocation computations are expanded into series of Legendre polynomials [Moritz, 1980]. The coefficients of the polynomials are derived from the error degree variances of the reference geopotential models for degrees 2 to 360, and from Tscherning and Rapp [1974] Model 4 degree variances for degree 361 to infinity. The details are given in Tscherning and Rapp [1974]. The actual computations of covariance functions used a modified version of a program in the computer package “GRAVSOF”.

After least squares collocation, the reference gravity anomaly values are restored to the final free-air anomaly values, to calculate final free-air anomalies:

$$\Delta g = \Delta g_{ref} + \Delta g_{res}, \quad (7.5)$$

where Δg_{ref} is the EIGEN-GL04C-derived gravity anomaly, and the other quantities are as defined above.

7.2.4 Assessment of results

The accuracy of the results was assessed by comparison with two global geopotential models, and with shipborne/airborne gravity data. The shipborne and airborne data was converted into free-air anomalies using the same procedure as with the terrestrial data. Comparison with the global models EIGEN-GL04C was performed to search for biases in our results, and comparison with shipborne or airborne data was used to estimate errors in the high-frequency component of our results. Differences between the data sets were calculated, with the expectation that these differences would fall within the uncertainties of altimetry-derived gravity anomalies suggested by Hwang et al. [2003], in which case we could verify that the results are indistinguishable from each other. Also, the comparison with both high and low frequency data can give some idea where our data fits in the spectrum of resolutions of gravity data available over lakes.

7.3 Results

7.3.1 Comparison of area results

The entire results of our gravity anomaly calculations are shown by the color plot in Figure 7.4. For comparison, Great Lakes bathymetry retrieved from NOAA/GLERL [Schwab and Sellers, 1996] is shown in Figure 7.5.

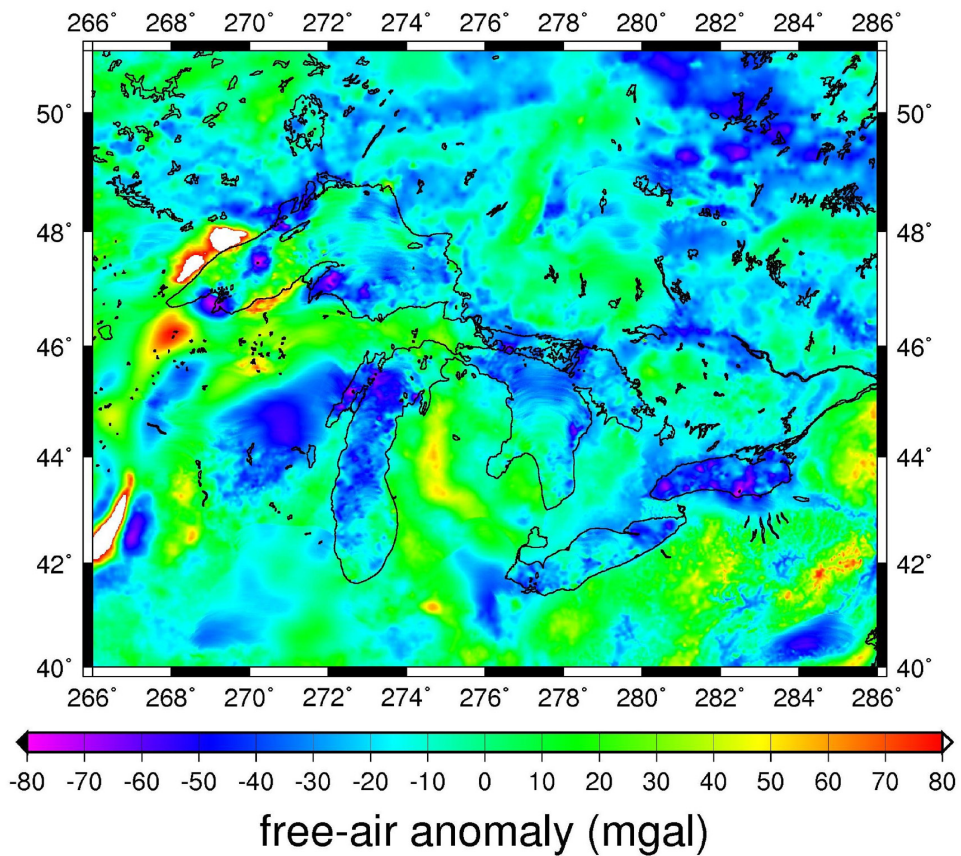


Figure 7.4: Results of free-air anomaly calculation for the Great Lakes.

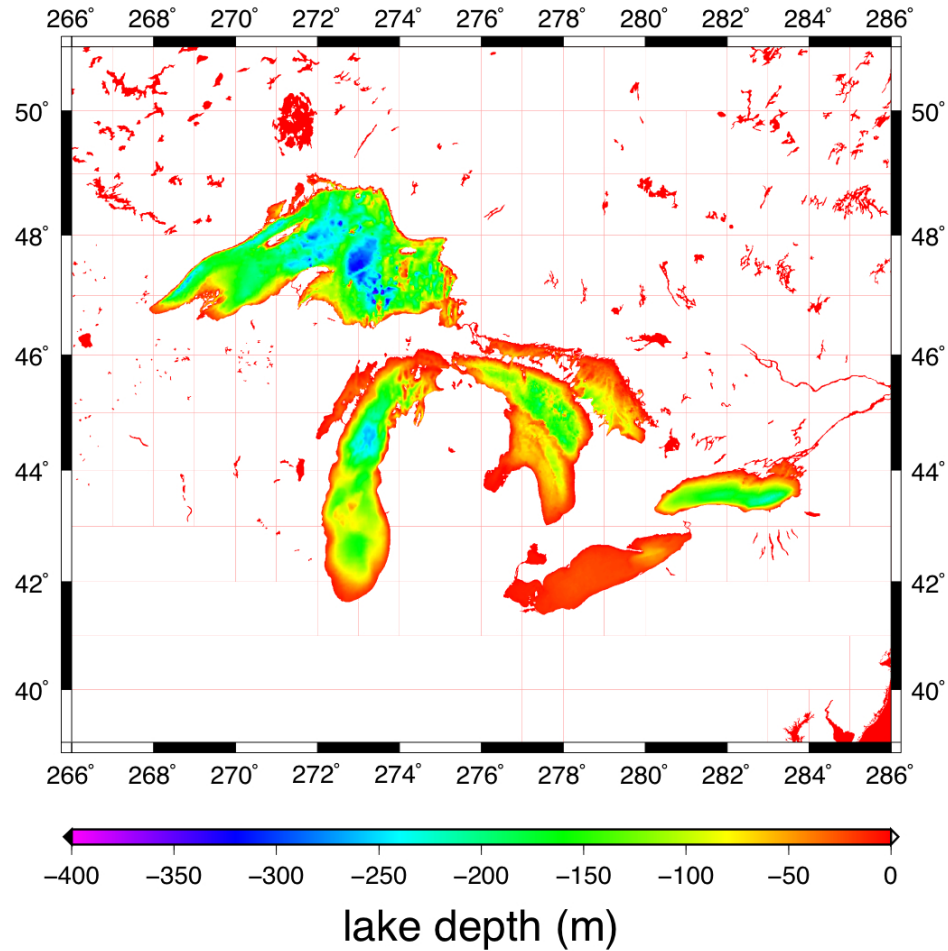


Figure 7.5: Bathymetry of the Great Lakes.

At first glance, the results show a significant correlation with lake depths. The free-air anomalies over lakes range from -80 to 20 mGal, with the lowest values in shallow waters and the noisiest results in bumpy areas. This is an encouraging sign of the usefulness of these results for density investigations, because the effects of these density contrasts (between the lake bed and the water) are not otherwise available in these areas. Gravity anomalies based on satellite observations (other than from satellite altimetry), while they cover this area, are observed too far from the density contrasts to register

their effects. The lack of response to high-frequency density contrasts is visible in the EIGEN-GL04C gravity field over the same area, expanded to degree 360, shown in Figure 7.6.

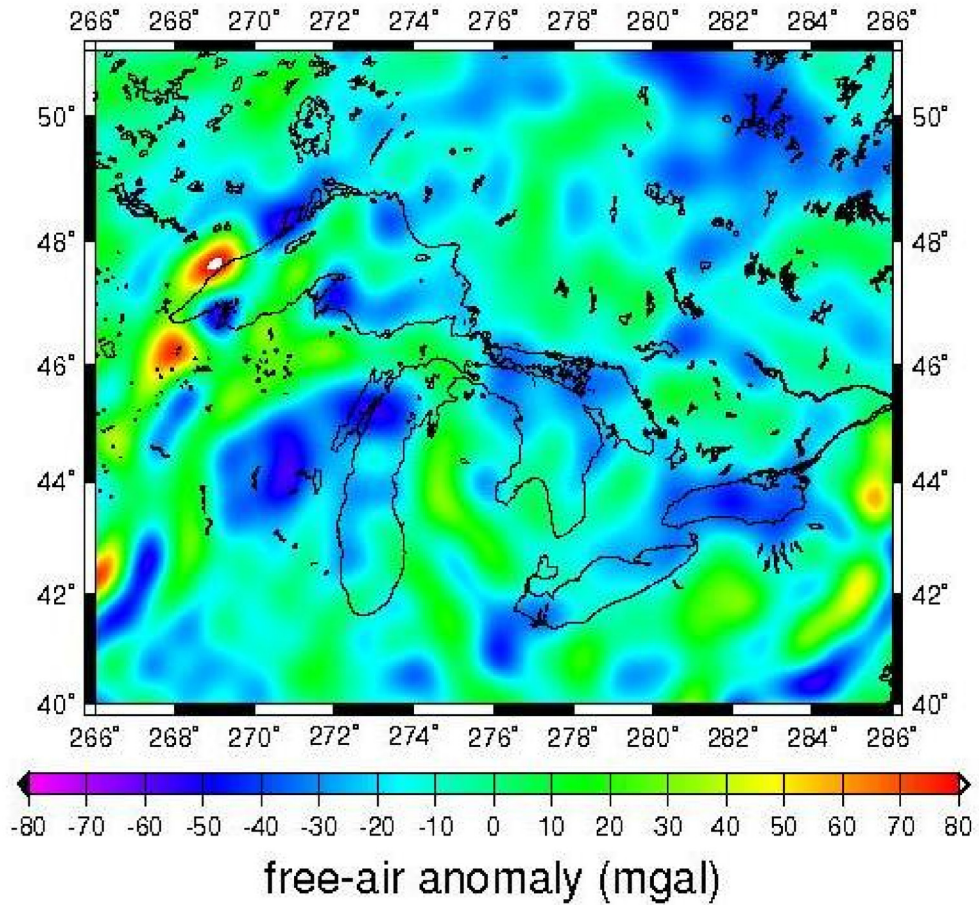


Figure 7.6: EIGEN-GL04C free-air anomalies over the Great Lakes.

Although Figures 7.4 and 7.6 show similar trends, the EIGEN-GL04C field is much smoother than the satellite altimetry results. Also, while the EIGEN-GL04C model does show some response to bathymetry, high-frequency bathymetric phenomena are not

distinguishable in the field. Thus satellite altimetry results provide additional high frequency information on topographic density formations neither available from low-resolution global geopotential fields, nor from low-frequency satellite gravimetry results.

7.3.2 Comparisons along test profiles

Our results were next compared to free-air anomalies from shipborne or airborne gravity observations over the lakes. In this way, the high-frequency component of our results could be tested. Figure 7.7 shows the results for comparisons with all shipborne and airborne data over the lakes. The profiles are labeled P1 to P13, in the order in which they were tested. Profiles P2, P9, P10 and P5 are drawn from airborne gravity surveys, while the other profiles come from shipborne surveys.

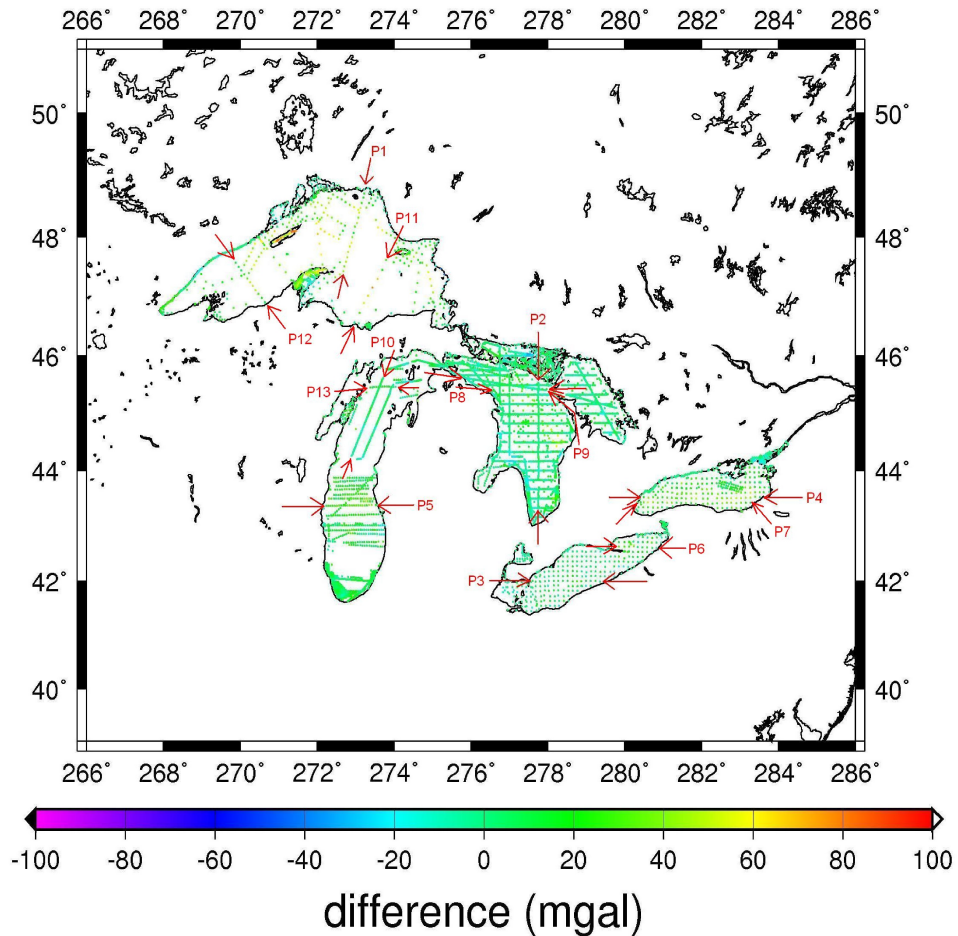
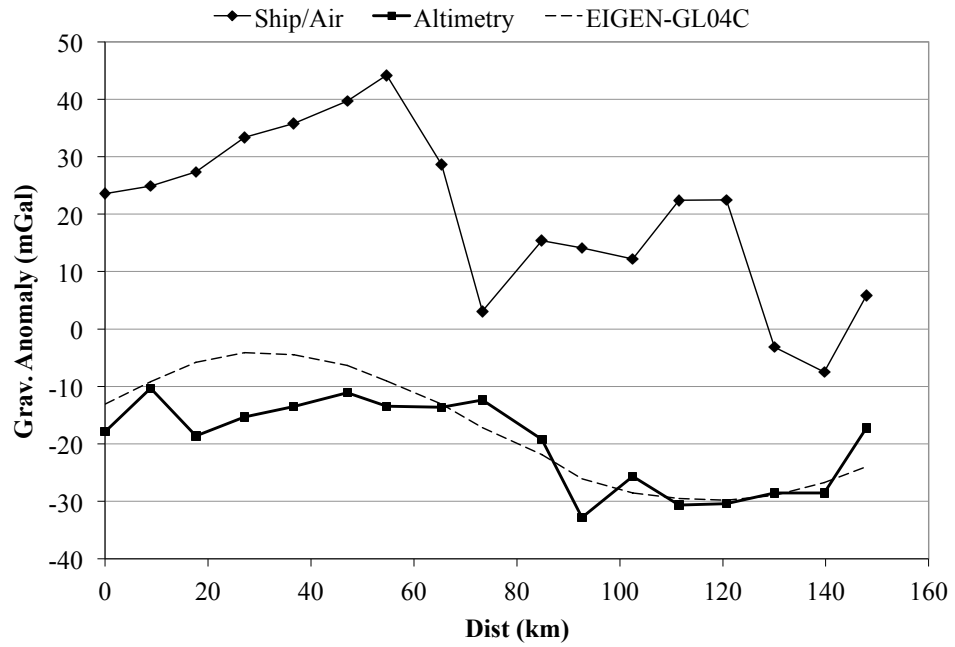


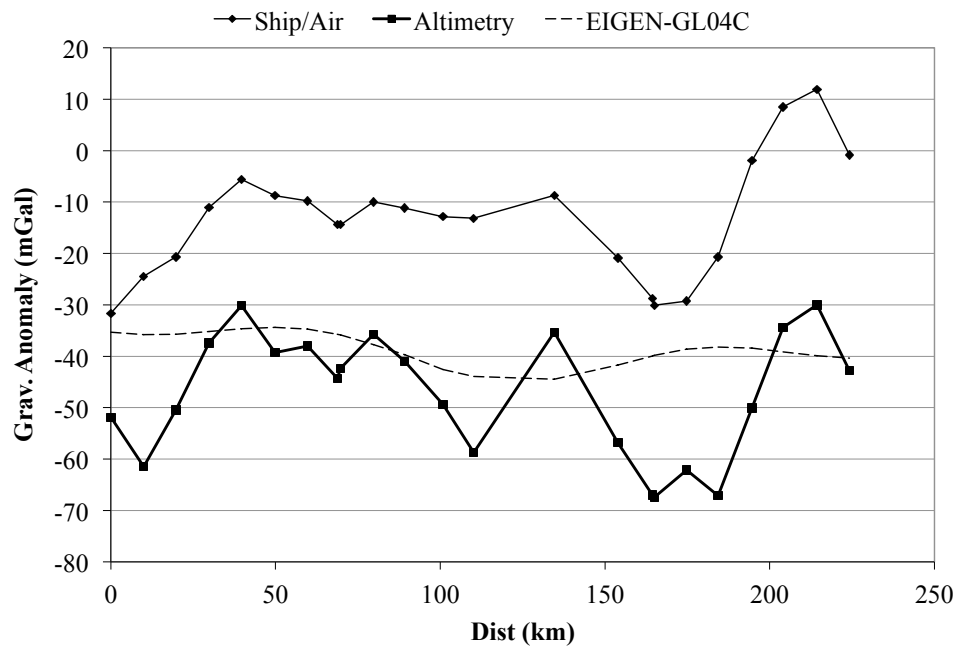
Figure 7.7: Results of comparisons with terrestrial gravity results.

Although as can be seen above many of the airborne and shipborne results used for comparisons were within at most twenty mGal of the altimetry results, in some cases there were significant differences. These are usually in the case of shipborne results, resulting from a large bias in shipborne data as compared to both results from satellite altimetry and from geopotential models. Typical examples are profiles P1 for Lake Superior, and P4 for Lake Ontario, shown in Figure 7.8. Gravity values given by EIGEN-GL04C are included in the plots (dotted line) alongside those from satellite

altimetry (thick line) and shipborne/airborne results (narrow line). This convention is continued in later profile plots.



(a)

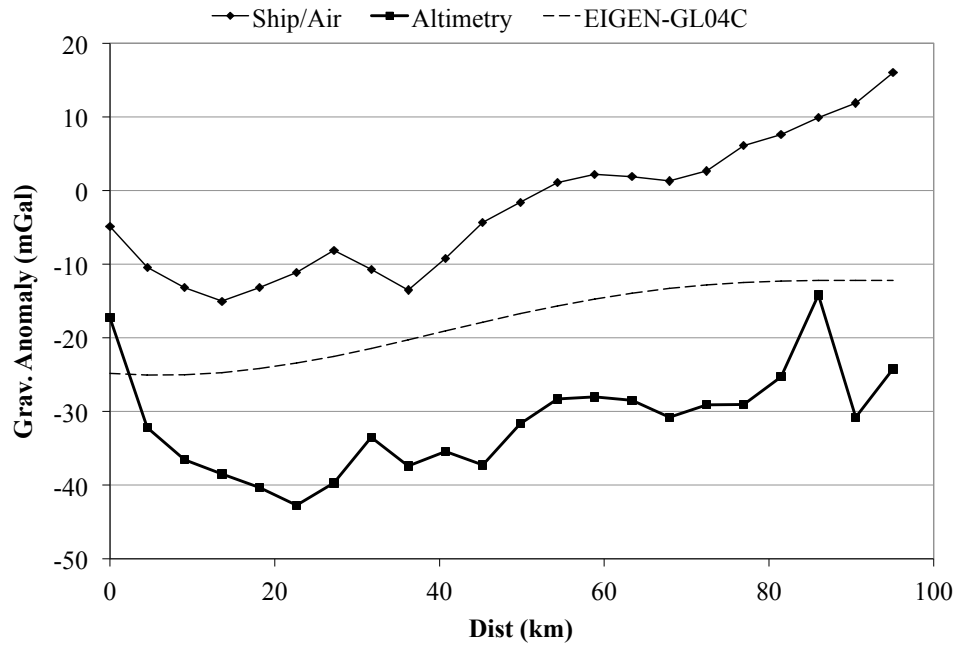


(b)

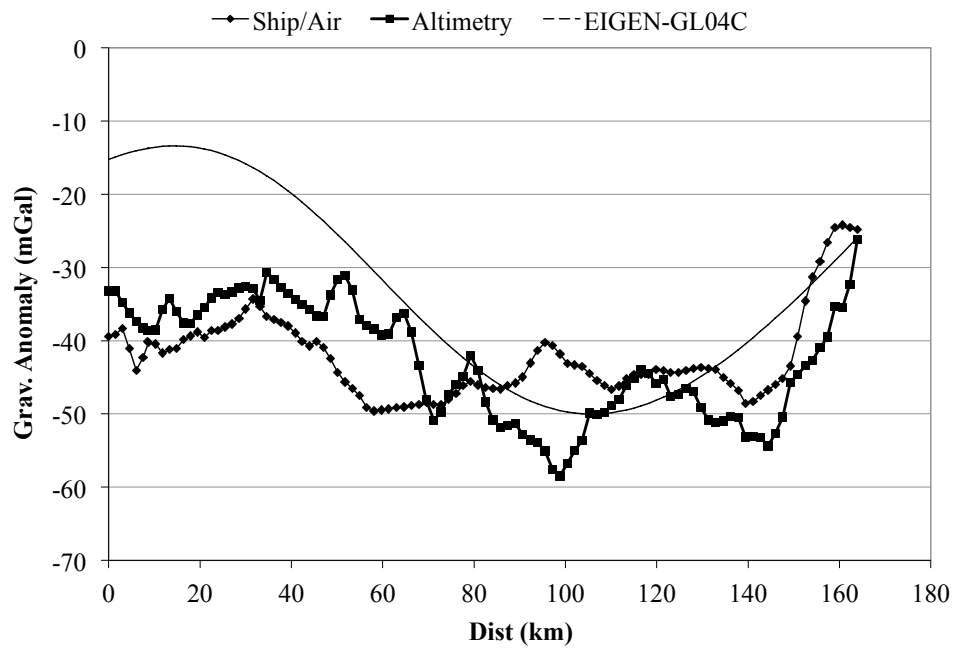
Figure 7.8: Profiles showing gravity for P1 (a) and P4 (b) from EIGEN-GL04C, shipborne, and satellite altimetry results.

These profiles show a distinct bias in the shipborne observations. Furthermore, P4 shows quite clearly the high frequency field visible from the satellite altimetry results. The wide dip near the right side of the graph is particularly telling, as it corresponds exactly with a dip in the bed of Lake Ontario. These results introduce an unexpected reason why satellite altimetry data is useful in studies of gravity over lakes: publicly available shipborne data are not all reliable.

In other areas, the shipborne/airborne data agreed well (within $\pm \sim 10$ mGal, without bias) with satellite altimetry results. This was usually the case with airborne data, such as along P2 and P9 in Lake Huron. In other cases, while airborne and altimetry results agreed very well with each other, they were different from EIGEN-GL04C results. This is the case for P10 over Lake Michigan. Both P9 and P10 are shown in Figure 7.9 as illustrations of agreement between satellite altimetry and airborne results.



(a)

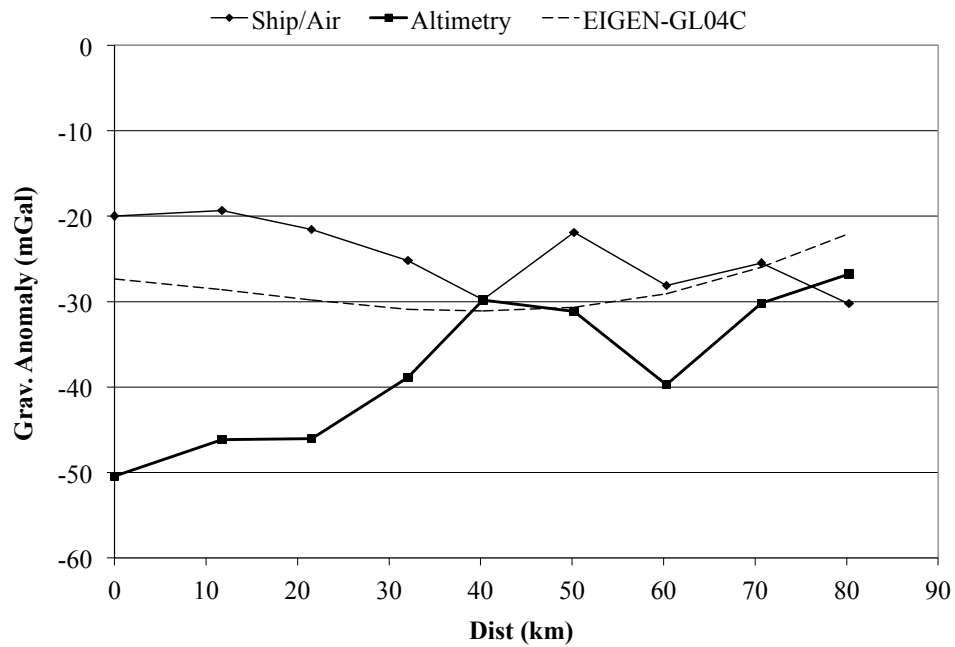


(b)

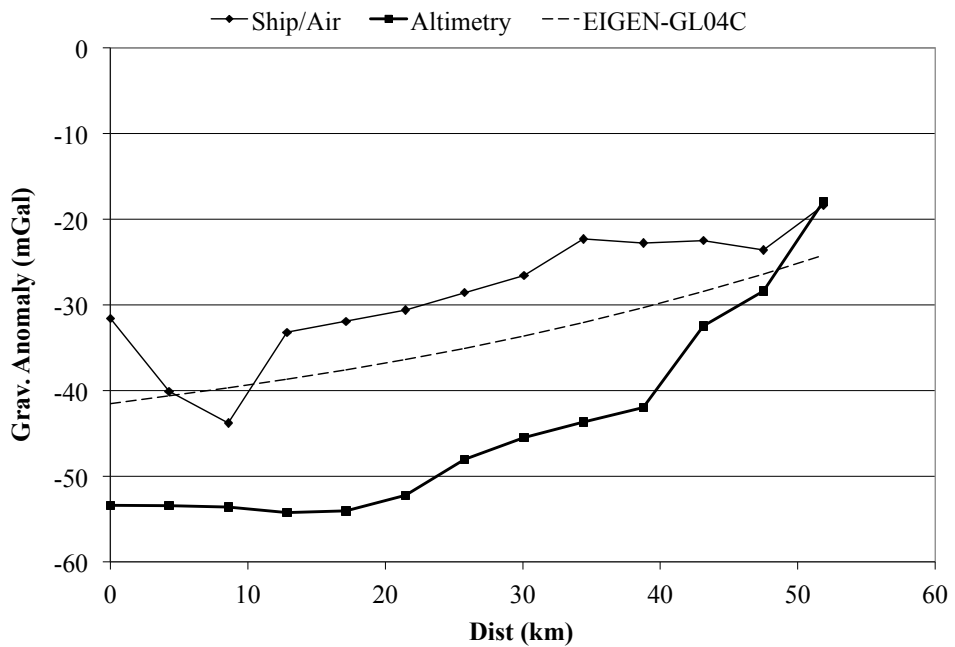
Figure 7.9: Profiles showing gravity for P9 (a) and P10 (b) from EIGEN-GL04C, airborne, and satellite altimetry results.

Note that the divergence between EIGEN-GL04C and airborne/altimetry results at the left side of Figure 7.9b is likely the result of a long narrow dip in the bed of Lake Michigan which runs along the first half of the profile. Because of the narrowness of this formation, it does not appear in the EIGEN-GL04C field at only degree 360, although it has a noticeable effect on the other two sets of results. It is noteworthy that satellite altimetry and airborne results register this effect with similar accuracy to each other. This implies a strong response to underwater density formations in satellite altimetry results.

Finally, there are some situations where the satellite altimetry results are simply inadequate, as revealed by large differences from both the EIGEN-GL04C and shipborne gravity. Two such situations occur for profiles P6 and P13, shown in Figure 7.10 below.



(a)



(b)

Figure 7.10: Profiles showing gravity for P6 (a) and P13 (b) from EIGEN-GL04C, shipborne, and satellite altimetry results.

Sometimes there are clear physical explanations for these differences, as with P6 in Lake Erie, which shows a difference of about 30 mGal between satellite altimetry results and shipborne/EIGEN-GL04C results at its west side. In that case, the difference grows as the shallow lake (maximum depth of 64m) becomes more shallow near to the shore. The difference is presumably a result of the effect of this shallowness on satellite altimetry results. Perhaps in the case of lakes – especially those with relatively shallow areas extending far from shore – it is better to decide which satellite altimetry data to use based on water depth, and not just proximity to a shoreline.

In occasional situations, however, satellite altimetry data shows deviations from EIGEN-GL04C and shipborne results for no apparent reason. While this was rare among the profiles we tested, it is the case for P13, where the altimetry results differ by up to 22 mGal from the shipborne results and show a bias from EIGEN-GL04C results of about 15 mGal along most of the profile. For other profiles, all differences between sources of gravity data have been explicable for one of the reasons above: a bias in the airborne/shipborne data, the inability of the EIGEN-GL04C field expanded to degree 360 to register local density contrasts (those having high-frequency signals), and the errors in satellite altimetry results over shallow waters. None of these effects is clearly responsible for the differences between results visible along P13. The left half of the profile at least is over deep water, and so errors in altimetry results over shallow waters cannot have caused the discrepancy. Comparison with bathymetry does not reveal any correlation with bathymetric formations, and even if it did we would expect to see these formations in shipborne results as well. And finally, the shipborne results agree well with EIGEN-GL04C, showing that the difference is in the altimetry results.

7.3.3 Statistical examination of results

Although our results were not rigorously tested, some comments can be made about their statistical behavior. In particular, the maximum, minimum and average differences between our satellite-altimetry derived gravity field and both the EIGEN-GL04C and shipborne/airborne gravity results, and their standard deviations, can be examined. These statistics are provided in Table 7.1.

Table 7.1: Statistics of differences in free-air anomalies between altimetry, EIGEN-GL04C and shipborne/airborne results (all values in mGal).

Profile	Altimetry – EIGEN-GL04C				Altimetry – Air/Shipborne			
	Max	Min	Avg	SD	Max	Min	Avg	SD
P1	7	-13	-2	5	-15	-58	-40	13
P2	2	-13	-4	4	9	-11	-2	4
P3	10	-16	-3	7	12	-20	-4	8
P4	10	-29	-9	12	-20	-48	-34	8
P5	8	-19	-13	6	-12	-43	-29	7
P6	1	-23	-9	8	3	-30	13	12
P7	21	-34	-9	17	-8	-48	-31	12
P8	2	-12	-4	6	-5	-29	-18	8
P9	5	-15	-5	5	10	-10	0	5
P10	5	-25	-10	8	15	-17	0	7
P11	1	-22	-9	9	-21	-77	-48	23
P12	17	-43	-16	19	-9	-50	-29	17
P13	6	-16	-10	7	1	-22	-16	7

Notice first that the altimetry results are consistently lower than the EIGEN-GL04C gravity. This is anticipated, since the global geopotential model represents a smoothing of the gravity field, and thus is less affected by the density anomalies represented by the lakes. Because the water in a lake has a lower density than surrounding topography, it

will reduce the value of gravity at the lake surface. However, while gravity at points on the lake's surface will be sensitive to these effects, a smoothed gravity field will be more strongly influenced by the more distant topographical masses surrounding lakes. Thus we expect the smooth EIGEN-GL04C field to be slightly stronger than one derived by satellite altimetry, seaborne or airborne observations.

If we follow the assumption that the EIGEN-GL04C field represents well the low-frequency gravity field over the lakes, we can consider the standard deviation of the differences between this and the altimetry results like an RMS error. If we do so, we can see an error in the differences of less than 13 mGal for most profiles, which is acceptable. However, the maximum and minimum values show that for most profiles there are some points which lie well outside of this range.

In contrast to differences with EIGEN-GL04C, differences with shipborne/airborne results do not show a variety of standard deviations. In some cases (profiles 4, 7 and 12), standard deviations of the differences are lower than for EIGEN-GL04C, suggesting that in these cases the shipborne/airborne data and the altimetry results both are modeling the high frequency component of the gravity field better than the EIGEN-GL04C model. In others (profiles 2, 3, 5, 8, 9, 10 and 13) the standard deviations are similar to those for the differences with the EIGEN-GL04C model. This is often the case for profiles based on airborne results (profiles 9, 10 and possibly 5), in which the airborne results tend to be smoother than the altimetry results. Finally, in some cases (profiles 1, 6 and 11) the standard deviations are much higher than those with the EIGEN-GL04C field. In these cases, it is often large peaks in the shipborne/airborne results which cause the difference. Note also that while some profiles show high magnitude minima for differences with

EIGEN-GL04C, this is somewhat deceiving since most of these are the result of high frequency bathymetric variations rather than errors in the altimetry results.

Also, in general the altimetry results agree better with the EIGEN-GL04C model than with the shipborne and airborne results. This implies that there is little bias in the altimetry results (no more than 16 mGal in magnitude, for these profiles), while there is certainly a larger bias in some of the airborne/shipborne results (as much as 48 mGal). Profiles where bias is especially present in shipborne results are 1, 4, 5, 7, 8 and 11. However, for some profiles (2, 3, 9 and 10), there is a very good agreement with shipborne/airborne results. For these profiles, the maximum and minimum differences are relatively small (they never exceed 20 mGal), while the standard deviation of the differences is even smaller (never exceeding 8 mGal) and the bias ranges from small (4mGal) to nonexistent.

7.4 Conclusion

Satellite altimetry data provide a higher frequency gravity field over lake areas than satellite-derived geopotential models, and is sometimes better than publicly available shipborne gravity data in the same areas. Altimetry results are mostly unbiased with respect to satellite-derived global geopotential fields such as EIGEN-GL04C. Where a bias between the two is present, it is usual explicable by reference to bathymetry formations which are captured by the altimetry-derived gravity field, but not by the low frequency geopotential fields. Furthermore, the altimetry results agree often with airborne and sometimes with shipborne gravity results, showing that they are able to

accurately model the high frequency component of the gravity field. In many cases where they do not agree with shipborne results, it appears that it is the shipborne data which is flawed, often having a constant bias from the EIGEN-GL04C field. However, the accuracy of altimetry results over lakes is on the order of tens of milligals, which is insufficient to distinguish many density formations. Noise of this order might easily be mistaken for lake density effects in the absence of data to validate the altimetry results. Furthermore, in some cases deviations of altimetry results from other data sources occur. Most of these are explicable due to shallow waters adversely affecting altimetry results, but in rare cases no explanation is apparent. Thus while altimetry promises to model well the high frequency gravity field in areas of sparse data over lakes, they still need to be refined before they can provide a reliable gravity field of high accuracy.

Chapter 7 References

- Andersen, O., P. Knudsen, and R. Trimmer (2001). "The KMS2001 Global Mean Sea Surface and Gravity Field." Paper presented at the International Association of Geodesy 2001 Scientific Assembly, Budapest, Hungary, September 2–7.
- Flechtner, F. (2006). *Combined Gravity Field Model EIGEN-GL04C*. Department 1, GFZ-Potsdam. [On-line] October 28, 2006. http://op.gfz-potsdam.de/grace/results/grav/g005_eigen-gl04c.html
- Hofmann-Wellenhof, B., and H. Moritz (2005). *Physical Geodesy*. Springer, New York, U.S.A.
- Huang, J., P. Vaníček, S. Pagiatakis, and W. Brink (2001). "Effect of topographical density on the geoid in the Rocky Mountains." *Journal of Geodesy*, Vol. 74, No. 11–12, pp. 805–815, doi: 10.1007/s001900000145.
- Hwang, C., E. Kao, and B. Parsons (1998). "Global marine gravity anomalies from Seasat, Geosat, ERS-1 and TOPEX/POSEIDON altimeter data." *Geophysical Journal International*, Vol. 134, No. 2, pp. 449–459.
- Hwang, C. (1999). "A Bathymetric Model for the South China Sea from Satellite Altimetry and Depth Data." *Marine Geodesy*, Vol. 22, No. 1, pp. 37–51, doi: 10.1080/014904199273597.
- Hwang, C., H. Hsu, and R. Jang (2002). "Global Mean Sea Surface and Marine Gravity Anomaly from Multi-satellite Altimetry: Applications of Deflection-geoid and Inverse Vening Meinsz Formulae." *Journal of Geodesy*, Vol. 76, No. 8, pp. 407–418, doi: 10.1007/s00190-002-0265-6.
- Hwang, C., and Y.-S. Hsiao (2003). "Orthometric corrections from leveling, gravity, density and elevation data: a case study in Taiwan." *Journal of Geodesy*, Vol. 77, No. 5–6, pp. 279–291, doi: 10.1007/s00190-003-0325-6.
- Hwang, C., and H.-Y. Hsu (2003) "Marine Gravity Anomaly from Satellite Altimetry: a Comparison of Methods over Shallow Waters." In *Satellite Altimetry for Geodesy, Geophysics and Oceanography*, Eds. C. Hwang, C. Shum and J. Li. Vol. 126 of *International Association of Geodesy Symposia*, Springer, New York, U.S.A., pp. 59–66.
- Kingdon, R., P. Vaníček, A. Ellmann, M. Santos, and R. Tenzer (2005). "Toward an improved orthometric height system for Canada." *Geomatica*, Vol. 59, No. 3, pp. 241–249.

- Moritz, H. (1980). *Advanced Physical Geodesy*. Abacus Press, Turnbridge, England.
- Sandwell, D., and W. Smith (1997). "Marine gravity anomaly from Geosat and ERS-1 satellite altimetry." *Journal of Geophysical Research*, Vol. 102, No. B5, pp. 10039–10054, doi:10.1029/96JB03223.
- Sandwell, D., and W. Smith (2005). "Retracking ERS-1 altimeter waveforms for optimal gravity field recovery." *Geophysical Journal International*, Vol. 163, No. 1, pp. 79–89, doi: 10.1111/j.1365-246X.2005.02724.x.
- Schwab, D., and D. Sellers (1996). "Computerized bathymetry and shorelines of the Great Lakes." NOAA Data Report ERL GLERL-16, Great Lakes Environmental Research Laboratory, Ann Arbor, Michigan, U.S.A.
- Smith, W., and D. Sandwell (1994). "Bathymetric Prediction from Dense Satellite Altimetry and Sparse Shipboard Bathymetry." *Journal of Geophysical Research*, Vol. 99, No. B11, pp. 21803–21824, doi: 10.1029/94JB00988.
- Tscherning, C., and R. Rapp (1974). "Closed covariance expressions for gravity anomalies, geoid undulations and deflections of the vertical implied by anomaly degree variance models." Reports of department of geodetic Science and Surveying, Report No 208, Department of Geodetic Science and Surveying, Ohio State University, Columbus, Ohio, U.S.A.
- Vergos, G., and M. Sideris (2002). "Improving the Estimates of Ocean Bottom Topography with Altimetry Derived Gravity Data Using the Integrated Inverse Model." *Vistas for Geodesy in the New Millenium*, Eds. J. Ádám and K.-P. Schwarz. International Association of Geodesy 2001 Scientific Assembly, Budapest, Hungary, September 2–7, 2001. *International Association of Geodesy Symposia*, Vol. 125, Springer, New York, U.S.A., pp. 529–534.
- Wessel, P., and W. H. F. Smith (1999). *The Generic Mapping Tools (GMT), Technical Reference and Cookbook*. University of Hawaii, Hawaii, U.S.A.

Chapter 8: Conclusion

8.1 Summary of findings from the 6 articles

This dissertation set out to investigate whether orthometric heights, determined either directly or from geodetic height observations in conjunction with accurate geoid modeling, could be determined to one centimetre accuracy using existing theory, numerical methods, and data sets. The problem has been addressed in six articles, covering new developments in all three areas.

8.1.1 Articles dealing with corrections to Helmert orthometric heights

The article “Toward an improved orthometric height system for Canada” demonstrates the practical evaluation of the terrain, density and NT geoid-generated gravity disturbance corrections to upgrade from Helmert to rigorous orthometric height. It also provides results showing the size and characteristics of these corrections. For a test area in the Canadian Rocky Mountains, the terrain correction is found to reach 31 cm in magnitude and to be predominantly negative, as expected. Negative gravity disturbances in the region, perhaps due to isostatic compensation, result in a predominantly positive NT geoid-generated gravity disturbance correction, reaching 21 cm in magnitude. The anomalous density correction is much smaller, with signs alternating according to density anomalies and magnitudes up to 7 cm, and is comparable to results from other studies. In the total correction to Helmert heights, the terrain and NT gravity disturbance corrections cancel each other significantly, so that the magnitude is at most 17 cm. The

large values of the corrections to Helmert heights indicate that, at least in some areas, these corrections must be applied to obtain accurate orthometric heights. The small values of the density correction, here computed from a laterally-varying DDM, show that even in a test area having very large heights and high density contrasts the anomalous density corrections are only a few centimetres. The remaining error from not applying a three-dimensional DDM is presumably less than that. Thus, even using two-dimensional DDMs, orthometric heights can be evaluated to an accuracy of a few centimetres – so long as that the input data is of sufficient quality and accurate numerical methods are applied.

“Computationally efficient correction to Helmert orthometric heights for terrain and density effects”, describes a method for calculating the terrain and anomalous density corrections that is accurate numerically to within about 1%, or up to 1 cm, according to testing in a “tower scenario”. The method also reduces computation time by at least 50% compared to alternative methods, demonstrating that rigorous orthometric heights can be calculated efficiently with little numerical error. Although the method used in this article was more refined than that of the preceding article, both produced similar results for similar test areas, thereby validating each other.

8.1.2 Articles on errors in laterally-varying density models for geoid determination

In “Modeling topographical density for geoid determination”, current methodologies for constructing three-dimensional DDMs and some existing DDMs are reviewed, with the conclusion that three dimensional DDMs that guarantee a centimetre-level geoid result

do not exist and cannot be practically realized. Next, a mathematical framework for calculating the DTE, PITE and SITE on geoidal height for three-dimensional bodies of anomalous density is proposed. This framework is applied using somewhat coarse numerical methods, that provide in the worst case numerical errors of 25% for the DTE (for small values of the DTE), but usually errors of 20% or below. The PITE and SITE results have less than 8% error in all cases.

Using the proposed methodology, simulations are performed using hypothetical density models designed to find a worst-case estimate of the errors in the laterally-varying model. For each simulation, Stokes's integration is performed on the DTE and SITE to convert them into effects on geoidal height, and the PITE is subtracted from these to find the total error in the geoid from all masses neglected in the laterally-varying model. The DTE and PITE are similar in magnitude, with both reaching about 1 cm for the most extreme test case, while the SITE is negligible. The DTE and PITE do not cancel each other in the worst-case, and the error discovered in this case has an effect on the geoid of 2.2 cm, for a shallow, slightly rotated disc, with density contrast of 660 kg/m^3 . Considering that this is the expected worst-case error, shortcomings in geoids computed from laterally-varying DDMs are expected to be smaller than about 2 cm in most cases.

The methodology is further demonstrated by evaluating the shortcomings of using a laterally-varying DDM to model the effects of the waters of Lake Superior in Canada. The lake waters are assigned a density of 1000 kg/m^3 , a density contrast of -1670 kg/m^3 relative to surrounding rock, which is assumed to have a density of 2670 kg/m^3 . Lake

Superior bathymetry provides the interface between the two densities for creating a three-dimensional DDM, and a two-dimensional DDM for comparison. The geoid error resulting from using the laterally-varying DDM only is calculated, and even for this large density contrast, only reaches 9 mm. If a laterally-varying DDM provides centimetre level accuracy for such an extreme density contrast, then in most areas, laterally-varying DDMs should be sufficient to produce precise geoid results.

“Effects of hypothetical complex mass-density distributions on geoidal height” adds to the previous result by examining the extent to which adjacent anomalous density masses cancel each other’s effects. This is done by creating two arrays of discs of anomalous density with high density contrasts, one array designed to maximize the DTE of the discs, and the other to maximize the PITE. Following publication of the previous paper, more extreme worst-case simulations for the DTE and PITE had been developed, that produced laterally-varying DDM errors twice as large as those in the previous article, or about 5 cm in magnitude. The principles used to develop these are listed in this article, and form a useful guide for what sort of density distributions are not well represented by a DDM that varies only laterally. These principles are, in order of importance: (1) the topographical elevation is large, (2) the anomalous density is distributed far from the geoid, and (3), there is a large density contrast. It is found that the DTEs of adjacent discs mitigate each other significantly, while the PITE’s do not. Although the DTEs of individual discs were four times larger than in the previous article, after Stokes’s integration, the DTE of the array of discs was under 1 cm in magnitude. The PITE, by contrast, is 5 cm in magnitude – the same magnitude as if there

were no other discs nearby. This article applies a slightly more refined numerical computation than the previous one, with errors in the DTE reduced to 18%, and in the PITE reduced to 5%. Considering that the worst-case scenario for the DTE, without adjacent discs, had an effect of 5 cm, this suggests that the numerical methods used to evaluate density effects can obtain about 1 cm accuracy.

8.1.3 Articles dealing with numerical and data issues

The article “Poisson downward continuation by the relaxed Jacobi method” proposes a regularization of the downward continuation by choosing a tolerance for the popular Jacobi iterative method in a way that accounts for the ill-conditioning of the problem. The suggested method is applied for an area in Papua New Guinea with heights of about 3300 m, using the AusSEGM synthetic gravity field [Baran et al., 2006] to provide data at a 1’ spacing, such that conditioning of the downward continuation problem is very bad. For a **B** matrix with condition number of about 1347, as estimated by the L_1 norm, the regularization by relaxing the Jacobi tolerance provides a solution of reasonable smoothness as compared to the result using a conventional choice of tolerance. The maximum difference between the gravity anomalies on the topographical surface and on the geoid using conventional methods is 1330 mGal, while after using the new regularization method it is less than 150 mGal.

Finally, in “Gravity Anomalies from retracked ERS and Geosat Altimetry over the Great Lakes: Accuracy Assessment and Problems”, gravity anomalies from satellite altimetry over the Great Lakes in North America are compared with those deduced from

the GRACE-based EIGEN-GL04C geopotential model and with airborne and shipborne gravity data along similar profiles. The results identify altimetry over lakes as a data source still in need of refinement. While in most cases, the altimetry results agree with the EIGEN-GL04C field to about 10 mGal RMS, and in many cases they agree this well with airborne/shipborne observations, in others there are discrepancies of up to 50 mGal between satellite altimetry and other data sources. Some of the EIGEN-GL04C discrepancies are explicable as the result of bathymetric features too small to be resolved in the EIGEN-GL04C field, and the discrepancies with much of the airborne/shipborne data seem to result from biases in the terrestrial data sources rather than the altimetry. However, there is no obvious source for some biases and discrepancies, and even where there is good agreement the range of discrepancies is often on the order of 30 or 40 mGal. The conclusion must be that while the altimetry results are approximately correct, and many of their large discrepancies with EIGEN-GL04C would be removed in averaging them over 5' or 1' cells as is common in geoid determination, further accuracy improvement is necessary. The biases between altimetry and other results are especially troubling, because these would not be removed by averaging.

8.1.4 Summary of Contributions

Taken together, these articles address a cross-section of the most important problems in orthometric height determination. They show that current theoretical developments in topographical density modeling can provide orthometric heights accurate to several centimetres in the worst case, and one centimetre or better in most cases, even using models of topographical density that only include lateral density variations. They

provide a description of what type of density distributions might reduce the accuracy of the lateral-density model, and show that orthometric heights must be calculated using the rigorous method, rather than Helmert's, to provide centimetre level accuracies in mountainous regions. Numerical methods are proposed for applying three-dimensional topographical density models, should they become available, to a numerical accuracy of about a centimetre; for calculating effects of terrain and laterally-varying density also to centimetre level accuracy; and for regularizing the downward continuation problem in a simple but effective way. Finally, satellite altimetry is assessed as a data source for geoid modeling over lakes, and found, while still in need of refinement, to hold some promise.

The question asked at the start of this dissertation is whether a physically meaningful height system can be practically realized. The answer is that the theoretical and numerical apparatus exist to realize such a system at the centimetre level in most areas, and to several centimetres in challenging areas. While existing gravity and topographical density data sets do not support this accuracy everywhere, new data sources, such as satellite altimetry over lakes, promise to fill some gaps in the current data.

8.2 Recommendations for further study

In future studies, it would be beneficial to investigate the numerical methods of topographical effect calculation for geoid determination as thoroughly as for the topographical corrections to orthometric height in Chapter 3. Likewise, errors in using laterally-varying DDMs for orthometric height corrections should be estimated,

following the procedure applied for geoid determination in Chapters 4 and 5.

For both orthometric heights and geoid determinations, an attempt to collect three-dimensional density information of sufficient quality over a sufficiently large and challenging area for validation purposes would be ideal. Some areas already have the extensive geophysical observations, including Bouguer anomaly maps, surficial and bedrock geology maps of high resolution, borehole data and seismic data, that can be used to create density models of relatively high resolution. The island of Taiwan is one such study area, as multiple three-dimensional DDMs with relatively high resolution (2 km cubes) have already been created covering the island, as well as a DEM at 40 m resolution, with supposed 1 m vertical accuracy [Yen and Hsieh, 2010]. Even the existing model, with 2 km cubes, would provide an interesting case study, although a model of higher resolution would be preferable.

Validation using borehole gravimetry would do much to support the theory of rigorous orthometric heights. An approach such as that of Strange [1982] could be replicated, using modern advances in borehole gravimetry, preferably in an area with large elevations and strong density contrasts.

The downward continuation method proposed in Chapter 6 could be improved by developing a fast and sufficiently accurate means of estimating the condition number of the \mathbf{B} matrix. It should also be validated by comparison to other regularization methods already used in downward continuation, like the Tikhonov regularization [Tikhonov, 1977]. It would further be useful also to test the downward continuation procedure on gravity anomalies determined at the topographical surface by spherical harmonic

synthesis using a GGM (e.g., the EGM2008 [Pavlis et al., 2008]), and comparing the downward continued result to anomalies on the geoid determined from the same GGM. This method would provide an assessment of the accuracy of the downward continuation more substantial than just examining the apparent roughness of the solution.

The vertical errors in GNSS are currently the most important data source to investigate for improvement of orthometric height determination from geodetic height observations. However, any improvement to gravity data that might provide gravity anomalies at higher resolutions is likely to improve geoid calculation results. As indicated by Chapter 7, further analysis of the errors in altimetry-derived gravity over lakes, and improved processing methods to mitigate these errors, are required for satellite altimetry to provide a useful source of gravity data over inland waters. This application may also be helped by new altimetry missions such as Jason-2/OSTM [Lambin et al., 2010].

Chapter 8 References

- Baran, I., M. Kuhn, S. Claessens, W. Featherstone, S. Holmes, and P. Vaníček (2006). “A synthetic Earth gravity model designed specifically for testing regional gravimetric geoid determination algorithms.” *Journal of Geodesy*, Vol. 80, No. 1, pp. 1–16, doi: 0.1007/s00190-005-0002-z.
- Lambin, J., R. Morrow, L.-L. Fu, J. Willis, H. Bonekamp, J. Lillibridge, J. Perbos, G. Zaouche, P. Vaze, W. Bannoura, F. Parisot, E. Thouvenot, S. Coutin-Faye, E. Lindstrom, and M. Mignogno (2010). “The OSTM/Jason-2 mission.” *Marine Geodesy*, Vol. 33, Supplement 1, pp. 4–25, doi: 10.1080/01490419.2010.491030.
- Pavlis, N., S. Holmes, S. Kenyon, and J. Factor (2008). “An Earth Gravitational Model to Degree 2160: EGM2008.” Paper presented at the 2008 General Assembly of the European Geoscience Union (ESU), Vienna, Austria, April 13–18.
- Strange, W. (1982). “Evaluation of orthometric height accuracy using bore hole gravimetry.” *Bulletin Géodésique*, Vol. 56, No. 4, pp. 300–311, doi: 10.1007/BF02525730.
- Tikhonov, A. N. and V. Y. Arsenin (1977). *Solutions of Ill-posed Problems*. John Wiley and Sons, New York, U.S.A.
- Yen, H.-Y., and H.-H. Hsieh (2010). “A Study on the Compatibility of 3-D Seismic Velocity Structures with Gravity Data of Taiwan.” *Terrestrial, Atmospheric and Ocean Sciences*, Vol. 21, No. 6, pp. 897–904, doi: 10.3319/TAO.2010.03.03.01(T)

Vita

- Candidate's full name:** Robert William Kingdon
- Place and date of birth:** Orangeville, Ontario, Canada / 14 November 1981
- Permanent address:** 1426 Grimm Road
Middle LaHave, NS, Canada B4V 3L6
Phone: 1-902-766-4604
Email: robert.kingdon@unb.ca
- Schools attended:** Glooscap Elementary School, Canning, N.S.,
Canada / 1987 to 1989
Centre Consolidated School, Lunenburg, N.S.,
Canada / 1989 to 1997
Park View Education Centre (International Baccalaureate
Program), Bridgewater, N.S., Canada / 1997 to 2000
- Universities attended:** University of New Brunswick, Fredericton,
New Brunswick, Canada / 2000 to 2012

Publications

- Kingdon, R., P. Vaníček, A. Ellmann, M. Santos, and R. Tenzer (2005). "Toward an improved orthometric height system for Canada." *Geomatica*, Vol. 59, No. 3, pp. 241–249.
- Nievinski, F., K. Cove, M. Santos, D. Wells, and R. Kingdon (2005). "Range-Extended GPS Kinematic Positioning using Numerical Weather Prediction Model." *Proceedings of the Institute of Navigation 61st Annual Technical Meeting*. Cambridge, M.A., U.S.A., June 27–29, 2005, pp. 902–911.
- Santos, M., P. Vaníček, W.E. Featherstone, R. Kingdon, B.-A. Martin, M.Kuhn and R. Tenzer (2006). "Relation between the rigorous and Helmert's definitions of orthometric heights." *Journal of Geodesy*, Vol. 80, No. 12, pp. 691–704. doi: 10.1007/s00190-006-0086-0.
- Ellmann, A., P. Vaníček, M. Santos, and R. Kingdon (2006). "Interrelation between the geoid and orthometric heights." *Proceedings of the 1st International Symposium of the International Gravity Field Service "Gravity Field of the Earth"*, Ed. R. Forsberg and A. Kilicoglu. Istanbul, Turkey, August 28–September 1, 2006. pp. 130–135.
- Kingdon, R., C. Hwang, Y.-S. Hsiao, and M. Santos (2007). "Gravity Anomalies from retracked ERS and GeoSat Altimetry over the Great Lakes: Accuracy Assessment and Problems." *Terrestrial, Atmospheric and Ocean Sciences*, Vol. 19, No. 1–2, pp. 93–102, doi: 10.3319/TAO.2008.19.1-2.93(SA).
- Kingdon, R., P. Vaníček, and M. Santos (2009). "Modeling topographical density for geoid determination." *Canadian Journal of Earth Sciences*, Vol. 46, No. 8, pp. 571–585, doi: 10.1139/E09-018.
- Kingdon, R., P. Vaníček, and M. Santos (2011). "Effects of hypothetical complex mass-density distributions on geoidal height." *Geodesy for Planet Earth*, Eds. S. Kenyon, M. Pacino and U. Marti. International Association of Geodesy IAG2009 "Geodesy for Planet Earth" Scientific Assembly, Buenos Aires, Argentina, 31 August–4 September, 2009. *International Association of Geodesy Symposia*, Vol. 135, Springer, New York (in press).
- Kingdon, R., and P. Vaníček (2011). "Poisson downward continuation solution by the Jacobi method." *Journal of Geodetic Science*, Vol. 1, No. 1, pp. 74–81, doi: 10.2478/v10156-010-0009-0.
- Vaníček, P., R. Kingdon, M. Santos (2012). "Geoid vs. quasi-geoid: a case of physics versus geometry." *Contributions to Geophysics and Geodesy* (in press).

Kingdon, R., P. Vaníček, M. Santos, and A. Ellmann (2012). “Efficient correction of Helmert orthometric heights for terrain and density effects.” *Computations and Geosciences* (in preparation).

Conference Papers

Kingdon, R., R. Tenzer, P. Vaníček, and M. Santos (2004). "Calculation of the spherical terrain correction to Helmert's orthometric height." Joint AGU/CGU Scientific Meeting, Montreal, Canada, May 17–21.

Kingdon, R., P. Vaníček, M. Santos, A. Ellmann, R. Tenzer (2005). "Corrections for the improvement of the Canadian height system." Paper presented at the 31st Canadian Geophysical Union Annual Scientific Meeting, Banff, Alberta, Canada, May 8–11.

Santos, M., F. Nievinski, K. Cove, R. Kingdon and D. Wells (2005). *Range-extended post-processing kinematic (PPK) in a marine environment*. ION GNSS 2005, Long Beach, California, United States of America, Sept. 13–16. Oral presentation.

Kingdon, R., A. Ellmann, P. Vaníček and M. Santos (2006). "The cost of assuming a lateral density distribution in corrections to Helmert orthometric heights." Paper presented at the American Geophysical Union 2006 Joint Assembly, Baltimore, Maryland, U.S.A., May 23–26.

Kingdon, R., A. Ellmann, P. Vaníček, and M. Santos (2006). "Estimating the cost to Helmert heights of a lateral approximation of the topographical density distribution." Canadian Geophysical Union Annual Scientific Meeting, Banff, Alberta, Canada, May 14–16.

Kingdon, R., C. Hwang, Y.-S. Hsiao, A. Ellmann, M. Santos, and P. Vaníček (2006). "Applications of satellite altimetry to evaluating effects of lake water on gravity and the geoid." International Association of Geodesy Workshop 2006: Coast and Land Applications of Satellite Altimetry, Beijing, China, July 20–22.

Kingdon, R., M. Santos, A. Ellmann, and P. Vaníček (2006). "Estimating the shortcomings of 2D density models in calculating topographical effects on gravity and orthometric heights." First International Symposium of The International Gravity Field Service (IGFS), Istanbul, Turkey, August 28–September 1.

Ellmann, A., P. Vaníček, M. Santos and R. Kingdon (2006). "The partnership of the precise geoid and orthometric heights." Canadian Geophysical Union Annual Scientific Meeting, Banff, Alberta, Canada, May 14–16.

Ellmann, A., P. Vaníček, M. Santos and R. Kingdon (2006). "Symbiosis of orthometric heights with the geoid." The 8th Geomatics for Informed Decisions (GOIDE) Annual Scientific Conference, Banff, Alberta, Canada, May 31–June 2.

- Kingdon, R., P. Vaníček, and M. Santos (2007). "A forward-modeling approach to estimating effects of three-dimensional topodensity on orthometric height." Canadian Meteorological and Oceanographic Society-Canadian Geophysical Union-American Meteorological Society Congress, St. John's, Newfoundland, Canada, May 28–June 1.
- Kingdon, R., P. Vaníček and M. Santos (2007). "Coping with topographical density in three dimensions: an application of forward modeling to orthometric height calculations." International Union of Geodesy and Geophysics XXIV General Assembly, Perugia, Italy, July 2–3.
- Kingdon, R., P. Vaníček and M. Santos (2008). "A forward modeling approach for estimation of 3D density effects on geoidal heights." Canadian Geophysical Union Annual Scientific Meeting, Banff, Alberta, Canada, May 11–14.
- Kingdon, R., P. Vaníček and M.C. Santos (2008). "Estimating the effects of 3D density variations on geoidal height using forward modeling." Gravity, Geoid and Earth Observation Symposium, Chania, Crete, Greece, June 23–27.
- Kingdon, R., P. Vaníček and M.C. Santos (2009). "Effects of hypothetical complex mass-density distributions on geoidal height." 2009 IAG Scientific Assembly, Buenos Aires, Argentina, 31 August–4 September.
- Kingdon, R., P. Vaníček and M.C. Santos (2010). "Testing Stokes's Integration Using Global Geopotential Models." Canadian Geophysical Union Annual Scientific Meeting, Ottawa, Ontario, Canada, 31 May–4 June.
- Kingdon, R., P. Vaníček and M.C. Santos (2010). "Testing Stokes's Integration Using Global Geopotential Models." AGU Meeting of the Americas, Foz do Iguaçu, Brazil, 8–12 August.
- Kingdon, R., P. Vaníček and M.C. Santos (2010). "The History and Future of Geoid Determination at UNB." Geomatics Atlantic 2010: Surveying the Past, Mapping the Future, Fredericton, New Brunswick, Canada, 27–29 October.
- Kingdon, R., P. Vaníček and M.C. Santos (2011). "Poisson Downward Continuation by the Relaxed Jacobi Method." CGU Annual Scientific Meeting, Banff, Alberta, Canada, 15–18 May.